Modelling and Simulation of Phenotypic Variability in Cardiac Tissue and Application to Stem Cell-Derived Cardiomyocytes

Louise Bowler

Lincoln College

University of Oxford

A thesis submitted for the degree of

Doctor of Philosophy

Hilary 2018

For Nana and Grandad

Abstract

Prediction of the safety of a novel pharmaceutical compound at the earliest possible stage of development is of great importance for drug discovery. Cardiac side-effects are a particular cause for concern, with several drugs such as Terfenadine and Cisapride having being withdrawn from the market due to adverse events. Investigation of the properties of novel compounds can be facilitated by the use of *in silico* models, which can provide a high-throughput and low-cost method of translating the known effects of a novel compound on multiple ion channels to effects on tissue-level electrophysiology.

In this thesis, we examine the case of monolayers of human stem cell-derived cardiomyocytes (hSC-CMs). In recent years, experimental systems utilising such monolayers have become more widely used, especially following their inclusion in the Comprehensive *in vitro* Proarrhythmia Assay (CiPA) initiative. In contrast to cells found in the adult heart, hSC-CMs beat spontaneously and are not necessarily spatially segregated by their subtype, or phenotype. These properties mean that the overall electrophysiological activity of a monolayer is sensitive to the spatial arrangement of the different types of cells. The simulation framework must therefore permit different spatial distributions of phenotypes.

The first part of this thesis is dedicated to the development of a simulation framework for modelling monolayers of hSC-CMs that incorporate phenotypic variability. While tissue containing regions of distinct cell types can be modelled using the bidomain equations, this approach is not computationally efficient when the cells are well-mixed. We test a novel approach, the *homogenised phenotypes* model, where the homogenisation process that underpins the bidomain equations is carried out over a small unit that contains two cell types.

In the second part of this thesis, we utilise the homogenised phenotypes model in simulations of the micro-electrode array, a device which is used to record extracellular field potentials from a monolayer of hSC-CMs, and compare our simulation predictions with experimental recordings. We investigate how variability in cellular phenotype and the distribution of these phenotypes throughout the monolayer affects the field potential, how this variability is manifest in simulations of drug block, and discuss the implications of our findings for the safety assessment process.

Acknowledgements

First and foremost, my thanks go to my supervisors, Gary Mirams and David Gavaghan, for their enthusiasm, energy and inspiration over the last five years. I would also like to thank Jonathan Whiteley for his help with the re-homogenisation of the bidomain equations. I couldn't have wished for better guidance as we worked on the paper that led to Chapter 5 of this thesis.

The Chaste development team, in particular Joe Pitt-Francis, Jonathan Cooper and Louie Cardone-Noott, were a huge help throughout this project. I am also grateful to Kate Harris (GlaxoSmithKline) and Mike Clements (Axion Biosystems) who provided the experimental data used in the later chapters of this thesis and kindly answered many of my questions about the micro-electrode array.

There were times during this DPhil that weren't smooth sailing, and I owe heartfelt thanks to everyone who gave me support when I needed it. Kylie Beattie, Anna Muszkiewicz and Beth McMillan were wonderful companions over many a lunch and dinner, dishing out encouragement and advice along with the food. My violin teacher, Stefan Spencer, used each lesson to give my mind a break from the DPhil with some refreshing and inspirational music, leaving me more motivated to carry on with everything that came my way. My thanks also go to Lincoln College for their generous financial support; to the college doctor, Dr Naomi Drury, for her advice; and to Dave Kay and Blanca Rodriguez for checking in with me so often during my final year.

I feel very lucky to have such wonderful friends and family who have been incredibly supportive throughout my time at Oxford. We may not always have been in the same city, but I have always been able to rely on my friends for great company, games, tea and holidays. I am forever grateful to my Mum and Dad, and my sisters Helen and Nicola, for believing in me and encouraging me for as long as I can remember. Finally, thank you to Ingolf for being there for me every step of the way.

Contents

List of Figures

List of Tables

Chapter 1

Introduction

In this chapter, we outline the motivation behind this thesis and then describe how each of the chapters addresses the research questions.

1.1 Motivation

Identification of drugs with a high risk of adverse effects on the heart is a pressing issue for the pharmaceutical industry. Failure to do so can result in the late-stage termination of a drug already in clinical trials, costing tens or hundreds of millions of pounds, or, in the worst-case scenario, the withdrawal of an unsafe drug from the market following reports of adverse events in patients (DiMasi et al., 2003; Laverty et al., 2011).

Wider use of *in silico* mathematical models of cardiac electrophysiology in safety assessment studies is now being encouraged by regulators and adopted by the pharmaceutical industry. Recent proposals by the Comprehensive *in vitro* Proarrhythmia Assay (CiPA) initiative have included simulation of the action potential in a single cardiac cell, under the effects of a novel pharmaceutical compound, as a means of assessing proarrhythmic potential, i.e. the risk of a pre-existing arrhythmia being made more frequent, or a new arrhythmia being

provoked, as a result of the therapy (Cavero and Holzgrefe, 2014). Such a systems biology-based approach can scale up information about the ion channel-blocking properties of a novel compound to give insight into the potential impact on the electrophysiology of a whole cardiac cell.

A second CiPA proposal is to expand the use of human stem cell-derived cardiomyocytes in the safety assessment process. Human stem cell-derived cardiomyocytes are widely available from commercial sources, can be cultured easily in the laboratory, are amenable for use in experiments and possess some of the electrophysiological characteristics of adult cardiomyocytes — properties which make them a promising tool for the cardiac safety assessment of novel pharmaceutical compounds, and potentially a viable alternative to tests on tissue derived from animals.

Many reports suggest that individual human stem cell-derived cardiomyocytes can be classified as one of three subtypes, or phenotypes, where the name of each phenotype reflects the similarity of the action potential morphology to that observed in particular regions of the adult heart (He et al., 2003). While the three subtypes do resemble the action potential of cells found in the adult heart, they are by no means identical. Unlike adult cardiomyocytes, stem cell-derived cardiomyocytes usually beat spontaneously, and also possess a less regular structure. The spatial arrangement of the subtypes is not fixed, and the impact of the phenotype arrangement on the resulting electrophysiological activity is not yet understood. Consequently, we do not yet know if or how the presence of different phenotypes contribute to the electrical signals recorded as part of the cardiac safety assessment process.

In this thesis, we use computational modelling to investigate the links between the spatial arrangement of the different phenotypes of stem cell-derived cardiomyocytes and biomarkers which quantify drug-induced effects on the electrical signals recorded from such cultures.

Modelling such a system brings its own challenges which we address in the first part of this thesis. At present, the majority of tissue and organ-scale cardiac sim-

ulations, and the modelling frameworks upon which they depend, consider only a single type of cell within a given region of tissue. For many cases, including those pertaining directly to the human heart, this is considered sufficient. However, the potentially small-scale spatial variation in phenotype within tissue cultures of human stem cell-derived cardiomyocytes calls for an alternative approach to be taken.

We compare two approaches to modelling these cultures: the *partitioned phenotypes* model, where we assume that cells of similar type are clustered together, and the *homogenised phenotypes* model, where we assume that the cells are well, but not necessarily evenly, mixed throughout the tissue. The *partitioned phenotypes* model is an adaptation of the usual implementation of the bidomain equations, a reaction-diffusion system often used to model the electrical activity within cardiac tissue. While it is a viable approach when there are clustered and distinct regions of each cell type, it becomes computationally inefficient when cells are more thoroughly mixed. We therefore propose an alternative, the *homogenised phenotypes* model, where we adapt the homogenisation process in the derivation of the bidomain equations to include several cell types.

We then investigate the electrophysiological properties of human stem cell-derived cardiomyocyte monolayers with different spatial arrangements of cellular phenotype, and perform a comparison against experimental data from microelectrode array recordings. Having developed our model, we simulate the monolayer under conditions where a drug has been applied, as would be done in a safety assessment study. This process allows us to compare the effects of simulated drugs on monolayers with different spatial arrangements of phenotype, and therefore to investigate the sensitivity of signals gathered during this process to the phenotype arrangement.

1.2 Overview of the Thesis

Chapter 2 introduces the biological and pharmacological topics that are of relevance to this thesis. We describe the structure and function of the human heart,

and explain how function may be compromised by the influence of drugs on the cardiac action potential. The present state of the cardiac safety testing paradigm is reviewed, followed by the proposals for future changes through the CiPA initiative. We then introduce simulations of cardiac electrophysiology and describe how they have already been used to enhance our understanding of the links between the ionic currents that underlie the cardiac action potential and the overall function of the heart. The distinct electrophysiology of human stem cell-derived cardiomyocytes is then described, before we conclude with an explanation of how these varied topics are tied together in this thesis.

In Chapter 3, we review the mathematical concepts behind cardiac simulation. We first explain how the cardiac action potential may be expressed by a series of ordinary differential equations that describe the ionic currents that flow through ion channels located in the cell membrane of cardiomyocytes. Moving to the tissue-scale, we then step through a derivation of the bidomain equations, a system of partial differential equations that are often used to model the dispersion of electrical activity through cardiac tissue.

Chapter 4 focusses on the numerical techniques that are used to solve the bidomain equations in this thesis. We start with a practical introduction to the finite element method, before showing how it may be applied to solve the monodomain equation, a simplified version of the bidomain equations. The remainder of the chapter briefly covers other numerical methods that may be employed during the process of solving the bidomain equations, and we finish with a description of the software package used for many of the simulations in this thesis: the *Cancer, Heart and Soft Tissue Environment*, Chaste.

In Chapter 5, we consider the first of the research questions that we discussed at the start of this introduction; namely, how should a system that contains small-scale spatial changes in phenotype be modelled? We describe two models, the *partitioned phenotypes* and *homogenised phenotypes* models, where the homogenisation procedure during the derivation of the bidomain equations is carried out differently. With appropriate changes to the implementation of the solver, the

traditional form of the bidomain model can be used to model cardiac tissue that is partitioned into distinct regions of a single cell type. We compare the partitioned phenotypes model to the homogenised phenotypes model, where several cell types are present in the spatial unit over which the homogenisation process is carried out. After verifying the homogenisation process and noting that the two models are equivalent in the limit of small partitioned regions, we draw some conclusions about which model is most suitable for use in simulations of human stem cell-derived cardiomyocytes.

Chapter 6 describes how the homogenised phenotypes model can be applied to simulations of monolayers of human stem cell-derived cardiomyocytes, as used in a safety assessment assay proposed by the CiPA initiative, the micro-electrode array. We first investigate how variability in cell type is linked to major morphological features in the field potential signals that are recorded by the micro-electrode array. In the second part of our investigation, we show how Gaussian random fields may be used to represent phenotypic heterogeneity throughout the monolayer. We demonstrate how this variability translates into variability in the biomarkers that quantify features of the field potential signal, and compare biomarkers from our simulations with experimental data.

We perform a pilot study of simulations of the micro-electrode array assay in Chapter 7. Using the methods of representing phenotypic variability from the previous chapter, we simulate the electrical activity in monolayers that are exposed to the effects of known drugs. We investigate how variability in phenotype is linked to the variability in biomarkers, and again carry out a comparison against experimental data. We also assess how well our simulations are able to reproduce the effects observed experimentally, and propose suggestions for improvements to the cellular electrophysiology model and the tissue-scale simulation process.

We conclude in Chapter 8 with a summary of how each of our investigations have contributed to simulation and our understanding of the micro-electrode array assay. We then describe the possible directions this work may take in the future, from experimental work that will help to overcome some of the limitations

present in this thesis to further simulations that illustrate how these techniques can be used to complement existing cardiac safety assays.

Appendix A1 contains descriptions of the computational approaches used for the simulations throughout this thesis. The supplementary information in Appendices A2 to A4 provides additional detail on the work presented in Chapters 5 to 7, respectively.

Chapter 2

Cardiac Electrophysiology and Drug Safety Assessment

The field of computational cardiac electrophysiology is very interdisciplinary, bringing together topics from physiology, pharmacology and applied mathematics. In the Introduction, we described how we aim to contribute to the investigation of the micro-electrode array assay by simulation studies of the electrophysiology of such a system.

In this chapter, we introduce the key concepts in each of the fields required to develop simulations of stem cell-derived cardiomyocytes and the micro-electrode array. We review the current state of research in cardiac safety pharmacology and simulation of cardiac electrophysiology, and explain how we will extend upon prior work to develop our simulations.

2.1 Chapter Outline

We begin the chapter with a wide-scale overview of the structure and functionality of the human heart in Section 2.2. We describe the cardiac action potential and how it is related to the contraction of the cardiac muscle, and then consider the consequences of disruption to the action potential.

We provide a brief history of the field of safety pharmacology and describe the current guidelines that are in place for cardiac safety testing in Section 2.3.

Section 2.4 covers a topic of major significance in this thesis: simulation of cardiac cells and tissue. We reserve the more mathematical aspects of this topic for Chapter 3, and keep the focus of this section on the history of the field and cases where models have been used to advance insight into cardiac biology.

In Section 2.5, we describe the generation and characteristics of human stem cell-derived cardiomyocytes and compare their electrophysiology to adult human cardiomyocytes.

We conclude the chapter in Section 2.6 with a discussion of how our research builds upon prior work. We identify gaps in our current abilities to perform simulations of systems such as the micro-electrode array and explain how each issue is addressed later in this thesis.

2.2 The Human Heart

The heart is one of the first functional organs in the human embryo, starting to beat around 22 days post-fertilisation (Schoenwolf et al., 2014). Throughout life, its function is critical to the wellbeing of the body. The task of the heart and the cardiovascular system is to transport blood around the body, which provides other organs and tissues with oxygen and nutrients, and removes carbon dioxide and other waste products.

2.2.1 Conduction and contraction

The human heart is composed of four chambers; the left and right atria and the left and right ventricles. The two atria are smaller, with thinner walls than the ventricles. Blood enters the atria from other parts of the body, and is pumped from there into the ventricles.

Both ventricles have thick walls, particularly the left ventricle. The right ventricle pumps blood towards the lungs, where it is oxygenated before passing back to the left side of the heart. The left ventricle is larger and undertakes the

physically-demanding task of pumping the blood around the rest of the body.

Cardiac muscle cells, or cardiomyocytes, are electrically excitable. The time-course of the potential difference across the cell membrane of a given cell is known as the action potential. The contraction of cardiac muscle follows the pattern of electrical excitation around the heart (Levick, 2012). The heartbeat is paced by a group of spontaneously beating cells, known as the sino-atrial node, which is found on the upper posterior wall of the right atrium. These cells excite their neighbours, with the wave of activity first passing over both atria. The ventricles are electrically insulated from the atria at all but one point, the atrio-ventricular node. Here, the action potential is delayed slightly, allowing the atria to complete their contraction before the next stage of the heartbeat begins.

The electrical stimulus then passes through the Bundle of His and the left and right bundle branches, before reaching the Purkinje fibres embedded in the walls of the ventricles. The nearby cells of the ventricular wall are stimulated at Purkinje-myocyte junctions, and the action potential wavefront passes quickly around the remainder of the ventricles. The subsequent contraction forces blood out of the ventricles and into the rest of the body.

Contraction of cardiac muscle is controlled by the action potential via the movement of calcium into and out of the cytoplasm of the cell. When the intracellular calcium concentration and then bound calcium reaches a certain threshold, myofilaments within the cardiomyocyte contract, shortening the cell (Bers, 2002). The force-concentration relationship is highly non-linear, and depends on the concentration of calcium and the sensitivity of the myofilaments to calcium (which is influenced by the stretching forces on the cell). The orientation of the cardiac tissue fibres dictates the direction in which the cardiomyocytes shorten, ensuring that blood is forced out of the chamber when the muscle contracts.

2.2.2 Cellular phenotypes within the heart

The cardiomyocytes within different regions of the heart are specialised for their particular function. Figure 2.1 shows the variety of action potentials that are

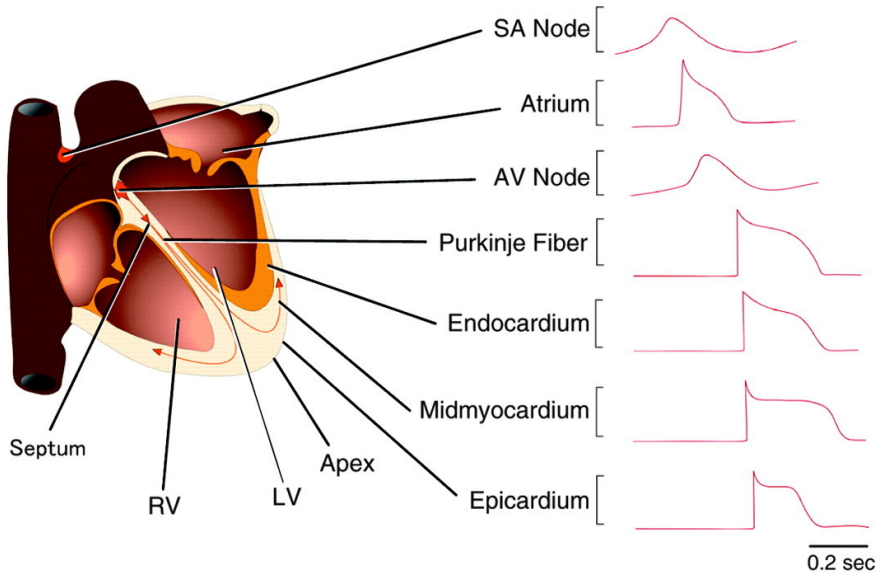

Figure 2.1: The action potentials of different phenotypes of cardiomyocyte in the heart. Cardiomyocytes in the sino-atrial and atrio-ventricular nodes spontaneously depolarise, while all others depolarise only when stimulated by nearby cells. Figure reproduced from Nerbonne and Kass (2005).

found in different areas of the heart.

The cells within the sino-atrial (SA) and atrio-ventricular (AV) nodes can spontaneously activate: they do not require a stimulus from a neighbouring cell in order to depolarise. The SA node is the dominant pacemaker for the whole heart. While the AV node can take over pacemaker function, the AV node has a slower pacemaker frequency and so, in healthy situations, it only depolarises following stimulation from the SA node (Levick, 2012, Chapter 4). The different forms of the atrial and ventricular action potentials are due the presence of a sustained outward current in atrial cardiomyocytes, and other differences in ion channel expression (Amos et al., 1996).

The impact of different action potentials on tissue-level activity due to variation in ion channel presence and expression is the chief focus of the remainder of this thesis, in the context of stem cell-derived cardiomyocytes.

2.2.3 Ion flow during the action potential

Despite the differences in the form of the action potential in different cellular phenotypes, very similar mechanisms are responsible for the changes in potential.

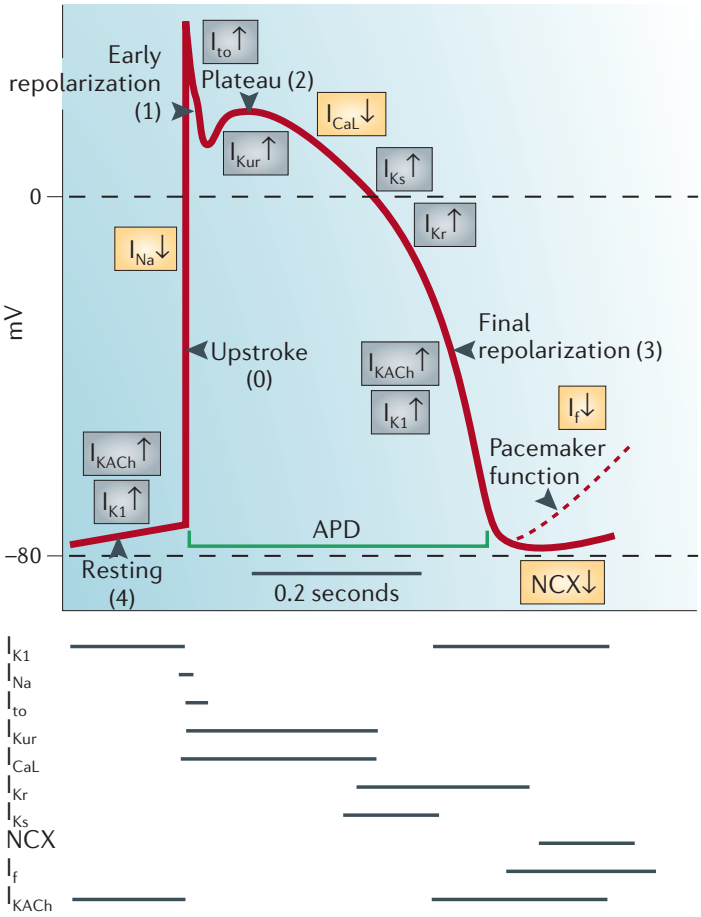

Figure 2.2: The ionic currents involved in the action potential of a cardiomyocyte. Currents marked with an upward arrow in a grey box flow out of the cell, and those with a downward arrow and yellow box flow in. The action potential shown by the bold red line would be typical for a ventricular cell; that of an atrial cell would be similar but with slightly different current contributions to result in a less pronounced plateau. The pacemaker current, I_f, is only found in cardiomyocytes from the SA and AV nodes; these are the only types of cell that spontaneously depolarise as indicated by the dashed red line. Figure reproduced from Nattel and Carlsson (2006).

Figure 2.2 shows how the different currents contribute to the change in membrane voltage across the cell membrane during a single beat, through the full timecourse of the action potential.

Following a stimulus, voltage-gated sodium channels open and allow sodium ions to flow into the cell, down their concentration gradient. This causes a rapid depolarisation, known as "Phase 0" of the action potential (Grant, 2009).

Phase 1, which follows, is a short period of repolarisation. This is caused by the rapid inactivation of the inward sodium current and activation of the

transient outward potassium current. It is thought that the interaction between this current and the following calcium current strongly influence the morphology of the action potential, especially the plateau (Greenstein et al., 2000).

Throughout Phase 2 of the action potential, calcium enters the cell through the L-type calcium calcium channels, which triggers the release of more calcium ions from the sarcoplasmic reticulum. This process is known as calcium-induced calcium release. The high intracellular calcium concentration results in calcium ions binding to the troponin C protein, which triggers contraction of the cardiac muscle (Bers, 2002). The inward flow of positively-charged calcium ions approximately balances the outward flow of potassium ions, leading to a plateau in the action potential.

During Phase 3, various potassium currents contribute towards the repolarisation of the cell. These are the rapid delayed rectifier current (also known by the name of the gene which encodes the ion channel through which the current passes, the human Ether-à-go-go-Related Gene, or hERG), the slow delayed rectifier current and the inward rectifier current (Nerbonne and Kass, 2005).

The final phase of the action potential differs between cells. In ventricular and other excitable cells, a constant resting potential is maintained during Phase 4. However, nodal type cells possess an additional current, the hyperpolarisation-activated current (also known as the "funny current"). This channel opens at low potentials and allows cations into the cell in a non-selective manner (DiFrancesco, 1993). The potential across the membrane increases until it triggers Phase 1 of the following action potential.

In addition to the ion channels discussed above, there are also several different types of ion exchangers and transporters present within the cell membrane. These play an important role in maintaining appropriate concentrations of sodium, potassium and other ions within the cell (Wang et al., 1996; Bers et al., 2003).

This overview has concentrated mainly on the principal currents of the action potential of a ventricular cell. Differences in current type and density give the va-

riety of action potentials discussed in Section 2.2.2; for example, nodal cardiomyocytes have lower fast sodium current density along with their hyperpolarisation-activated current, and atrial cardiomyocytes have a further potassium current, the ultra-rapid current (Nerbonne and Kass, 2005). Further details on the action potential will be given in Section 3.2, which describes the electrochemical gradients that influence the movement of ions and the state of the ion channels.

2.2.4 Disruption to the action potential

The contraction of cardiomyocytes is closely linked to the intracellular calcium present during the plateau phase of the action potential. The coordinated beating action of the heart is thus dependent upon the correct form and timing of the action potential.

However, the action potential can be disrupted for various reasons. Structural changes to ion channels caused by genetic mutations can have profound effects on the action potential. Mutations of the fast sodium channel are associated with Brugada syndrome (Dumaine et al., 1999), while several different mutations contribute to the different subtypes of Long QT (LQT) Syndrome, all of which result in a prolonged action potential (Roden et al., 1996). The major subtypes are LQT1, LQT2 and LQT3, which affect the slow delayed rectifier, fast delayed rectifier and fast sodium currents, respectively (Shimizu and Antzelevitch, 1998; Curran et al., 1995; Wang et al., 1995). Each subtype of the syndrome is caused by a mutation in a gene which encodes for a subunit of the affected ion channel. The structural changes to the protein result in altered current flow through the channel or changes to the opening/closing dynamics. These changes can lead to early after-depolarisations (additional depolarisations that occur during Phases 2 and 3 of the action potential) which can trigger arrhythmias.

In particular, Torsades de Pointes (TdP), a polymorphic ventricular tachycardia, can occur in patients with LQT Syndrome. The name “Torsades de Pointes” originates from the form of the electrocardiogram recorded from patients. In Figure 2.3, the characteristic “twisting of the points” can be seen during arrhythmic

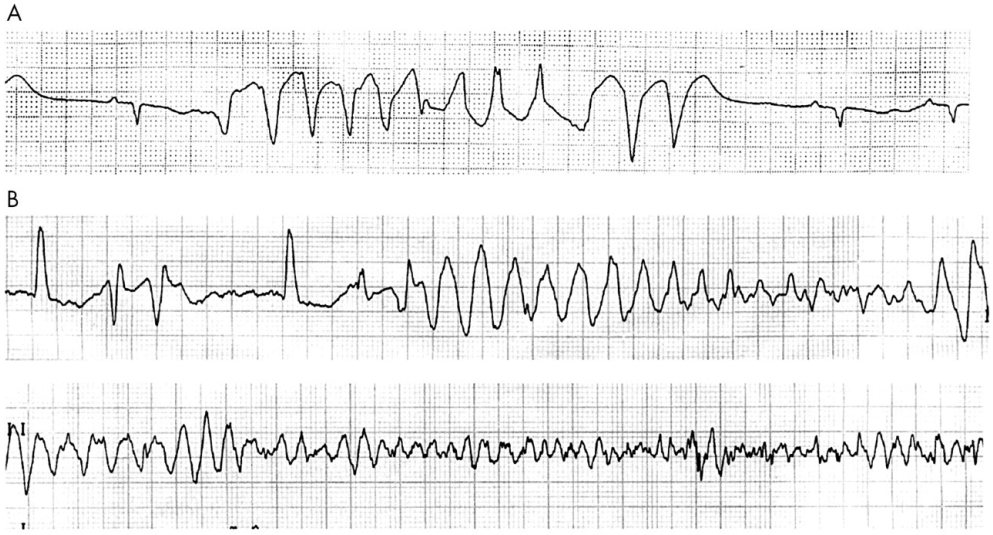

Figure 2.3: Example electrocardiograms from patients experiencing Torsades de Pointes. The top panel, A, shows a self-terminating arrhythmia, while the case in the middle and lower panels, B, degenerates into ventricular fibrillation. Figure reproduced from Yap and Camm (2003).

episodes. Despite having relatively few symptoms of the disease for the majority of their lives, the abnormal heart rhythm caused by TdP can result in sudden cardiac death in LQT patients.

Ion channel function can also be affected by external mechanisms. Anti-arrhythmic drugs often work by blocking a particular type of ion channel. The Vaughan-Williams I, III and IV classes of anti-arrhythmics work by reducing the fast sodium, rapid delayed rectifier and L-type calcium currents respectively (Zipes and Jalife, 2009, Chapter 96). While the action of anti-arrhythmics on ion channels is intended, their influence on cardiomyocytes in other regions of the heart can occasionally induce more serious types of arrhythmia than that which was originally being treated (Nattel and Carlsson, 2006).

Non-cardiac drugs can also bind to ion channels and affect their function. Reports of arrhythmia, in particular Torsades de Pointes, caused by the unintended actions of drugs have highlighted the importance of being aware of these potential side effects before drugs are made available to patients; consequently, much effort has recently been put into refining the tests used by Safety Pharmacology departments within pharmaceutical companies.

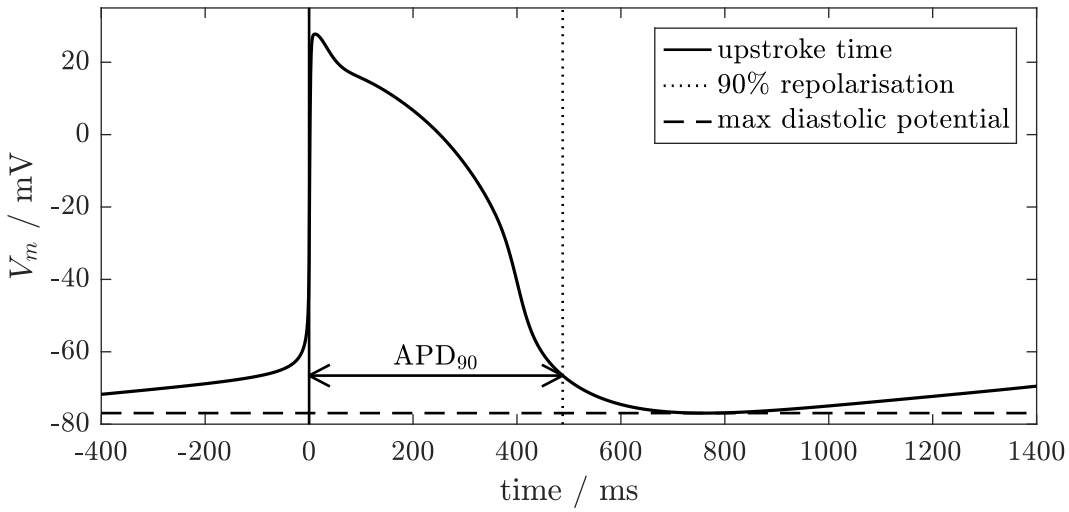

Figure 2.4: Biomarkers of the cardiac action potential. The most widely-used biomarkers are indicated on this simulated action potential from a ventricular-like human stem cell-derived cardiomyocyte, generated using the Paci et al. (2013a) model. This particular type of cell will be discussed in more detail in Section 2.5.

2.2.5 Features of the action potential

When discussing the differences in action potential morphology between different types of cardiac cell, or how the morphology is influenced by some external factor, it is often convenient to express these properties in terms of *biomarkers*. Some of the most widely-used biomarkers are shown in Figure 2.4.

The start of the action potential, or upstroke, is defined as the time at which the transmembrane voltage increases fastest during a given beat. The numerical value of the gradient in voltage at this time is termed the upstroke velocity. The timing of the upstroke can also be used to calculate the inter-beat period, and therefore the beat rate.

The most repolarised potential during a given beat is known as the maximum diastolic potential. This measure is widely used in cells which beat spontaneously, as they do not exhibit a constant resting potential as found in most other types of cardiomyocyte (see Section 2.2.2).

Definition of the duration of the action potential is somewhat more flexible. The action potential duration, or APD, is defined as the time at which a given percentage of repolarisation is achieved following the upstroke time. It is most

common to refer to the APD_{90}, which is indicated in Figure 2.4. The use of several different variants of APD, such as APD_{30}, can be used to provide information on the shape of the action potential; for instance, whether it is triangular in shape, or exhibits a well-defined plateau region.

Changes to each of these biomarkers are used widely to indicate the effect of a drug on the action potential, and to identify whether the level of change is likely to be detrimental to the overall function of the cell (and therefore the heart). We now discuss the cardiac safety assessment process in more detail.

2.3 Cardiac Safety Testing in Drug Development

Every novel compound developed by the pharmaceutical industry must undergo toxicity and safety screens before human trials of the compound's safety and efficacy can begin. Cardiac safety testing is of particular importance. Compounds often exhibit off-target effects in addition to their intended action; should a compound bind to or interfere with the kinetics of the ion channels in the heart, normal electrophysiological function can be compromised. This can lead to rare events such as cardiac arrhythmia, which can potentially be fatal.

Due to the risks involved, a series of assays are performed before a novel compound is tested in humans. Binding assays detect whether a new compound binds to particular ion channels. More complex tests look at the effects of the drug on a single cardiomyocyte or cardiac tissue, either *ex vivo* or *in vivo*.

Prior to the late 1990s, these tests were generally performed by the drug discovery group that developed the compound as specialised safety pharmacology teams did not exist at this time (Redfern et al., 2002). However, following several instances where drugs had to be withdrawn from the market after being used by the public for several years, the guidance on safety testing was updated.

2.3.1 Safety guidelines

The withdrawn drugs included Cisapride, which was associated with heart rhythm abnormalities (Henney, 2000) and Terfenadine, which caused ventricular arrhyth-

mias in some patients (Josefson, 1997). The arrhythmias were initiated by a relatively simple molecular interaction: block of the hERG channel by the drugs led to action potential prolongation as the flow of potassium out of the cardiomyocytes was restricted (Carlsson et al., 1997; Roy et al., 1996). As both drugs were treatments for relatively minor illnesses (heartburn and hayfever, respectively), the associated risk was too great, and they were withdrawn from the market. The common mechanism of action of these drugs, and others, influenced subsequent safety guidelines, promoting a focus on the hERG channel.

The International Conference on Harmonisation (ICH) S7A guidelines covered strategies for testing for adverse effects to the cardiovascular, nervous and respiratory systems (ICH, 2001). The cardiovascular component of this "core battery" of tests recommended that quantities such as blood pressure, heart rate and changes in the electrocardiogram be studied. However, the authors recognised that these tests did not necessarily pick up the likelihood of ventricular arrhythmias such as Torsades de Pointes.

The true incidence of drug-induced TdP is difficult to quantify, being low in the general population (Molokhia et al., 2008; Sarganas et al., 2014). However, drugs at the higher end of the risk scale, for example Sotalol and Quinidine, have been linked to TdP in approximately 1% and up to 9% of patients respectively. (Schwartz and Woosley, 2016). Drug-induced TdP is associated with an appreciable risk of sudden cardiac death; for instance, of the 97 reports of TdP in patients taking Cisapride between 1983 and 1999, six were fatal (Darpö, 2001).

The risk of such outcomes led to the publication of the ICH S7B and E14 guidelines (ICH, 2005a; ICH, 2005b). ICH S7B focussed specifically on delayed ventricular repolarisation as that is closely associated with the onset of arrhythmia (Yap and Camm, 2003). ICH E14 set out guidance for the "thorough QT/QTc" study, wherein the QT interval of the electrocardiogram is monitored in healthy volunteers. Following a baseline assessment of each volunteer's QT interval, they are divided into at least two groups, one of which will receive a placebo, and the other, the drug that is being assessed. More complex arrange-

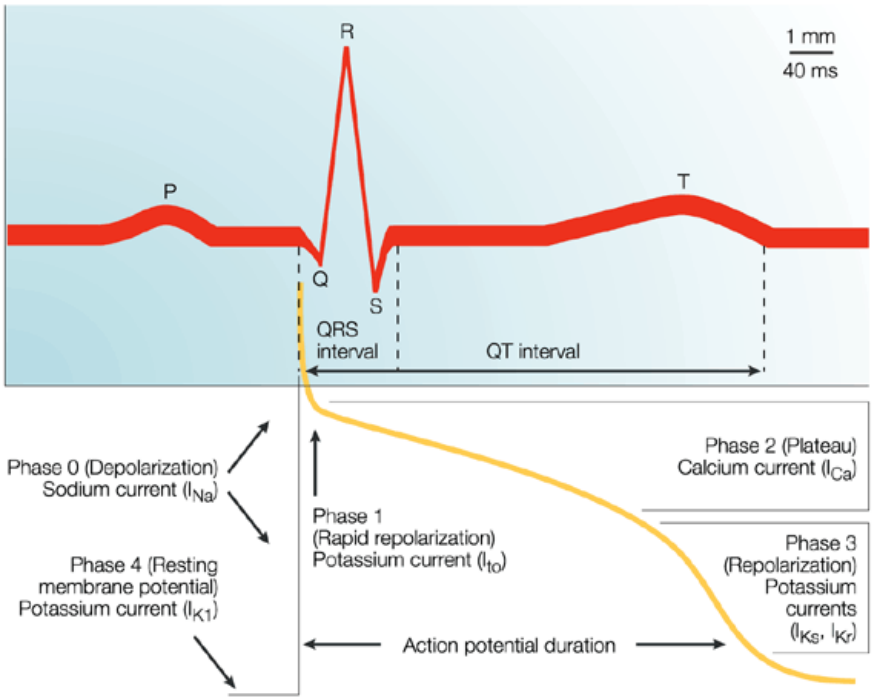

Figure 2.5: Comparison of the electrocardiogram and the cardiac action potential. The major morphological features of the electrocardiogram are labelled P–T. The QRS complex is associated with depolarisation of the cardiac tissue, while the length of the QT interval is closely correlated with the duration of the action potential. Reproduced from Fermini and Fossa (2003).

ments such as the inclusion of a positive control arm and cross-over studies have also been used (see, for example, Malik et al. (2012)). If prolongation of the rate-corrected QT interval (the QTc) by more than 10 ms is detected, further electrocardiogram studies are carried out in later stages of the trial to identify those drugs that pose an appreciable arrhythmic risk (Shah, 2005).

An *in vitro* screen for block of the hERG channel is standard procedure for each new compound. Following this, an *in vivo* assessment of the QT interval in dogs, monkeys or guinea pigs is made (Hammond et al., 2001). As Figure 2.5 shows, the QT interval on the electrocardiogram is correlated with the action potential duration. The QT interval therefore serves as an indication of the impact of the drug on the repolarisation time of the tissue (Fermini and Fossa, 2003). A commonly-used additional test is a study of the action potential parameters in a single or multi-cellular cardiomyocyte preparation.

While successful at preventing hERG block-related arrhythmogenic drugs

from reaching the market, there are still concerns about the safety testing system. The desire for a "fail fast, fail cheaply" approach to drug testing can lead to novel compounds being removed from the development pipeline at an early stage following an indication of hERG block or QT prolongation (Heijman et al., 2014). However, the effects of a drug may be more complex than this; if other ion channels are also blocked, they can compensate for the effects of reduced potassium current. It has been reported that QT prolongation is not always sufficient to indicate that a compound will cause arrhythmia (Lawrence et al., 2005; Hondeghem, 2006).

Over 25% of compounds which are removed from development during the preclinical testing stage are removed due to cardiovascular concerns picked up during safety tests (Laverty et al., 2011). However, not all potential issues are detected at this time; some are picked up in the later stages of clinical trials. With the increased use of computational modelling and the arrival of novel assays such as stem cell-derived cardiomyocytes, a new initiative for cardiac safety testing is now under development.

2.3.2 Typical safety pharmacology screening

The typical starting point of a safety pharmacology assessment is an ion channel screen to identify whether the compound binds to any important proteins of interest. This will include an assessment of how well the molecule binds to hERG, but other ion channels may also be checked, depending on the priorities and other tests of the company. In addition, the panel will also include molecules related to other organ systems such as G protein-coupled receptors and enzymes (Bowes et al., 2012).

A variety of methods are used for ion channel screens, which have varying levels of throughput. The gold standard of manual, single-cell patch-clamping is precise yet time-consuming, so higher-throughput options are favourable. These include hetrologous expression systems, where the hERG channel (or another) is expressed in non-cardiomyocytes such as human embryonic kidney or Chinese

hamster ovary cells. The block of the channel by the applied drug can then be determined by methods such as radioligand displacement binding (Chiu et al., 2004; Diaz et al., 2004), membrane potential dye, and rubidium efflux (Tang et al., 2001). Automated patch-clamp methods provide a medium-throughput approach (Bridgland-Taylor et al., 2006), but the variability between their results can be appreciable (Elkins et al., 2013).

Tissue or organ scale assays are low-throughput in comparison, but provide details of how the QT interval is affected by the drug. The rabbit ventricular wedge (Wang et al., 2008) is a commonly used *ex vivo* assay, while the effect of the drug on a whole heart can be examined using the Langendorff preparation of an isolated heart (Hamlin et al., 2004), or QT studies of a conscious animal (Toyoshima et al., 2005; Hamlin, 2007). Thorough QT studies are also carried out to provide an initial assessment of QT prolongation associated with the drug, although the timing of this assay may vary (Darpo, 2010; Wiśniowska et al., 2017).

2.3.3 CiPA: the Comprehensive *in vitro* Proarrhythmia Assay

The CiPA initiative was proposed in 2013 as a paradigm to detect compounds that cause the Torsades de Pointes ventricular arrhythmia, replacing the current focus on detecting delayed ventricular repolarisation. As delayed ventricular repolarisation does not necessarily lead to TdP, and nor is it the only cause, the regulators had become concerned that the development of compounds had become restricted due to a focus on hERG block and QT prolongation, even though other effects of the compound may counteract the risk of arrhythmia (Sager et al., 2014; Fermini et al., 2016). While drug-related reports of TdP have been linked to hERG block and QT prolongation, not every drug that blocks hERG or prolongs the QT interval causes TdP (Fenichel et al., 2004). Given that new assays had recently become available, the decision was made to try to move to a set of tests which would be human-relevant and more specific in picking out those compounds likely to cause TdP.

The proposed tests are divided into four components (Gintant et al., 2016):

1. Examine the effects of the compound on human ion channels *in vitro*.
2. Reconstruct the action potential with the effects of the compound using an *in silico* (mathematical) model of an adult human ventricular cell.
3. Confirm the expected effects using human stem cell-derived cardiomyocytes.
4. Use clinical ECG (electrocardiogram) readings to check for any unexpected effects of the compound.

Components one and four adapt aspects of safety assessment that are already carried out. Until now, the main application of ion channel screens has been to identify interactions between the hERG channel and the new drug. The first of CiPA's components will extend this to multiple ion channels, so that the drug's propensity to block currents such as I_{CaL}, I_{Na}, $I_{\text{late Na}}$, I_{K1}, I_{Ks} and I_{to}, in addition to I_{Kr}, will be known at an early stage (refer to Figure 2.2 for details of these currents' contributions to the cardiac action potential). As in the thorough QT studies that are carried out at present, the fourth component will identify any impact on the ECG in smaller-scale trials.

The second and third components utilise newer methods, which we discuss shortly: *in silico* models of cardiac electrophysiology in Section 2.4, and human stem cell-derived cardiomyocytes in Section 2.5.

The CiPA initiative is not yet ready for industry-wide adoption, but a great amount of work is currently in progress on evaluating and refining each of the intended components (Cavero et al., 2016; Colatsky et al., 2016; Crumb Jr. et al., 2016). Once that work is completed, a new set of regulatory guidelines will be proposed to the pharmaceutical industry.

2.4 Simulations of Cardiac Electrophysiology

The concept of describing the ionic currents that cross the cell membrane with ordinary differential equations originated with Hodgkin and Huxley in their series of papers on the action potential of the squid giant axon (Hodgkin and Huxley, 1952b; Hodgkin and Huxley, 1952c; Hodgkin and Huxley, 1952d), which culmi-

nated in the first cellular electrophysiology model (Hodgkin and Huxley, 1952a). Like a cardiomyocyte, the axon is an excitable cell, albeit with a different structure and function. The axon is specialised for propagating a signal down its length, so the action potential can be of much shorter duration than it is in the cardiomyocyte. Nevertheless, the mechanisms involved in excitation and recovery for both types of cells are fairly similar.

Hodgkin and Huxley viewed the axon membrane and associated ion channels as an electrical circuit, where the cell membrane acted as a capacitor in parallel with three separate resistor-voltage source branches. These branches represented the potassium, sodium and leak (chloride and other ions) currents. The conductance of the resistors in the sodium and potassium branches were variable to reflect the voltage-gating of the ion channels. We return to the Hodgkin-Huxley model later, in Chapter 3, where we discuss how the electrical circuit representation can be expressed as a system of ordinary differential equations.

2.4.1 Cardiac cellular electrophysiology models

Following the success of the Hodgkin-Huxley model, Noble (1962) demonstrated how the model could be adapted for cardiomyocytes; specifically, cardiac Purkinje fibre cells. Noble modified the potassium current, splitting it up into two components to model separately two different types of potassium current present in cardiac cells which have different rates of response to the changing membrane voltage.

As more detailed knowledge of the ionic currents and properties of the ion channels in cardiac cells became available, further models were developed in a similar manner. The updated version of the Noble (1962) model, McAllister et al. (1975), included the recently discovered calcium current, and as more experimental data became available this model was updated again (DiFrancesco and Noble, 1985). With data from other species and cell types, the number of models continued to grow.

Some of the most notable include the Beeler and Reuter (1977) model (the

first ventricular cell model), the Luo and Rudy (1991) and Luo and Rudy (1994) series of models (for guinea pig ventricular cells) and the Priebe and Beuckelmann (1998) model (the first human ventricular cell model). The most up-to-date human ventricular cell models are those of Iyer et al. (2004), ten Tusscher et al. (2004), ten Tusscher and Panfilov (2006), Grandi et al. (2010), O'Hara et al. (2011) and Asakura et al. (2014); the Courtemanche et al. (1998) and Grandi et al. (2011) models are popular choices for simulating human atrial action potentials. For a more thorough overview of the many different cell models now available, see Fink et al. (2011) and Noble et al. (2012).

The later models have greater levels of complexity; they were often adapted from a previous model with additional currents or changes to ion channel kinetics (Niederer et al., 2009). To enable easy re-use of the models, versions in the CellML language (Garny et al., 2008) are available in a public repository[1].

In addition to these complex models, simplified versions of action potential models are useful for studies of tissue dynamics where the precise details of the separate currents are not required. In these phenomenological models, the individual currents are not represented. Instead, the action potential is represented by a smaller system of ordinary differential equations. The most well-known of these phenomenological models is the FitzHugh-Nagumo model (FitzHugh, 1961; Nagumo et al., 1962), which is comprised of a fast activation variable and a slow inactivation variable along with three constant parameters that tune the beat rate and action potential duration (Xu et al., 2014). The three-variable Fenton and Karma (1998) and the four-variable Bueno-Orovio et al. (2008) models offer more complex alternatives that more closely represent the action potential morphology of cardiomyocytes.

2.4.2 Models of cardiac tissue

Reaction-diffusion equations are partial differential equations with two components: the diffusion term describes the spread of a quantity throughout the

[1] `https://www.cellml.org/`

medium, while the reaction term acts as a source or sink of the quantity. Equations of this type are well-suited for modelling the spread of electrical potential in cardiac tissue.

The bidomain equations are a pair of reaction-diffusion equations that represent the passage of the electrical potential through the intracellular and extracellular domains of cardiac tissue on a macroscopic scale. They were first described by Tung (1978), who derived them from the principle of charge conservation and Ohm's law. They can also be derived using a homogenisation approach, which scales up from the microscopic scale to the macroscopic one (Keener and Panfilov, 1996; Richardson and Chapman, 2011). The underlying assumption for this derivation is that the cardiac tissue can be considered as a repeating pattern of many identical units (cells), which can be represented by a single homogenised unit. We provide a more detailed description of the bidomain problem in the context of this project in Chapter 3. Under specific circumstances, the bidomain equations can be simplified to the monodomain equation; which is more computationally tractable (Potse et al., 2006).

Each of the monodomain and bidomain equations requires an expression for the transmembrane current at every point in space. This can be provided by a single-cell cardiac electrophysiology model, such as those described in the previous section. There are several simulation packages available which allow easy combination of the single-cell ordinary differential equations and the reaction-diffusion partial differential equations; these include Chaste (Pitt-Francis et al., 2009; Mirams et al., 2013) and CARP (Vigmond et al., 2003), amongst others (Seemann et al., 2010; Heidenreich et al., 2010). These packages typically employ the finite element method to solve the partial differential equations (Pathmanathan et al., 2010), although the finite difference method has also been used successfully. For a comparison of the different codes, see Vigmond et al. (2008) and Niederer et al. (2011).

Simulations of the whole heart have been used to investigate the effects of genetic mutations (Sadrieh et al., 2014), drugs (Zemzemi et al., 2013) and changes

to the properties of cardiac tissue due to myocardial infarction (Cardone-Noott et al., 2014) on the electrocardiogram.

The bidomain equations have been extended to systems where two electrically active cell types are present, through the extended bidomain (or tridomain) equations (Sachse et al., 2009). In addition to being used to simulate mixtures of cardiomyocytes and fibroblasts, the extended bidomain equations have also been applied to simulations of the gut, where cells of Cajal and smooth muscle cells are present (Buist and Poh, 2010; Corrias et al., 2012).

All of these approaches exclusively consider the electrical activity in the tissue, rather than the contraction of the tissue or heart. Electromechanical simulations couple the calcium dynamics from the electrophysiological model to a mechanical model of tissue deformation. This enables cases such as stretch-activated arrhythmias to be examined in detail (Trayanova et al., 2011).

Insights can also be gained from simpler models of cardiac tissue. The cable equation has traditionally been used to simulate the progression of the action potential down the axon of a neuron, and this simplification to one dimension greatly reduces the complexity of cardiac simulations. Gima and Rudy (2002) investigated how alterations to the ionic currents resulted in changes to the ECG using this method.

Other simulations of tissue take an entirely discrete approach. Winslow et al. (1993) extended the electrical circuit description of a single cell into one that modelled cells within a tissue sample via additional resistors, to show that frequency entrainment in the sino-atrial node could be achieved with relatively low cell-cell coupling. A different type of discrete model, cellular automata, was used by Christensen et al. (2015) to look at the effects of structural heterogeneities on the propagation of the action potential through tissue, with relevance to atrial fibrillation. As the discrete approach can explicitly model the connections between cells, it is more appropriate than the continuous monodomain or bidomain models in certain cases, when predictions at or below the cell scale are required due to cellular-scale heterogeneity.

2.4.3 Insights into safety pharmacology from simulation studies

Simulations of the action potential have been of great assistance in understanding the properties of multi-ion channel blocking drugs such as Ranolazine (Noble and Noble, 2006; Belardinelli et al., 2006) and Amiodarone (Yuan et al., 2015). Each of these drugs would normally be considered high-risk due to their hERG-blocking abilities, but their concurrent block of the late sodium and L-type calcium currents respectively have been shown to be protective against the onset of TdP. Simulations can also be utilised to investigate the impact of channel kinetics and state-dependent binding on the overall effect of a drug (Lee et al., 2016c).

Computational techniques are also useful for moving from ion channel block data to measures of arrhythmic risk. Biomarkers quantifying action potential prolongation (Mirams et al., 2011) and occurrence of early after-depolarisations (McMillan et al., 2017) from simulations have out-performed traditional estimates of arrhythmic risk based on hERG block alone. Mistry et al. (2015) and Cummins Lancaster and Sobie (2016) have also proposed risk classifiers based on features of the action potential from simulations or directly from multiple ion channel block. Recently, risk markers based on simulations that incorporate inter-cell variability have been suggested (Passini et al., 2017).

In silico versions of tissue studies such as the rabbit ventricular wedge have been proposed as a potential way of reducing the number of assays which involve the use of animal tissue (Beattie et al., 2013). The effects of drugs on the QT interval in humans can be directly simulated using models of the human torso (Zemzemi et al., 2013).

As we discussed in Section 2.3.3, the CiPA proposals include a component that utilises *in silico* investigations of arrhythmic risk. The CiPA *in silico* working group is currently developing modifications to the O'Hara et al. (2011) model of the ventricular action potential to capture the dynamic interactions between drugs and the hERG channel (Li et al., 2017; Dutta et al., 2017).

2.5 Human Stem Cell-Derived Cardiomyocytes

Human embryonic stem cells were first derived by Thomson et al. (1998) from human blastocysts, and it was shown that the cells could differentiate into all three germ layers. Three years later, the first report of embryonic stem cell-derived cardiomyocytes (hESC-CMs) was published (Kehat et al., 2001). The authors noted that stem cell-derived cardiomyocytes could have many potential applications, ranging from the study of human cardiac development to safety assays and cardiac tissue repair.

Despite their success as a model of cardiomyocytes, the ethical issues surrounding embryonic stem cell-derived cardiomyocytes remained a problem. An alternative method of deriving stem cells that did not involve the destruction of an embryo was therefore preferable. Such a method was developed by Takahashi et al. (2007), who induced adult human fibroblasts back into a pluripotent state by the retroviral transduction of four transcription factors. Once the transcription factors were present inside the fibroblasts, some of the fibroblasts returned to a pluripotent state, from which they could potentially develop into any type of cell. These cells were later induced into a cardiac lineage by Zhang et al. (2009). Cardiomyocytes derived from this induction process are referred to as human induced pluripotent stem cell-derived cardiomyocytes, or hiPSC-CMs.

Since then, both lab-specific and commercial lines of stem cell-derived cardiomyocytes have been studied. Production methods have been improved to increase the purity of cardiomyocytes within these cultures, as the earliest contained a substantial component of other cells, such as fibroblasts (Burridge et al., 2011; Mummery et al., 2012). Despite induced pluripotent stem cell-derived cardiomyocytes coming from different sources (dermal fibroblasts, peripheral blood mononuclear cells, and others), any epigenetic memory within the cells is not considered to have a great impact on the electrophysiology of the resulting hiPSC-CMs (Riedel et al., 2014).

The characteristics of hESC-CMs and hiPSC-CMs are described together in the following sections; we refer to the two types together as stem cell-derived

cardiomyocytes, or hSC-CMs. Generally, the attributes of the two types have been reported to be similar (Gherghiceanu et al., 2011), with any variation in cells from different sources being comparable to cell-to-cell variability (Lopez-Izquierdo et al., 2014). The pharmacological responses of the two types of hSC-CM have also been shown to be comparable (Yokoo et al., 2009).

2.5.1 Electrophysiology and maturation

Stem cell-derived cardiomyocytes have an immature electrophysiology compared with adult cardiomyocytes, and have been reported to resemble more closely foetal cardiomyocytes than adult cardiomyocytes (Synnergren et al., 2012). The physical and electrophysiological properties of hSC-CMs change over time as they continually mature (Lundy et al., 2013; Robertson et al., 2013; van den Heuvel et al., 2014). This is due to changing expression levels of the different ion channels, as can be seen in Figure 2.6.

Characteristics associated with immaturity One of the most notable features of the electrophysiological immaturity of hSC-CMs is the presence of spontaneous beating behaviour (the mechanism of which we will discuss in more detail shortly). Pacemaker cells within tissue cultures have maintained stable beat rates over days or weeks (Mehta et al., 2011; Mandel et al., 2012). However, the continuous process of maturation means the spontaneous beat rate may drop over longer periods in culture (He et al., 2003). Structurally, hSC-CMs are small and rounded, in contrast to the rod-like shape of adult cardiomyocytes. However, their shape and size develop over time, which we shall return to later in this section.

Control of maturation The culture conditions influence how quickly stem cell-derived cardiomyocytes mature. Specialised culture medium (Ribeiro et al., 2015), the addition of growth hormones (Yang et al., 2014), the presence of non-cardiomyocytes (Kim et al., 2009), increased size of the tissue culture (Werley et al., 2017) and application of external pacing and stretching (Eng et al., 2016; Shen et al., 2017) have all been reported to assist in the maturation process, likely because these conditions are more similar to those in the developing embryo (Zhu

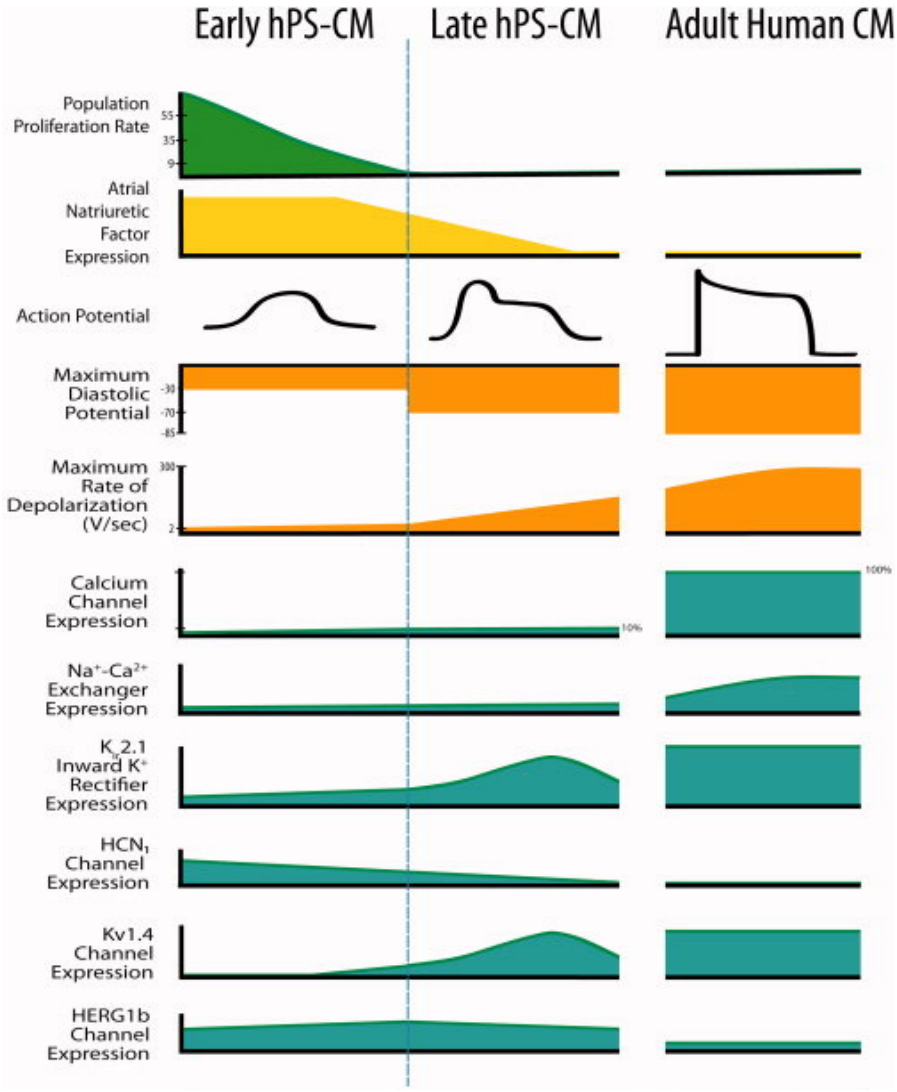

Figure 2.6: Differences between early (21–35 days) and late (over 35 days) stage stem cell-derived cardiomyocytes. The morphology of the action potential develops over time as the changing levels of ion channel expression alter the contributions of the different ionic currents. Figure reproduced from Robertson et al. (2013).

et al., 2014). Extra-long culture times (upwards of 80 days) have resulted in a much more adult-like morphology of the cells in addition to the changes in the action potential (Kamakura et al., 2013; Lundy et al., 2013).

Inward rectifier current The inward rectifier current, I_{K1}, in hSC-CMs has appreciable differences to that in adult cardiomyocytes. Some reports have found no evidence of this current in hSC-CMs (Satin et al., 2004), while others have reported it as being very low or negligible (Ma et al., 2011; Doss et al., 2012). In adult cardiomyocytes, the I_{K1} current maintains a resting potential of around

−85 mV during Phase 4 of the action potential. The lack of I_{K1} results in a comparatively high maximum diastolic potential in hSC-CMs, meaning that other currents can then cause spontaneous depolarisation. During the maturation process, there is a significant increase in the Kir2.1 protein, and the inward rectifier current consequently increases in density (Sartiani et al., 2007). As the key current implicated in the immaturity of the cells, attempts have been made to increase I_{K1} and thus obtain a more adult-like electrophysiological response. This has been achieved by promoting production of the Kir2.1 ion channel protein (Lieu et al., 2013; Vaidyanathan et al., 2016) and by calculation and external provision of I_{K1} from an *in silico* model (Bett et al., 2013; Verkerk et al., 2017).

Rapid delayed rectifier current The rapid delayed rectifier current, I_{Kr}, was identified in the vast majority of cells tested as part of many studies (He et al., 2003; Jiang et al., 2010; Honda et al., 2011; Ma et al., 2011; Doss et al., 2012). The current density and activation kinetics of the channel are similar to adult cardiomyocytes (Ma et al., 2011), but it has been proposed that it has an additional function in hSC-CMs: given the low I_{K1} density, I_{Kr} is also thought to be involved in setting the maximum diastolic potential (Doss et al., 2012).

Fast sodium current Similarly to the rapid delayed rectifier current, the fast sodium current, I_{Na}, is present in hSC-CMs and the channels have properties consistent with those from adult cardiomyocytes (Satin et al., 2004; Ma et al., 2011), however, neuronal Nav1.7 channels have also been detected in addition to the expected Nav1.5 ion channels (Moreau et al., 2017). The contribution of I_{Na} to the action potential upstroke is less than in adult cardiomyocytes, due to the higher maximum diastolic potential and contribution of the funny current to the upstroke (Goodrow et al., 2018). It retains its involvement in the conduction of the activation wave across tissue (Riedel et al., 2014) even though significant heterogeneity in the upstroke velocity of the action potential has been reported (Pekkanen-Mattila et al., 2010).

Hyperpolarisation-activated pacemaker (funny) current The funny current, I_{f}, is not present in the atrial and ventricular cells of the adult heart but is vitally important to the pacemaking functionality of cells in the sino-atrial and atrio-ventricular nodes. It is present in all hSC-CMs, where it plays a key role in their spontaneous depolarisation (Satin et al., 2004; Ma et al., 2011). Bosman et al. (2013) noted that the co-location of HCN4-Cav3 (a funny current channel protein and calveolin 3) influences the activation of the channel, changing it to occur only at a more negative voltage. A change in the relative proportions of the other HCN isomers also influences the activation of the funny current channel (Sartiani et al., 2007). This process is likely involved in the reduction of spontaneous activity seen as hSC-CMs mature.

L-type calcium current The properties of the hSC-CM L-type calcium channel are thought to be similar to its adult counterpart (Xu et al., 2002; He et al., 2003; Ma et al., 2011; Hwang et al., 2015). Ma et al. (2011) reported that the current density was slightly higher in hiPSC-CMs than in adult cardiomyocytes, at approximately $-17\,\mathrm{pA/pF}$, but Sartiani et al. (2007) reported lower peak I_{CaL} values of around $-4\,\mathrm{pA/pF}$ in hESC-CMs.

Calcium subsystem In contrast to many of the currents discussed so far, the calcium subsystem is much less developed. Dolnikov et al. (2005) proposed that contraction of hSC-CMs used calcium ions from outside the cell to supplement the store within the sarcoplasmic reticulum. However, Hwang et al. (2015) noted that while the sarcoplasmic reticulum was not fully developed, calcium release could be stimulated by the addition of caffeine. This immature movement of calcium ions may act as a redundant pacemaker in hSC-CMs (Choi et al., 2015). Over time, the calcium subsystem and structure of the sarcoplasmic reticulum mature (Ivashchenko et al., 2013; Jones et al., 2016).

Other currents The remaining currents do not have such an obvious effect on the action potential as those described above. The slow delayed rectifier current, I_{Ks}, has been detected in hSC-CMs (Ma et al., 2011) and is thought to be involved

in the repolarisation reserve, as it is in the adult heart (Braam et al., 2013). The transient outward current, I_{to}, has also been detected in hSC-CMs (Jiang et al., 2010; Ma et al., 2011), but Ma et al. (2011) noted that it could not be separated into its fast and slow components. The exchange currents (Na^+–Ca^{2+}, Na^+–K^+, Na^+–H^+ and Cl^-–OH^-) have all been found in hiPSC-CMs and appear to have similar kinetics to those in adult cells (Fine et al., 2013).

Physical structure The physical structure of hSC-CMs also changes as they mature. Adult cardiomyocytes have a rather elongated shape, and the cells are aligned within the cardiac muscle. In contrast, hSC-CMs are smaller and have a generally circular shape (although this can be somewhat irregular). Typical diameters range from 10–50 μm (Snir et al., 2003; Gherghiceanu et al., 2011; Ma et al., 2011). Specialised substrates can cause the cells to take on a mature shape and the activation wavefront to travel at an increased conduction velocity (Carson et al., 2016). Culturing the cells in three dimensions rather than on a flat surface has also been shown to increase the electrophysiological maturity of hSC-CMs, although this may also be influenced by the length of the culture time (Otsuji et al., 2010; Zhang et al., 2013; Eng et al., 2016). Pasqualini et al. (2015) proposed metrics of maturity based on the level of sarcomere organisation, which may in future be a promising way of comparing physical and electrophysiological maturity.

Gap junctions and conduction velocity As in adult cardiomyocytes, gap junctions are present at the interface between adjacent cells in hSC-CM tissue samples. Reports of the conduction velocity vary and appear to depend on the source of the cells used. Low velocities of 1.5 to 5 cm/s have been reported by Satin et al. (2004), Mehta et al. (2011), Kadota et al. (2013), and Kucera et al. (2015) which were likely due to a combination of slower activation time and reduced number of gap junctions compared with adult cells. These low velocities can increase over time as the cultures mature (Zhu et al., 2017). Using a commercial source of hiPSC-CMs, Lee et al. (2012) observed much high conduction velocities of around 20 cm/s which is much closer to the 35 to 50 cm/s found in adult cardiac

tissue. Using specialised substrates, conduction velocities of up to 44 cm/s have been reported (Herron et al., 2016).

2.5.2 Cellular phenotypes

Patch-clamp studies of hSC-CMs have shown that the cells exhibit action potentials resembling those of atrial, ventricular and nodal type cells from the adult heart (He et al., 2003; Zhang et al., 2009; Ma et al., 2011). The criteria for classifying the cells as atrial-, ventricular-, or nodal-like differ between studies, but are usually based on the action potential duration and maximum diastolic potential. The ventricular-like phenotype has an enhanced plateau, while the action potential duration of the atrial-like and nodal-like phenotypes is appreciably shorter. The nodal-like phenotype has a slower upstroke and a raised maximum diastolic potential due to increased I_{f}, indicated by prominent expression of the HCN4 gene (Yechikov et al., 2016).

The subtypes can also be distinguished by differences in gene expression, but this is not always a practical method during studies of the cells' electrophysiology (Jonsson et al., 2010; Kadota et al., 2013; Yechikov et al., 2016). Figure 2.7 shows the features of the three phenotypes of hiPSC-CM described by Ma et al. (2011).

Reports of the relative proportions of the three phenotypes have generally been inconsistent, and this problem is compounded by the lack of a standard classification mechanism. The ventricular phenotype has usually been reported as the most numerous, with 50–60% found by Ma et al. (2011) and Doss et al. (2012) and 93% by Braam et al. (2013). Using a small sample, Riedel et al. (2014) found marginally more atrial-like cells.

Production of single-phenotype hSC-CM cultures has been attempted by a number of groups; however, finding truly phenotype-specific markers for each phenotype has proved challenging. Atrial-like and ventricular-like hSC-CMs have been obtained through modulation of retinoic acid levels (Zhang et al., 2011; Devalla et al., 2015), ventricular-like hSC-CMs by using the MCL-2v antibody as identification (Bizy et al., 2013; Weng et al., 2014), atrial-like hSC-CMs through

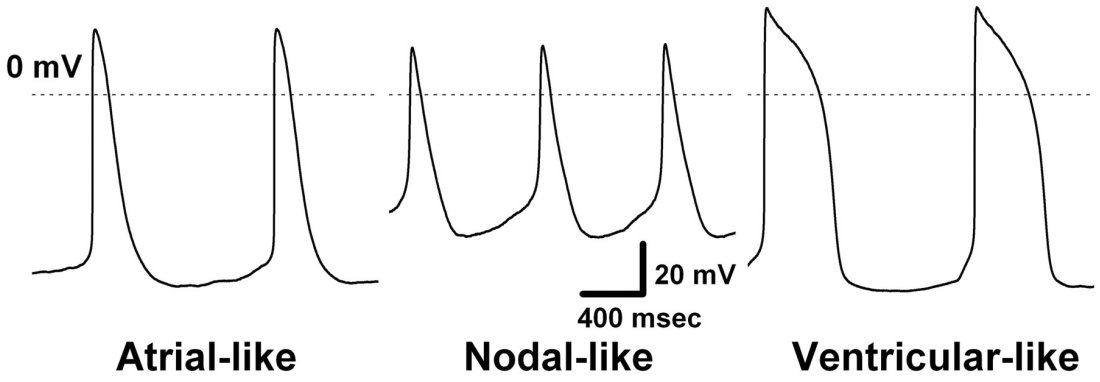

APs (n=59)	Interval (sec)	MDP (mV)	Peak (mV)	Amp (mV)	dV/dt_{max} (V/sec)	APD10 (msec)	APD30 (msec)	APD90 (msec)	APD30-40 /APD70-80
Atrial-like (n=13)	1.2±0.2	-73.5±1.5	26.7±1.4	100.2±2.1	26.2±3.9	60.8±5.5	123.1±10.3	286.2±21.2	1.1±0.1
Nodal-like (n=14)	1.0±0.1	-60.1±2.4	19.5±2.0	79.6±2.9	5.5±0.4	65.3±18.4	111.8±15.9	254.7±20.5	1.0±0.1
Ventricular-like (n=32)	1.7±0.1	-75.6±1.2	28.3±1.0	104.0±1.1	27.8±4.8	74.1±4.8	180.0±10.7	414.7±21.8	2.5±0.2

Figure 2.7: Examples of atrial-like, nodal-like and ventricular-like hiPSC-CM action potentials. In this case, the values of $APD_{30} - APD_{40}/APD_{70} - APD_{80}$ and the maximum diastolic potential (MDP) were used to classify the action potentials. Figure reproduced from Ma et al. (2011).

sarcolipin-based selection (Josowitz et al., 2014) and nodal-like hSC-CMs using a specialised culture medium (Schweizer et al., 2017). These purified cell cultures will be useful in studies of drugs or diseases that affect only particular regions of the heart (Chen et al., 2016; Laksman et al., 2017).

Identification of cellular phenotype in larger samples has been the focus of much debate. Zhu et al. (2016) used optical mapping to obtain the action potentials of separate hESC-CMs within a small cluster. An automated classification method proposed that the action potentials could be categorised into either two or three distinct phenotypes, which appeared to cluster spatially. Vestergaard et al. (2017) also reported single-phenotype regions in hESC-CM clusters. However, Du et al. (2015) found that such clear regions were not present in monolayers of hiPSC-CMs. The study raised the question of whether there are indeed three separate cellular phenotypes or whether a more continuous spectrum of phenotypes is more realistic (Giles and Noble, 2016; Kane et al., 2016; Bett et al., 2016; Kane and Terracciano, 2017).

2.5.3 Use in safety assays

To test the suitability of hSC-CMs for safety pharmacology assays, drugs with well-understood properties have been applied to the cells in a variety of different experiments: manual and automated single-cell patch-clamp (Gibson et al., 2014; Lee et al., 2016b), sharp micro-electrode (Jonsson et al., 2010; Nalos et al., 2012), the micro-electrode array (Harris et al., 2013; Clements and Thomas, 2014), optical mapping (Attin and Clusin, 2009; Kadota et al., 2013; Herron, 2016) and impedance assays (Guo et al., 2011a; Guo et al., 2013; Doherty et al., 2015). These techniques have also been used in combination to provide complimentary datasets (Clements et al., 2015; Rast et al., 2015; Obergrussberger et al., 2016).

Many of the studies listed above reported changes comparable to those observed in other assays such as the rabbit ventricular wedge. However, this was not always the case. Jonsson et al. (2012) found that early after-depolarisations could be elicited from drugs that blocked the hERG channel, but not drugs that blocked other channels. L-type calcium channel blockers such as Nifedipine have been associated with both increases (Guo et al., 2011a; Harris et al., 2013) and decreases (Ben-Ari et al., 2014) in beat rate. While hSC-CMs have exhibited increased beat rate following application of L-type calcium channel agonists (Mehta et al., 2011), this effect was not as pronounced as expected (Ji et al., 2014).

Despite questions having been posed over the suitability of hSC-CMs for cardiac safety testing, given the presence of three cellular phenotypes and their continuously changing electrophysiological characteristics (Rocha et al., 2017; Goversen et al., 2017), the use of hSC-CMs in cardiac safety assessment is set to expand. Other assays that are in use today also have their drawbacks; for instance, the ion channels present in mammalian tissue assays do not exactly match those found in humans. To support the latest CiPA proposals, multi-site validation studies of hSC-CM tissue assays have been proposed (Blinova et al., 2017). These would consist of an analysis of the effects of specified drugs using standardised protocols for the optical mapping and micro-electrode array assays. In this thesis, we focus on the micro-electrode array.

The micro-electrode array

The micro-electrode array (MEA) records the field potential below a sample of hSC-CMs using a grid of small electrodes. Biomarkers such as the beat rate, spike amplitude and field potential duration can be calculated from the field potential (Fejtl et al., 2006; Spira and Hai, 2013). The field potential duration is considered to be analogous to the QT interval from the ECG (Halbach et al., 2003). When drugs are applied to hSC-CMs within the MEA, changes in the field potential duration and other biomarkers are recorded, typically as the percentage change in the value compared to control. As the electrodes of the MEA do not interfere directly with the cells, these systems can be maintained for days or weeks at a time. This provides opportunities for longer-term studies of the effects of drugs which may pick up more complex problems than ion channel block, such as interference with ion channel regulation and trafficking to the cell membrane.

Studies of the MEA with hESC-CMs and hiPSC-CMs have generally found that changes to the field potential duration reflect the QT prolongation observed in previous assays. Changes to the beat rate and occurrences of early after-depolarisations have also been found as expected (Braam et al., 2010; Guo et al., 2011b; Mehta et al., 2011; Braam et al., 2013; Harris et al., 2013; Navarrete et al., 2013; Clements and Thomas, 2014; Nozaki et al., 2014). Several of these studies compared the MEA assay to either hERG block or other *in vitro* assays as predictors of Torsades de Pointes, and found that the MEA showed comparable levels of sensitivity. However, some differences between hSC-CMs in the MEA and other assays have been noted, such as to I_{Ks} blockers which produced a less pronounced response than expected (Braam et al., 2013).

Improvements in MEA technology are presently underway. In addition to improving the maturation state of the cells, as discussed in Section 2.5.1, patterning of the MEA surface is also able to influence the shape of the cells and therefore the dispersion of activation, leading to a more realistic conduction pattern (Stancescu et al., 2015). Changes to the physical form of the electrodes may lead to improved signal quality in future MEAs (Spira and Hai, 2013).

2.5.4 Other uses of stem cell-derived cardiomyocytes

In addition to their applications in safety pharmacology that form the focus of this thesis, human stem cell-derived cardiomyocytes have many other uses. On a related theme to safety pharmacology, hSC-CMs can also be used to identify the level of cardiotoxicity associated with anti-cancer drugs (Cohen et al., 2011; Talbert et al., 2015; Maillet et al., 2016).

Patient-specific hSC-CMs can be produced, enabling customised assessment of the cardiac safety of drugs for those with specific genetic conditions (Itzhaki et al., 2011; Matsa et al., 2011; Braam et al., 2013). They can also be used for identifying the electrophysiological mechanism behind diseases such as Brugada syndrome, where the genetic reason for the syndrome is not known in all cases (Veerman et al., 2016). Patient-specific hSC-CMs also hold promise for cardiac tissue repair and pacemaker replacement (Gu et al., 2012; Chauveau et al., 2017).

2.5.5 Simulations

Following on from the models of the action potential in adult human cardiomyocytes that were discussed in Section 2.4.1, parametrisations are also available for the specific electrophysiology of human stem cell-derived cardiomyocytes. The first was the Paci et al. (2012) model of hESC-CMs in early and late stages of maturation, which was later developed into the Paci et al. (2013a) model using a more detailed hiPSC-CM dataset, that of Ma et al. (2011), for parametrisation. The Paci et al. (2013a) model consists of two parametrisations, one for atrial-like and the other for ventricular-like hiPSC-CMs. To date, no specific model has been published for the nodal-like stem cell-derived cardiomyocyte.

The Paci et al. (2013a) model has been used to investigate the presence of spontaneous beating in hiPSC-CMs by modification to the simulated I_{Na}, I_{f} and I_{K1} currents. Application of an appropriate I_{K1} current calculated using an *in silico* model has been shown to produce a more adult-like action potential and response to drugs (Bett et al., 2013; Verkerk et al., 2017). Further investigation of the differences between hiPSC-CM and adult cardiomyocyte electrophysiology

has demonstrated that hiPSC-CMs are generally more sensitive to the effects of I_{CaL} and I_{K1} block than adult cells (Paci et al., 2015).

Simulations of hiPSC-CM tissue are a relatively recent development, with *in silico* studies of the CellDrum assay (Frotscher et al., 2015; Frotscher et al., 2016) and the micro-electrode array (Abbate et al., 2018) providing the first examples of simulated signals from tissue-scale assays under the effects of drugs.

2.5.6 Stem cell-derived cardiomyocytes and the CiPA initiative

Now that we have discussed both human stem cell-derived cardiomyocytes and the CiPA initiative, we can consider the impact of the proposed changes on the cardiac safety assessment process.

As a relatively new cell type, assays based on hSC-CMs should not be considered a drop-in replacement for existing methods — but they are likely to be a valuable complement. Existing tests based on mammalian tissue are time consuming, expensive and ethically questionable to many, and hSC-CMs offer an improvement on each of these issues. Great care has so far been taken in validating the conclusions from hSC-CM assays, with studies such as those of Harris et al. (2013) comparing hSC-CM assays against the current standard tests, and the results of the first multi-site comparisons are now becoming available (Millard et al., 2018). As we reported in Section 2.3.1, the present safety assessment process is effective but not as efficient as desired; maintaining a rigorous validation process throughout the refinement of the CiPA proposals will be vitally important for increasing confidence in the proposals and supporting their eventual adoption.

Unsurprisingly, given the association between Torsades de Pointes, blockade of the hERG channel and action potential prolongation, the CiPA proposals for hSC-CM assays focus primarily on the action potential duration (in optical mapping studies) and the field potential duration (in the micro-electrode array assay). However, many more biomarkers can be derived from the action and field potentials which yield further details of the action of a drug. The links between biomarkers of the field potential and blockade of key ionic currents have been

investigated by Tixier et al. (2018). Further studies connecting these additional biomarkers of the field potential to those of the electrocardiogram, and hence arrhythmic risk, would be of assistance in drawing closer comparisons between the proposed assays and the thorough QT studies that are carried out at present. The familiar T-wave of the electrocardiogram is associated with a corresponding feature, the repolarising wave, in the field potential from the MEA assay; however, the links between the Q, R and S waves and features of the depolarising spike are less well understood, and the P wave does not have a clear analogue in the field potential signal. A thorough investigation of the links between these different types of signal would therefore be highly useful in refining our understanding of the risk associated with drugs that affect ion channels that pass the highest amount of current in the early stages the cardiac action potential, such as the fast sodium current. Other features, such as changes to conduction, may also be apparent from MEA studies but will also not fall under CiPA's repolarisation-focussed remit. The value of these additional tests, and others such as electrocardiogram studies during Phase I trials, should not be overlooked.

The tissue-scale assays under consideration by CiPA have so far mainly utilised hiPSC-CMs from commercial cell lines, and there has been little mention of the characteristics of the donors from whom the stem cells were derived. Expansion of the proposed assays beyond one or two "typical" cell lines could prove very fruitful for safety assessment: as we discussed in Section 2.5.4, patient-specific hiPSC-CMs recapitulate the electrophysiological characteristics of their donor and could therefore provide an avenue for additional assessment of drugs on particularly at-risk subpopulations. However, implementation of such an approach would be a substantial undertaking, and may be better left until hSC-CM assays are more established.

2.6 Development of Research Questions

In this review, we have seen that human stem cell-derived cardiomyocytes hold great promise for use in the cardiac safety assessment process, but their differences

from the cardiomyocytes in the adult human heart call for caution at the present time.

There are several factors to address. Human stem cell-derived cardiomyocytes are not fully differentiated: several of their ionic currents differ substantially from their adult counterparts, they lack alignment in their spatial orientation and exhibit a reduced conduction velocity compared to that observed in adult cardiac tissue. The action potential in isolated hSC-CMs varies from cell to cell, with action potential morphologies that resemble those of atrial, nodal and ventricular cells in the adult heart. At the present time, there is no definitive classification metric for placing hSC-CMs into one of the three proposed categories, and there is not yet a consensus on the spatial distribution of the phenotypes in tissue culture preparations.

In Section 2.4.3 of this chapter, we saw how the use of *in silico* models can be of assistance in the cardiac safety assessment process. We therefore propose to utilise tissue-scale modelling of human stem cell-derived cardiomyocytes to investigate some of the issues outlined in the previous paragraph.

We aim to investigate how phenotypic variability in hSC-CMs can impact the conclusions drawn from the micro-electrode array assay. The combinations of hSC-CMs and the micro-electrode array are included in the third proposal of the Comprehensive *in vitro* Proarrhythmia Assay; our efforts to study and improve upon the interpretation of the assay through computational means are therefore timely.

2.6.1 Research questions

Our first research question concerns the development of a simulation framework for hSC-CMs where the cellular phenotype differs throughout the tissue. The bidomain equations assume that there are large regions where the cellular phenotype is the same, so that the ionic currents can therefore be represented by the same cellular electrophysiology model. In the case of hSC-CM tissue, the phenotypes change on a shorter spatial scale than they do in the adult heart.

In Chapter 5, we compare two methods for simulating the electrical activity in tissue with potentially rapid spatial variation in phenotype.

The second topic of this thesis is the investigation of how phenotypic variability in hSC-CM tissue cultures affects the cardiac safety assessment process. In Chapter 6, we examine how changes of phenotype affect the field potential, the signal that is recorded in the micro-electrode array assay. Having developed the computational model of the micro-electrode array, we then perform a detailed qualitative comparison of simulated and experimental data from the drug safety assessment process in Chapter 7. We assess how much variability in the field potential is linked to the phenotypic variability in the hSC-CMs, and see how large this effect is as the applied drug concentrations are increased. We can then make a statement on how important the underlying variation in cell type is to the field potential signal, and whether this requires further investigation by experimentalists before the micro-electrode array assay is brought into wider use in the pharmaceutical industry. The comparison of experimental and simulated data under a variety of drug-influenced conditions also allows us to identify areas in which the model requires improvement, both on the cellular and tissue scale. We therefore end Chapter 7 with recommendations for further development of the micro-electrode array model.

Before we can begin to develop our multi-phenotype simulation framework, we must first understand the presently used techniques for simulating cardiac tissue. The following two chapters describe the theory behind models of cardiac electrophysiology on the cellular and tissue scales, and the methods used to obtain numerical solutions to those models.

Chapter 3

Models of Cellular and Tissue-Level Electrophysiology

In the previous chapter, we discussed how the change in membrane voltage in a cardiomyocyte may be modelled by a system of ordinary differential equations that represent the flow of charged ions into and out of the cell. We now describe the mathematical formulation of such cellular electrophysiology models, using the seminal Hodgkin and Huxley (1952a) model as an example. We then consider how cellular electrophysiology models may be coupled together in order to simulate the electrical properties of cardiac tissue. We describe the properties of the bidomain model, a system of two partial differential equations that are coupled to a cellular electrophysiology model.

3.1 Chapter Outline

In Section 3.2, we build up a description of the cardiomyocyte as an electrical circuit. We begin by calculating the equilibrium potential of a specific ion, at which the ion's concentration gradient is balanced by the potential difference across the cell membrane. We show how the equilibrium potential may be used in the calculation of the ionic currents, before describing how a model of cellular

electrophysiology can be constructed by considering the flow of several different ions across the cell membrane.

We then discuss the bidomain model, a continuum representation of the electrical activity within cardiac tissue. We provide a brief derivation of the model in Section 3.3, and also demonstrate how the bidomain equations may be reduced to the monodomain equation in certain circumstances. Our work in Chapter 5 builds upon the formulation of bidomain equations by extending their derivation to cover the case where two or more cell types (the electrophysiology of which would be represented by different cellular electrophysiology models) are well-mixed.

3.2 Cellular Electrophysiology Models

Cardiomyocytes are excitable cells: when stimulated, they produce a rapid change in membrane potential if the stimulus is above a given threshold. This change in potential is known as the action potential, and is linked to the flow of calcium ions into the intracellular space and thus to the contraction of the cell (see Section 2.2 for details). The action potential is caused by the movement of ions across the cell membrane via ion channels and ATP-activated transporters. To understand the action potential, we begin by considering the balance of ionic concentrations and the intra and extracellular potentials before moving on to look at how the cell as a whole acts as an excitable electrical circuit.

3.2.1 The Nernst equation

Following Keener and Sneyd (2008), let us consider a system containing two ions: positively charged S, and negatively charged S'. A cell membrane which is impermeable to ions separates the intracellular and extracellular domains. Ion channels specific to ion S allow the positively charged ions to pass across the membrane, while negatively charged S' are restricted to their original side of the membrane.

We start with electrically balanced but different concentrations of both ions

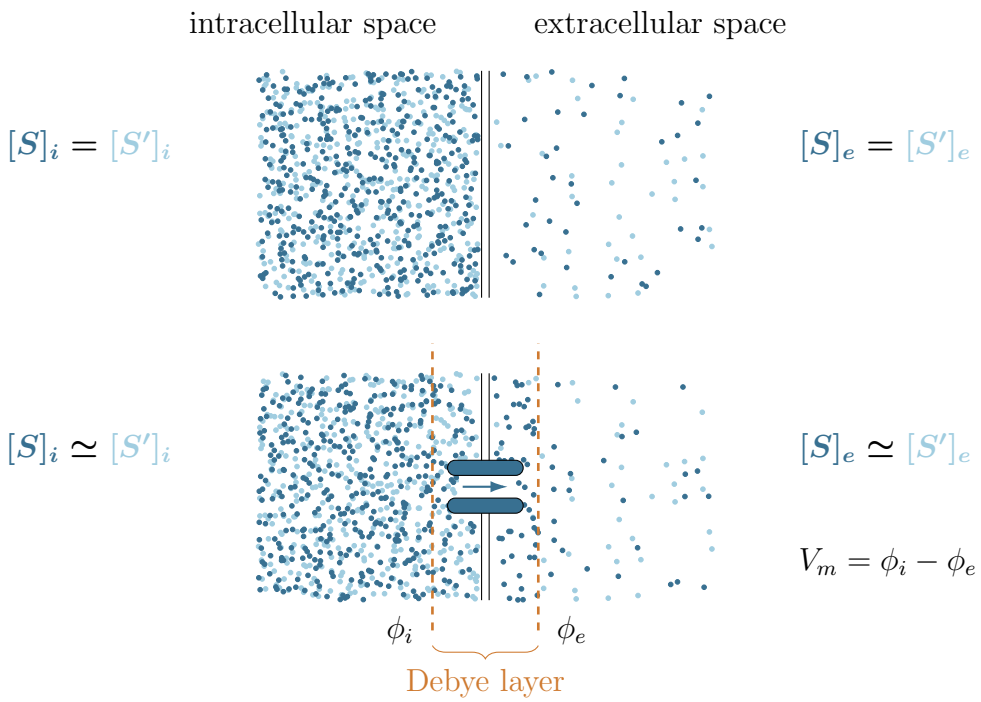

Figure 3.1: A cell membrane with selectively permeable ion channels. The two ions, S and S' (shown in dark and light blue respectively) have equivalent but opposing changes. Their concentrations are denoted by square brackets, and the intracellular and extracellular concentrations by subscripts i and e respectively. Only ions of type S may pass through the selective ion channels in the cell membrane. Top: ions S and S' are present in equal concentrations on each side of the membrane. Both the intracellular and extracellular regions are electrically neutral. Bottom: Introduction of selective ion channels results in the movement of some S ions to the extracellular space (see main text for full details). The movement of S indicated by the arrow continues until the electrical field set up by the imbalance of S and S' in the Debye layer (indicated by the dashed orange lines) balances the concentration gradient. The spaces on either side of the membrane are no longer electrically neutral, giving rise to the membrane potential, V_m, which is defined as the difference in electrical potential between the two spaces, $V_m = \phi_i - \phi_e$.

on either side of the membrane, as shown in the top panel of Figure 3.1. If we then introduce ion channels of the type that selectively allows ions of type S to pass through, some of those ions in the vicinity of the membrane and ion channels move down their concentration gradient from the intracellular to the extracellular space. This process introduces a charge imbalance in the regions of space close to the membrane, which is illustrated in the lower panel of Figure 3.1. At this point, there are two opposing effects on ions of type S: the concentration gradient is in the direction of the extracellular space, while the gradient of the electrical field

is in the direction of the intracellular space. These two effects reach equilibrium after the movement of a relatively small number of ions. In regions distant from the membrane, the concentrations of the two ions are almost unchanged from their original values and the regions remain electrically neutral. Close to the membrane (typically on the scale of nanometers), the charge imbalance is maintained, with this region being known as the Debye layer. The imbalance of charge gives rise to a potential difference across the cell membrane, the membrane potential, V_m, which is defined as the difference in electrical potential between the intra and extracellular regions, such that $V_m = \phi_i - \phi_e$.

Let us now consider the Gibbs free energy of ion S on either side of the membrane,

$$G_{S,i} = G_S^0 + RT\ln([S]_i) + zF\phi_i, \tag{3.1}$$

$$G_{S,e} = G_S^0 + RT\ln([S]_e) + zF\phi_e, \tag{3.2}$$

with subscripts i and e denoting the intracellular and extracellular regions respectively. The first term, G_S^0 denotes the standard free energy for a 1 M solution of ion S; this is the same on either side of the membrane. The second and third terms represent the chemical and electrical potential of the system, where z is the charge on ion S and F is Faraday's constant.

From this, we can calculate the difference in free energy,

$$\Delta G_S = G_{S,i} - G_{S,e}, \tag{3.3}$$

$$= G_S^0 + RT\ln([S]_i) + zFV_i - G_S^0 - RT\ln([S]_e) - zFV_e, \tag{3.4}$$

$$= RT\ln\left(\frac{[S]_i}{[S]_e}\right) + zF(\phi_i - \phi_e), \tag{3.5}$$

$$= RT\ln\left(\frac{[S]_i}{[S]_e}\right) + zFV_m, \tag{3.6}$$

where we have used the definition of the membrane potential given above ($V_m = \phi_i - \phi_e$).

The potential at which the propensity of ions S to move down their concentration gradient is balanced by the electric field set up by the differences in concentrations of S and S' on either side of the membrane is known as the

Nernst potential. We can obtain the Nernst potential for ion S, V_S, by solving equation (3.6) at equilibrium. If we set $\Delta G = 0$, we obtain

$$V_S = \frac{RT}{zF} \ln \left(\frac{[S]_e}{[S]_i} \right). \tag{3.7}$$

3.2.2 Ohmic ionic currents

If we assume that the resistance of the ion channels is Ohmic (i.e. the voltage drop across the channel is proportional to the current), we can derive the following expression for ionic current S:

$$V_m = r_S I_S + V_S, \tag{3.8}$$

$$I_S = \frac{1}{r_S}(V_m - V_S), \tag{3.9}$$

$$I_S = g_S(V_m - V_S), \tag{3.10}$$

where r_S and g_S are the resistance and conductance of the membrane to ion S respectively.

We can use this formulation to calculate the total ionic current across the cell membrane due to ions i,

$$I_{\text{ion}} = \sum_i g_i(V_m - V_i), \tag{3.11}$$

where we have denoted the equilibrium potential for each ion by V_i.

3.2.3 Circuit representation of an electrically active cell

Equation (3.10) shows us how each ionic current across a cell membrane may be considered as a variable resistor (with resistance r_S or conductance g_S) and a driving voltage (V_S). If we include a representation of the cell membrane, the cellular system can be considered as an electrical circuit. Hodgkin and Huxley were the first to develop this style of circuit representation in the context of the action potential in the giant axon of a squid. The resulting equivalent circuit in Figure 3.2. In the Hodgkin and Huxley (1952a) model, only charge carried by sodium, potassium and chloride ions is considered. Movement of these ions gives rise to the sodium, potassium and leak currents indicated in Figure 3.2.

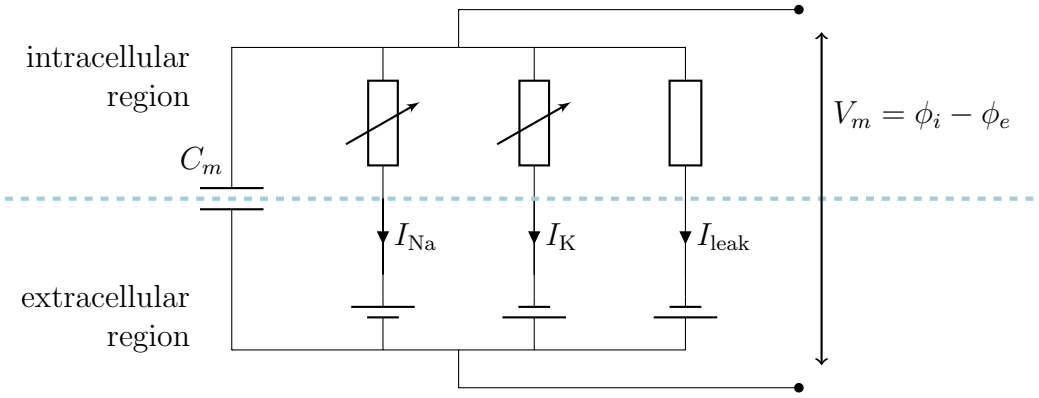

Figure 3.2: A circuit representation of the Hodgkin and Huxley (1952a) model. The cell membrane is shown in blue. The orientation of the voltage sources indicates the direction of the driving voltage for each ion from equation (3.11). The resistances of the I_{Na} and I_{K} channels are variable, depending on the membrane voltage.

If the cell membrane is modelled as a capacitor, we can use Kirchoff's current law to show that the total current is zero:

$$0 = C_m \frac{\mathrm{d}V_m}{\mathrm{d}t} + I_{\text{ion}}(\mathbf{u}, V_m), \tag{3.12}$$

where $I_{\text{ion}}(\mathbf{u}, V_m)$ is the sum of the total ionic currents, $\sum_{i=1}^{n} I_i(\mathbf{u}, V_m)$. The $\mathbf{u}$ are state variables (which determine the probability that the ion channels are open), and other variables which influence the ionic currents (e.g. the intra- and extracellular concentrations of each type of ion).

If we rearrange this as a differential equation for the membrane voltage, V_m, we can see how this quantity may be calculated:

$$\frac{\mathrm{d}V_m}{\mathrm{d}t} = -\frac{1}{C_m}\left(\sum_{i=1}^{n} I_i(\mathbf{u}, V_m)\right). \tag{3.13}$$

If we also wish to include an additional stimulus current, the derivation proceeds as

$$0 = C_m \frac{\mathrm{d}V_m}{\mathrm{d}t} + I_{\text{ion}}(\mathbf{u}, V_m) + I_{\text{stim}}, \tag{3.14}$$

$$\frac{\mathrm{d}V_m}{\mathrm{d}t} = -\frac{1}{C_m}\left(\sum_{i=1}^{n} I_i(\mathbf{u}, V_m) + I_{\text{stim}}\right). \tag{3.15}$$

3.2.4 Gating variables

To solve equation (3.15), we must know how the different ionic currents change over time. We have assumed that their conductance is Ohmic, so for ion i,

$$I_i = g_i(V_m - V_i), \tag{3.16}$$

where g_i is the conductance of the cell membrane to ion i and V_i is the reversal potential for ion i, calculated from the Nernst equation. However, the conductance is not constant over time; it is influenced by the dynamics of the channel and the membrane voltage, as many ion channels in cardiomyocytes are voltage gated. The channel conductance can therefore be expressed as

$$g_i = \bar{g}_i f(V_m, t), \tag{3.17}$$

where $\bar{g}_i$ is the maximum possible conductance of that type of ion channel and $f(V_m, t)$ is a function of the membrane voltage and time that gives the probability of this type of ion channel being open. As there are so many ion channels per cell, this deterministic open probability is a good approximation for the proportion of stochastically-opening single channels that are in an open state at any given time (Pullan et al., 2005).

The exact form of $f(V_m, t)$ changes between ion channels and cellular electrophysiology models. Experimental data is required to find the structure and parameters of this function. In the Hodgkin and Huxley (1952a) model, the best fit to the potassium conductance was obtained by

$$g_{\mathrm{K}} = \bar{g}_{\mathrm{K}} n^4, \tag{3.18}$$

where n is a gating variable which evolves in time according to

$$\frac{\mathrm{d}n}{\mathrm{d}t} = \alpha_n(1 - n) - \beta_n n, \tag{3.19}$$

and the forms of α_n and β_n were parametrised based on experimental data,

$$\alpha_n = 0.01\frac{V_m + 10}{\exp\left(\frac{V_m+10}{10}\right) - 1} \quad \text{and} \quad \beta_n = 0.125\exp\left(\frac{V_m}{80}\right), \tag{3.20}$$

where V_m is given in mV. At very negative[1] potentials, the α_n term dominates, n increases and the potassium current is activated. n is consequently known as an activation variable.

Hodgkin and Huxley took the same approach with the sodium current, but a quartic gating variable was not sufficient to describe the dynamics of the sodium conductance. Instead, they used an activation variable m and an inactivation variable h, and concluded that the sodium conductance could be expressed as

$$g_{\mathrm{Na}} = \bar{g}_{\mathrm{Na}} m^3 h. \tag{3.21}$$

The variables m and h evolve in time as n does in equation (3.19), but the parametrisations for α_m, β_m, α_h and β_h are different to reflect the properties of the sodium current.

At the time, not much was known about the leak current, so it was given a constant value of conductance.

Since then, the discovery of further ionic currents and more detailed experimental data on their behaviour has led to the development of many other ion and action potential models, such as those models of cardiac cellular electrophysiology that were described in Section 2.4.1.

While cellular electrophysiology models are able to give us insight into the temporal dynamics of the action potential, they do not enable investigation of the spatial propagation of activation wavefronts around cardiac tissue. The following section describes one of the most widely-used methods for modelling cardiac electrophysiology on the tissue-scale, the bidomain equations.

3.3 The Bidomain Equations

The bidomain equations are widely used throughout cardiac modelling as they allow for the extracellular potential to be calculated separately from the intracellular potential, as well as permitting the simulation of domains outside the

[1] In the Hodgkin and Huxley (1952a) model, the convention for the direction of current flow is the opposite of most cardiac electrophysiology models: inward currents are positive and the transmembrane potential is negative when depolarised.

heart. Experimental measurements, such as the potential differences recorded between electrodes in the electrocardiogram, can be compared with quantities derived from the extracellular potential.

The bidomain equations rely on the assumption that cardiac tissue can be modelled as two distinct yet connected spaces; the intracellular and extracellular domains. Rather than explicitly modelling the fine structure of the cells, such as the cytoplasm, gap junctions and membrane, these qualities are homogenised over throughout the domain, giving an "average" electrical potential that does not show the very small-scale variations due to the presence of microscopic features. In the homogenisation process, we assume that the macrostructure of the domain is accurately represented by repeating units of the microstructure; i.e. that cells with a consistent set of properties repeat regularly throughout the domain.

Later in this thesis, in Chapter 5, we return to the derivation of the bidomain equations for tissue composed of multiple cell types, where the homogenisation process follows that of previous authors (Keener and Panfilov, 1996; Keener and Sneyd, 2009; Richardson and Chapman, 2011), but considers variations in the parameters that are homogenised over due to the presence of two or more types of cell. In this section, we therefore present a brief derivation of the bidomain equations through a shorter, macroscale, approach. This derivation assumes that the intracellular and extracellular domains are homogeneous from the start, but nevertheless provides interesting insight into the physical principles behind the bidomain equations.

3.3.1 Macroscale derivation of the bidomain equations

To derive the bidomain equations, we consider the tissue to be a two-phase medium, consisting of the intracellular and extracellular domains which are denoted by the subscripts i and e throughout this derivation. These domains are separate but continuously connected. Within both domains, currents are generated by the movement of charged ions; in cardiomyocytes, sodium, potassium and calcium ions act as the primary charge carriers. The current density in each

domain is made up of an Ohmic component, $\mathbf{J} = \sigma\mathbf{E}$, and a stimulus component, $\mathbf{J}^{\text{stim}}$. If we then express the electrical field $\mathbf{E}$ as the gradient of a scalar potential ϕ, we obtain

$$\mathbf{J}_i = -\sigma_i \nabla\phi_i + \mathbf{J}_i^{\text{stim}}, \qquad \text{and} \tag{3.22}$$

$$\mathbf{J}_e = -\sigma_e \nabla\phi_e + \mathbf{J}_e^{\text{stim}}, \tag{3.23}$$

for the current densities within the intracellular and extracellular domains.

We begin our derivation of the bidomain equations by applying the principle of conservation of current to the tissue. The current passing out of the intracellular domain is equal to that entering the extracellular domain, so we may write

$$\nabla \cdot \mathbf{J}_i + \nabla \cdot \mathbf{J}_e = 0. \tag{3.24}$$

If we then use the expressions for current density given in equations (3.22) and (3.23), we obtain

$$-\nabla \cdot (\sigma_i \nabla\phi_i) + \nabla \cdot \mathbf{J}_i^{\text{stim}} - \nabla \cdot (\sigma_e \nabla\phi_e) + \nabla \cdot \mathbf{J}_e^{\text{stim}} = 0, \tag{3.25}$$

which we may simplify to

$$\nabla \cdot (\sigma_i \nabla\phi_i) + \nabla \cdot (\sigma_e \nabla\phi_e) = \nabla \cdot \mathbf{J}_{total}, \tag{3.26}$$

where we have defined the total stimulus current as $\mathbf{J}_{total} = \mathbf{J}_i^{\text{stim}} + \mathbf{J}_e^{\text{stim}}$. If we rearrange the above equation (simplification is achieved through the addition of the term $-\nabla \cdot (\sigma_i \nabla\phi_e) + \nabla \cdot (\sigma_i \nabla\phi_e) = 0$ to the left hand side) and recall the definition of the membrane voltage, $V_m = \phi_i - \phi_e$, we come to the first bidomain equation after the following steps:

$$\begin{aligned}
\nabla \cdot (\sigma_i \nabla\phi_i) - \nabla \cdot (\sigma_i \nabla\phi_e) + \nabla \cdot (\sigma_i \nabla\phi_e) + \nabla \cdot (\sigma_e \nabla\phi_e) &= \nabla \cdot \mathbf{J}_{total}^{\text{stim}}, \\
\nabla \cdot \big(\sigma_i \nabla(\phi_i - \phi_e)\big) + \nabla \cdot \big((\sigma_i + \sigma_e) \nabla\phi_e\big) &= \nabla \cdot \mathbf{J}_{total}^{\text{stim}}, \\
\nabla \cdot (\sigma_i \nabla V_m) + \nabla \cdot \big((\sigma_i + \sigma_e)\nabla\phi_e\big) &= I_{total}^{\text{stim}},
\end{aligned} \tag{3.27}$$

where we have expressed the total current density in the first bidomain equation, equation (3.27), as a volume stimulus current.

To obtain the second bidomain equation, we begin by equating the flow of charge out of the intracellular space to the current that crosses the cell membrane,

$$-\nabla \cdot \mathbf{J}_i = \chi I_m.$$

We can now calculate the second bidomain equation after applying a similar simplification process to that we used to obtain the first bidomain equation,

$$\begin{aligned}
\nabla \cdot (\sigma_i \nabla \phi_i) - \nabla \cdot \mathbf{J}_i^{\text{stim}} &= \chi I_m, \\
\nabla \cdot (\sigma_i \nabla \phi_i) - \nabla \cdot (\sigma_i \nabla \phi_e) + \nabla \cdot (\sigma_i \nabla \phi_e) - I_i^{\text{stim}} &= \chi I_m, \\
\chi I_m - \nabla \cdot \big(\sigma_i \nabla (V_m + \phi_e)\big) &= -I_i^{\text{stim}}, \\
\chi \left(C_m \frac{\partial V_m}{\partial t} + I_{ion}(\mathbf{u}, V_m) \right) - \nabla \cdot \big(\sigma_i \nabla (V_m + \phi_e)\big) &= -I_i^{\text{stim}}, \qquad (3.28)
\end{aligned}$$

where we have split the transmembrane current in the second bidomain equation, equation (3.28), into capacitative and ionic components, as discussed in Section 3.2.3.

To complete the bidomain equations, we express the time evolution of the state variable vector $\mathbf{u}$ with

$$\frac{\partial \mathbf{u}}{\partial t} = \mathbf{f}(\mathbf{u}, V_m), \qquad (3.29)$$

where $\mathbf{f}$ is an electrophysiology model of the form described in Sections 2.4.1 and 3.2.

The boundary conditions for the bidomain equations can either be based on a surface stimulus which is applied across the external boundary (Pathmanathan et al., 2010), or alternatively, no-flux boundary conditions may be used. In this thesis, the following no-flux conditions for both domains are used unless stated otherwise. That is,

$$\mathbf{n} \cdot \big(\sigma_i \nabla (V_m + \phi_e)\big) = 0, \qquad \text{and} \qquad (3.30)$$

$$\mathbf{n} \cdot (\sigma_e \nabla \phi_e) = 0, \qquad (3.31)$$

where $\mathbf{n}$ is the outward unit normal vector.

3.3.2 Reduction to the monodomain equation

When the intracellular and extracellular conductivities are directly proportional to one another, i.e. for a scalar α, $\sigma_i = \alpha\sigma_e$, the two bidomain equations may be reduced to the monodomain equation (see Keener and Sneyd, 2009, for details).

The monodomain equation is given by

$$\chi\left(C_m\frac{\partial V_m}{\partial t} + I_{ion}\right) + I^{\text{stim}} = \nabla\cdot(\sigma\nabla V_m), \tag{3.32}$$

where the conductivity may be defined in terms of σ_i and σ_e from the equivalent bidomain problem,

$$\sigma = \frac{\sigma_i\,\sigma_e}{\sigma_i + \sigma_e}. \tag{3.33}$$

Similarly to the bidomain equations, the no-flux boundary condition is

$$\mathbf{n}\cdot(\sigma\nabla V_m) = 0. \tag{3.34}$$

3.4 Summary

In this chapter, we have shown how the ionic currents across the membrane of a single electrically active cell may be represented by a system of ordinary differential equations. Cellular electrophysiology models of this type are central to the field of cardiac modelling: we may use them in their unaltered state for examining the time evolution of the different ionic currents, and we can investigate the impact of drugs or disease on the action potential by tuning ion channel conductances or kinetics.

Our derivation of the bidomain equations set out the assumptions that underpin the bidomain model and illustrated its main features. We will revisit the derivation in Chapter 5, where we propose an extension to the model to account for tissue in which several different types of cell are present.

We now move on to Chapter 4, where we detail the numerical methods used for evaluating the solutions to cellular electrophysiology models and the bidomain equations. We particularly focus on the methods used in the *Cancer, Heart and Soft Tissue Environment* software package, which we use for carrying out the simulations in Chapters 6 and 7.

Chapter 4

Numerical Methods

In the previous chapter, we derived the monodomain and bidomain equations that will form the basis of the simulations of cardiac tissue later in this thesis. It is not possible to derive analytic solutions for the monodomain and bidomain equations in most circumstances, so in this thesis we apply one of the most widely used methods of deriving an approximate solution to these equations: the finite element method. The finite element method is often favoured in the context of cardiac simulations due to the way in which complex geometries, such as that of the heart, can be represented using a finite element mesh, and the natural way in which no-flux boundary conditions can be implemented. In this chapter, we describe the implementation of the finite element method for problems in cardiac electrophysiology, and describe other solvers and software packages that are also useful for this purpose.

4.1 Chapter Outline

In Section 4.2, we apply the finite element method to a simple steady-state problem in one dimension to illustrate the main concepts behind the method. We then proceed to the monodomain equation in Section 4.3, where we take a sim-

ilar approach to the first example but take additional steps to demonstrate how the time-evolution aspect of the problem is discretised. The extension to the bidomain equations is straightforward but notationally complex; we therefore focus on the monodomain equation in the majority of this chapter but briefly cover the extension to the bidomain equations in Section 4.3.3.

Having concluded Section 4.3 with the matrix form of the solution to the monodomain equation, we then describe the linear solvers and other techniques that are required in Section 4.4. In Section 4.5, we describe several software libraries used in computational cardiac electrophysiology, with a particular focus on the *Cancer, Heart and Soft Tissue* (Chaste) library, which we use for the bidomain simulations in Chapters 6 and 7.

4.2 An Introduction to the Finite Element Method

As our aim in this chapter is to describe the implementation of the finite element method, we illustrate its use through examples rather than providing a full mathematical treatment. There are many excellent resources which go far beyond the scope of this thesis in terms of mathematical detail, for instance Brenner and Scott (2002), Whiteley (2017) and the lecture notes of Süli (2012). In this example, we restrict ourselves to one spatial dimension as the extension to two or three dimensions is straightforward.

Let us take Poisson's equation as our example problem; the diffusion term within is also found in the monodomain equation. Poisson's equation may be written as

$$\frac{\mathrm{d}^2 u}{\mathrm{d}x^2} = -f(x), \quad \text{on } \Omega = (0, L) \tag{4.1}$$

in one dimension. We impose boundary conditions

$$u|_{x=0} = u_0 \qquad \text{and} \qquad \left.\frac{\mathrm{d}u}{\mathrm{d}x}\right|_{x=L} = 0, \tag{4.2}$$

in order to demonstrate the implementation of both Dirichlet and Neumann boundary conditions.

For the classical solution to equation (4.1), u, to exist, we require that u must be twice differentiable, and that the solution holds over the entire domain Ω. The requirement for these conditions to be met leads equation (4.1) being referred to as the *strong form* of Poisson's equation.

4.2.1 The weak form

If we convert our problem to the *weak form*, less stringent conditions are placed on the differentiability of u. To obtain the weak form of equations (4.1) and (4.2), we first multiply by a test function w and then integrate over the domain Ω. A test function is a function that is continuous on Ω, as are its spatial derivatives, except at a finite number of points. Where Dirichlet boundary conditions are applied, the test function is zero. We therefore move towards the weak form with the following steps,

$$\begin{aligned}
\int_0^L \frac{\mathrm{d}^2 u}{\mathrm{d}x^2}\, w \,\mathrm{d}x &= -\int_0^L f\, w \,\mathrm{d}x, \\
\left[\frac{\mathrm{d}u}{\mathrm{d}x}\, w\right]_0^L - \int_0^L \frac{\mathrm{d}u}{\mathrm{d}x}\frac{\mathrm{d}w}{\mathrm{d}x} \,\mathrm{d}x &= -\int_0^L f\, w \,\mathrm{d}x, \\
\int_0^L \frac{\mathrm{d}u}{\mathrm{d}x}\frac{\mathrm{d}w}{\mathrm{d}x} \,\mathrm{d}x &= \int_0^L f\, w \,\mathrm{d}x,
\end{aligned}$$

where we have used the properties of the test functions, $w(x = 0) = 0$, and the Neumann boundary condition from equation (4.2) to remove the first term that arose from performing the integration by parts.

We may now state the weak form of equations (4.1) and (4.2) as

Find $u \in W$ such that $u(0) = u_0$ and

$$\int_0^L \frac{\mathrm{d}u}{\mathrm{d}x}\frac{\mathrm{d}w}{\mathrm{d}x} \,\mathrm{d}x - \int_0^L f\, w \,\mathrm{d}x = 0, \quad \forall w \in W, \tag{4.3}$$

where

$$W := \{w \in H^1(0, L) \,|\, w(0) = 0\},$$

i.e. W is an infinite-dimensional Sobolev space on the interval $(0, L)$ which is zero where the Dirichlet boundary conditions are imposed. A Sobolev space is

a Hilbert space where the function and its first derivative are continuous across the domain Ω, with

$$H^1(\Omega) = \left\{ w \in L^2(\Omega) \;\middle|\; \frac{\partial w}{\partial x} \in L^2(\Omega) \right\}, \tag{4.4}$$

where L^2 is the space of square-integrable functions. We can now observe that the conditions on the spatial derivatives of the solution u are weakened; only the first derivative is now required to be continuous.

4.2.2 Approximate solution

To compute our approximate solution to the problem, we replace W by a finite-dimensional subspace, $W_h \in W$. W_h consists of piecewise polynomial functions; we examine these functions in more detail shortly. We now state the approximate version of equation (4.3) as

Find $u_h \in W_h$ *such that* $u_h(0) = u_0$ *and*

$$\int_0^L \frac{\mathrm{d}u_h}{\mathrm{d}x} \frac{\mathrm{d}w_h}{\mathrm{d}x} \,\mathrm{d}x - \int_0^L f\, w_h \,\mathrm{d}x = 0, \quad \forall w_h \in W_h. \tag{4.5}$$

4.2.3 Basis functions and construction of the linear system

The linearly independent functions that make up space W_h are known as basis functions. In practise, it is common to rely on linear basis functions due to the simplicity of implementation, although there has been research into the use of higher-order methods in the context of cardiac simulations (Arthurs et al., 2012).

Examples of linear basis functions are shown in Figure 4.1. Each basis function is supported only in a small region of the domain. In Figure 4.1, we have divided to domain Ω into $N = 10$ equally sized sections, or finite elements. In this case, the length of the elements, h, is constant; this is not a necessary condition, but aids in the clarity of later discussion. At each node i of the domain, the basis functions are given by

$$\phi_i(x_j) = \delta_{ij}. \tag{4.6}$$

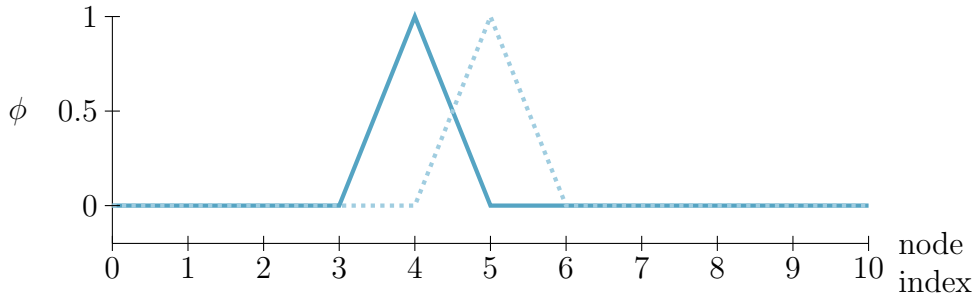

Figure 4.1: Linear basis functions for the finite element method. In this example, we have subdivided domain Ω into ten subintervals, or finite elements. The 5th and 6th basis functions, $\phi_4(x)$ and $\phi_5(x)$, are shown as solid and dashed lines respectively. The product of these two basis functions is non-zero in only the 5th mesh element, $4 < x < 5$.

The approximate solution u_h may be written in terms of basis functions, as the product of a point-wise approximate solution U_i and a basis function ϕ_i at each of the $N + 1$ nodes,

$$u_h(x) = \sum_{i=0}^{N} U_i \phi_i(x). \tag{4.7}$$

We also note that our basis functions are a suitable choice for our test functions w, apart from at $x = 0$, where w must be zero due to the Dirichlet boundary condition. We can now write down the discrete version of the approximation to the weak form,

$$\textit{Find } U = (U_0, U_1, ..., U_N)^T \in \mathbb{R}^{N+1} \textit{ such that } U_0 = u_0 \textit{ and} \tag{4.8}$$

$$\sum_{i=1}^{N} U_i \int_0^L \frac{\mathrm{d}\phi_i}{\mathrm{d}x} \frac{\mathrm{d}\phi_j}{\mathrm{d}x} \,\mathrm{d}x - \int_0^L f\,\phi_j \,\mathrm{d}x = 0, \quad \text{for } j = 0, 1, ..., N. \tag{4.9}$$

Equation (4.9) may equivalently be written as a linear system,

$$\mathbf{Ku} - \mathbf{f} = 0, \tag{4.10}$$

where the entries in matrix $\mathbf{K}$ and vector $\mathbf{f}$ are given by

$$(k_{ij}) = \int_0^L \frac{\mathrm{d}\phi_i}{\mathrm{d}x} \frac{\mathrm{d}\phi_j}{\mathrm{d}x} \,\mathrm{d}x, \qquad \text{and} \tag{4.11}$$

$$(f_j) = \int_0^L f\,\phi_j \,\mathrm{d}x. \tag{4.12}$$

Calculation of the entries in $\mathbf{K}$ is a relatively simple process, which we discuss shortly in Section 4.2.4. The approach taken for $\mathbf{f}$ varies. If function f is constant

in x, the integral is simple to calculate. Otherwise, the integral can either be computed by any suitable numerical method, or by noting that the function $f(x)$ may, like u_h, be written as the product of a point-wise approximation to f and the basis function at each of the nodes. This technique is known as matrix-based assembly, which we discuss in further detail in Section 4.3.2 in relation to the monodomain equation.

Equation (4.10) can be solved for $\mathbf{u}$ using the linear solvers described in Section 4.4.1. This yields the numerical solution U_i at nodes $i = 0, ..., N$. If required, the continuous form of the solution can then be calculated using equation (4.7).

4.2.4 Stiffness and mass matrices

The matrix $\mathbf{K}$ from equation (4.10) occurs in the finite element discretisation process of many partial differential equations. It is often referred to as the *stiffness matrix* from its presence in structural mechanics applications. The entries of the matrix can be calculated given the values of the derivatives of the basis functions within each element,

$$\phi_0(x) = \begin{cases} -(x - x_1)/h & \\ 0 & \end{cases} \qquad \frac{\mathrm{d}\phi_0(x)}{\mathrm{d}x} = \begin{cases} -1/h & \text{if } x_0 < x < x_1 \\ 0 & \text{otherwise} \end{cases}$$

$$\phi_j(x) = \begin{cases} (x - x_{j-1})/h & \\ -(x - x_{j+1})/h & \\ 0 & \end{cases} \qquad \frac{\mathrm{d}\phi_j(x)}{\mathrm{d}x} = \begin{cases} 1/h & \text{if } x_{j-1} < x < x_j \\ -1/h & \text{if } x_j < x < x_{j+1} \\ 0 & \text{otherwise} \end{cases}$$

$$\phi_N(x) = \begin{cases} (x - x_N)/h & \\ 0 & \end{cases} \qquad \frac{\mathrm{d}\phi_N(x)}{\mathrm{d}x} = \begin{cases} 1/h & \text{if } x_{N-1} < x < x_N \\ 0 & \text{otherwise.} \end{cases}$$

If we compute the entries of $\mathbf{K}$ using equation (4.11) and the above expressions for the derivatives, we obtain

$$(k_{i,i}) = \int_{x_{i-1}}^{x_i} \frac{\mathrm{d}\phi_i}{\mathrm{d}x}\frac{\mathrm{d}\phi_i}{\mathrm{d}x}\,\mathrm{d}x + \int_{x_i}^{x_{i+1}} \frac{\mathrm{d}\phi_i}{\mathrm{d}x}\frac{\mathrm{d}\phi_i}{\mathrm{d}x}\,\mathrm{d}x = 2/h \tag{4.13}$$

$$(k_{i,i-1}) = \int_{x_{i-1}}^{x_i} \frac{\mathrm{d}\phi_i}{\mathrm{d}x}\frac{\mathrm{d}\phi_{i-1}}{\mathrm{d}x}\,\mathrm{d}x = -1/h \tag{4.14}$$

$$(k_{i,i+1}) = \int_{x_i}^{x_{i+1}} \frac{\mathrm{d}\phi_i}{\mathrm{d}x}\frac{\mathrm{d}\phi_{i+1}}{\mathrm{d}x}\,\mathrm{d}x = -1/h. \tag{4.15}$$

Most of the entries in $\mathbf{K}$ take the values given in equations (4.13) to (4.15), with the main diagonal being $2/h$, and the first diagonals $-1/h$. The exceptions occur at the boundaries: at node N, equation (4.13) lacks the term from node $i+1$, so $(k_{N,N}) = 1/h$. We also noted earlier that the test functions are zero where Dirichlet boundary conditions are applied; we therefore set $(k_{1,1}) = 1$.

Later in this chapter, we introduce the *mass matrix*, $\mathbf{M}$, which is calculated in a similar manner. The mass matrix is generated when terms such as

$$\int_0^L \phi_i \, \phi_j \, \mathrm{d}x \tag{4.16}$$

are found in the discretised version of the approximate weak form of the problem (i.e. at the stage of equation (4.9)).

4.3 Solving the Monodomain Equation with the Finite Element Method

In this section, we describe the process of solving the monodomain equation using the finite element method. We do not give a description of the bidomain problem here as it is handled in a very similar manner to the monodomain problem, but with necessarily more complex notation due to the presence of both intra and extracellular potentials. We refer the reader to Pathmanathan et al. (2010) for more details on solving the bidomain equations using the finite element method.

In Section 3.3.2, we saw that the strong form of the monodomain equation may be written as

$$\chi \left(C_m \frac{\partial V_m}{\partial t} + I_{\text{ion}}(\mathbf{u}, V_m) \right) - \nabla \cdot (\sigma \nabla V_m) + I_{\text{vol}} = 0, \tag{4.17}$$

on domain Ω and time interval $[0, t]$, which is coupled to a cellular electrophysiology model that simulates the dynamics of the state variables,

$$\frac{\partial \mathbf{u}}{\partial t} = f(\mathbf{u}, V_m), \tag{4.18}$$

and is subject to the boundary condition

$$\mathbf{n} \cdot (\sigma \nabla V_m) = 0. \tag{4.19}$$

In this example, we assume that the conductivity, $\sigma = \sigma(\mathbf{x})$, while the surface area to volume ratio, χ, and capacitance per unit area C_m, are constant across the entire domain.

4.3.1 Temporal discretisation

A fully implicit temporal discretisation of the monodomain and bidomain equations is computationally expensive to solve, so a widely used alternative discretisation is to treat the diffusion term implicitly and the reaction term explicitly, in what is often termed a semi-implicit approach (Pathmanathan et al., 2010).

To make the notation clearer, we use v^n to represent the membrane voltage, V_m, at a particular time-step n, where we have divided our time-interval $[0, t]$ into $N + 1$ equal steps. We discretise the time derivative using the backward Euler method,

$$\chi C_m \frac{v^n - v^{n-1}}{\Delta t} + \chi I_{\text{ion}}^{n-1} - \nabla \cdot (\sigma \nabla v^n) + I_{\text{vol}}^{n-1} = 0, \quad \text{for } n = 0, \ldots, N,$$

and then group terms from timesteps n and $n-1$ on the left and right sides of the equation, respectively,

$$\chi C_m v^n - \Delta t \nabla \cdot (\sigma \nabla v^n) = \chi C_m v^{n-1} - \Delta t \chi I_{\text{ion}}^{n-1} - \Delta t I_{\text{vol}}^{n-1}, \text{ for } n = 0, \ldots, N. \quad (4.20)$$

From here onwards, we will drop the statement of the time discretisation $n = 0, \ldots, N$ for brevity.

4.3.2 Spatial discretisation

We now cast equation (4.20) into the weak form, as we did for the Poisson equation in Section 4.2.1. First, we multiply by test functions w and integrate over the domain Ω,

$$\int_\Omega \chi C_m \, w \, v^n - \Delta t w \nabla \cdot (\sigma \nabla v^n) \, \mathrm{d}\mathbf{x} = \int_\Omega \chi C_m \, w \, v^{n-1} - \Delta t \chi w I_{\text{ion}}^{n-1} - \Delta t w I_{\text{vol}}^{n-1} \, \mathrm{d}\mathbf{x},$$

and then integrate by parts to remove the second derivative

$$\int_\Omega \chi C_m w\, v^n \,\mathrm{d}\mathbf{x} - \Delta t\Big([w\,\sigma\nabla v^n]_\Omega - \int_\Omega \nabla w \cdot (\sigma \nabla v^n)\,\mathrm{d}\mathbf{x}\Big) = \int_\Omega \chi C_m w v^{n-1}\,\mathrm{d}\mathbf{x} - \Delta t \int_\Omega \chi w I_{\text{ion}}^{n-1} - w I_{\text{vol}}^{n-1}\,\mathrm{d}\mathbf{x}.$$

The no-flux boundary condition from equation (4.19) can be utilised to remove the first term in the brackets of the equation above. We can then state the weak form of the problem as

$$\textit{Find } v^n \in W \textit{ such that } \int_\Omega \chi C_m w\, v^n \,\mathrm{d}\mathbf{x} + \Delta t \int_\Omega \nabla w \cdot (\sigma \nabla v^n)\,\mathrm{d}\mathbf{x} = \int_\Omega \chi C_m w\, v^{n-1}\,\mathrm{d}\mathbf{x} - \Delta t \int_\Omega \chi w I_{\text{ion}}^{n-1} - w I_{\text{vol}}^{n-1}\,\mathrm{d}\mathbf{x},$$

where

$$W := \{w \in H^1(\Omega)\} = \left\{ w : \int_\Omega (w^2 + w'^{\,2})\,\mathrm{d}\mathbf{x} < \infty \right\}.$$

In contrast to our previous example, we now require no additional constraints on W as Dirichlet boundary conditions are not applied.

If we move from the infinite-dimensional space W to the finite-dimensional subspace $W_h \in W$, we can write down the approximate version of the weak form,

$$\textit{Find } v_h^n \in W_h \textit{ such that } \int_\Omega \chi C_m w_h\, v_h^n \,\mathrm{d}\mathbf{x} + \Delta t \int_\Omega \nabla w_h \cdot (\sigma \nabla v_h^n)\,\mathrm{d}\mathbf{x} = \int_\Omega \chi C_m w_h\, v_h^{n-1}\,\mathrm{d}\mathbf{x} - \Delta t \int_\Omega \chi w_h I_{\text{ion}}^{n-1} - w I_{\text{vol}}^{n-1}\,\mathrm{d}\mathbf{x}.$$

The approximate solution at time-step n, v_h^n, may be expressed in terms of the product of a node-wise approximation and the basis functions,

$$v_h^n(\mathbf{x}) = \sum_{i=0}^{M} V_i^n \phi_i(\mathbf{x}), \tag{4.21}$$

where we have used $M+1$ nodes across domain Ω. We may then pose the discretised form of the problem as

$$\textit{Find } V^n = (V_0^n, V_1^n, ..., V_M^n)^T \in \mathbb{R}^{N+1} \textit{ such that}$$
$$\chi C_m \sum_{j=0}^{M} \Big(\int_\Omega \phi_i\, \phi_j \,\mathrm{d}\mathbf{x}\Big) V_j^n + \Delta t \sum_{j=0}^{M} \Big(\int_\Omega \nabla\phi_i\, \sigma\, \nabla\phi_j \,\mathrm{d}\mathbf{x}\Big) V_j^n = \chi C_m \sum_{j=0}^{M} \Big(\int_\Omega \phi_i\, \phi_j \,\mathrm{d}\mathbf{x}\Big) V_j^{n-1} - \Delta t \int_\Omega \chi \phi_j I_{\text{ion}}^{n-1} - \phi_j I_{\text{vol}}^{n-1}\,\mathrm{d}\mathbf{x}. \tag{4.22}$$

In the previous section, we noted that there are several approaches for evaluating integrals such as the final term in equation (4.22). Here, we perform matrix-based assembly of the ionic and stimulus current vectors. If we assume that the currents may each be written as the product of a node-wise approximation to their values and the basis functions, such that

$$I_{\text{ion}}^{n-1}(\mathbf{x}) = \sum_{i=0}^{M} I_{\text{ion},i}^{n-1}\phi_i(\mathbf{x}) \qquad \text{and} \qquad I_{\text{vol}}^{n-1}(\mathbf{x}) = \sum_{i=0}^{M} I_{\text{vol},i}^{n-1}\phi_i(\mathbf{x}), \tag{4.23}$$

we may rewrite the discretised form of the problem as

$$\begin{aligned} &\textit{Find } V^n = (V_0^n, V_1^n, ..., V_N^n)^T \in \mathbb{R}^{N+1} \textit{ such that} \\ &\chi C_m \sum_{j=0}^{M} \left(\int_\Omega \phi_i \, \phi_j \, \mathrm{d}\mathbf{x} \right) V_j^n + \Delta t \sum_{j=0}^{M} \left(\int_\Omega \nabla\phi_i \, \sigma \, \nabla\phi_j \, \mathrm{d}\mathbf{x} \right) V_j^n = \\ &\chi C_m \sum_{j=0}^{M} \left(\int_\Omega \phi_i \, \phi_j \, \mathrm{d}\mathbf{x} \right) V_j^{n-1} - \Delta t \sum_{j=0}^{M} \left(\int_\Omega \phi_i \, \phi_j \, \mathrm{d}\mathbf{x} \right) \left(\chi I_{\text{ion},j}^{n-1} - I_{\text{vol},j}^{n-1} \right). \end{aligned} \tag{4.24}$$

In Section 4.2.4, we noted that integrals such as the types observed in equation (4.24) can easily be evaluated. In two or three dimensions, the evaluation is slightly more complex as the elements are either triangles or tetrahedra rather than lines, leading to the basis functions being non-zero over a larger number of elements. A detailed discussion of this point may be found in Whiteley (2017, Section 7.3). Once the required integrals have been calculated, we may write equation (4.24) as the linear system

$$\left(\chi C_m \mathbf{M} + \Delta t \mathbf{K}(\sigma)\right) \mathbf{v}^n = \chi C_m \mathbf{M} \mathbf{v}^{n-1} - \Delta t \mathbf{M} \mathbf{b}^{n-1}, \tag{4.25}$$

where $\mathbf{b}$ is a vector sum of the two currents at time $n-1$, with entries

$$(b)_i = \chi I_{\text{ion},i}^{n-1} + I_{\text{vol},i}^{n-1}. \tag{4.26}$$

To obtain the solution to the monodomain equation on the time interval $[0, t]$, equation (4.25) is repeatedly solved for time-steps $n = 1, \ldots, N$ to obtain the membrane voltage at time-step n, $\mathbf{v}^n$. Obtaining the solution to equation (4.25) requires the use of a linear solver such as those described later in this chapter, in Section 4.4.1. The matrices $\mathbf{K}$ and $\mathbf{M}$ are sparse (tridiagonal in one dimension), a

feature which may be taken advantage of to improve the efficiency of the solution process.

In Chapter 5, we apply the approach discussed in this section to solve the monodomain equation in systems containing two different types of cell, which are represented by different cellular electrophysiology models.

4.3.3 Extension to the bidomain equations

The later parts of this thesis, Chapters 6 and 7, utilise the bidomain equations to simulate the transmembrane and extracellular potentials in cultures of human stem cell-derived cardiomyocytes. The application of the finite element method to the bidomain equations to generate a linear system is very similar to that of the monodomain equation, but the notation is far more complicated due to the presence of the second coupled partial differential equation. Rather than provide a complete description of the discretisation process, we refer the reader to Pathmanathan (2012).

If the same process used throughout Section 4.3 is applied to the bidomain equations as presented in equations (3.27), (3.28), (3.30) and (3.31), the resulting linear system is

$$\begin{pmatrix} \chi C_m \mathbf{M} + \Delta t \mathbf{K}(\sigma_i) & \mathbf{K}(\sigma_i) \\ \mathbf{K}(\sigma_i) & \mathbf{K}(\sigma_i + \sigma_e) \end{pmatrix} \begin{pmatrix} \mathbf{v}^n \\ {\mathbf{\Phi_e}}^n \end{pmatrix} = \begin{pmatrix} \chi C_m \mathbf{M} + \Delta t \mathbf{M} \mathbf{b} \\ 0 \end{pmatrix}. \tag{4.27}$$

4.4 Further Techniques for Implementing the Monodomain and Bidomain Models

We now discuss further techniques that are required to numerically solve partial differential equations, specifically the monodomain and bidomain equations, using the finite element method.

4.4.1 Linear solvers

The stiffness and mass matrices, $\mathbf{K}$ and $\mathbf{M}$, that arise from the discretisation of the solution to the monodomain and bidomain equations are highly sparse; iter-

ative methods can therefore be employed very effectively to solve linear systems such as those in equations (4.25) and (4.27) (Clayton et al., 2011). Krylov subspace methods such as conjugate gradients are widely used, and specific preconditioners have been noted to improve performance (Potse et al., 2006; Bernabeu et al., 2010).

4.4.2 Ordinary differential equation solvers

A wide variety of methods are available for solving systems of ordinary differential equations such as cellular electrophysiology models. The most simple are the forward Euler method and low order Runge-Kutta methods (see Süli and Mayers (2003) for an overview). However, the stiffness present in cellular electrophysiology models calls for small time-steps to be taken in order to achieve accurate and stable results with explicit methods.

Alternatives include the Rush-Larson method (Rush and Larsen, 1978; Marsh et al., 2012), which was developed specifically for cellular electrophysiology models, and adaptive methods such as the Sundials CVODE solver (Hindmarsh et al., 2005) and Matlab's `ode15s`. Even with adaptive methods, solving the ordinary differential equations can still take a high fraction of the computational time in tissue simulations; techniques such as lookup tables and partial evaluation of the model have therefore also been employed (Cooper et al., 2015).

4.5 Software Packages for Computational Cardiac Electrophysiology

The cardiac modelling community is active in creating and sharing software for solving both single-cell and tissue-scale problems.

While the ordinary differential equation solvers discussed in Section 4.4.2 may be used to simulate the activity of a single cardiomyocyte given a cardiac electrophysiology model, tools such as OpenCOR (Garny and Hunter, 2015), the Cardiac Electrophysiology Web Lab (Cooper et al., 2016) and Myokit (Clerx et

al., 2016) offer a more interactive experience.

Tissue-scale solvers include CARP (Vigmond et al., 2003), OpenCMISS (Nickerson et al., 2015), CHeart (Lee et al., 2016a) and Chaste (Mirams et al., 2013), all of which use the finite element method to solve the bidomain equations. The properties of several of these solvers have been compared in a verification study (Niederer et al., 2011).

4.5.1 Chaste

The simulations in Chapters 6 and 7 in this thesis utilise the *Cancer, Heart and Soft Tissue Environment*, or Chaste, a package developed by the Computational Biology Group at the University of Oxford. The project began in 2005, when the group identified the need for a cardiac electrophysiology library that was open source, developed with the latest programming methodologies, extensible, and well-tested. Long-term maintenance of the library was a particular priority (Pitt-Francis et al., 2009). Chaste has been widely used for both cardiac (Zemzemi et al., 2013) and cell-based simulations (Dunn et al., 2013).

The simulations in Chapters 6 and 7 of this thesis use the bidomain solver that is implemented within Chaste. The finite element implementation utilises linear basis functions, and the resulting linear system is solved using the PETSc implementation of the conjugate gradient method or the GMRES solver. The cellular electrophysiology models are solved using CVODE.

4.6 Summary

In this chapter we described the numerical methods used to perform monodomain or bidomain simulations of the electrical activity within cardiac tissue, with a focus on the Chaste library. We showed how the finite element method may be applied to the monodomain equation to generate a linear system that can be solved numerically to obtain the transmembrane voltage at each time-step of the simulation. We also discussed how this process can be adapted for the bidomain equations.

In the next chapter, we modify the derivation of the bidomain equations to be representative of a system that contains two different types of cardiac cell that are well-mixed. We perform simulations of such a system using a custom Matlab implementation of the finite element method, and compare our modified approach to a traditional implementation, where cells of the same type occupy distinct regions of the tissue.

Chapter 5

Models of Multiple Cellular Phenotypes in Cardiac Tissue

At the time of writing, the paper upon which this chapter is based, "Representation of Multiple Cellular Phenotypes Within Tissue-Level Simulations of Cardiac Electrophysiology" was in revision following a positive first set of reviews from the Bulletin of Mathematical Biology. The paper was published in January 2019 (Bowler et al., 2019). The paper was co-authored by myself, Gary Mirams, David Gavaghan and Jonathan Whiteley. The re-homogenisation of the bidomain equations was performed and written by Jonathan Whiteley. The rest of the work presented in this chapter is mine, and was done under the guidance of the co-authors. We describe the process by which the model was derived in Section 5.2.4, and the complete derivation, as prepared for the paper by Jonathan Whiteley, may be found in Appendix A2.

In the previous two chapters, we explained how the electrical activity within cardiac tissue may be modelled using the monodomain or bidomain equations, coupled to a cellular electrophysiology model that represents the ionic currents that pass across the membrane of a particular type of cardiac cell. We then described the process of solving the coupled system using the finite element method.

In this chapter, we move on to a more complex system. As we noted in Section 2.5, human stem cell-derived cardiomyocytes have been reported to possess different action potential morphologies depending on an underlying cellular phenotype. In order to simulate the monolayers of stem cell-derived cardiomyocytes used in micro-electrode array experiments, it is necessary for our simulation framework to be suitable for multi-phenotype systems. In this chapter, we describe two models that can be used to simulate cardiac tissue that contains two phenotypes, and which may easily be extended to further phenotypes.

We term the two models the *homogenised phenotypes* model and the *partitioned phenotypes* model. The partitioned phenotypes model is what we would consider to be the "traditional" form of the bidomain model, where different cellular electrophysiology models are used in selected regions of the domain. The homogenised phenotypes model is derived through an adaptation of the usual bidomain derivation, in which we explicitly include cells of different phenotype within the periodic unit that we homogenise over. The resulting equations are similar to those of the bidomain equations, but permit spatially varying proportions of the two cellular phenotypes to be used over the domain. We perform one-dimensional simulations in order to validate the homogenised phenotypes model, and draw some initial conclusions about the implications of phenotypic variability in spontaneously beating cardiac tissue.

Throughout the remainder of this thesis, we often refer to the homogenised and partitioned phenotypes models as the HP and PP models, respectively.

5.1 Chapter Outline

We begin this chapter with a review of the different cellular phenotypes reported in human stem cell-derived cardiomyocytes, which were briefly discussed in Section 5.2. Using this information, we propose several requirements that must be met by our chosen simulation framework. We consider the methods that are presently available for performing tissue-scale simulations of multi-phenotype systems, and conclude that a specialised approach is more preferable than adapting

existing models. We then discuss the approach taken to derive the homogenised phenotypes model in Section 5.2.4. The full derivation, along with the reduction to the partitioned phenotypes model, may be found in Appendix A2.

The implementation of the homogenised phenotypes and partitioned phenotypes models is described in Section 5.3. We explain the adaptations that must be made to the cellular electrophysiology model for the implementation of the homogenised phenotypes model, and comment on how simulations of more than one cell type requires extra care to be taken in the implementation of the partitioned phenotypes model. Section A1.1 extends upon the description in Section 5.3; it provides further detail on the implementation of the two models in the custom Matlab code used for the simulations in this chapter.

In Section 5.4, we introduce the simulations that we carry out in this chapter. The simulations have two aims: first, to validate the homogenisation that we carried out to derive the homogenised phenotypes model, and second, to illustrate the differences between the two models. Before using the homogenised and partitioned phenotypes models in the simulations, we carry out convergence studies which are described in Section 5.5. In Section 5.6, we discuss the results of our simulations and how they relate to the biological system of the stem cell-derived cardiomyocyte monolayer in the micro-electrode array.

We conclude in Section 5.8 with a comparison of the homogenised and partitioned phenotypes models and proposals for their use in two-dimensional simulations of human stem cell-derived cardiomyocytes.

5.2 Development of a Mathematical Model for the Electrophysiology of Multi-Phenotype Tissue

In Section 2.6, we stated that one of the aims of this thesis is to develop a methodology for simulating the electrical activity within tissue preparations of human stem cell-derived cardiomyocytes (hSC-CMs) that incorporates variability in action potential morphology between cells. In this section, we briefly summarise the

present knowledge of variability in hSC-CMs and state the properties that our model must possess if it is to be suitable for use in simulations of such a system. We describe the present modelling methodologies that are available, and propose an alternative approach which is better suited for modelling the particular properties of hSC-CMs.

5.2.1 Evidence for multiple cellular phenotypes in human stem cell-derived cardiomyocyte tissue cultures

In Section 2.5, we discussed the electrophysiology of human stem cell-derived cardiomyocytes, with particular reference to the similarities and differences from the cardiomyocytes found in the adult heart. Many studies of single-cell hSC-CM electrophysiology have noted that the action potential may take one of three distinct morphologies, resembling the action potentials found in the ventricles, atria or sino-atrial node of the adult human heart (He et al., 2003; Zhang et al., 2009; Ma et al., 2011). This has led cells of such type to be termed ventricular-like, atrial-like and nodal-like. Action potentials from each of these three types were shown previously in Figure 2.7.

Determination of the distribution of these phenotypes within tissue-scale cultures of hSC-CMs is an ongoing and active area of research, with no consensus at the time of writing. Small clusters of human embryonic stem cell-derived cardiomyocytes have been found to contain one or two separate regions of distinct action potential morphology (Zhu et al., 2016; Vestergaard et al., 2017), while monolayers of human induced pluripotent stem cell-derived cardiomyocytes have been reported to contain a more continuous spectrum of action potential morphologies (Du et al., 2015). The proposal for a spectrum of phenotypes has itself been the subject of debate (Giles and Noble, 2016; Kane et al., 2016; Bett et al., 2016), with the inability to estimate maximum diastolic potential (an action potential biomarker often used in the phenotype classification process) through optical mapping studies posing further difficulties. Although the work of Du et al. (2015) did include application of a gap junctional blocker to decouple the activity

of neighbouring cells, the amount used would not have been sufficient to entirely decouple the system. Therefore, we can identify two possibilities: that phenotype may be subject to more gradual changes through space than previously reported (which runs in contradiction to single-cell studies), or that cells of different phenotype are sufficiently mixed that the action potentials observed on a larger scale appear to change gradually (which would be a reasonable assumption given that the cells used in this study were supplied as a cryo-preserved suspension of cells).

While precise identification of cellular phenotype is clearly an area where more work is merited (and we will touch again on this point in Chapter 8), for now, we shall assume that tissue preparations of hSC-CMs are likely to have either large regions of a single phenotype, in the case of human embryonic stem cell-derived cardiomyocytes, or a mixture of phenotypes, in the case of commercially supplied human induced pluripotent stem cell-derived cardiomyocytes.

5.2.2 Requirements for our model

Given our knowledge of the arrangement of phenotypes in hSC-CM cultures, we can therefore place some requirements upon our modelling framework:

- The distinct electrophysiology of atrial-like, ventricular-like and nodal-like hSC-CMs must be included in the model. In order to do so, our framework must be suitable for at least three distinct cell types, and preferably be easy to modify should future experimental work indicate that hSC-CM action potentials are better classified into fewer or more groups.
- We must be able to represent spatial variation in the proportions of cells of a given phenotype, ranging from regions that are entirely of single phenotype to those that are more equally mixed.

5.2.3 Existing approaches for simulating tissue containing multiple cellular phenotypes

Discrete approaches to simulations of cardiac electrophysiology are inherently well-suited to cases where each cell has variable characteristics, as every cell is

modelled independently (Winslow et al., 1993; Oren and Clancy, 2010). However, simulation of every individual cell can pose a high computational cost when large systems are considered. This makes the discrete approach less practical for systems such as the hSC-CM tissue cultures that we wish to simulate, which typically occupy regions of around 1 cm in diameter.

While differences in cell type are not explicitly included in the traditional form of the bidomain equations, variability in the cellular electrophysiology model can be incorporated if sufficient care is taken in the implementation of the numerical scheme. The mesh must be carefully partitioned into regions where a single cell type is present; if the cells are well-mixed, these regions are very small and the computational demands of such a fine mesh can be considerable. However, this process is not problematic when the regions are larger.

The extended bidomain equations were first developed for simulation of cardiac muscle containing cardiomyocytes and fibroblasts (Sachse et al., 2009), and for simulation of the gastrointestinal system (Buist and Poh, 2010). Their structure is similar to that of the bidomain equations, but a second intracellular domain is added. However, there are limitations to this approach for the case of hSC-CMs. The derivation of the extended bidomain equations assumes that all cells are connected to cells of both their own type and the second type, which may not be the case in hSC-CM cultures where the proportions of the different phenotypes varies more dramatically than in those systems for which the extended bidomain simulations were developed. In addition, we note that the extended bidomain equations, in their present form, only permit mixtures of two different types of cell. Substantial amounts of work would be required to refactor the computational solvers for use with higher numbers of cellular phenotypes.

We therefore choose to take an alternative approach. In this chapter, we investigate a modified form of the bidomain equations, where the homogenisation process through which the equations are derived is performed over small regions that contain a mixture of cell types. This approach is flexible, in that further cellular phenotypes can easily be added to the model; computationally efficient,

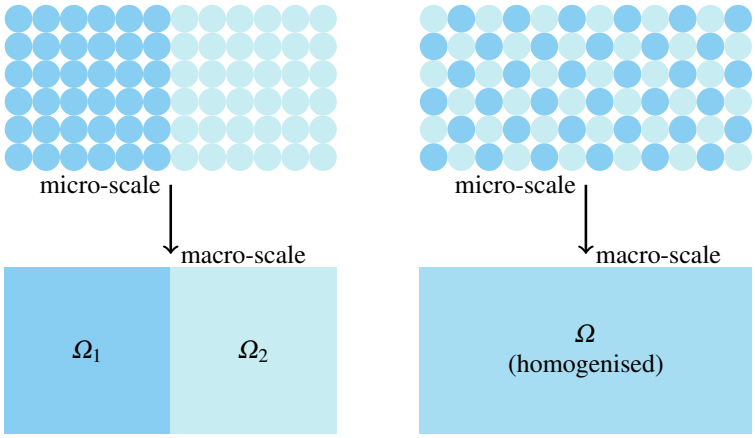

Figure 5.1: Comparison of the partitioned phenotypes and homogenised phenotypes models. The case on the left may be divided into two partitioned regions, each containing a single type of cell. Systems of this type may be simulated using the *partitioned phenotypes* model. Partitioning the case on the right into single-phenotype regions would result in many tiny partitions. Performing the homogenisation process over regions containing both types of cell using the *homogenised phenotypes* approach is therefore preferable.

as there is no requirement to precisely partition the mesh into regions of a single cell type; and is able to naturally model variability in the proportions of cell types, ranging from exclusively one type to an equal mix.

We refer to the new model as the *homogenised phenotypes* model (often shortened to the HP model), and compare it to the traditional form of the bidomain model with partitioned regions (the *partitioned phenotypes*, or PP model). The two approaches are illustrated in Figure 5.1.

5.2.4 Derivation of the homogenised and partitioned phenotypes models

The derivation of the homogenised phenotypes model follows that of the bidomain model that has been presented by many other authors (for example, Keener and Panfilov, 1996; Keener and Sneyd, 2009; Bruce et al., 2014) with a modification to the domain over which the homogenisation process is carried out. This is shown in Figure 5.2, where there are two different types of cell present in the marked domain over which the homogenisation is to be carried out. The full derivation of the homogenised phenotypes model was prepared for the paper, Bowler et al.

(2019), by Jonathan Whiteley; rather than present this derivation with minor modifications, the version from the paper may be found in Appendix A2.

The derivation is now summarised briefly. Initially, the derivation proceeds according to that of the traditional bidomain equations. We assume that cardiac tissue may be divided into two continuously interconnected regions, the intracellular and extracellular domains. Within these domains, the intracellular and extracellular currents may be considered Ohmic, as we discussed previously in Section 3.3. This tissue differs from that treated in the usual form of the bidomain equations in that it contains two different types of cell, which may have different properties. The cells are arranged in a periodic lattice, shown in Figure 5.2. The dimensions of this periodic unit, l, are much smaller than the lengthscale of the solution, L; typical values for the parameters would be $l \approx 200\,\mu\text{m}$ (the diameter of a small group of cells) and $L \approx 2000\,\mu\text{m}$ (the typical length of a region of tissue undergoing the rapid depolarisation phase of the action potential). We can then treat the solutions on the micro and macroscales separately, and may write the intracellular and extracellular potentials, ϕ_i and ϕ_e, as asymptotic expansions in the parameter $\delta = l/L$. Substituting the expanded forms of ϕ_i and ϕ_e into the equations for the ionic currents and the conservation of current throughout the domain Ω yields terms in different powers of δ. Integrating terms in certain powers of δ over first the intracellular, and then separately the extracellular, domains returns us to the usual form of the bidomain equations, but with variability in cell type built into the model.

For two cellular phenotypes, the governing equations of the homogenised phenotypes model are given by

$$\nabla \cdot (\sigma_i \nabla V_m + (\sigma_i + \sigma_e)\, \nabla \phi_e) = I_{total}^{\text{stim}} \tag{5.1}$$

$$\chi\left(C_m \frac{\partial V_m}{\partial t} + I_{\text{ion}}\right) - \nabla \cdot (\sigma_i \nabla (V_m + \phi_e)) = -I_i^{\text{stim}}, \tag{5.2}$$

with

$$C_m = \rho_1\, C_{m1} + \rho_2\, C_{m2}, \tag{5.3}$$

$$I_{\text{ion}} = \rho_1\, I_{\text{ion},1}(V_m, \mathbf{u}_1) + \rho_2\, I_{\text{ion},2}(V_m, \mathbf{u}_2), \tag{5.4}$$

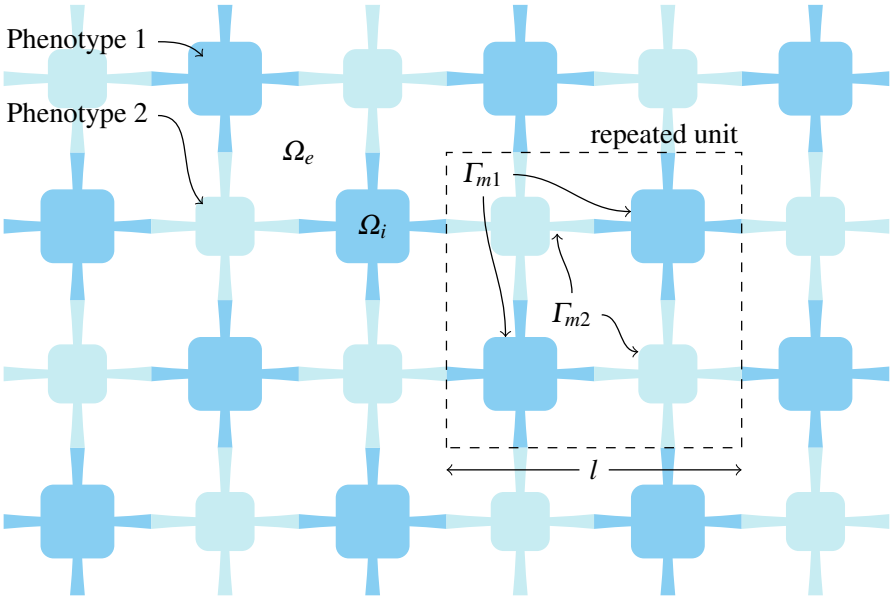

Figure 5.2: Cells of two different phenotypes in the homogenised phenotypes model. The repeated unit is made up of both cell types; it should be noted that the two types do not have to be present in equal proportions. Ω_i and Ω_e denote the intracellular and extracellular domains respectively. The surface area of the cell membrane within the repeated unit is given by $\Gamma_m = \Gamma_{m1} + \Gamma_{m2}$. The lengthscale of the solution, L, is assumed to be much larger than the lengthscale of the repeated unit, l.

where the subscripts indicate the cell type, and ρ_1, ρ_2 denote the relative proportions of cell membrane of each type of cell within the unit volume over which the homogenisation is performed. We note that we have modified the notation from Appendix A2 to fit with that already established in the earlier chapters of this thesis, and have returned the equations to their usual dimensional form with a stimulus current. Further cellular phenotypes beyond the two indicated here are simple to add to the model.

We can see that the bidomain equations themselves (equations (5.1) and (5.2)) are identical to those we derived in Chapter 3 (equations (3.27) and (3.28)); it is in the form of the capacitance and ionic current where the effects of the altered homogenisation process can be seen. Implementation of the homogenised phenotypes model therefore requires no changes to existing bidomain solvers, which is a great advantage for this approach relative to the extended bidomain model.

5.3 Implementation

In Section 4.3, we described how a numerical solution to the monodomain and bidomain equations may be obtained through the finite element method. We now explain briefly how this approach is modified for each of the homogenised and partitioned phenotypes models. The full details of the Matlab implementation of the finite element method for the simulations in this chapter may be found in Section A1.1.

We describe these changes in terms of the monodomain model, which we use for the simulations throughout this chapter. As we do not investigate the extracellular potential at this stage, and assume constant intra and extracellular conductivities, the bidomain model may be equivalently represented by the monodomain model.

If we briefly recall from Chapter 3, the monodomain model may be written as

$$\chi \left(C_m \frac{\partial V_m}{\partial t} + I_{ion} \right) + I^{\text{stim}} = \nabla \cdot (\sigma \nabla V_m), \tag{5.5}$$

with the no-flux boundary condition

$$\mathbf{n} \cdot (\sigma \nabla V_m) = 0. \tag{5.6}$$

Following application of the finite element method detailed in Section 4.3, the linear system to be solved for $\mathbf{v}$ (the nodal vector of membrane voltage V_m) at time-step n may be written as

$$(\chi C_m \mathbf{M} + \sigma \mathbf{K})\, \mathbf{v}^n = \chi C_m \mathbf{M} \mathbf{v}^{n-1} - \Delta t \mathbf{M} \mathbf{b}^{n-1}, \tag{5.7}$$

where $\mathbf{M}$ and $\mathbf{K}$ are the mass and stiffness matrices and $\mathbf{b}$ is the sum of the nodal values of ionic and stimulus currents, $\mathbf{b} = \chi \mathbf{i}_{\text{ion}} + \mathbf{i}_{\text{vol}}$.

5.3.1 The homogenised phenotypes model

In equations (5.1) to (5.4), we noted that the differences from the normal formulation of the bidomain model occur in the terms C_m and I_{ion}, which are replaced

by weighted averages of the values from the two phenotypes, according to the proportion of cell membrane from each cell type at a given location in the domain. The same holds true for the homogenised phenotypes form of the monodomain equation: the only changes required in the implementation are to the values of C_m and I_{ion}. This will particularly affect the entries of vector $\mathbf{b}$ from equation (5.7).

In Section A1.1.1, we provide a more detailed description of how these changes are implemented for a monodomain problem, and describe some optimisations that may be made during the calculation of the homogenised ionic currents.

Throughout this chapter, we assume that cells of the two types under consideration have the same size and shape. We can therefore define ρ_1 and ρ_2 in an alternative manner: the relative proportions of the cell membrane of the two cell types are equivalent to the relative proportions of the numbers of each of those types.

5.3.2 The partitioned phenotypes model

In the partitioned phenotypes model, the values of the parameters χ, C_m and σ, along with the ionic current I_{ion}, are dependent on which of the cell types are present in a given area. For simplicity, we hold χ, C_m and σ constant throughout this chapter. We must therefore consider how the values of I_{ion} are defined.

There are two possibilities: either we define the model phenotype (and therefore the cellular electrophysiology model used to calculate I_{ion}) at the nodes of the mesh, or at the elements of the mesh. The node-wise approach is simpler to implement from a computational perspective, but the boundaries between regions of different phenotype are not clearly defined. The element-wise approach overcomes this problem, but requires additional stages in the implementation to ensure that vector $\mathbf{b}$ (from equation (5.7)), which contains the nodal values of the ionic current, is calculated correctly.

Details of the two approaches and their implementations may be found in Section A1.1.2. We compare the numerical convergence properties of the two methods in Section 5.5, and choose to use the element-wise approach for the

partitioned phenotypes simulations later in this chapter as the boundaries of regions of different phenotype are well-defined.

5.4 Description of Simulations

Now that we have demonstrated the implementation of the homogenised and partitioned phenotypes models, we now compare the two models by simulating a one dimensional fibre. Using the simulations outlined below, we aim to verify that our homogenised model produces the behaviour that is expected of it, i.e. that the behaviour of the partitioned phenotypes model approaches that of the homogenised phenotypes model as the partition size tends towards zero. We also wish to compare the partitioned phenotypes and homogenised phenotypes models for different distributions of phenotypes, and to assess the regimes under which each model is valid.

We have divided our simulations into six sets that we describe below. In the first five sets, we use the phenomenological FitzHugh-Nagumo action potential model. This model can provide a wide range of action potential morphologies if its three parameters are altered. In the final set of simulations, we use the physiological Paci et al. (2013a) models of atrial-like and ventricular-like hSC-CM electrophysiology.

5.4.1 List of simulations

Set 1: This set of simulations is designed to test whether the action potentials of the PP model tend towards those of the HP model as the size of the unit that we homogenise over is decreased; that is, in the limit $\delta \to 0$ that we discussed in Section 5.2.4. We increase the numbers of partitioned units throughout the fibre, therefore decreasing the size of the partitioned unit while the relative proportions of the two model phenotypes are kept constant. The arrangement of the model phenotypes within the fibre may be found in the top panel of Figure 5.3. The biomarkers derived from the action potentials of the PP systems are compared to those from the HP case. We test four different pairs of parametrisations of the

FitzHugh-Nagumo model, with the pairs covering all combinations of spontaneous and excitable activity.

Set 2: In our second stage of verification, we test two sizes of partitioned unit and alter the relative proportions of the two model phenotypes, ρ_1 and ρ_2, throughout the series of simulations, and compare the beat rates from both models. Our aims here are twofold: firstly, we wish to determine whether the beating condition of the FitzHugh-Nagumo model (spontaneous activity only occurs if α, one of the model parameters, is less than zero) holds in the fibres, and secondly, we investigate whether the beat rate of the PP model matches that of the HP model. The layout of model phenotypes is shown in the middle panel of Figure 5.3.

Set 3: We will see later that the model phenotype used at the boundaries of the fibre can have an impact on the location of the pacemaker region. Our third set of simulations investigates the effects of the boundary phenotype in more detail. The bottom panel of Figure 5.3 shows how the fibre is partitioned into n units. When n is even, the system has a different model phenotype at either end. For odd n, the phenotypes at both ends of the fibre are the same. We examine how the activation pattern and conduction velocity are affected by the presence of a slow or fast-beating model phenotype at the boundaries of the fibre.

Set 4: Until now, our investigations have assumed constant proportions of the two model phenotypes throughout the fibre. However, this assumption is unrealistic in a biological context: whatever the actual distribution of cell types, they are unlikely to be consistent throughout the entire tissue. We therefore compare the activity of a homogenised fibre where the two model phenotypes are set in a smoothly varying pattern to a small-unit version of the PP model. In the fibre where the HP model is used, the proportions of the two model phenotypes are given by

$$\rho_1(x) = 0.5 + A \sin\left(\frac{2\pi x}{L}\right) \quad \text{and} \tag{5.8}$$

$$\rho_2(x) = 1 - \rho_1(x), \tag{5.9}$$

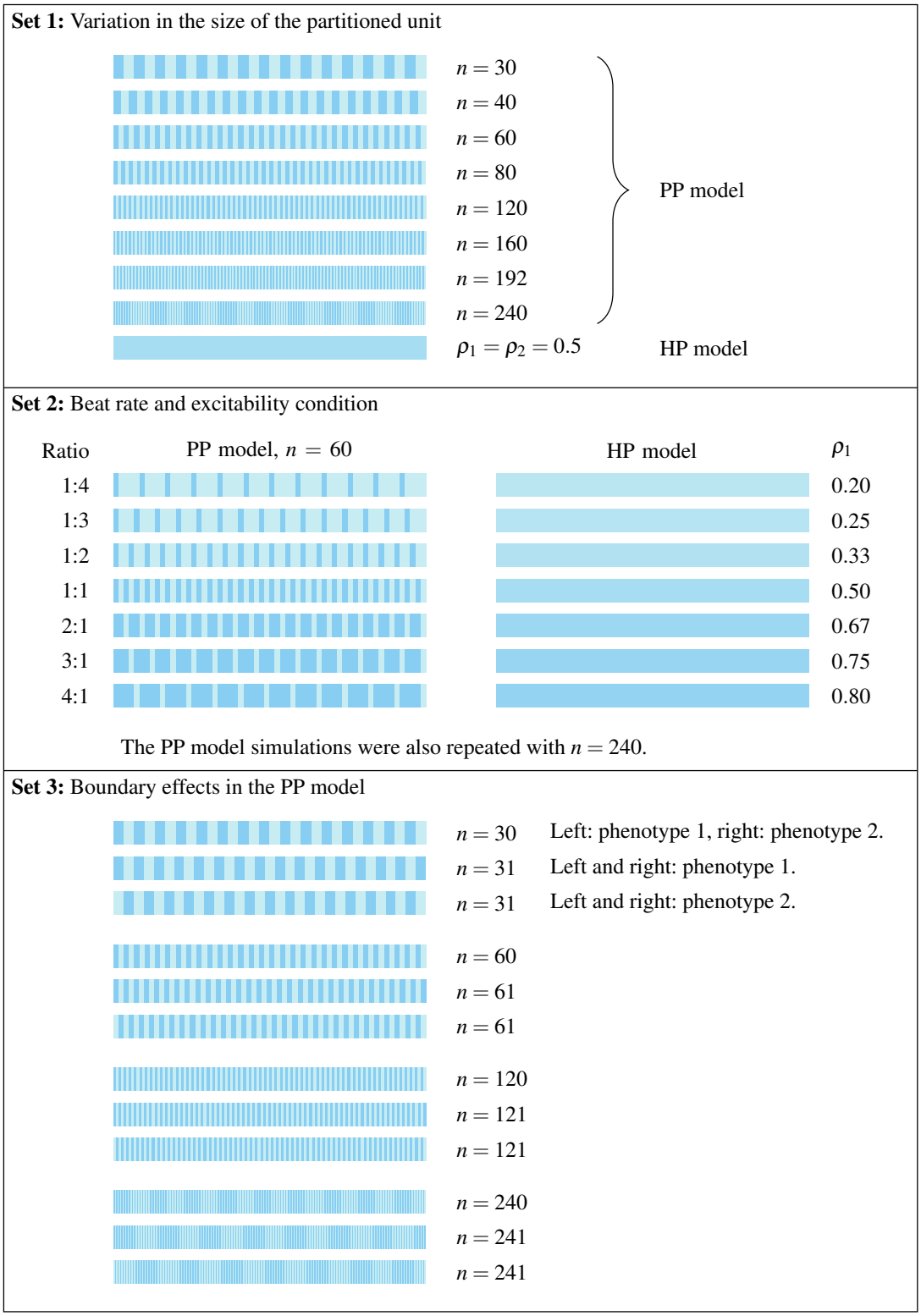

Figure 5.3: Spatial layout of the different phenotypes in the first three sets of simulations. The dark and light shades of blue represent regions where one of two different model phenotypes is exclusively present. Intermediate colours denote the homogenised model with appropriate values of ρ_1 and ρ_2 (the relative contributions of each phenotype). When the PP model was used, the domain was divided into n equally sized partitioned units.

where the amount of variation is set by parameter A (with $A \leq 0.5$) and L is the length of the fibre. In the PP model, the pattern is generated by first dividing the fibre into n partitioned units. At the centre of each unit, ρ_1 and ρ_2 are calculated according to the above equations. Each partitioned unit is then split into proportions ρ_1 and ρ_2, with the left-hand section of each unit designated as phenotype 1, and the remainder as phenotype 2. The layouts are shown in the top panel of Figure 5.4.

Set 5: We now introduce some random variation into the partitioned phenotype layouts used in the Set 4 simulations. In the PP model, the model phenotype is assigned to each of the partitioned units with the probability

$$\mathrm{P}(\text{unit is phenotype 1}) = 0.5 + A \sin\left(\frac{2\pi x_{\text{unit}}}{L}\right), \tag{5.10}$$

where x_{unit} is the centre-point of each partitioned unit. We also impose the restriction that an equal number of units with each of the two phenotypes are present in the fibre. For each of our choices of parameter A, we simulate 15 different arrangements of model phenotypes. The ρ_1 and ρ_2 values in the HP model are set in the same manner as in the Set 4 simulations. Examples of the phenotype layouts can be found in the middle panel of Figure 5.4. We primarily examine the activation times, with the aim of determining whether the HP and PP models give consistent results with regard to the location of the pacemaker and conduction velocity.

Set 6 (physiologically-based system): Our final set of simulations closely follows the design of those in Set 5, but a physiological cell model is used rather than a phenomenological model. The first cell model is the ventricular-like model of Paci et al. (2013a), while the second model is the atrial-like model from the same paper. In addition to altering the parameter A, we also alter the number of units that the fibre is partitioned into. Examples of the layouts can be seen in the bottom panel of Figure 5.4. For each case, we can consider how well the HP model result represents that of the PP model, and see what physical size of the partitioned unit that this corresponds to.

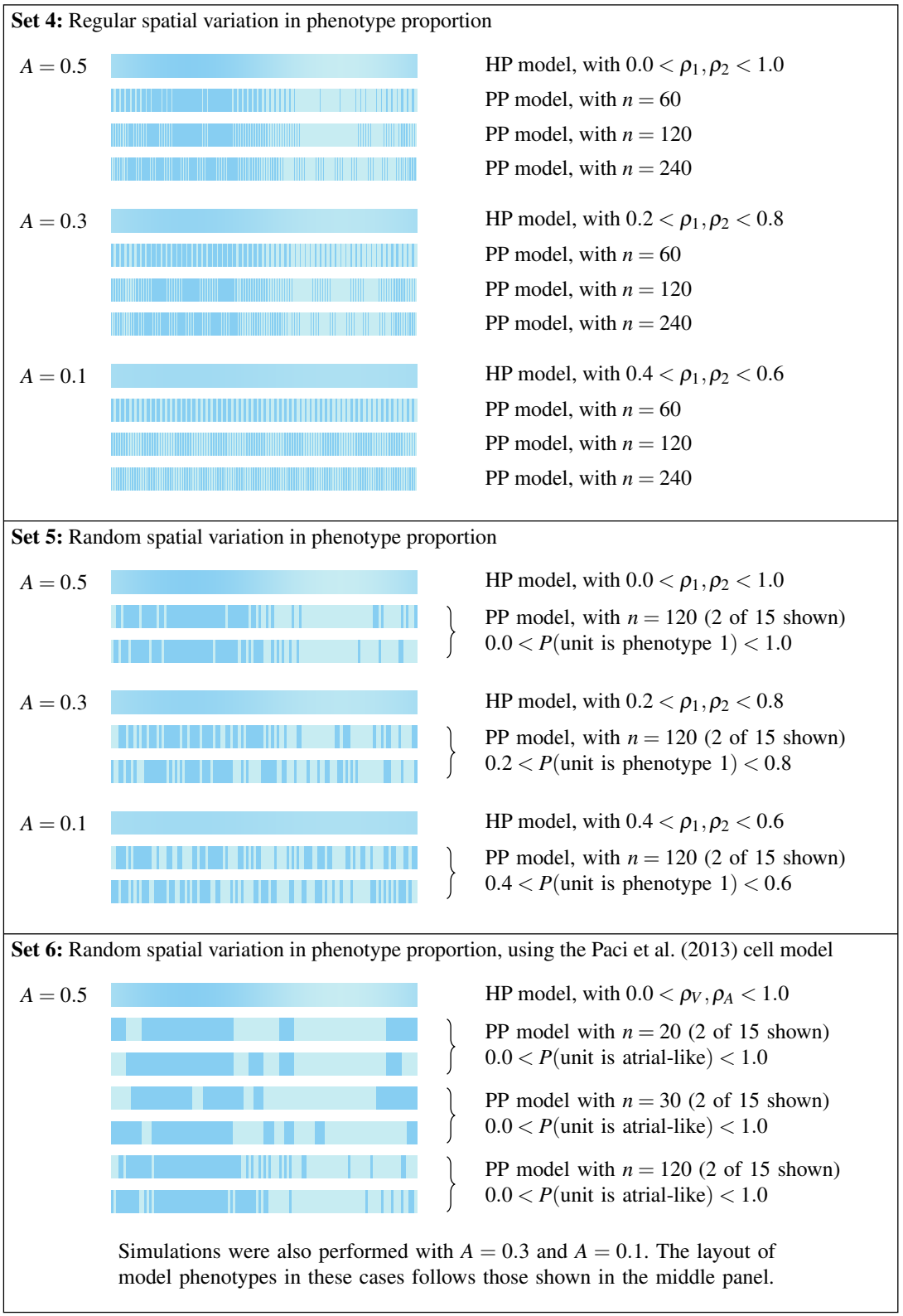

Figure 5.4: Spatial layout of the different phenotypes in the final three sets of simulations. As in the previous figures, the two shades of blue represent two different model phenotypes. In Sets 4 and 5, we utilise the parametrisations of the FitzHugh-Nagumo model, while in Set 6, we use the Paci et al. (2013a) models of atrial-like and ventricular-like hSC-CM electrophysiology.

5.4.2 Parameters of the cellular electrophysiology and monodomain models

For simplicity and flexibility, we use the FitzHugh-Nagumo model (FitzHugh, 1961; Nagumo et al., 1962, hereafter referred to as the FHN model) with different parameter sets to represent action potentials of different cellular phenotypes for simulation Sets 1–5. The FHN model may be used as an abstract model of cardiac electrophysiology; it captures the main qualitative features of the action potential such as excitability (extending to self-excitability for appropriate choices of parameter values) and a fast upstroke. The FHN model does not simulate individual ionic currents as the physiological models of Hodgkin and Huxley (1952a), Noble (1962) and other biophysically-based models do; rather, it is a phenomenological model that contains an activation variable which is akin to the membrane voltage (we consequently use the notation V_m for consistency with our previous descriptions of cell and tissue-scale simulations) and an inactivation variable w. The model is written as

$$I_{\text{ion}}(V_m, w) = V_m(V_m - \alpha)(1 - V_m) - w \tag{5.11}$$

$$\frac{\mathrm{d}w}{\mathrm{d}t} = \epsilon V_m - \beta w, \tag{5.12}$$

where we have written the parameters of the FHN model in terms of α, β and ϵ rather than the usual α, γ and ϵ (our variable $\beta = \epsilon\gamma$). α, β and ϵ all vary across the fibre to represent the action potentials of different cellular phenotypes. The α parameter determines the excitability of the system. If $\alpha < 0$, the system will self-excite; otherwise, a stimulus is required. We refer to these two types of model as 'self-exciting' and 'excitable', respectively (however, we do note that an action potential can also be triggered by a stimulus in self-exciting models).

The linearity of the model in α, β and ϵ means that the homogenised case can simply be implemented by calculating the homogenised parameters, e.g. $\alpha_H = \rho_1\alpha_1 + \rho_2\alpha_2$ (similarly for β and ϵ) and using these values in the usual formulation of the FHN model given in equations (5.11) and (5.12).

For this investigation, we define six sets of the α, β and ϵ parameters for

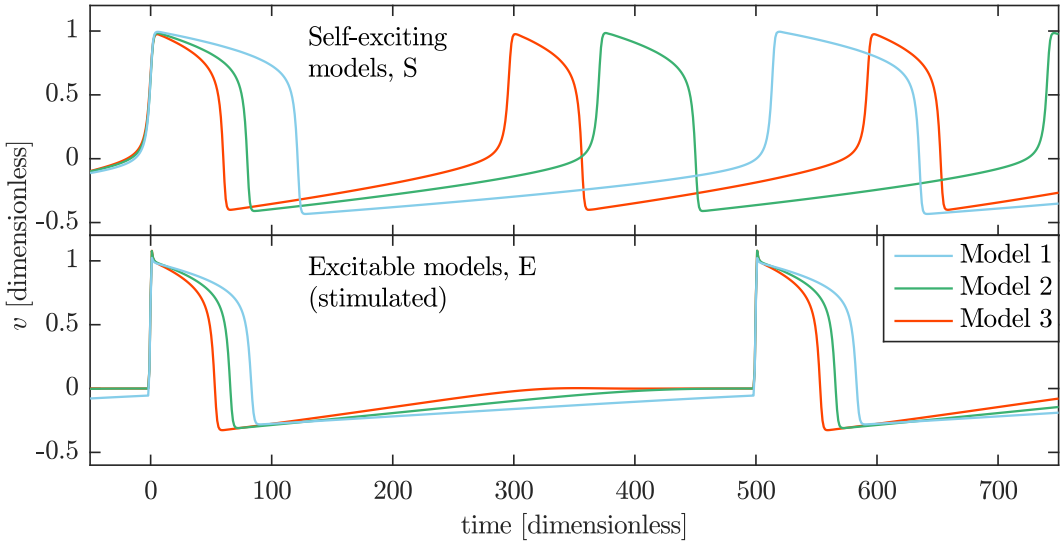

Figure 5.5: Action potentials of the six parametrisations of the FitzHugh-Nagumo model. The three self-exciting models (top) beat at their natural frequencies, while the excitable models (bottom) are stimulated every 500 time units. Upstroke times have been aligned at time = 0.

Name	α	β	ϵ	rate	APD_{90}	MDP
Model S1	-0.12	2×10^{-7}	0.002	0.0019	122.0	-0.433
Model S2	-0.08	3×10^{-7}	0.003	0.0027	81.3	-0.410
Model S3	-0.06	4×10^{-7}	0.004	0.0034	61.6	-0.400
Model E1	0.12	2×10^{-7}	0.002	N/A	84.6	-0.281
Model E2	0.08	3×10^{-7}	0.003	N/A	67.1	-0.310
Model E3	0.06	4×10^{-7}	0.004	N/A	54.3	-0.326

Table 5.1: Values of the FHN model parameters α, β and ϵ. These sets of parameters were used to produce the different action potentials shown in Figure 5.5. Alongside, we list the dimensionless values of beat rate, action potential duration (APD) and maximum diastolic potential (MDP) for each model.

three self-exciting (S1–S3) and three excitable (E1–E3) models. The parameters chosen for these models result in action potentials with clearly different beat rates and action potential duration and have a range of positive and negative α values, meaning that both spontaneous and excitable cell types are represented.

By beating spontaneously, the self-activating models are representative of hSC-CM action potentials, while the excitable models are closer to those produced by adult cardiomyocytes. The parameters of the six forms of the FHN model are listed in Table 5.1, with the action potentials shown in Figure 5.5. The parameters

Parameter	Value (FHN model)	Value (Paci et al. (2013a) model)
C_m	1	$1\,\mu\mathrm{F\,cm^{-2}}$
χ	1	$1400\,\mathrm{cm^{-1}}$
σ	1	$0.3\,\mathrm{mS/cm}$
x-domain	0–100	0–1 cm
x-step	0.013	0.000 52 cm
simulation duration	8000	20 s
time step (PDE)	2^{-10}	2.5×10^{-4} s
time step (ODE)	2^{-10}	5×10^{-6} s
initial conditions	$v = 1 \times 10^{-3}$ $w = 0$	As listed in the supplement of Paci et al. (2013a)
stimulus period	500	N/A
stimulus duration	2	N/A
stimulus magnitude	-0.4 at $0 < x < x_{\mathrm{end}}/30$	N/A

Table 5.2: Tissue-level parameters for monodomain simulations. The stimulus was only applied when the model combinations present in the fibre would not otherwise spontaneously activate. All quantities in the FHN simulations are dimensionless.

relevant to the monodomain simulations are given in Table 5.2.

In our final set of simulations, we use a physiologically-based cellular electrophysiology model to examine the differences between the HP and PP models in the context of hSC-CMs. The Paci et al. (2013a) model is available in two parametrisations, one for atrial-like and the other for ventricular-like hSC-CM electrophysiology. At the present time, there is no model available for the nodal-like cells, so for that reason and for simplicity we restrict ourselves to including only atrial-like and ventricular-like cell types in our simulations. The ionic current of the HP version of the Paci et al. (2013a) model is calculated using equation (5.4) and the ionic currents from the original atrial-like and ventricular-like versions of the model. The parameters needed for the monodomain simulations are given in the right-hand column of Table 5.2.

5.5 Convergence Analysis

Before performing the simulations described in the previous section, it is important to check that the code is working as expected and that we achieve the

expected rates of numerical convergence. Verification of the monodomain solver code was performed by utilising an analytic solution to the monodomain equation proposed in Pathmanathan and Gray (2014). By using a simple ODE system in place of an action potential model, the authors were able to compute analytic solutions for the monodomain, bidomain and bidomain-with-bath systems in one, two and three dimensions. We compared the solution of the one-dimensional monodomain problem to that computed by the monodomain solver used for the simulations throughout this chapter, and found that the expected results were generated and the errors due to the space and time steps (denoted by h and k, respectively) converged at the appropriate rates.

To assess the convergence properties of the simulations in this chapter, we began by testing a simple simulation composed entirely of Model S1, one of the self-activating FHN models. However, this system exhibits entirely synchronous activation — this behaviour merits more discussion than there is space for here, so we will return to the topic in Section 5.5.3. We therefore use a slightly more complex system for our convergence analysis.

We instead test a selection of the simulations from Set 1, with an emphasis on the simulation with 240 partitioned units (the smallest size of partitioned unit tested). We alternate the Model S1 and Model S3 parametrisations of the FitzHugh-Nagumo model across the partitioned units.

Following Pathmanathan and Gray (2014), we computed two error metrics,

$$||V_m||_{L^\infty(L^2)} = \max_{t\in[0,T]} ||V_m(t)||_{L^2(\Omega)},$$
$$\text{where} \quad ||V_m(t)||^2_{L^2(\Omega)} = \int_\Omega V_m^2 \,\mathrm{d}x \quad \text{and}$$
$$||V_m||_{L^2(H^1)} = \left(\int_0^T ||V_m(t)||^2_{H^1(\Omega)} \,\mathrm{d}t\right)^{1/2},$$
$$\text{where} \quad ||V_m(t)||^2_{H^1(\Omega)} = \int_\Omega V_m^2 + |\nabla V_m|^2 \,\mathrm{d}x.$$

which should converge at rates of $\mathcal{O}(h^2 + k)$ and $\mathcal{O}(h + k)$, respectively. The error metrics are based on the differences between the values of the activation value achieved in the reference simulations and the other simulations, so that

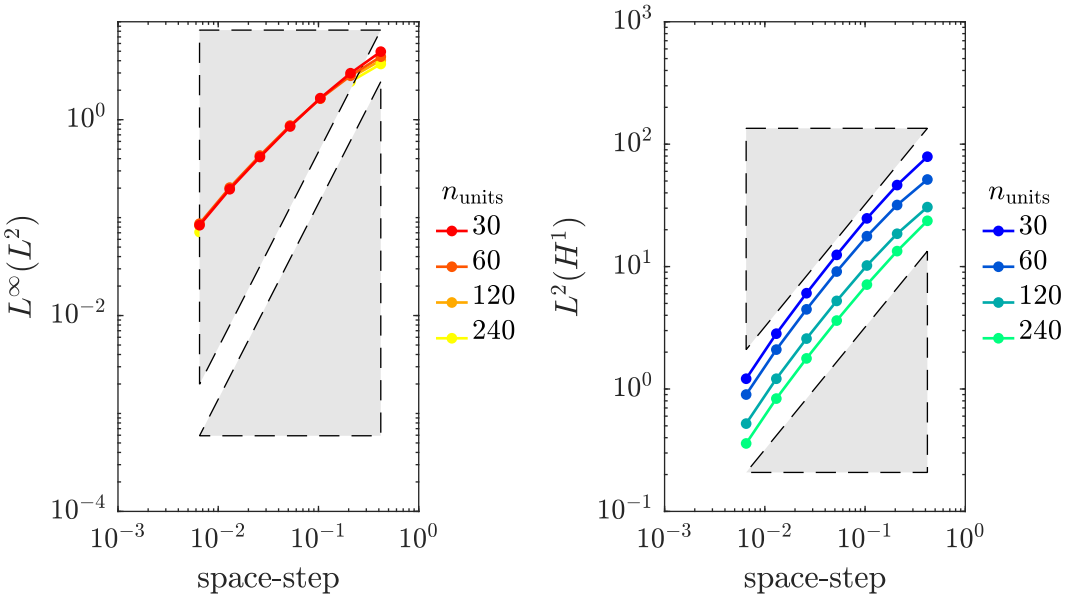

Figure 5.6: Spatial rates of convergence using the node-wise partitioned phenotypes model. The $L^\infty(L^2)$ convergence metric is shown on the left, and the $L^2(H^1)$ metric is shown on the right. The expected rates of convergence, $\mathcal{O}(h^2)$ and $\mathcal{O}(h)$, are indicated by the gradients of the triangles alongside the error markers.

$V_m = |V_{m,\text{computed}} - V_{m,\text{reference}}|$. As we have no analytic solution to compare these simulations to, we instead use the simulation with the finest spatial or temporal steps as our reference solution.

In Sections 5.5.1 and 5.5.2, we examine the convergence properties of the node-wise and element-wise implementations of the PP model that were described in Section 5.3. We do not specifically show the convergence properties of the HP model as it is essentially implemented as a single-phenotype version of the PP model with different parameters of the cellular electrophysiology model at each node.

5.5.1 Convergence of node-wise partitioned phenotypes model

As we discussed in the previous section, using the node-wise implementation of the PP model should not give us an accurate result due to the errors accumulated during the integration of the ionic current.

In Figure 5.6, we show how the rate of spatial convergence is weaker than would be expected. The two error metrics each clearly reduce at a slower rate

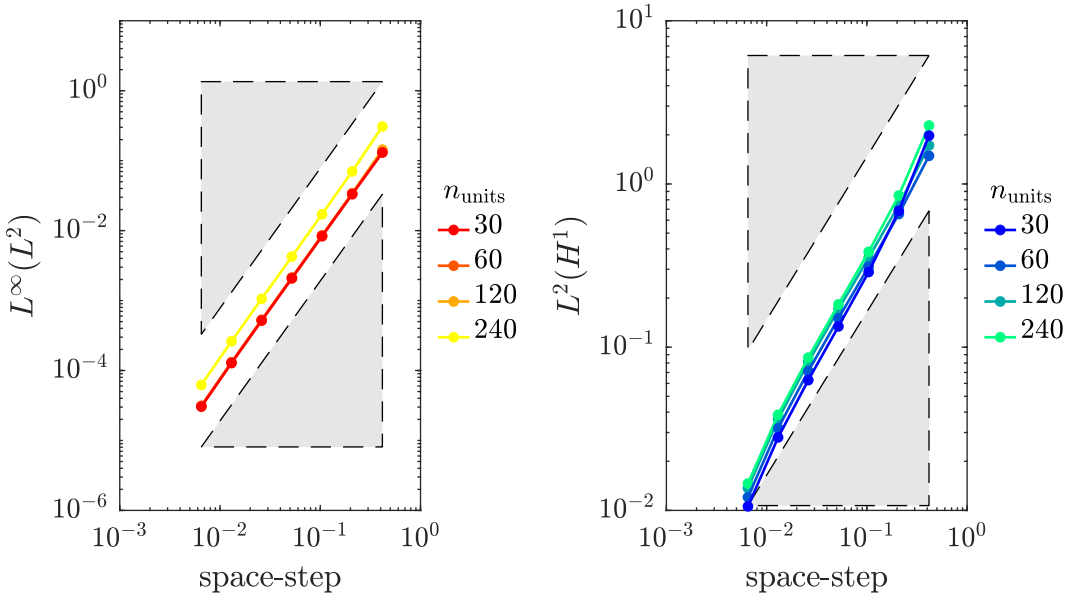

Figure 5.7: Spatial rates of convergence using the element-wise partitioned phenotypes model. The left plot shows the $L^\infty(L^2)$ convergence metric and expected rate of $\mathcal{O}(h^2)$, and the right shows the $L^2(H^1)$ metric and $\mathcal{O}(h)$ rate.

than expected, highlighting how this method is not ideal for use in simulations where there are many regions of different phenotype.

5.5.2 Convergence of element-wise partitioned phenotypes model

In contrast to the node-wise implementation, the rate of spatial convergence in the element-wise implementation is as expected. In Figure 5.7, the error metrics decrease at the rate indicated by the dashed lines. This plot confirms that the properties of the element-wise implementation are as expected from the underlying theory. Given the much weaker convergence in the node-wise implementation, we will use the element-wise implementation of the PP model for all the remaining simulations in this chapter.

Figure 5.8 shows the rate of convergence as the PDE time-step, k, is reduced. The ODE time-step was held constant for this series of simulations, but letting the ODE time-step vary so that it was equal to the PDE time-step produced very similar results. Again, we see that we achieve the expected rates of convergence.

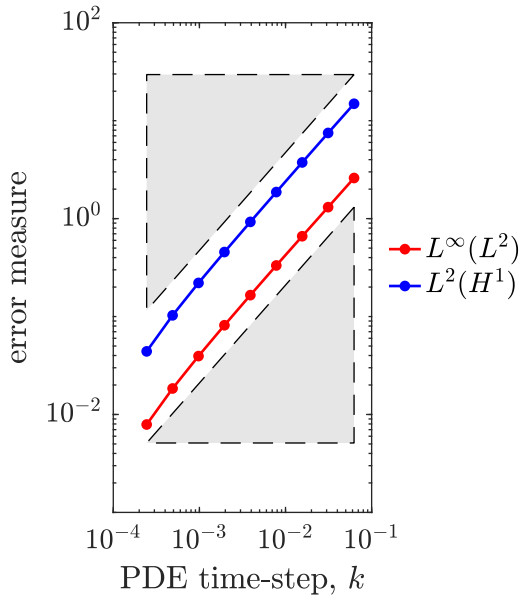

Figure 5.8: Temporal (PDE time-step) rates of convergence using the element-wise partitioned phenotypes model. The expected convergence rate of $\mathcal{O}(k)$ is indicated by the slope of the grey triangles.

5.5.3 A note on synchronisation of coupled oscillators

We briefly mentioned in the previous section that synchronous activation was observed in one-dimensional fibre simulations where the same parametrisation of the FHN model was used throughout the entire fibre. There are numerous examples of oscillator coupling in biology leading to synchronised activity, from the flashing of fireflies to metabolic synchrony in yeast (Strogatz, 2000). Many of the biological examples are of weakly coupled, all-to-all systems, which have been described by Winfree (1967), Kuramoto (1981), and Mirollo and Strogatz (1990), amongst others. Our example of synchronous beating is not surprising given the results of the Kuramoto model, namely that weakly-coupled systems of coupled oscillators will synchronise given sufficiently similar frequencies of oscillation. In our case, the identical action potentials across the fibre met this condition, with the identical initial conditions giving no room for variation from the fully synchronous state.

5.6 Comparison of the Partitioned and Homogenised Phenotypes Models

Now that we have confirmed the convergence properties of our models, we can discuss the simulations that we proposed in Section 5.4. The features of the action potential, or biomarkers, to which we frequently refer, were shown previously in Figure 2.4.

5.6.1 Set 1: Variation in the size of the partitioned unit

In our first set of simulations, we utilise the layout of phenotypes shown in the top panel of Figure 5.3 with four different combinations of the cellular electrophysiology models described in Section 5.4.2. Both models are present in equal proportions, so we have $\rho_1 = \rho_2 = 0.5$ in the HP model, which gives us α_H values that are above and below zero (recalling that spontaneous beating occurs if $\alpha < 0$) across the range of models we tested. The model phenotype combinations are as follows:

Models S1 and S3: both self-exciting, with $\alpha_H = -0.09$;
Models S1 and E2: self-exciting and excitable respectively, with $\alpha_H = -0.02$;
Models S3 and E2: also self-exciting and excitable, but with $\alpha_H = 0.02$; and
Models E1 and E3: both excitable, with $\alpha_H = 0.09$.

The first two combinations listed have similar characteristics to action potential morphologies typical of hSC-CMs. In the first, both models are able to spontaneously activate (although they do so at different rates). The second combination is indicative of more mature cultures of hSC-CMs; one self-activating and one excitable phenotype are now present but the combination should still spontaneously beat. The third case is similar to the second, but spontaneous activation is no longer expected. The final case corresponds to a mixture of two types of mature cells, neither of which activate spontaneously. As spontaneous activity was not anticipated in the final two combinations of model phenotypes due to the positive values of α_H, a stimulus was applied to the left-hand side of

the fibre.

As we described in Section 5.4.1, the primary aim of the Set 1 simulations is to validate our homogenisation procedure. We therefore expect to see that the action potentials of the PP model tend towards those of the HP model as the number of partitioned units is increased, and the size of each partitioned unit gets smaller.

We examine three biomarkers to investigate the validity of our homogenisation. The first two, the action potential duration, APD_{90}, and maximum diastolic potential, MDP, are calculated from the action potential at a particular location. The third biomarker is the tissue-level conduction velocity, calculated from the activation times throughout the fibre.

Validation of the homogenisation process: APD_{90} and MDP

In Figure 5.9, we plot the APD_{90} for the PP simulations with varying numbers of partitioned units, n, and the HP simulations with the four different combinations of model phenotype. On the left of the figure, we plot the APD_{90} across the entire fibre for selected cases: the HP model, the PP model with small partitioned units ($n = 240$) and the PP model with large partitioned units ($n = 30$). On the right-hand side, we plot the minimum and maximum values of the APD_{90} that occur over the central region of the fibre. As the stimulus can have a substantial effect on the value of the APD_{90} and other biomarkers, only the values between $x = 35$ and $x = 65$ are taken into account in these plots.

We plot the maximum diastolic potential (MDP) in a similar manner in Figure 5.10. These two figures can now be used to judge the success of the homogenisation process. In the plots on the left of Figures 5.9 and 5.10, we can see that the biomarkers of small-unit PP model closely follow those of the HP model. In the large-unit PP model, substantial spatial variation of the biomarkers is observed; this variation is approximately 5% of the value of the biomarkers and such variation could conceivably be detected in the APD_{90} by experimental techniques such as optical mapping (the MDP is difficult to measure in tissue

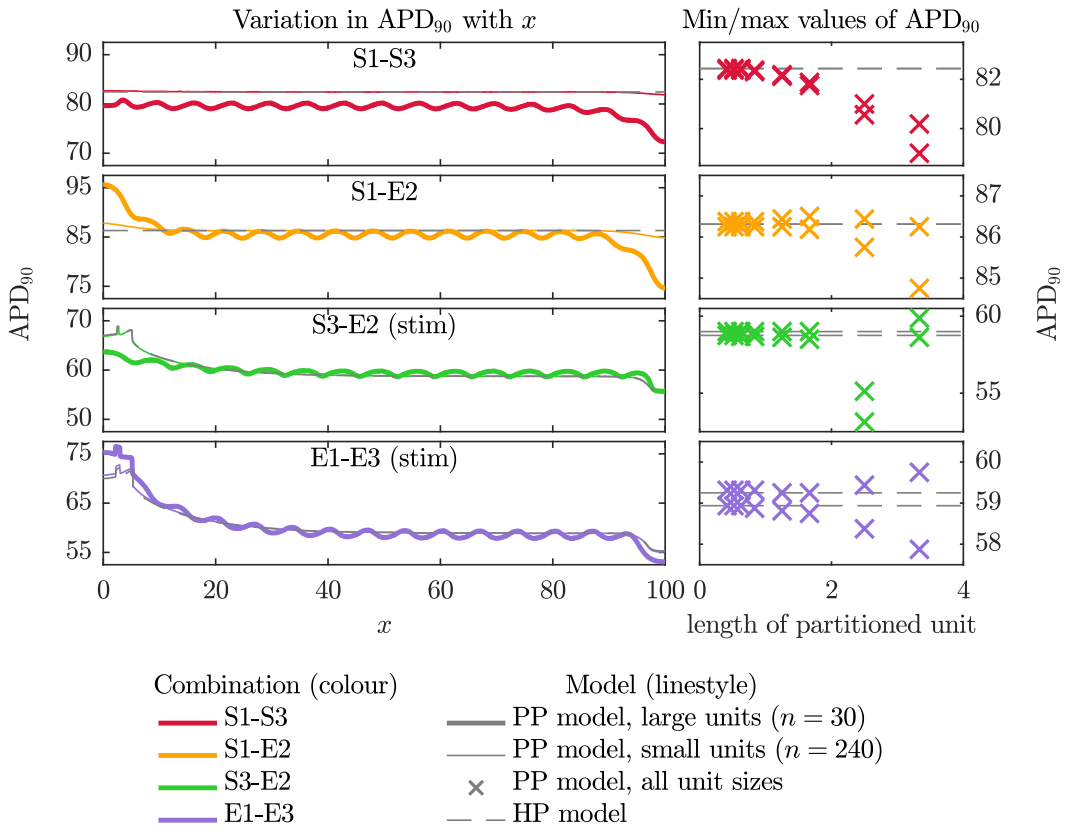

Figure 5.9: Variation in APD_{90} (time to achieve 90% repolarisation) during the final beat in Set 1 simulations. Left: variation in APD_{90} across the fibre for the smallest and largest sizes of partitioned unit, along with the homogenised case. Right: the minimum and maximum APD_{90} values found in the region $35 < x < 65$ in each simulation. See the top panel of Figure 5.3 for the layout of model phenotypes across the fibre. In the simulations where the fibre could not self-excite (Models S3 and E2, and Models E1 and E3, shown in the lower two panels), the influence of the stimulus on the APD_{90} can be observed in the region $x < 10$.

unless sharp microelectrodes are used). In the plots on the right of Figures 5.9 and 5.10, we clearly see the trend that we expected: as the size of the partitioned unit decreases, the values of the biomarkers tend towards those observed in the HP model. The confirms that our homogenisation process has worked as expected.

Anomalous biomarker values

The results shown in Figures 5.9 and 5.10 generally follow a smooth trend as the size of the partitioned unit decreases and the biomarkers of the PP model approach those of the HP model. However, there is an exception to this trend

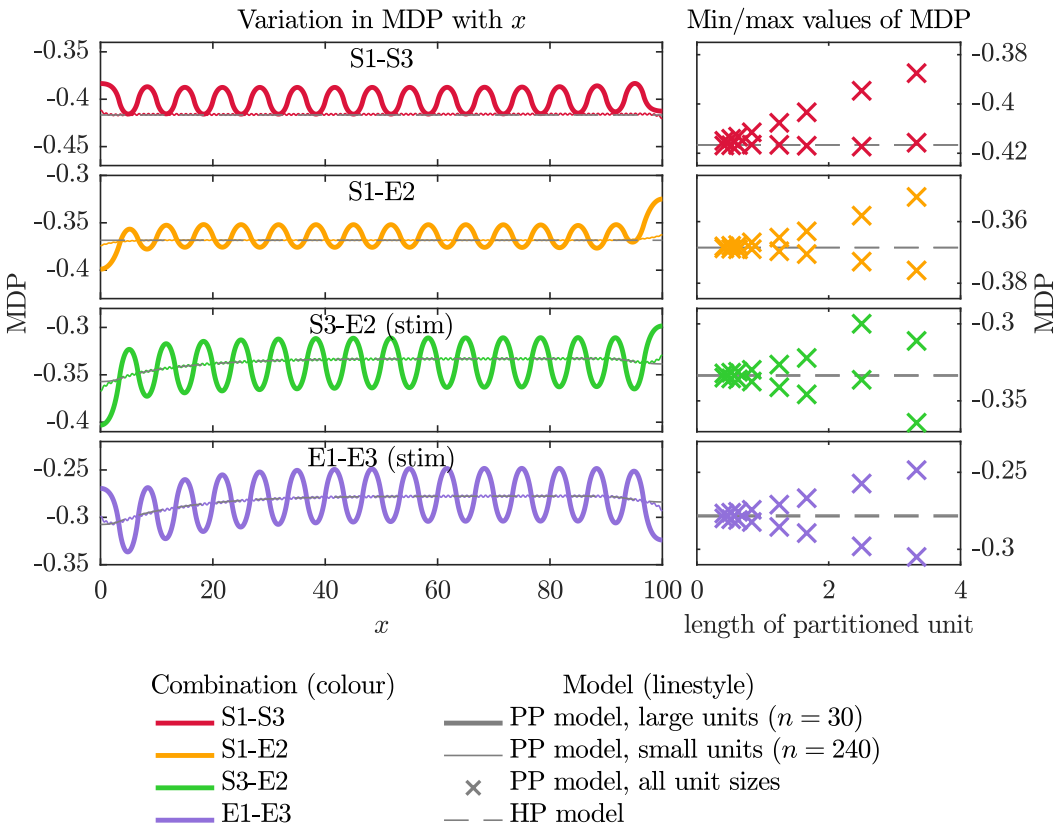

Figure 5.10: Variation in maximum diastolic potential (MDP) from Set 1 simulations. Left: variation in MDP across the fibre for the smallest and largest sizes of partitioned unit, along with the homogenised case. Right: the minimum and maximum MDP values found in the region $35 < x < 65$ in each simulation.

that can be seen in the APD_{90} biomarker when Models S3 and E2 were used (third panel of Figure 5.9). This is due to the large size of the partitioned units in this case — we cannot assume that the value of α_H (and the implications for spontaneous beating) is valid in this regime.

In this example, the large-unit simulations of the Model S3-E2 combination are able to spontaneously activate. The action potentials therefore switch between spontaneous and stimulated, as the stimulus at the left of the fibre is still applied every 50 time units. The change in beat rate has an impact on the APD_{90}, which can be seen in Figure 5.9: the final beat in the simulation with the second-largest partitioned unit was spontaneous rather than triggered by the stimulus. This is also the case for the simulation with the largest partitioned unit, but with a less marked effect on the APD_{90} due to differences in the offset

between the spontaneous beat and the stimulus. This result does indicate an important difference in the characteristic behaviour of the PP and HP models, but in the regime of the large partitioned unit, we would not necessarily expect the results of the HP and PP models to match.

Boundary effects

In Figures 5.9 and 5.10, we note that the biomarker values vary with the model phenotype across the fibre. However, the values at the boundaries of the fibre differ from those in the middle. This is due to the travelling activation wave, $V_m = f(x - ct)$, being unable to meet the no-flux boundary condition if it was to continue in the same way that it passed across the middle of the domain.

The impact of the no-flux boundary condition on the action potential duration has previously been investigated by Cherry and Fenton (2011), who simulated a single-phenotype domain and noted that the APD_{90} was shorter in the vicinity of the boundaries. If we consider a travelling wave approaching the boundary, we note that the section immediately prior to the boundary will repolarise before the section at the boundary itself. To meet the no-flux boundary condition, the membrane voltage at the boundary therefore reduces sooner than it otherwise would, leading to a shorter APD_{90} than in the rest of the fibre.

As we have a dual-phenotype fibre, our situation is slightly more complex, but we still see the effects reported by Cherry and Fenton (2011) in many of the simulated fibres. Rather than only being influenced by the direction of the travelling wave, the biomarkers are also influenced by the underlying model phenotype. We observe prolongation of APD_{90} at some boundaries (particularly prominent in the $n = 30$ S1–E2 system), where the model with the intrinsically longer APD_{90} also acts as the pacemaker, causing it to take longer to depolarise than the same model would if it were in the centre of the fibre.

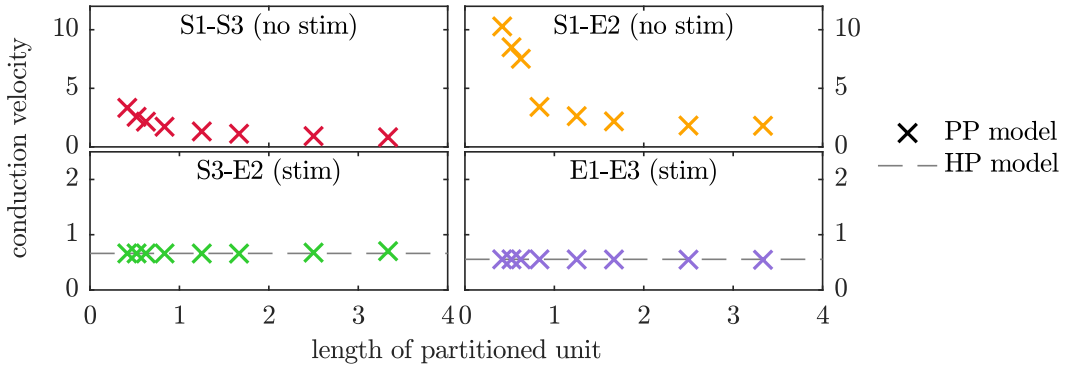

Figure 5.11: Conduction velocity of the travelling waves in the Set 1 simulations. The conduction velocity was calculated through the region $35 < x < 65$. When the HP model was used for the self-exciting systems, the activation time was identical throughout the entire fibre. This is equivalent to the conduction velocity being infinite; consequently, the top two panels do not indicate the conduction velocity of the HP model.

Validation of the homogenisation process: Conduction velocity

Our final biomarker of interest, the conduction velocity, is calculated on the tissue-scale. In Figure 5.11, we plot the conduction velocity of the HP and PP models when the four phenotype combinations were used.

In the stimulated fibres, we observe good agreement between the conduction velocity if the HP and PP models of all sizes of partitioned unit. However, this is not the case in the spontaneously activating fibres. The S1-S3 and S1-E2 HP model fibres activate entirely synchronously, giving an infinite conduction velocity. This is to be expected, given that we have a system of coupled, identical oscillators that have consistent initial conditions at the start of the simulation. The small-unit PP models approach this limit, with clear increases in conduction velocity as we approach the limiting case of well-mixed phenotypes. As we can see that the biomarker values of the small-unit PP models tend towards those of the HP model, we can again state our confidence in the homogenisation procedure.

Biological interpretation

Given how the biomarkers and conduction velocity of the PP model tend towards those of the HP model as the size of the partitioned unit decreases, we conclude

that these methods give consistent results in the well-mixed limit. We are unlikely to come across a biological situation with such regular spatial distributions of model phenotype, and the behaviour apparent in this set of simulations agrees with that conclusion. If the cell types were so regularly arranged, we would expect synchronous (or very fast) activation. However, the experimental reports (see Section 2.5.1) have shown that conduction velocities in hSC-CM monolayers are lower than those reported in adult cardiac tissue, and pacemaker regions are not exclusively located at the tissue boundaries.

5.6.2 Set 2: Comparison of beat rate using the partitioned and homogenised phenotypes models

In our second stage of the verification of the HP model, we first look to see whether the beating condition of the FitzHugh-Nagumo model ($\alpha < 0$ for spontaneous beating) holds, and then compare the beat rates of fibres simulated using the PP and HP models.

We pair each self-activating action potential model (S1, S2, S3) with each of the excitable models (E1, E2, E3). We alter the relative proportions of the two models, ρ_1 and ρ_2, in both the HP and PP fibres, giving us a range of model combinations with different values of the homogenised parameter $\alpha_H = \rho_1\alpha_1 + \rho_2\alpha_2$. We perform two sets of simulations with the PP model, one with mid-sized partitioned regions ($n = 60$) and another with much smaller partitioned regions ($n = 240$). The partitioned units are assigned a model phenotype in a regular pattern. Rather than alternating the phenotype of each partitioned unit, the precise layout is determined by the relative proportions of the two phenotypes (see Figure 5.3 for further details).

Validation of the homogenisation process: Spontaneous beat rate

We plot the beat rates of the PP and HP fibres in Figure 5.12, as crosses and dots respectively.

We first examine the discrepancy in beat rate between the HP and PP models

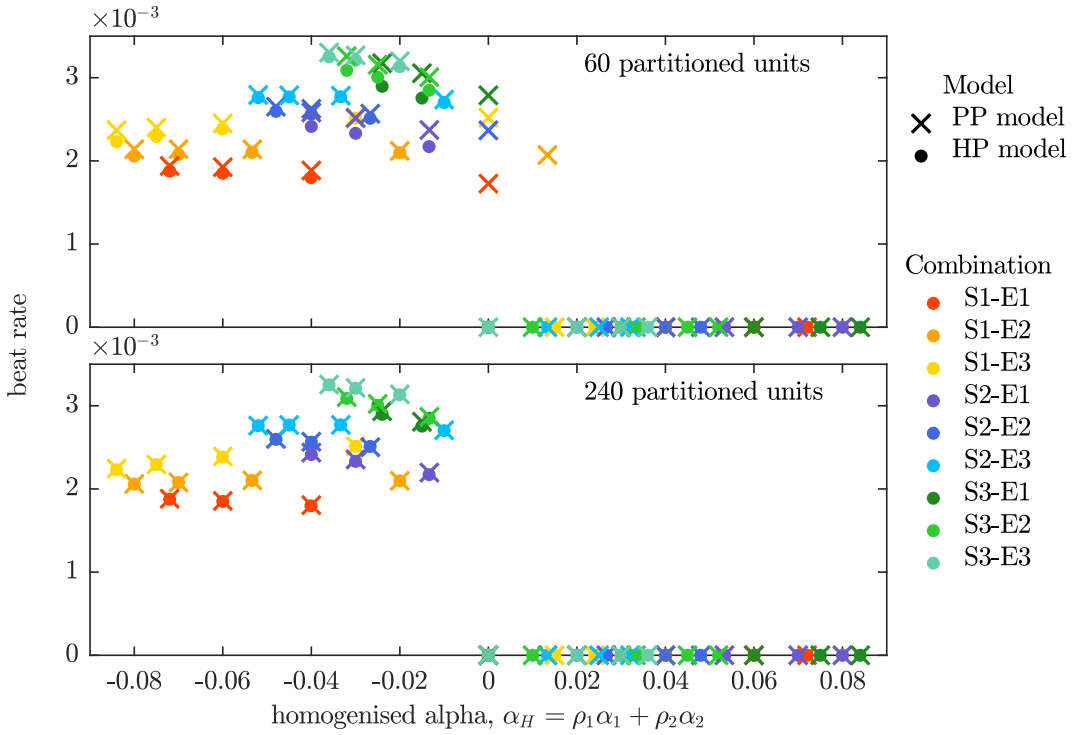

Figure 5.12: Beat rate from Set 2 simulations. The fibre was partitioned into 60 (top) and 240 (bottom) equally sized regions. The model phenotype layout can be seen in Figure 5.3. The relative proportions of the two model phenotypes are altered for each of the combinations listed in the legend, giving different values of the homogenised α_H parameter. The beat rates of fibres using the partitioned model (with $n = 60$ or 240, crosses) and the homogenised model (dots) are compared.

in both panels of Figure 5.12. The beat rates of the HP and PP models differ more when the partitioned units are large (top panel) than when the partitioned units are small (bottom panel). As we again see that the small-unit PP model gives more similar results to the HP case, this acts as a further demonstration of the validity of the homogenisation process.

Validation of the homogenisation process: Excitability criterion

We now look at a particularly interesting region, that around $\alpha_H = 0$. In the large-unit PP model, we can see that the beating condition of the FHN model is not quite adhered to: there are several cases in the top panel of Figure 5.12 where spontaneous beating occurs even though $\alpha_H = 0$, and one case when $\alpha_H > 0$. We discussed a comparable scenario in the previous section (Set 1 series of simulations), when we noted that activation of a spontaneously beating model

phenotype could occur at the fibre boundary, even when one would otherwise expect the fibre to be quiescent based on the homogenised value of the parameter α. When we use the larger-sized partitioned units ($n = 60$, top panel of Figure 5.12), there are a few cases where spontaneous activity arises from the boundary even though we have $\alpha_H \geq 0$. In contrast, spontaneous activity from the HP model strictly occurs only when $\alpha_H < 0$, and the excitation is fully synchronised across the fibre as there is no spatial variation in model phenotype.

Biological interpretation

With this set of simulations, we have shown how activation is initiated at the boundary given a repetitive pattern of model phenotypes, even when the two types are not present in the same proportion. As we have noted previously, synchronised activity or activity exclusively originating from the boundaries are not consistently reported from experiments. We must therefore investigate the effects of the boundary phenotype and spatial heterogeneity to see if we can reproduce the type of activation waves observed experimentally.

5.6.3 Set 3: Influence of the boundary phenotype on activation

To examine the effect of the phenotype of the unit at the boundary on activation in the PP model, we alter the model phenotype that is located at the boundary of three otherwise similar phenotype layouts. We use Models S1 and S3 for this investigation as their spontaneous activity is representative of the beating of hSC-CMs. In the first case, where we have an even number of partitioned units, the outer model phenotype on the left hand side of the fibre is Model S1, while that at the right is Model S3. In the other two cases, we have an odd number of units (one more than in the even-n cases). In one of these, Model S1 is present at both boundary units, while in the other Model S3 is present at both boundaries. We test these three patterns of model phenotypes with a range of sizes of partitioned units.

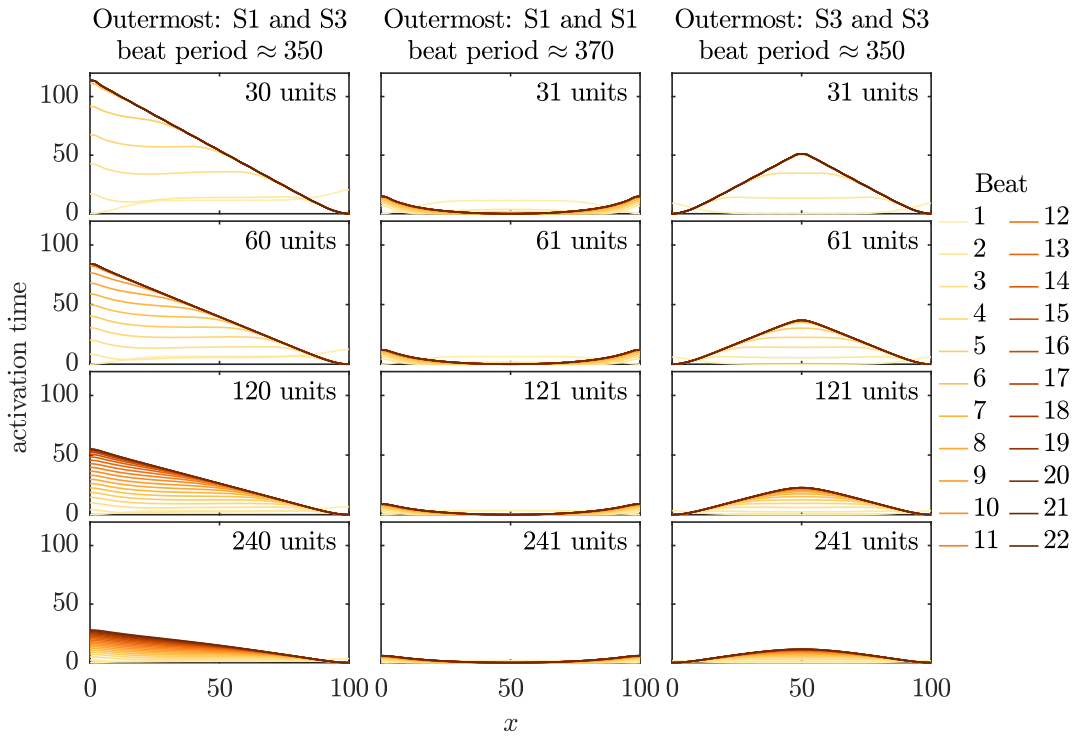

Figure 5.13: Activation times of all recorded beats during the Set 3 simulations. The fibres were divided into 30 or 31 partitioned units (top), 60 or 61 units, 120 or 121 units and 240 or 241 units (bottom). The activation times are normalised so that the earliest activation time during each beat is set to 0. The layouts of the model phenotypes are shown in the third panel of Figure 5.3, and the phenotypes of the partitioned units located at the boundaries are additionally listed at the top of the plots.

Activation sequence with different boundary phenotypes

We plot the activation times of every beat in each of the three cases in Figure 5.13. In each row of the figure, we move to a smaller size of the partitioned unit: at the top, we have 30 or 31 units, with 60 or 61, 120 or 121, and 240 or 241 in the rows below.

Throughout the simulations shown in Figure 5.13, the origin of activation is consistent as the number of partitioned units is increased. The activation wave always originates from a region of the faster-beating model phenotype; if Model S3 is present at one of the boundaries, the activation wave originates there. In the central case, activation begins at the central instance of Model S3, as the slower-beating Model S1 takes longer to reach the activation threshold at the boundaries than it does elsewhere, as we discussed in Section 5.6.1.

In all cases plotted in Figure 5.13, several beats occur before activation settles into a steady pattern. As we start off with identical initial conditions across the entire fibre, the first beat occurs near-simultaneously across the entire fibre before the dominant pacemaker begins to take over. While the process of settling to a steady state is due to the identical initial conditions across the fibre in this case, change in the pacemaker location has also been observed in other spontaneously activating tissue preparations following changes in environmental conditions (Kienast et al., 2014).

The increase in conduction velocity (indicated by the decreasing slope of the activation time plots) as the size of the partitioned unit decreases shows that the action potentials tend towards synchronisation in the homogenised limit, as we indeed saw in Figure 5.11. We also see near-synchronisation in the central case, despite the partitioned units still being relatively large. Rather than one region clearly triggering the activation of the rest of the fibre, as in the other two phenotype arrangements, the units at the boundaries activate less readily than the units in the centre. This eventually leads to near-synchronised activation, rather than conduction, across the centre of the fibre, with slightly slower activation of Model S1 in the units at the boundary. Note that the conduction velocity in the central case is considerably faster than that on the right, where the activation wave has travelled for the same distance.

Biological interpretation

The conclusions drawn from this set of simulations have two distinct implications for the experimental case. First, we have seen that more uniform distribution of phenotype leads to higher values of conduction velocity that tend towards full synchronisation as the size of the partitioned unit decreases. Second, we can identify two features that influence the position of the pacemaker region. As expected, the underlying excitability of both phenotypes (here, represented by α) is important. However, the presence of a boundary can modify the location of the pacemaker, as it influences whether the local model phenotypes activate faster

or slower than usual. Our demonstration has shown that pacemaker location is sensitive to the local arrangement of phenotypes, but the fact that pacemaker location is highly variable in experiments points to there being a more irregular arrangement of phenotypes than we have so far investigated.

5.6.4 Set 4: Spatial variation in phenotype proportion

Our previous investigations have focussed on regularly repeating patterns of phenotypes, which are not necessarily representative of the biological situation. We now introduce spatial variation in the model phenotype, with the proportions of the two model phenotypes set by equations (5.8) and (5.9).

We utilise two pairs of model phenotypes in this set of simulations. Models S1 and S3, and Models S1 and E2 have beating features similar to hSC-CM cultures: the Model S1-S3 combination has two self-activating phenotypes with different beat rates, while the Model S1-E2 combination represents a slightly more mature culture where one of the cell types is no longer self-exciting.

Activation sequence with spatially varying phenotypes

Figure 5.14 shows the activation time of the final beat in each of the simulations (the earliest activation time has been normalised to time = 0). We note that introducing some spatial variation into the arrangement of phenotypes has caused the pacemaker region to move away from the boundary in the case of the S1–S3 pair, and also in the S1–E2 pair for the case $A = 0.1$.

The value of A, which is indicative of the amount of variation in phenotype, can be seen to influence the conduction velocity (the gradient of the activation time). In Section 5.5.3, we commented that systems where there is less variation in natural frequency of coupled oscillators are more prone to synchronisation; we are seeing the same effect as we move from high values of A to low values of A.

We also note that the activation patterns of the PP and HP models match well in most of the simulations. Notable differences can only be seen in the S1–E2 pair with $A = 0.5$, where we can clearly observe the expected effect of the small-unit

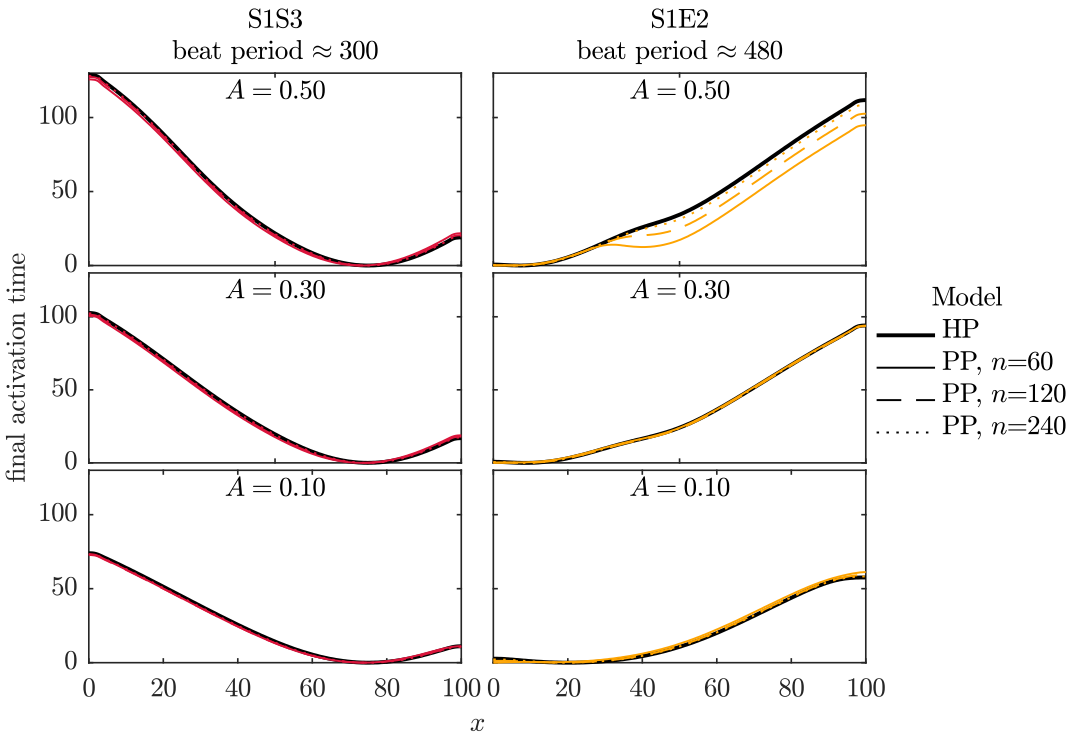

Figure 5.14: Activation times of the final beat in the Set 4 simulations. The models used in each simulation were S1-S3 (representing immature cells, left) and S1-E2 (representing more mature cells, right). In the top panel, we have $0 < \rho_1, \rho_2 < 1$, in the middle $0.2 < \rho_1, \rho_2 < 0.8$, and at the bottom $0.4 < \rho_1, \rho_2 < 0.6$. The bold black line shows the activation time from the homogenised model. The thinner coloured lines show the activation time from the 15 repeats of the partitioned model (each repeat has a slightly different phenotype layout). For more details of the model phenotype layout, see Figure 5.4.

PP model exhibiting a more similar activation pattern to the HP model than the large-unit PP model.

Biological interpretation

With these simulations, we have shown that even small amounts of spatial variability are able to prevent synchronisation of the action potential in spontaneously activating systems. Including this manner of spatial variation in model phenotype gives rise to the steady activation waves reported from monolayer cultures. Generally, the presence of a large region of a faster-beating phenotype acts as the pacemaker for the rest of the tissue. Our simulations suggest that activation from boundary regions may be seen more often in more mature cultures (represented

by the S1-E2 simulation in Figure 5.14), where the interaction of the boundary and pacemaker region has a greater effect than is observed otherwise.

5.6.5 Set 5: Random spatial variation in phenotype proportion

We now examine how adding random variability in model phenotype across the fibre affects the activation sequence, by defining the probability that each partitioned takes on phenotype 1 as stated in equation (5.10). We alter parameter A from equation (5.10) across our three investigations, to give us three distributions of the two model phenotypes with different amounts of variability across the fibre (see Figure 5.4 for details).

Activation sequence with spatially varying phenotypes

In Figure 5.15, we plot the activation time of the final beat as a bold black line for the HP model and red/orange thin lines for the PP model. We have 15 repeats of the PP model simulations due to the different random arrangements of model phenotypes, as shown in Figure 5.4.

If we compare the different combinations of model phenotype (S1-S3 on the left, S1-E2 on the right), we observe that the leading pacemaker site is far more consistent in the case where the two self-exciting models, Models S1 and S3, are used. In the Model S1-S3 combination, the pacemaker site is located at the largest region of Model S3, which has a faster intrinsic beat rate than Model S1 (see Figure 5.4, where Models S1 and S3 are shown as dark and light blue, respectively).

In the case of Models S1 and E2, the pacemaker site varies between the HP and PP models far more and we cannot therefore rely on the HP model to represent the range of activation sequences observed in the PP model. Despite this, the conduction velocities are still similar.

If we compare the activation time plot with the phenotype layout in Figure 5.4, we see that the pacemaker is located either at the boundary or at a large region of Model S1 (dark blue; Model E2 is shown in light blue). However, the HP model

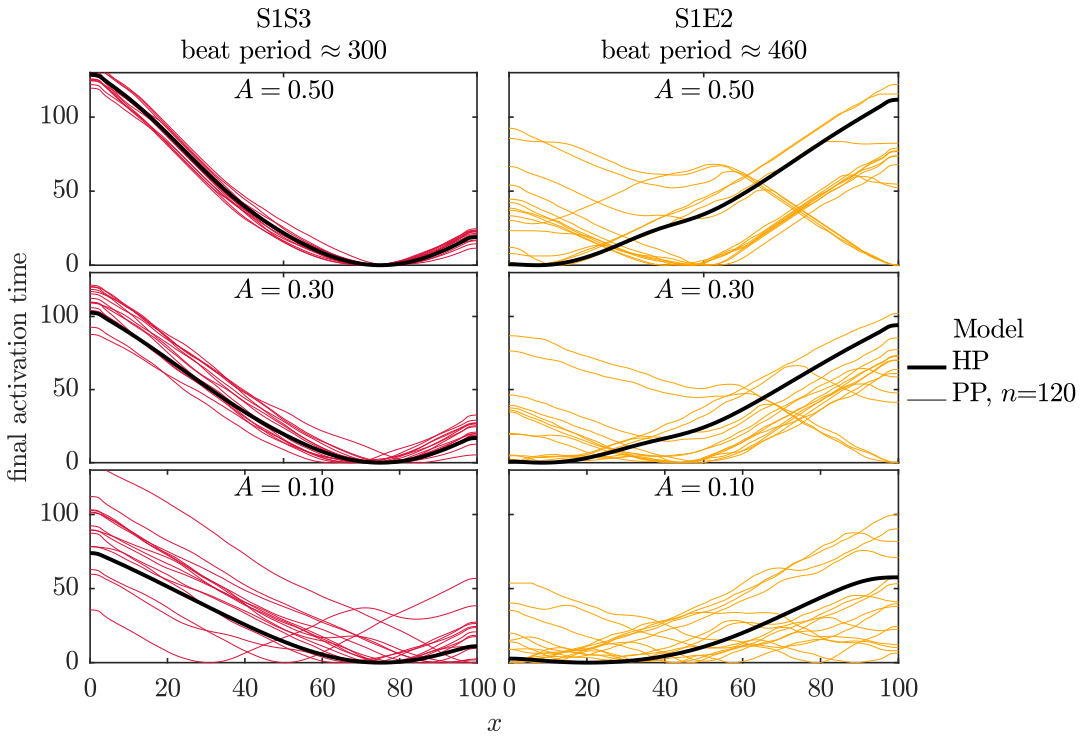

Figure 5.15: Activation times of the final beat in the Set 5 simulations. As in the previous figure, the plots on the left were generated with Models S1-S3, and those on the right with Models S1-E2. In the top panel, we have $0 < \rho_1, \rho_2 < 1$, in the middle $0.2 < \rho_1, \rho_2 < 0.8$, and at the bottom $0.4 < \rho_1, \rho_2 < 0.6$. The bold black line shows the activation time from the homogenised model. The thinner coloured lines show the activation time from the 15 repeats of the partitioned model (each repeat has a slightly different phenotype layout). For more details of the model phenotype layout, see Figure 5.4.

can act as a good representation of the PP model in the first example, where Models S1 and S3 are used.

The correlation between the activation times of the PP and HP models weakens as we reduce the amount of variation in phenotype across the fibre (i.e. when A is low). In these cases, particularly when we have $A = 0.1$, the pacemaker region is no longer consistent between the HP and PP models.

With these two observations, we can conclude that the HP model can represent the activity of the PP model when two conditions are met: first, that there is a substantial amount of spatial variation in phenotype (i.e. A is not small) and second, when the pacemaker location is determined primarily by the positioning of the phenotypes and is not influenced by the domain boundaries.

Biological interpretation

Our discussion of the Set 4 simulations in the previous section has provided us with a good starting point for our physiologically-based model simulations, as it has indicated that we need to introduce spatial variability in phenotype before we can obtain the steady excitation waves from non-boundary pacemakers that are observed experimentally. We have now seen that introducing a random perturbation to the phenotype arrangement can alter the pacemaker region, but that this effect is more prominent in some systems than others.

Where there are large amounts of variation in the proportions of the two phenotypes, the pacemaker region generally follows that of the largest region of the faster-beating model phenotype. In cases where the distribution of phenotypes across the fibre is smoother, the impact of the boundary appears to play a greater role in the location of the pacemaker region. This observation would be interesting to explore experimentally, but at present there is little data available regarding pacemaker locations in hSC-CM cultures.

5.6.6 Set 6: Random spatial variation in phenotype proportion

In order to choose the most appropriate model out of the HP and PP models, we need to understand the spatial scales at which the HP model can be considered a valid representation of the PP model. To do so, we now consider a physiologically-based cellular electrophysiology model. We use the Paci et al. (2013a) models of atrial-like and ventricular-like hSC-CM electrophysiology which are arranged in a similar manner to the simulations we performed in Set 5. The atrial-like model has a faster beat rate and shorter APD_{90} than the ventricular-like model.

We arrange these two phenotypes in a similar manner to that of the previous series of simulations, which is shown in the second panel of Figure 5.4. We investigate the impact of varying parameter A, which sets the amount of variation in phenotype across the fibre, and see how well the PP model with different numbers of partitioned units can represent the HP model for each value of A.

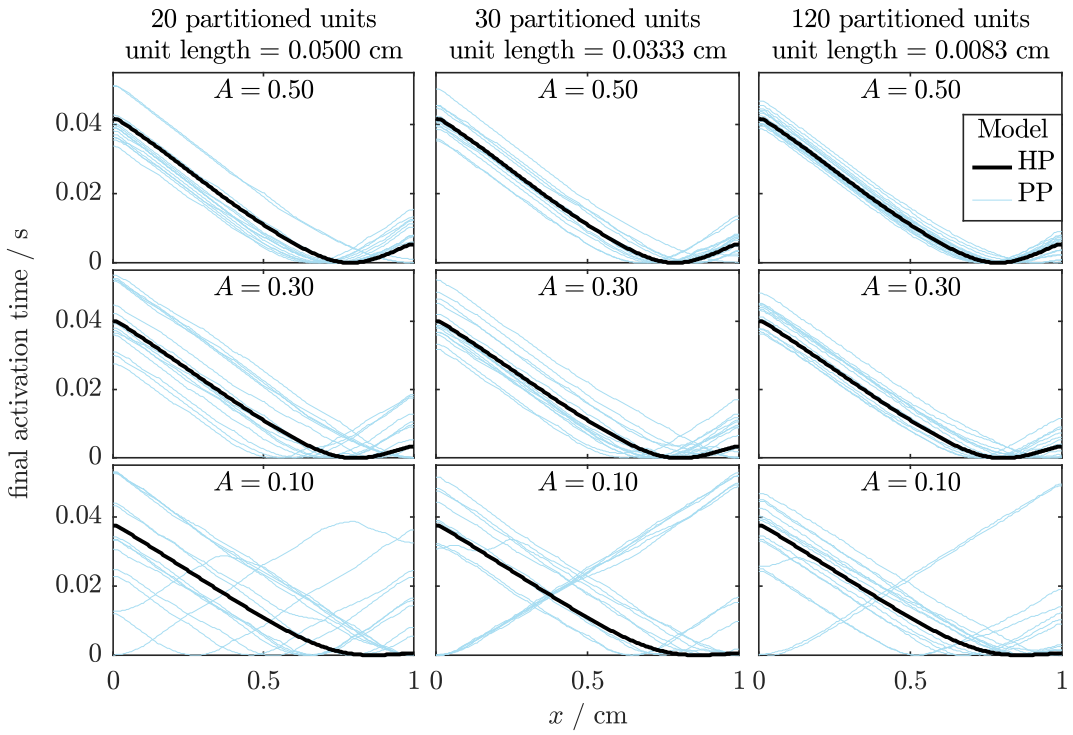

Figure 5.16: Activation times of the final beat of the Set 6 simulations, using the Paci et al. (2013a) models of ventricular-like and atrial-like electrophysiology. As in Figure 5.14, we have $0 < \rho_V, \rho_A < 1$, $0.2 < \rho_V, \rho_A < 0.8$, and $0.4 < \rho_V, \rho_A < 0.2$ in the top, middle and bottom panels respectively. Results from the HP model are shown as a bold black line; the thin, coloured lines represent the 15 repeats of the PP model. From left to right, we have partitioned the fibres into 20, 30 and 120 units.

Activation sequence with spatially varying phenotypes

In Figure 5.16, we plot the final activation times of the simulations with varied numbers of partitioned units and values of A. From left to right, the figure shows the activation times of fibres divided into 20, 30 and 120 partitioned units. As we are now dealing with a dimensional simulation, this corresponds to patches of cells that are approximately 500, 330 and 80 µm across. The typical size of a hSC-CM varies, but even the smallest size of partitioned unit that is tested here would correspond to at least four cells. As in the previous section, we decrease the amount of variability in phenotype from top to bottom of the figure, with parameter A set to 0.5, 0.3 and 0.1 in each row.

In the previous section, we noted that the HP model is able to capture the overall behaviour of the PP model very well when there is substantial variation

in phenotype, or a high value of A. Discrepancies came to light in the situations with less variability in the bottom row of plots — the pacemaker region was no longer consistent throughout the entire series of simulations using the PP model, and the HP model was unable to exhibit the beating behaviour of these cases. We see the same trend here; the only simulations with many different pacemaker locations are those with little variability in phenotype (low A).

However, we note that even when the location of the pacemaker is not consistent between different phenotype arrangements in the PP model, the conduction velocity (given by the gradient of the activation times) is very similar in almost all simulations. The only exception to this is for the low-A simulations that use the HP model, where we see a close to flat activation time profile that corresponds to a large pacemaking region over which activation is near-simultaneous.

As we do not observe much variation in the activation profile as we vary the number of partitioned units, we can conclude that the amount of variation in phenotype given by A is more important in setting the pacemaker location than the size of the partitioned regions. The results shown here indicate that it is only when the tissue contains regions of single phenotypes that are above 0.05 cm across that we will have to consider using the PP model rather than the HP model.

From these results, we can propose that the HP model can be used for simulations of hSC-CM cultures as long as there is a substantial amount of variability across the region. The only limitation of this approach occurs when there is a similar distribution of the two phenotypes across the domain (seen in the bottom row of Figure 5.15). In this case, the region that acts as the pacemaker in the PP model is not consistent as the precise arrangement of the partitioned units is altered and therefore cannot match that obtained by using the HP model.

If this distribution occurred in real cultures, it would present a substantial challenge for modelling: without knowledge of where all regions of a single cell type are, it would be difficult to achieve the same activity pattern through simulation.

In the other cases that we presented above, we can achieve very similar activity patterns without much detailed knowledge of how the phenotypes are distributed. As long as the two phenotypes are non-uniformly distributed throughout the fibre, we anticipate that we will be able to use the HP model to simulate the observed activity pattern.

Biological interpretation

Much of our interpretation of this final series of simulations follows that of Sets 4 and 5 that utilised similar phenotype arrangements with the FHN model. However, now we can interpret the results in a physiological context.

We noted earlier that while there are discrepancies between the activation sequences of PP and HP models at low values of A, the conduction velocities were generally consistent. Now, we can see that the change in conduction velocity is very small as we move from large to small values of A, even as the pacemaker region becomes less consistent between repeated simulations. This indicates that only very small amounts of phenotypic variability are required if we are to avoid synchronisation of the action potentials in hSC-CM cultures, which is in agreement with the lack of experimental reports about such effects.

5.7 Discussion

We have investigated two models for including several cellular phenotypes within simulations of cardiac tissue. In the partitioned phenotypes (PP) model, the simulated domain contains distinct regions where a single model phenotype is present. The homogenised phenotypes (HP) model assumes a well-mixed sample of cells, which we represent as a homogenised system. We have verified that the electrical activity generated by small-region instances of the PP model tends towards that of the HP model, as expected.

Use of the PP model requires that the mesh is sufficiently fine in order to capture the geometry of the partitioned regions as closely as possible. As we have shown in our simulations, this is easy to achieve in one dimension. However, far

more refined meshes (at least in the vicinity of the region boundaries) would be required for two or three-dimensional simulations. The HP model is more flexible in these cases, as we can use a standard mesh with the two cell types represented by using homogenised ionic model parameter values.

Our simulations have demonstrated that a range of behaviours can originate from mixed-phenotype cultures of self-activating cells.

First, we observed synchronised activation of the entire simulated tissue when using the HP model to represent well-mixed populations of cells with consistent proportions of the two types throughout the entire domain. This phenomenon has not been reported in any studies of hSC-CM monolayers, so we can infer that this type of consistent mixing does not occur in monolayers of the cells.

The second behaviour we observed was the near-synchronisation that arose from regularly-partitioned fibres. While the reports of conduction velocity in hSC-CM monolayers in the literature are highly variable (as we discussed in Section 2.5.1, they range from 2–20 cm/s), there have been no reports of values higher than those reported in adult cardiac tissue. The circumstances under which this behaviour was observed in our simulations were rather constrained, with small-sized partitioned units and a regular repeating pattern of the model phenotypes required for notably high conduction velocities to occur. With this in mind, we can again say that this behaviour is unlikely to occur in a biological situation: it would require the two phenotypes of cell to be split into small, regularly-sized regions throughout the tissue and such regularity is not a typical feature of biological tissues.

With the introduction of variability into the distribution of model phenotypes throughout the fibre, we were able to observe the final behaviour: waves of electrical activity that emanated from a single pacemaker region. This is typical of what is reported from optical mapping and MEA studies of hSC-CM monolayers (see, for example Lee et al., 2012). There is usually a single pacemaker, but its location may be anywhere within the tissue and it is not restricted to the boundary. This behaviour originates from what might reasonably be expected to be

the most likely arrangement of phenotypes in biological tissue; that of an uneven mix of the two cell types. Our HP and PP models give consistent simulations of the electrical activity patterns when there is a substantial amount of variation in the proportions of the two phenotypes across the fibre. When the variation in the proportions of the phenotypes is more subtle, a wider range of pacemaker locations are produced from simulations using the PP model. We can therefore propose that the HP model is suitable for simulating a range of phenotype distributions that are relevant to the biological situation, with the PP model only being required when the full range of pacemaker locations must be considered when there is little phenotypic variability across the tissue.

5.8 Conclusions

In this chapter, we have compared two techniques for simulating cardiac tissue containing two types of cell. We have found that the homogenised phenotypes model is a valid approach for simulating most levels of spatial variability in cell type, with accurate simulation of distinct regions through the partitioned phenotypes model only needed if precise knowledge of the activation pattern is required from the simulation.

Implementation of the homogenised phenotypes model is relatively simple, requiring only changes to the cellular electrophysiology model and to the values of the parameters used in the monodomain or bidomain equations. A further advantage is that specialised meshes for each spatial distribution of phenotype are not required, as would be the case if using the partitioned phenotypes model.

Given these advantages, we use the homogenised phenotypes model throughout the next two chapters, where we investigate the impact of spatial heterogeneity in cell type in two-dimensional hSC-CM cultures. While the one-dimensional simulations discussed in this chapter have proved illuminating in explaining some properties of hSC-CM biomarkers and activation sequences, working in two dimensions has the advantage of the simulated data being directly comparable to experimental preparations. Our aim in the next chapter is therefore to com-

pare simulated signals from two-dimensional hSC-CM monolayers to experimental data of the type that would be used in the drug safety assessment proposals of the Comprehensive *in vitro* Proarrhythmia Assay Initiative.

Chapter 6

Simulations of Stem Cell-Derived Cardiomyocyte Monolayers in the Micro-Electrode Array

In Chapter 5, we set out two models that may be used to simulate the electrical activity in cardiac tissue that contains different subtypes, or phenotypes, of cells. The *partitioned phenotypes* (PP) model can be used when the cell types are arranged in discrete clusters throughout the domain, while the *homogenised phenotypes* (HP) model can simulate the case where the cell types are well (although not necessarily evenly) mixed.

Now that we are able to simulate the cell combinations that are present in monolayers of stem cell-derived cardiomyocytes, we can move our focus to the micro-electrode array assay. Given the recent proposals of the Comprehensive *in vitro* Proarrhythmia Assay (CiPA) initiative for tissue-scale assays based on human stem cell-derived cardiomyocytes, use of the micro-electrode array has expanded. In the previous chapter, we determined that some level of heterogeneity in the action potential is necessary if the tissue is to generate steady activation waves, as experimentally reported. However, the impact of action potential variability through different cellular phenotypes on the form of the field potential

has not been considered as a factor which may affect the biomarkers that are subsequently used in the safety assessment process.

In this chapter, we simulate the micro-electrode array with different arrangements of cellular phenotypes. We perform an initial exploration of the effects of cellular heterogeneity on key system parameters (the origin of the activation wave, the speed of the activation wave and the form of the signals recorded by the experimental system). At this stage, it would be inappropriate to perform a full parametrisation of all aspects of the model, for reasons that we will cover in more detail later. Instead, we focus on a qualitative comparison of key findings from simulated and experimental data.

Our aim in this chapter is to investigate the extent of heterogeneity in cellular phenotype required to produce signals from a simulated micro-electrode array that resemble those observed experimentally. We carry suitable arrangements of cellular phenotypes forward into Chapter 7, where we investigate the performance of the model under conditions affected by the presence of ion channel-blocking drugs. We use these comparisons to investigate how the conclusions drawn from the micro-electrode array assay may be affected by the arrangement of cellular phenotypes, and identify aspects of the model where improvement is required.

6.1 Chapter Outline

We begin Section 6.2 with a description of the experimental system that we wish to simulate; that of the micro-electrode array (MEA). The MEA was described briefly in Chapter 2; here, we extend that description with a more detailed discussion of the devices used by our experimental collaborators. We also list the experimental data that we have available for comparisons with our simulation studies, and discuss the major components of the signal recorded by the MEA, the field potential.

In Section 6.3, we describe the cellular electrophysiology models that can be used to simulate the distinct action potentials of human stem cell-derived cardiomyocytes. In Chapter 2, we mentioned the Paci et al. (2013a) models of

the electrophysiology of atrial-like and ventricular-like human induced pluripotent stem cell-derived cardiomyocytes (hiPSC-CMs), and later used these two model variants for our final simulations in Chapter 5. However, this approach has not been taken by all groups attempting tissue-scale simulations of hSC-CMs. We therefore discuss the alternatives, as well as recent extensions to the Paci et al. (2013a) model.

We then move on to the simulations themselves. As in any simulation study, we have had to select the components of the physical system that are represented in our model. The assumptions in our model are discussed in Section 6.4, along with the choices of parameters for the bidomain equations. In Section 6.5, we perform simulations with simple arrangements of the cellular phenotypes to investigate their impact on the field potential. We move to more complex arrangements of phenotypes in Section 6.6, from which we select phenotype distributions that yield field potentials most similar in form to those observed experimentally. In Section 6.7, we then compare the values of several commonly-used biomarkers from the simulations with experimental data.

6.2 Experimental System: The Micro-Electrode Array

The development of the micro-electrode array[1] was inspired by the need for non-invasive recording of electrical signals from cellular cultures over a long period of time. The first MEA was developed by Thomas Jr. et al. (1972), who produced a device approximately $2.5 \times 2.5\,\text{cm}$ across that contained 30 gold-plated nickel micro-electrodes in the central region. When testing the device on embryonic chicken cardiomyocytes, signals were detected from several recording electrodes simultaneously and it was possible to resolve the arrival time of the activation wave. A schematic of this early MEA is shown in Figure 6.1. Despite recent advances in manufacturing techniques and changes to the dimensions of the device, the core components remain similar.

[1]The micro-electrode array is also referred to in the literature as the multielectrode array; conveniently with the same abbreviation, MEA.

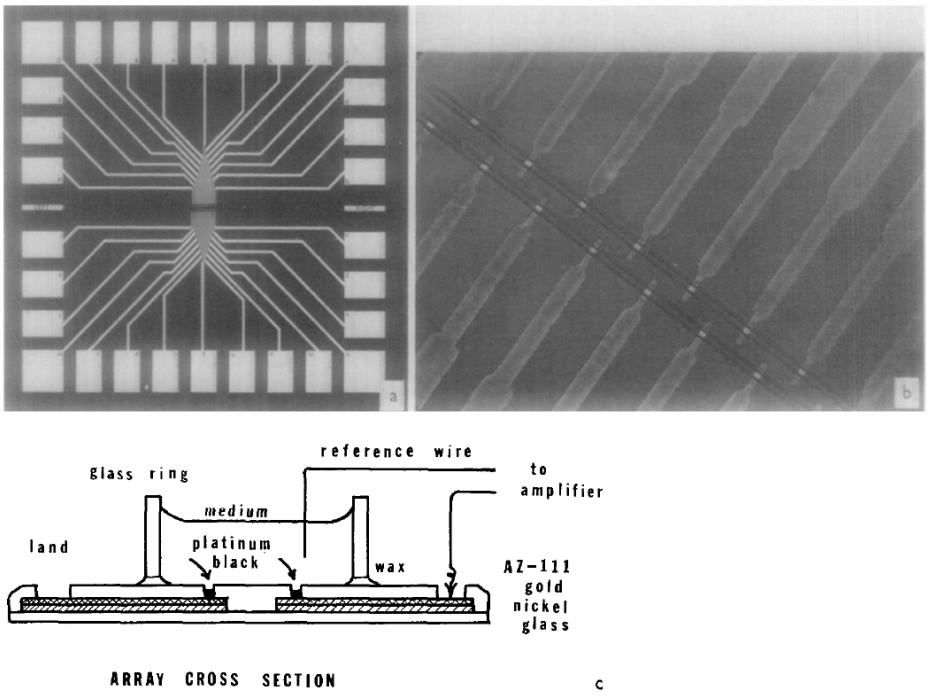

Figure 6.1: The layout of an early micro-electrode array. (a) Plan of the MEA layout. (b) Tips of the MEA electrodes. (c) Cross-section of the MEA. Figure reproduced from Thomas Jr. et al. (1972).

The field potential (FP) recorded by the electrodes of the MEA is the potential difference between the reference electrode and a recording electrode, which picks up contributions from all cells in the vicinity. In early MEAs, the reference electrode was connected to the culture medium (see Figure 6.1), but later models have incorporated larger, and sometimes multiple, reference electrodes on the base of the plate.

MEAs are also used regularly in neuroscience, and the interest from both the neuroscience and cardiac safety communities has encouraged the development of more varieties of MEA. Novel designs include protruding electrodes that are curved or pointed to ensure greater contact with the cell membrane and hence better signal quality (Spira and Hai, 2013). Smaller MEAs are also being developed, which are well-suited to studies of the type proposed by CiPA. These are better-suited for high throughput assays: 48 and 96-well plate versions are available from manufacturers such as Axion Biosystems (Atlanta, USA) and MultiChannel Systems (Reutlingen, Germany). These systems have the advantage of

being able to repeat many experiments simultaneously — ideal for the assessment of novel pharmaceutical compounds.

6.2.1 Experimental data

The experimental data to which we compare our simulated recordings was kindly provided by Kate Harris and colleagues, from GlaxoSmithKline (Ware, UK), and Mike Clements, from Axion Biosystems (Atlanta, USA).

Data from GlaxoSmithKline

The data provided by GlaxoSmithKline consists of three datasets previously published in Harris et al. (2013), which were passed on to us in Autumn 2013.

Each dataset contained FP recordings from MEA assays to which a different drug was applied at a variety of concentrations. The first drug, Cisapride, exclusively blocks the hERG channel. The second, Nifedipine is an L-type calcium channel blocker, while the third, Terfenadine, is a mixed channel blocker which primarily impacts the hERG channel at low concentrations.

We were also provided with two activation time maps, which list the times at which the activation wave arrived at each of the 59 recording electrodes. Using this information, we were able to calculate the conduction velocity of the activation wave.

The specific MEA model used in these experiments was 60EcoMEA-Glass-pr-T, produced by MultiChannel Systems. hiPSC-CMs were obtained from Cellular Dynamics International (Madison, USA).

Data from Axion Biosystems

The data provided by Axion Biosystems was prepared as part of their CiPA Phase II study (Colatsky et al., 2016). 28 compounds were assessed for arrhythmic risk using hiPSC-CMs (from Cellular Dynamics International) and their own 96-well MEAs. We were provided with the data in late December 2017.

The Maestro system was used to record data from 96-well MEA plates (Classic

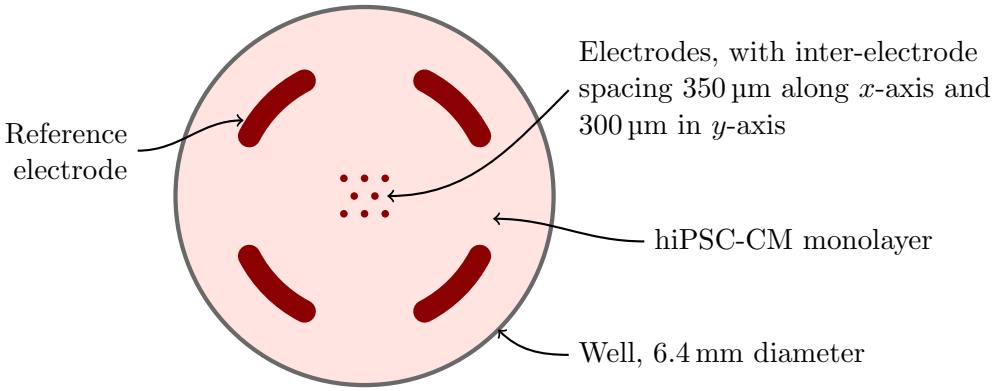

Figure 6.2: The geometry of an MEA. As the majority of our experimental data were obtained using an Axion Biosystems 96-well micro-electrode array, we based the our simulations upon the geometry of this particular MEA model.

MEA 96). We based the simulations in this chapter on the geometry of this 96-well MEA. A schematic of the MEA is provided in Figure 6.2.

6.2.2 Field potential biomarkers

As we have noted in Section 2.2.5 with relation to the action potential, biomarkers are useful for quantifying features of biological signals. In Figure 6.3, we show a typical experimental field potential together with the most commonly-used biomarkers: spike amplitude and field potential duration. Further biomarkers can then be calculated based on these quantities.

Figure 6.3 also highlights the two main parts of the field potential — the depolarising spike and the repolarising wave. The depolarising spike occurs when the tissue around the electrode rapidly depolarises during Phase 0 of the action potential. If we use the time at which the depolarising spike occurs as a marker of the start of each beat, we can calculate the inter-beat, or RR[2], interval and can therefore obtain the beat rate. Knowledge of the time at which the beat starts (the activation time) also enables calculation of the conduction velocity of the activation wave, or CV.

The field potential duration, FPD, is calculated as the time between the depolarising spike and the peak of the repolarising wave. As the FPD is influenced

[2]The RR interval is referred to as such due to the similarity between the depolarising spike of the field potential and the QRS complex of an electrocardiogram.

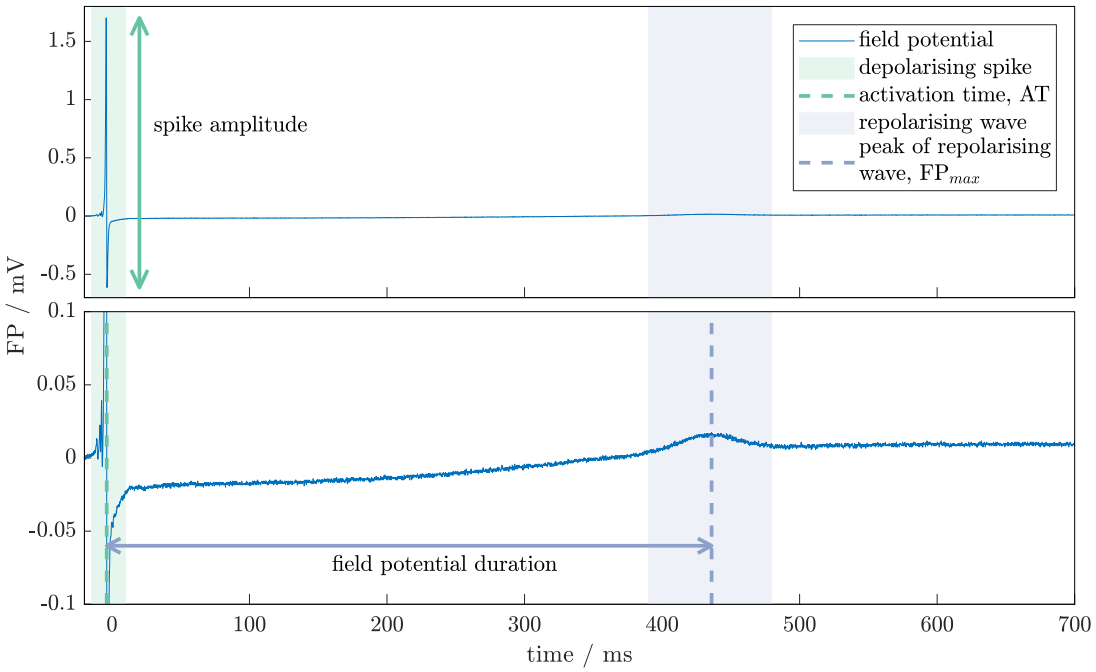

Figure 6.3: Major features of a field potential signal. The y-scale is enhanced in the lower plot to show the detail of the repolarising wave. The depolarising spike, repolarising wave and some of the most widely-used biomarkers are shown on this field potential from a MultiChannel Systems 60EcoMEA. Data provided by GlaxoSmith-Kline.

by the beat rate, correction formulae are often applied to remove this rate dependence, giving the corrected field potential duration, or FPDc. Fridericia's and Bazett's formulae are the most commonly-used, but alternatives developed specifically for use in MEA studies have also recently been proposed (Izumi-Nakaseko et al., 2017). These corrections take the form $\mathrm{FPDc} = \mathrm{FPD}/\mathrm{RR}^n$, where n varies depending on the formula used.

The relationship between the field potential and the action potential has been investigated by comparing MEA recordings with those of a patch clamp or sharp microelectrode applied at the same time. Halbach et al. (2003) reported that the minimum value of the field potential occurred at the same time as the upstroke of the action potential in cultures of embryonic murine cardiomyocytes. They also noted that a biomarker known as $\mathrm{FP}_{\mathrm{rise}}$ (the time over which the sharp depolarisation of the field potential occurred) was notably longer in the pacemaker regions, due to the slower depolarisation in the action potential. In comparison,

the FP_{rise} throughout the rest of the tissue was generally consistent and shorter. Halbach et al. defined the field potential duration, or FPD, as the time between the minimum value of the FP and the maximum value of the later deflection during the repolarising wave, which was reported to be correlated with the value of APD_{90}. Many of the biomarkers discussed in Halbach et al. (2003) are not widely used at present, but they do indicate that the field potential holds more information than is available in the commonly-used set of biomarkers.

6.2.3 Calculation of biomarkers

Biomarker values were calculated from the simulated datasets using a custom set of Matlab routines. The simulated field potential from Axion Biosystems' 96-well MEA was obtained at each of the eight recording electrodes (see Figure 6.2), giving eight values of each electrode-level biomarker from each simulation. One electrode from each well was selected for analysis. The chosen electrode was that with the closest value of the field potential duration to the average value across the eight electrodes. The values of the biomarkers presented in the analysis are the median value from the last three beats of the simulation, unless otherwise stated. This approach taken to minimise the effects of any features that were misidentified during the automated analysis.

Biomarkers from the experimental datasets were obtained directly from collaborators where possible; otherwise the previously mentioned Matlab routines were used.

Activation time and beat rate

The activation time is defined as the time of the steepest decrease in field potential during the depolarising spike. As the depolarising spike is the most prominent feature in the field potential, it could be identified by a simple thresholding algorithm. The activation time could then be located within each of the detected depolarising spikes.

The inter-beat, or RR interval, was then calculated by taking the difference

between subsequent activation times. The beat rate could then easily be obtained.

Spike amplitude

Once the depolarising spike had been identified, the spike amplitude was found by simply taking the difference between the maximum and minimum values of the field potential during this phase.

Conduction velocity

Having obtained the activation time at all the eight electrodes during each beat, the conduction velocity could then be calculated. There are many methods for calculating CV, some of which are better-suited to certain data modalities than others. A selection of these methods are reviewed in Cantwell et al. (2015), from which we selected the two used in this thesis.

The first of these was based upon the finite difference method, where the gradient of the activation time is used to determine the conduction velocity. For the second, a quadratic surface was fit to the activation times, and the gradient of this surface was then used to calculate the CV. Section A3.2 contains details of the implementations of the two methods and the validation process, along with a comparison of the two algorithms. The figures in this chapter use values obtained from the latter algorithm, with the former used as a method of checking for potential issues in the calculation.

Field potential duration and corrected field potential duration

Having determined the activation times, the field potential was divided up into different beats. As we shall see in the following section, the morphology of the repolarising wave does not necessarily take the form of the simple peak seen in Figure 6.3. If the peak was not as clearly defined as that in Figure 6.3, the final major deflection in the field potential prior to the next beat was taken to be the peak of the repolarising wave.

The field potential duration was then calculated by taking the difference be-

tween the time at which the peak of the repolarising wave occurred and the activation time.

As discussed above, the corrected field potential duration, or FPDc, is often used because the FPD itself is known to be correlated to the beat rate. Following many experimental studies (such as Harris et al., 2013), we used Fridericia's formula to calculate the FPDc:

$$\mathrm{FPDc} = \frac{\mathrm{FPD}}{\mathrm{RR}^{1/3}}, \tag{6.1}$$

where RR is the RR interval and all times are in seconds.

Repolarising wave amplitude

While the amplitude of the repolarising wave is not commonly examined in the cardiac safety assessment process, we shall see later in this chapter that it is sensitive to the amount of variability in cellular phenotype across the monolayer. The amplitude of the repolarising wave is calculated by taking the difference between the minimum and maximum values of the field potential in the interval between one depolarising spike and the next. As the repolarising wave is the most prominent feature in this region of the field potential, such a calculation yields the amplitude of the repolarising wave.

6.3 Cellular Electrophysiology Models for Human Stem Cell-Derived Cardiomyocytes

The first cellular electrophysiology model specifically designed for human stem cell-derived cardiomyocytes was that of Paci et al. (2012). This model was based upon the Grandi et al. (2009) model of ventricular cardiomyocytes, which was re-parametrised based on experimental and literature data on human embryonic stem cell-derived cardiomyocyte electrophysiology at early and late stages of development. Two currents that are not present in adult cardiomyocytes were added to the Grandi et al. (2009) model. These were the hyperpolarisation-activated pacemaker (funny) current, I_{f}, and the T-type calcium current, I_{CaT}. While the

Paci et al. (2012) model reproduced qualitative changes to features of the action potential when the application of ion channel-blocking drugs was simulated, it was weaker at representing the action potential itself, with faster repolarisation than depolarisation being one of the most notable features.

The follow-up model, Paci et al. (2013a), was based upon the previous version and incorporated data from a very complete study of human induced pluripotent stem cell-derived cardiomyocyte electrophysiology (Ma et al., 2011). The distinct electrophysiology of atrial-like and ventricular-like cardiomyocytes was simulated by tuning the channel conductances based on the differences in ion channel expression between adult atrial and ventricular cardiomyocytes.

The Paci et al. (2013a) model has subsequently been further extended, with versions now available for simulations of different subtypes of Long QT syndrome (Paci et al., 2013b; Paci et al., 2014). The models have also been used in population studies that incorporate the variability thought to be present in ionic currents from cell to cell (Paci et al., 2015).

While studies such as this thesis and Abbate et al. (2018) have used the specialised Paci et al. (2013a) models, other classes of model have also been used to simulate human stem cell-derived cardiomyocyte electrophysiology. Phenomenological models such as the FitzHugh-Nagumo model (FitzHugh, 1961; Nagumo et al., 1962) can be parametrised to exhibit spontaneous beating, as observed in hSC-CMs. Although models of this type do not simulate individual ionic currents, they are nevertheless useful for studying activation of cardiac tissue when coupled with the monodomain or bidomain equations, as we demonstrated in Chapter 5. The minimal ventricular cell model of Bueno-Orovio et al. (2008) was used by Tixier et al. (2018) to simulate the action potentials of cells with long and short action potential durations. However, the Bueno-Orovio et al. (2008) model does not exhibit spontaneous beating as is often observed in human stem cell-derived cardiomyocytes.

More complex models of adult cardiomyocytes have also been used. Frotscher et al. (2015) used the McAllister et al. (1975), Seemann et al. (2006), ten Tusscher

and Panfilov (2006), and Chandler et al. (2009) models in simulations of the CellDrum assay and concluded that the simulations that used the ten Tusscher and Panfilov (2006) model provided the best fit to their experimental data, due to the large proportion of ventricular-like cells present in the hiPSC-CMs used. Later work by the same group, Frotscher et al. (2016), simulated heterogeneous cell distributions in the CellDrum assay using the ten Tusscher and Panfilov (2006) and Chandler et al. (2009) models for ventricular and nodal cells, and also introduced the Paci et al. (2013a) atrial-like model to simulate the final reported cellular phenotype.

6.4 Development of the Micro-Electrode Array Model

In this section, we describe the framework for simulating the MEA. As we are now simulating a two-dimensional system using the bidomain equations, the computational cost of solving the problem is far larger than it was for the one-dimensional simulations in Chapter 5. We therefore utilise the *Cancer, Heart and Soft Tissue Environment* simulation library (Chaste) for the simulations in this chapter, which was described in Section 4.5.1.

We cover different aspects of the MEA simulations in the following sections, starting with a review of the bidomain equations and the geometry of the system with particular discussion of the reference electrode. We then list the other parameters used in the simulation, both those of the bidomain equations and of the cellular electrophysiology model.

As we are performing an initial exploration of the model at this stage, the vast majority of parameters described in this section are set at their default values while we focus on investigating the impact of heterogeneity in cell type throughout the monolayer on the simulated signals. At the end of this chapter, and also in Chapter 7, we identify aspects of the model where the parameter values need further refinement with additional experimental data.

6.4.1 The bidomain equations

In the simulations that we performed in Chapter 5, we were interested in the membrane voltage alone as an output and could therefore solve the simpler monodomain equation rather than the bidomain equations. As in Chapter 5, we still use constant values of intra- and extracellular conductivity across the domain so the monodomain equation would still be a suitable model for the electrical activity. However, solving the bidomain equations also provides us with the extracellular potential, which is equivalent to the field potential from the MEA.

For spatially constant values of intracellular and extracellular conductivities, σ_i and σ_e, and no applied stimulus, the bidomain equations may be written as

$$\chi\left(C_m\frac{\partial V_m}{\partial t}+I_{\text{ion}}(\mathbf{u},V_m)\right)-\sigma_i\nabla^2(V_m+\phi_e)=0, \qquad \text{and} \tag{6.2}$$

$$(\sigma_i+\sigma_e)\nabla^2\phi_e+\sigma_i\nabla^2V_m=0, \tag{6.3}$$

which are coupled to the cellular electrophysiology model

$$\frac{\partial\mathbf{u}}{\partial t}=\mathbf{f}(\mathbf{u},t), \tag{6.4}$$

which are solved on domain Ω. All the stimulus currents have been set to zero for the work presented in this chapter as the electrophysiology models used here are able to self-excite.

6.4.2 Geometry of the micro-electrode array

The geometry of the micro-electrode array simulated in this chapter is based on that of the 96-well MEA system by Axion Biosystems. Each of the wells has diameter 6.4 mm at the base, and a monolayer of hSC-CMs covers this surface. Our finite element mesh is therefore constructed to be bounded by this circular domain. No-flux boundary conditions are imposed at the well boundary as current is unable to flow through the walls of the well. As the monolayer is only a single cell thick, its height is very small compared to the other dimensions of the monolayer. We therefore use a two-dimensional mesh for the simulations.

The eight low-noise recording electrodes are situated in a group at the centre of the MEA. The electrodes are circular in shape, with a diameter of 50 µm. As this size is small compared to the typical size of a finite element in the mesh, we consider the electrodes as perfect insulators that gather point measurements of the field potential. A comparison of ideal and non-ideal impedance models for the electrodes has previously been carried out by Moulin et al. (2008), who found that modelling the electrodes as perfect insulators was a suitable approach if the measurement system was well-designed. Each electrode is therefore represented by a single node of the finite element mesh, and the field potential is obtained from the extracellular potential, part of the solution to the bidomain equations.

The tips of the electrodes in the 96-well MEA are composed of gold, a low resistance material, so we may therefore anticipate that the presence of the electrodes could alter the local extracellular conductivity in their vicinity. Given the small size of the electrodes, we have assumed that these effects are small in comparison to the field potential signal. Refinements to the mesh could be made in future to more accurately delineate the metallic regions, and with those changes, future work could incorporate a more detailed investigation of these effects.

6.4.3 The reference electrode

The field potential, the signal measured by an MEA, is a measurement of the potential difference between a recording electrode and the reference electrode. In most modern MEA systems, the reference electrode covers a large region outside the recording area. In the case of the EcoMEA and MEA200 systems used at GlaxoSmithKline, the reference electrode covers a triangular region to the left of the recording electrodes. In the Axion Biosystems 96-well MEA, which we use as the basis for our simulations in this chapter and the next, there are several large reference electrodes placed symmetrically around the outside of the recording electrodes. Note that the reference electrode is not grounded; it takes a passive measurement of the extracellular potential across an area (in the ideal case, without influencing it).

The bidomain equations have two outputs, the membrane voltage V_m and the extracellular potential ϕ_e. If a grounded electrode (implemented as a Dirichlet boundary condition for ϕ_e) is not set, the bidomain problem is singular as ϕ_e is defined only up to a constant. This issue is overcome in the Chaste library by solving the linear system with implementations of the conjugate gradients or GMRES algorithms that use the null-space (which are available through the PETSc package). Physically, this can be interpreted as setting

$$\int_\Omega \phi_e \, \mathrm{d}\mathbf{x} = 0, \tag{6.5}$$

which is equivalent to taking the average extracellular potential over the entire domain as a reference potential at each point in time (Pathmanathan et al., 2010).

The field potential (FP) is defined as the potential difference between a recording electrode and the average potential over the reference electrodes, $\phi_{e,\mathrm{ref}}$, such that

$$\mathrm{FP} = \phi_e - \phi_{e,\mathrm{ref}}. \tag{6.6}$$

If, as in Chaste, Equation (6.5) is implemented to ensure the problem is not singular, the reference electrode(s) will not necessarily have a zero average potential, $\phi_{e,\mathrm{ref}}$, as the average is taken over only a subset of the total area. We therefore cannot consider the field potential, FP, to be equal to the extracellular potential, ϕ_e.

However, this is a reasonable approximation in many cases: in the Axion Biosystems MEA, the reference electrodes are large and located such that the activation wave (with its fast changes in ϕ_e) rarely passes over all four reference electrodes at the same time. Calculation of $\phi_{e,\mathrm{ref}}$ yields a value that is smaller than ϕ_e; sufficient to have a minor influence on the amplitude of the field potential, but not on the overall morphology of the field potential signal.

For reasons of computational efficiency, we have therefore chosen to make the approximation that FP $\approx \phi_e$ throughout this chapter. In Section A1.2.2, we show examples of field potentials computed with explicitly implemented reference electrodes, and discuss several ways through which their effects could be implemented in bidomain simulations carried out using Chaste. The implementations

essentially involve computing Equation (6.5), but over the reference electrodes rather than the entire domain, such that

$$\int_{\Omega_{\text{ref}}} \phi_{e,\text{ref}} \, \mathrm{d}\mathbf{x} = 0. \tag{6.7}$$

Our comparisons of the field and extracellular potentials in Section A1.2.2 showed no difference in qualitative behaviour, with the general morphology of the depolarising spike and repolarising wave unchanged. In terms of biomarkers, the slight difference in amplitude of the field and extracellular potentials caused small changes in the values of the spike and repolarising wave amplitudes. The conduction velocity, beat rate, and field potential duration (biomarkers based on the timing of features of the extracellular/field potential) were unaffected.

6.4.4 Finite element mesh

Finite element meshes were generated using Gmsh 3.0.6 (Geuzaine and Remacle, 2009). Gmsh is particularly suited to the generation of meshes for the MEA as it automatically refines the mesh in the vicinity of the circular outer boundary, and nodes at the location of the recording electrodes can be specified. Having defined the radius of the mesh and the location of other key features, meshes with different target inter-node distances could be generated. Figure 6.4 shows two meshes with different values of inter-node spacing. Elements of the meshes were labelled, with those belonging to the reference electrode highlighted in green.

Convergence analysis

Following a convergence study, a mesh with maximum inter-node spacing of 100 µm and a PDE time-step of 0.01 ms were selected for the following simulations. The methodology and results of the convergence simulations are discussed in Section A3.1. While our results indicated that a 150 µm mesh would give us appropriate levels of error, we do increase the complexity of the phenotype arrangements later in this chapter. We therefore chose to err on the side of caution, and use a mesh with a slightly smaller inter-node spacing to better capture the variation in cellular phenotype across the mesh.

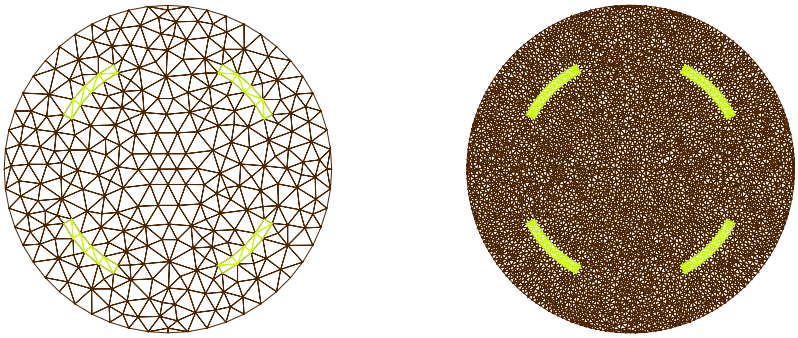

Figure 6.4: Finite element meshes used in simulations of the 96-well MEA. Left: mesh with maximum inter-node spacing of 400 µm, used for testing purposes only. Right: mesh with maximum inter-node spacing of 100 µm, used in the simulations throughout this chapter. Elements in the reference electrode are coloured green.

Parameter	Value
χ	$1400\,\mathrm{cm}^{-1}$
C_m	$1\,\mu\mathrm{F/cm}^2$
σ_i	$0.3\,\mathrm{mS/cm}$
σ_e	$7.0\,\mathrm{mS/cm}$

Table 6.1: Tissue-level parameters for bidomain simulations of the MEA. Most parameters are kept at the Chaste default values, with the exception of the intracellular conductivity, σ_i.

6.4.5 Parameters of the bidomain equations

The tissue-level parameters in the bidomain equations are left at the default values in Chaste, apart from the intracellular conductivity, σ_i. The intracellular conductivity is tuned to give conduction velocities of approximately 16 cm/s, as calculated from activation time maps provided by GlaxoSmithKline. This value of conduction velocity is similar to that reported by other groups studying monolayers of hiPSC-CMs from the same supplier (Lee et al., 2012). The values of the tissue-level parameters are given in Table 6.1.

6.4.6 Cellular electrophysiology model

In Chapter 5, we developed the partitioned phenotypes (PP) and the homogenised phenotypes (HP) models. The literature on the subject of the spatial distributions of cellular phenotypes in cultures of hSC-CMs is rapidly developing, and so we note that the decisions we have made here in regard to the best way of modelling

a hSC-CM monolayer may change as more information becomes available.

Recent publications point to differences in the phenotypic arrangement between cultures of human embryonic and human induced pluripotent stem cell-derived cardiomyocytes. The former have been shown to exhibit phenotypic clustering within each sample of cells (Zhu et al., 2016; Vestergaard et al., 2017), while there is less evidence for this in the latter, with reports of variation in action potential parameters across the monolayer (Du et al., 2015). However, reports of action potential variability in hiPSC-CMs have not yet identified whether there is difficulty in classifying the cells into subtypes based on the action potentials of single cells (Kane and Terracciano, 2017), or whether there are distinct phenotypes that have become mixed during the culture and transportation of the cells.

As we consider only monolayers composed of hiPSC-CMs in this thesis, we choose to represent their variation in phenotype using the homogenised phenotypes model. This permits us to introduce gradual spatial variation in phenotype, which should, based upon our studies in the previous chapter, result in action potential parameters that vary across the domain.

The cellular electrophysiology model that we use is a homogenised version of the Paci et al. (2013a) models of atrial-like and ventricular-like hiPSC-CM electrophysiology. The ionic current is calculated using

$$I_{\text{ion}} = \rho_{\text{A}}\, I_{\text{ion,A}} + \rho_{\text{V}}\, I_{\text{ion,V}}, \tag{6.8}$$

where $I_{\text{ion,A}}$ and $I_{\text{ion,V}}$ are the ionic currents of the atrial-like and ventricular-like cell types, and

$$\rho_{\text{V}} = 1 - \rho_{\text{A}}, \tag{6.9}$$

where ρ_{A} and ρ_{V} represent the relative proportions of the cell membrane of the two cell types per unit volume of tissue. Given that is it not possible to distinguish between atrial-like and ventricular-like hiPSC-CMs from their physical shape and size alone, we assume that both types cells are the same size and have the same amount of cell membrane. We can therefore adopt the alternative definition of ρ

used in the previous chapter: under these conditions, ρ_A and ρ_V can equivalently be defined as the relative proportions of the numbers of the two types of cell within the same unit volume.

For now, we have not included a representation of nodal-like cells in our simulations. Many reports have indicated that the nodal-like cells are the least numerous out of the three subtypes (Ma et al., 2011), and at present, there is no mathematical model of nodal-like hSC-CM electrophysiology available. This simplification also assists in the ease of interpretation and implementation. In theory, adding a third cell type is simple — the cellular electrophysiology model would need to be modified to include a contribution from the third cell type, but few changes would need to be made to the relevant Chaste code. This could easily be carried out in the future, should our results indicate that it may be a useful point to investigate further.

The initial conditions of the cellular electrophysiology model are derived from those listed in Paci et al. (2013a). For a range of values of ρ_{V}, we simulate 10 s of activity in a single cell, using the initial conditions from the Supplementary Information of Paci et al. (2013a). We then identify the values of the state variables at the final time at which the action potential increases past -70 mV. At the start of each monolayer simulation, the instance of the cell model located at each node of the finite element mesh is initialised with this set of state variables from the single-cell simulation with the same value of ρ_{V}. If the value of ρ_{V} at the node does not match the tested values, the initial conditions are determined by interpolating from the initial conditions at the closest two values of ρ_{V}.

6.5 Influence of the Spatial Distribution of Cellular Phenotypes on the Field Potential

In this section, we link the major features of the field potential to the location of the pacemaker region and distribution of the cellular phenotypes.

Parameter	Values			
x	0.0			
y	0.0	0.1	0.2	0.3
r	0.05	0.1		
a	0.25	0.5	0.75	1.0

Table 6.2: Parameter values used to set the location of the atrial-like pacemaker region. Simulations were performed using all 16 combinations of parameters. Parameters x and y give the coordinates of the centre of the pacemaker region in relation to the centre of the monolayer (x is kept constant due to the symmetry of the monolayer). r denotes the radius of the pacemaker region, and a is the maximum contribution of the atrial-like model within the pacemaker (i.e. $\rho_{\mathrm{A,max}}$). All parameters have units of cm, apart from a, which is dimensionless.

6.5.1 Description of simulations

For our first series of simulations, we use a simplified arrangement of cellular phenotype. We simulate a monolayer of cells of diameter 6.4 mm, as would be used in the Axion Biosystems 96-well MEA (see Section 6.4.2 for further details of the mesh). All nodes in the mesh are set to have a ventricular-like proportion (denoted by ρ_{V} in the cellular electrophysiology model) of one, apart from within a small pacemaker region. The centre of the pacemaker is denoted by coordinates (x, y), and the pacemaker region has radius r. Within the pacemaker region, the value of ρ_{V} varies linearly, from 1 at the outer edges to $1 - a$ in the centre, where a is the maximum value of the atrial proportion, ρ_{A}.

The full range of parameters tested is listed in Table 6.2, and examples of the phenotype layout can be seen in Figure 6.5. The value of x was not varied due to the symmetry of the MEA. As the atrial-like cells (and therefore the atrial-like model) have a faster beat rate than the ventricular-like cells/models, regions of high ρ_{A} (and hence low ρ_{V}) act as a pacemaker for the rest of the tissue.

We simulated 10 s of activity in monolayers with each of the parameter combinations listed in Table 6.2, and the features of the field potential during the final beat of each simulation are discussed below.

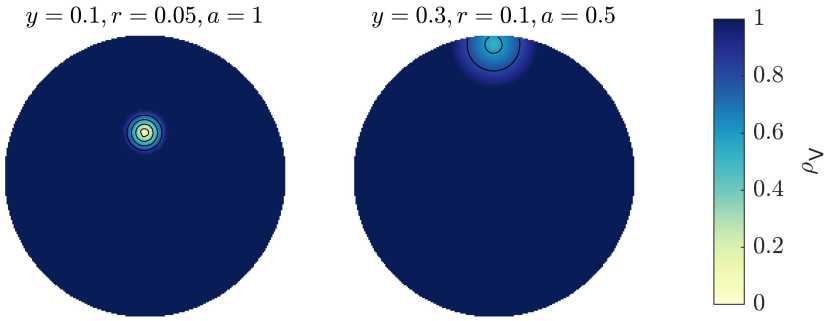

Figure 6.5: Examples of simple phenotype layouts. Regions where the atrial-like model made the largest contribution to the ionic current act as pacemakers for the rest of the tissue.

6.5.2 Features of the field potential

In Figure 6.6, we plot the depolarising spike of the final beat in each of the simulations discussed above. We show data from two electrodes: Electrode 1 is located at the top left of the group of eight, while Electrode 6 is located at the bottom left.

We can immediately see that the distance of the pacemaker region from the electrodes has an impact on the morphology of the depolarising spike. When the pacemaker region is located in the immediate vicinity of the electrodes (i.e. $y = 0$ and $y = 0.1$), the depolarising spike consists simply of a fast polarising phase followed by slower depolarisation. Up until the action potential begins, the entire domain has similar membrane potential, so the field potential is close to zero. The flow of positive ions from the extracellular space into the intracellular space at the start of the action potential then causes the field potential to become more negative. If we recall the condition given in equation (6.5), we can see how the field potential then returns to zero as the extracellular space becomes similarly depolarised over the entire tissue as the activation wave spreads. However, when the electrode is located further away from the pacemaker region, the potential at the electrode's location is more positive than average, resulting in the presence of a positive deflection in the field potential prior to the steep repolarisation.

We then move onto the second major feature of the field potential, the repolarising wave. In Figure 6.7, we show the repolarising wave from Electrodes

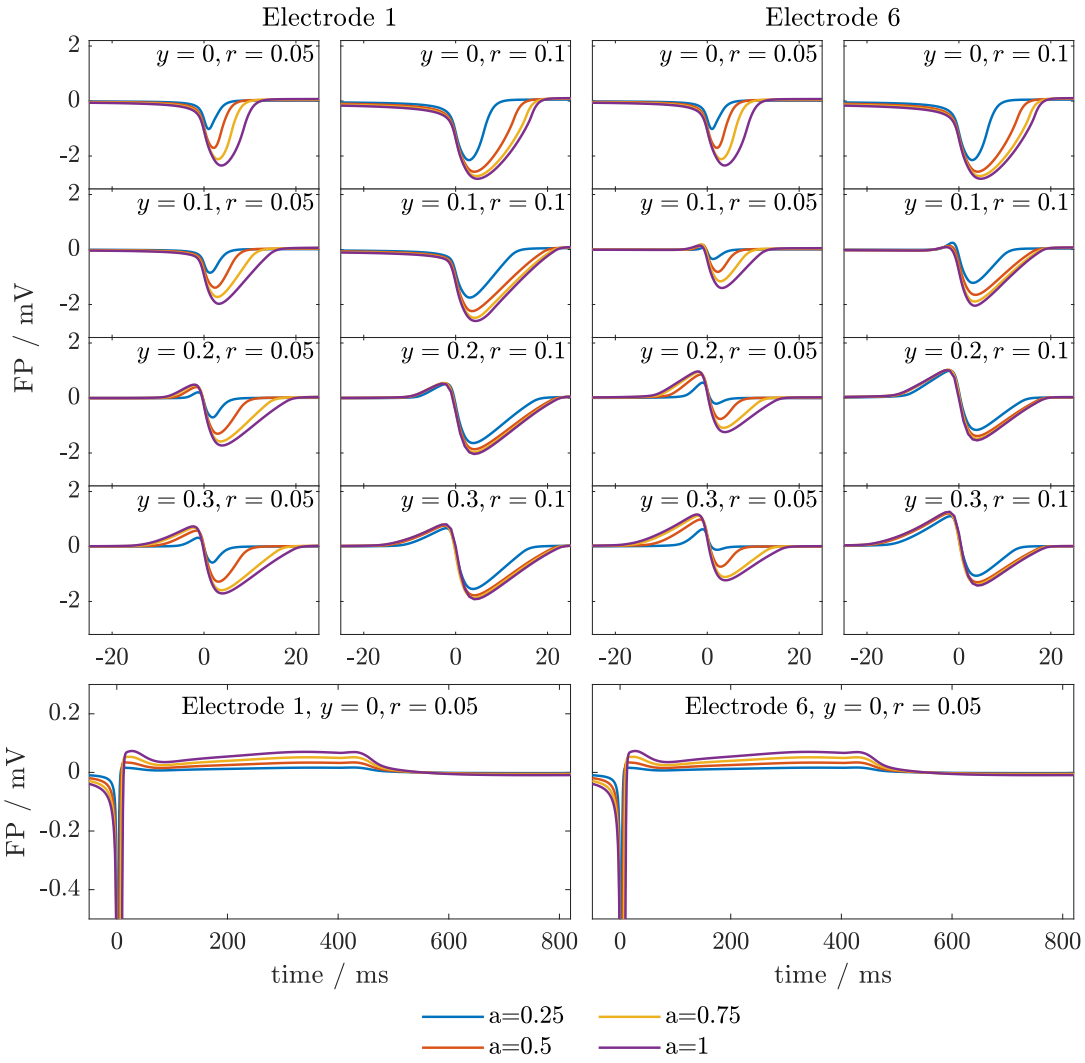

Figure 6.6: Influence of the properties of the pacemaker on the depolarising spike. Top panels show the detail of the depolarising spike as y (the y-coordinate of the centre of the pacemaker region), r (the radius of the pacemaker region) and a (the maximum value of ρ_{A}) are altered. Lower panels show examples of the field potential over the entire beat.

1 and 6. As we previously noted for the depolarising spike, the value of y (and hence the distance between the electrode and pacemaker region) has an important role in the morphology of the wave. When the pacemaker and electrodes are well-separated (i.e. $y = 0.2$ and $y = 0.3$), the repolarising wave is made up of one clear deflection away from zero, and the peak of the wave (which is required for the calculation of FPD) can easily be identified. In contrast, the peak of the wave is harder to identify when the pacemaker region is close to the electrode, and can

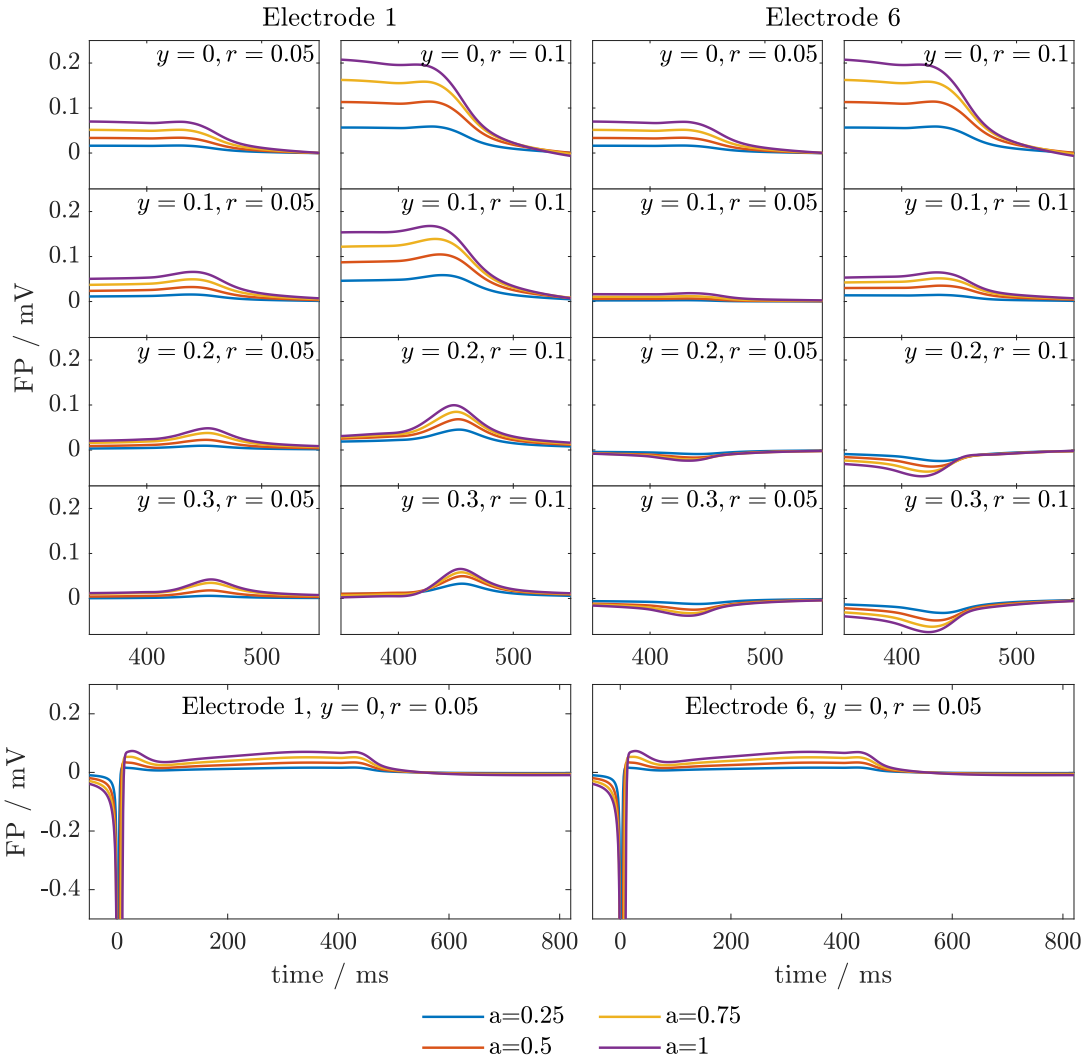

Figure 6.7: Influence of the properties of the pacemaker on the repolarising wave. Top panels show the detail of the repolarising wave as y (the y-coordinate of the centre of the pacemaker region), r (the radius of the pacemaker region) and a (the maximum value of ρ_{A}) are altered. Lower panels show examples of the field potential over the entire beat.

be further complicated by the low amplitude of the repolarising wave when a is small. Low values of a correspond to less variability in phenotype between the pacemaker and remainder of the tissue — there is consequently less variability in the upstroke/downstroke of the action potential across the domain, and this is reflected in the lower amplitudes of the features of the field potential.

The final feature to note is the change in polarity of the repolarising wave between Electrodes 1 and 6 at higher values of y. During repolarisation, positive

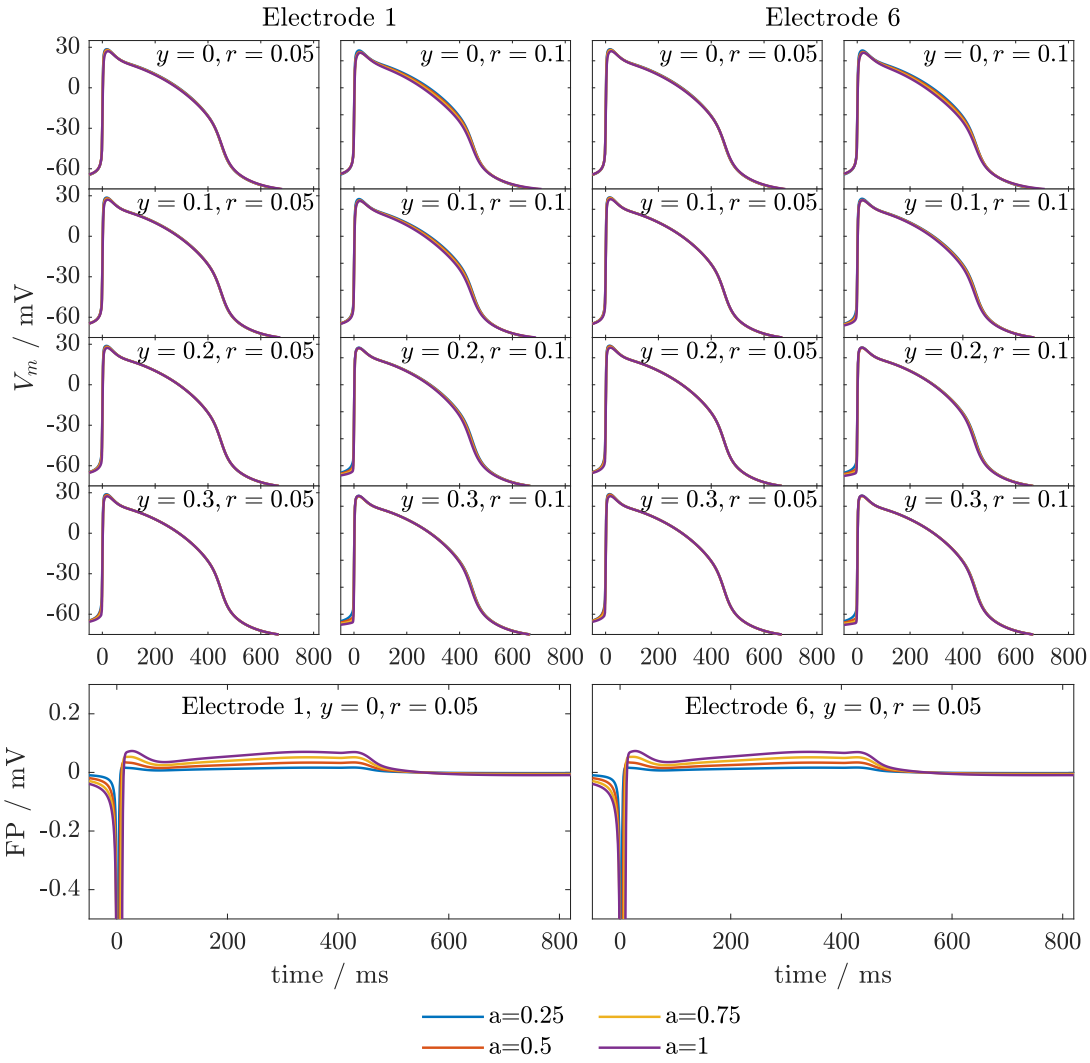

Figure 6.8: Influence of the properties of the pacemaker on the action potential. Top panels show the action potential as y (the y-coordinate of the centre of the pacemaker region), r (the radius of the pacemaker region) and a (the maximum value of ρ_{A}) are altered. For comparison, the lower panels show examples of variability in the field potential across the same time period.

ions flow out of the cells, causing the membrane voltage to decrease. The positive ions increase the potential of the local extracellular region relative to the rest of the tissue, leading to a positive deflection in the field potential. By the time that repolarisation occurs in areas of the tissue further away from the pacemaker (i.e. Electrode 6), the tissue in these areas has lower potential than areas elsewhere, giving the negative morphology of the repolarising wave.

In contrast to the field potential, the action potential shows little variability

as the simulation parameters are altered. Figure 6.8 shows the action potential at Electrodes 1 and 6, presented in the same manner as Figures 6.6 and 6.7. While clear changes in the polarity and form of the field potential were present in Figures 6.6 and 6.7, the changes in the action potential were confined to the shape of the action potential during depolarisation.

6.6 Initial Selection of Phenotype Layout

In the previous section, we saw that the distribution of cellular phenotypes in the hiPSC-CM monolayer has an impact on the form of the field potential. As our eventual goal is to simulate the field potential following the addition of drugs to the MEA, we require a suitable choice of phenotype distribution for these simulations.

From this point of the chapter onwards, we use Gaussian random fields as the basis of our phenotype distribution. The form of the Gaussian random fields that we use in this chapter are based on two parameters; in this section, we therefore perform an initial series of simulations to select parameter values that produce monolayers with activity similar to that observed experimentally. A more detailed study of biomarkers in the selected field parametrisations is carried out later in Section 6.7.

In this section, we simulate monolayers generated with 49 different parametrisations of the Gaussian random field. We examine the activation pattern and conduction velocity, CV, in each monolayer.

The value of CV is correlated to the upstroke velocity of the action potential and the number of gap junctions (and therefore ease of ion flow) between cells, which is represented in simulations by the intracellular conductivity, σ_i. We saw in the previous chapter that CV is also affected by the underlying distribution of cellular phenotype — if the distribution of phenotypes is sufficiently homogeneous and isotropic, the monolayer may synchronise and the CV tends towards infinity. Given the lack of reports of synchronisation from MEA and optical mapping experiments, the value of CV is a useful guide to whether the simulated distribution

of phenotypes is physiologically realistic. We can therefore use CV as a guide to whether the simulated phenotype distribution is a reasonable representation of the physical case.

6.6.1 Description of simulations

Before we select the phenotype arrangements considered in this set of simulations, we must consider what is known from experiments. The monolayers of hiPSC-CMs used in the MEA are often derived from commercial sources — the cells are cryo-preserved by the manufacturers and are thawed prior to plating. Due to this transportation method, it is reasonable to assume some degree of mixing occurs during this process. This assumption is supported from optical mapping studies of hiPSC-CM monolayers where the cells were obtained from commercial sources. Du et al. (2015) reported no phenotypic clustering of biomarkers across the hiPSC-CM monolayers that they studied. This is in contrast to studies of hESC-CMs, where cells are cultured in undisturbed clusters from which spatial grouping of distinct cell types has been reported (Zhu et al., 2016; Vestergaard et al., 2017).

In the previous chapter, we saw that very well-mixed systems of cells of different phenotype would synchronise. As this phenomenon has not been reported in the literature on hSC-CMs, we can conclude that the mixing of phenotypes must be uneven in order to generate steady excitation across the monolayer.

Gaussian random fields for phenotype distribution

Random fields are commonly used to model situations where the values in a field are spatially correlated in some way: they might represent, for example, the porosity of rocks, or the velocity of a turbulent fluid. Recently, they have been proposed as a method of expressing the differences in ionic current across stem cell-derived cardiomyocyte monolayers (Tixier et al., 2018). We extend this suggestion by utilising the value of the random field as the relative contribution of one cell type in the homogenised phenotypes model that we developed in

Parameter	Values						
l_c	0.025	0.05	0.075	0.1	0.15	0.2	0.3
σ	0.05	0.075	0.1	0.15	0.2	0.3	0.4
μ	0.5						

Table 6.3: Parameters of the Gaussian random fields used for setting the ventricular-like proportion across the monolayer. 3 fields were generated for each combination of parameters l_c and σ, giving 147 simulations in total.

Chapter 5.

We refer the reader to Lord et al. (2014, Chapter 7) for details of the definitions of the Gaussian random fields used throughout this chapter, and to Section A3.3 for a description of the field generation algorithm.

The properties of the random fields are influenced by the parametrisation of the covariance matrix used in the fields' construction. We use a Gaussian covariance function, which gives the correlation between any two nodes in the mesh as

$$c_{i,j} = \sigma^2 \exp\left(\frac{(x_i - x_j)^2 + (y_i - y_j)^2}{l_c^2}\right), \qquad \text{for } i = 1, 2, ..., M, \tag{6.10}$$

where M is the number of nodes in the mesh. The two parameters used to generate these entries, the correlation length, l_c, and variance, σ^2, influence the extent of spatial heterogeneity across the simulated domain. Seven values each of l_c and σ were used for the preliminary tests performed in this section.

We generated Gaussian random fields using all combinations of seven values of l_c and seven values of σ, which are listed in Table 6.3. The mean value of the field, μ was kept constant at 0.5, denoting an equal proportion of atrial-like and ventricular-like cells throughout the simulated domain, regardless of how they are mixed. The choice of μ was based on reports that the proportion of ventricular-like cells is close to 50% (Ma et al., 2011). The values of l_c were chosen so that values varied from much smaller than the domain size to comparable to the domain size (past this point, the field would be almost homogeneous across the domain Ω). The parameter σ acts as a scaling factor on the amplitude of the random field. Values were chosen so that at small σ, ρ_{V} remained close to

the mean of 0.5 across the whole field. The upper limit of σ was set such that some regions of fields generated with the highest σ were outside the physiological bounds of ρ_V; these regions were given ρ_V values of 0 or 1, as appropriate.

We note that fields generated with low values of l_c and high values of σ have rather rapid spatial variation, and therefore may be better suited to being simulated using the partitioned phenotypes model discussed in Chapter 5. However, the resolution of the finite element mesh is rather high to start with, so for ease of implementation we use the homogenised phenotypes model for the preliminary set of simulations.

Once the field parameters l_c and σ have been chosen, sampling of the field generates *realisations*: versions of the field that appear different, but have the same statistical properties. A total of 128 realisations of each field were pre-generated, the first three of which were used for the preliminary simulations (giving a total of 147 simulated monolayers). The remainder of the realisations were retained for use in simulations later in this chapter. Examples of selected fields are shown in Figure 6.9.

Simulation parameters

The parameters of the bidomain equations were set as described in Section 6.4 and Table 6.1. An initial condition of $V_m = -70\,\text{mV}$ was applied at all nodes. 10 s of activity was simulated; the analysis of the activation pattern and CV used the field potentials generated during the final simulated beat.

6.6.2 Identification of phenotype distributions with physiologically realistic activation sequences and conduction velocity

The top half of Figures 6.10 to 6.12 shows the ventricular-like proportion, ρ_V, across each monolayer generated with the parameters listed in Table 6.3. Below the ρ_V plots, we show the activation time during the final beat of each simulation. All monolayers spontaneously activated, so the origin of activation varied depending upon the distribution of phenotypes. Activation times are given rela-

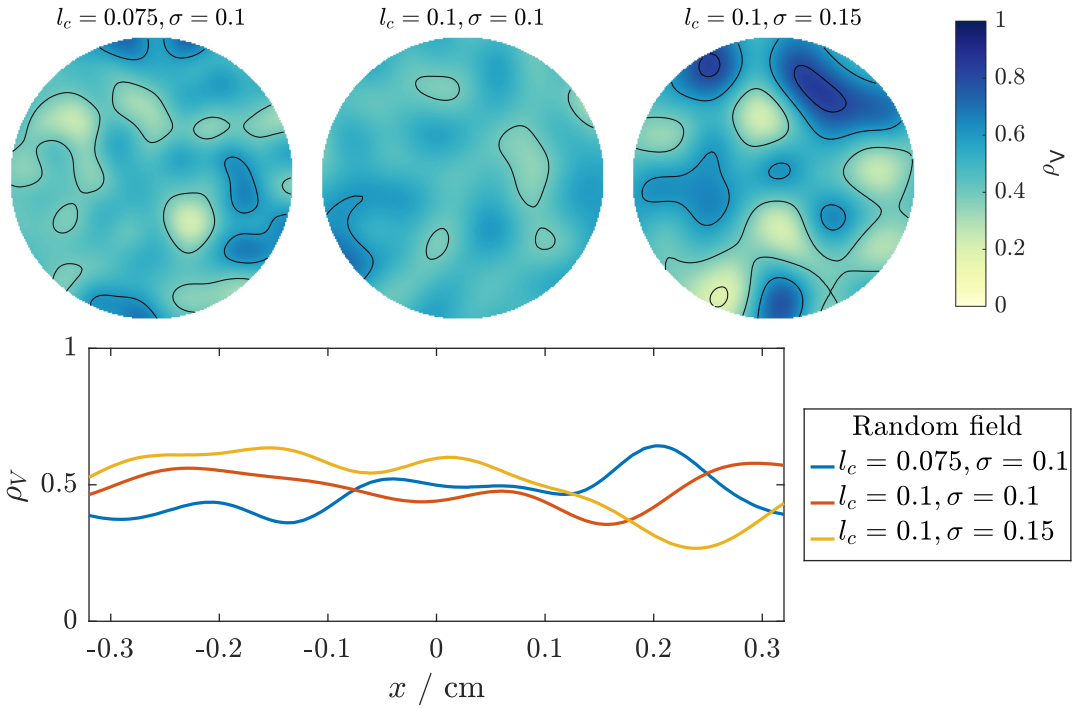

Figure 6.9: Examples of phenotype distributions based on Gaussian random fields. The first realisation of each of three parameter combinations is shown. Contours mark out intervals of 0.2 in the value of ρ_V. The lower plot shows the value of ρ_V along the line $y = 0$. The MEA has a radius of 3.2 mm, with the origin taken to be at the centre (see also Figure 6.2).

tive to the earliest time of activation during the beat. The correlation length, l_c, is varied across the columns of the subplots, and σ down the rows.

Even without calculating numerical values of the CV, it is immediately obvious from the activation time plots that the level of heterogeneity in the phenotype distribution has an impact on the CV. The phenotype distributions with low values of both l_c and σ have little variation in ρ_V and exhibit similar activation times across the monolayer, indicating that they are approaching the synchronised regime. In the majority of the other simulations, a single pacemaker emerges and paces the entire monolayer from one location. There are a few exceptions where dual pacemakers occur, e.g. in the centre plot on the bottom row of Figure 6.10.

We now wish to identify which phenotype arrangements have physiologically realistic values of conduction velocity. Figure 6.13 shows the median values of CV from each monolayer, calculated using data from the eight electrode locations. The polynomial surface fit-based algorithm was used to produce the values used

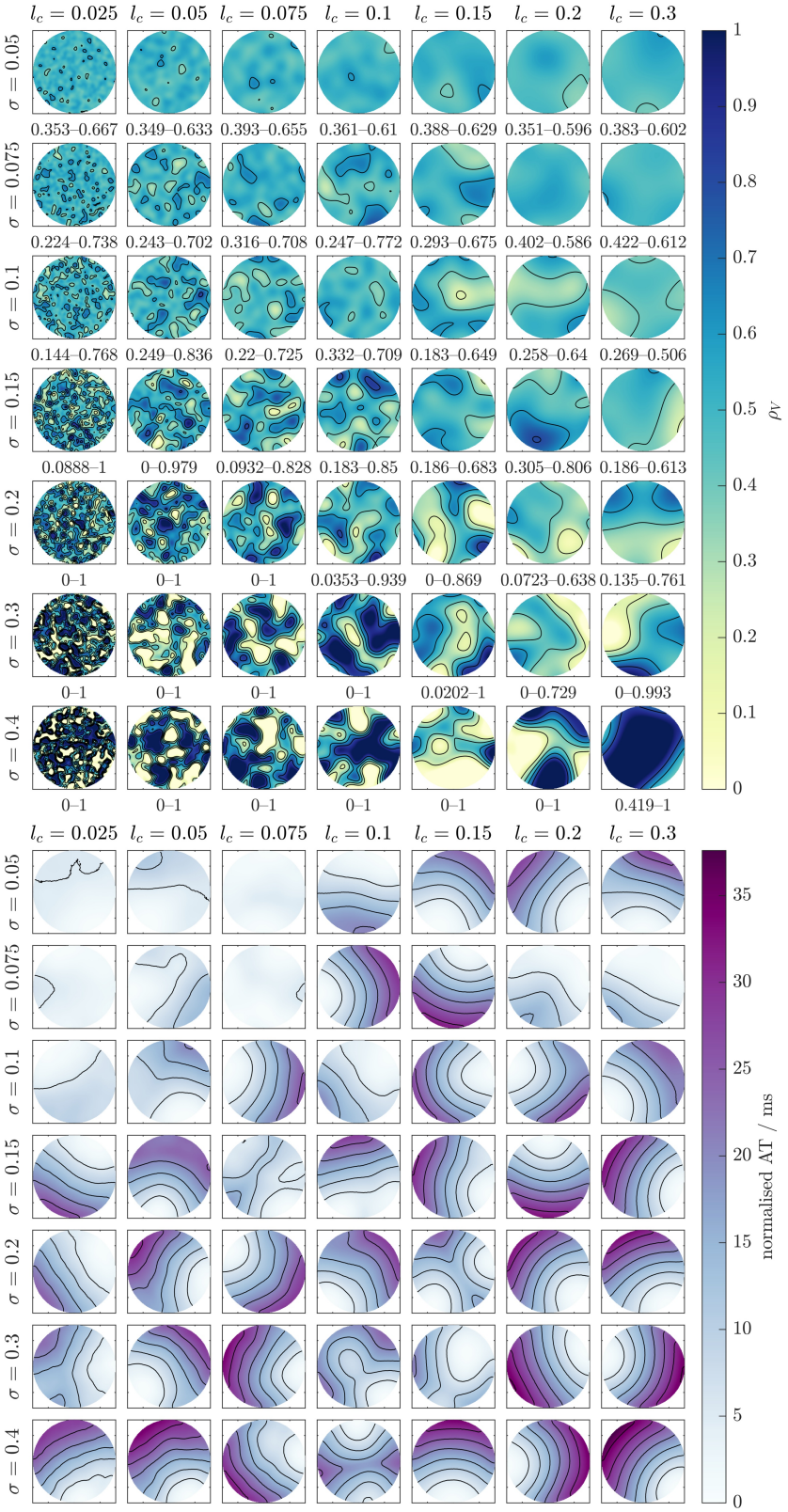

Figure 6.10: Phenotype distribution and activation time (1 of 3). Top: Values of ρ_V based on the first realisation of each Gaussian random field. Minimum and maximum values of ρ_V are indicated below each plot. Bottom: activation times of the final beat in each monolayer.

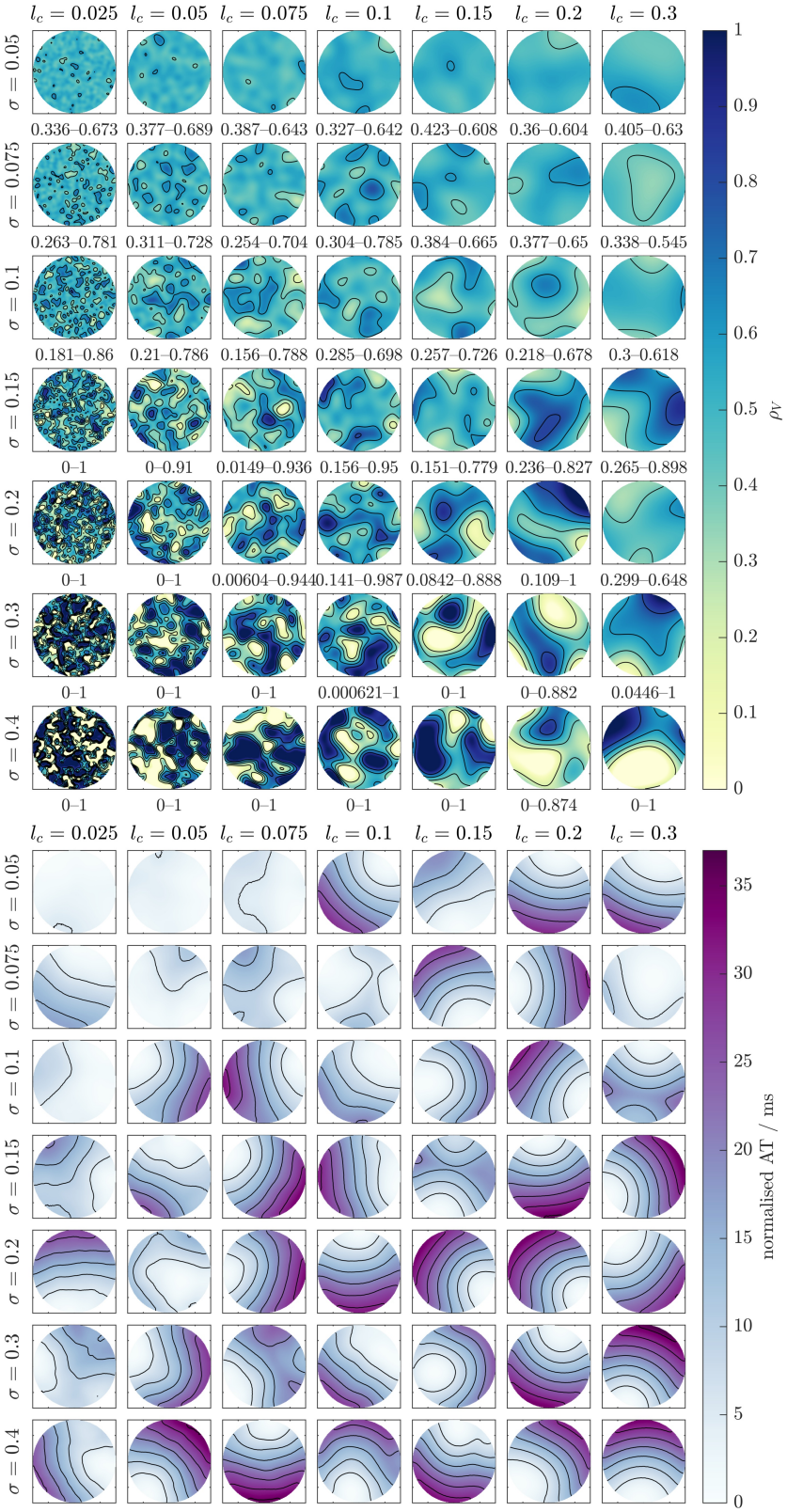

Figure 6.11: Phenotype distribution and activation time (2 of 3). Top: Values of ρ_V based on the second realisation of each Gaussian random field. Minimum and maximum values of ρ_V are indicated below each plot. Bottom: activation times of the final beat in each monolayer.

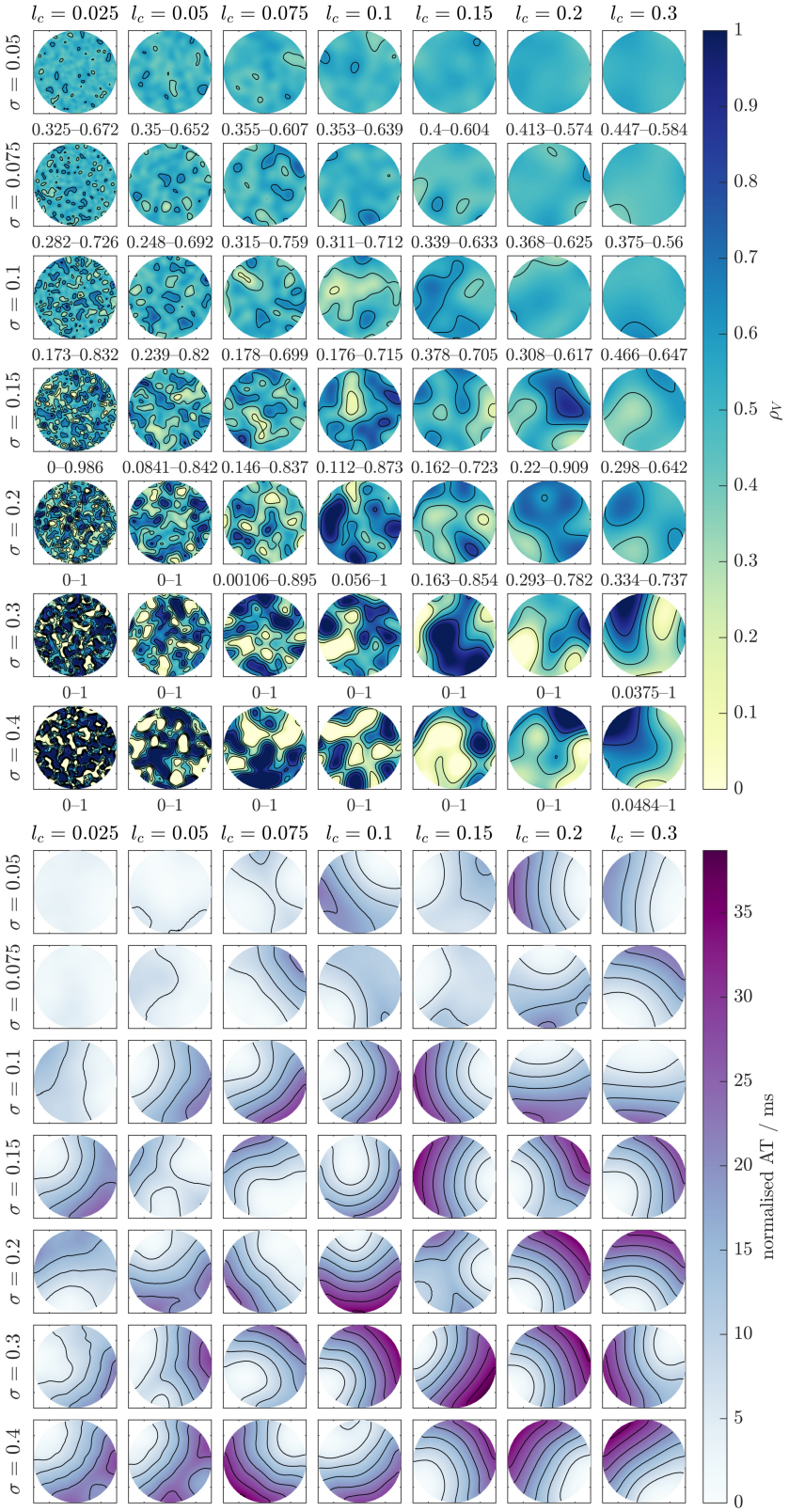

Figure 6.12: Phenotype distribution and activation time (3 of 3). Top: Values of ρ_V based on the third realisation of each Gaussian random field. Minimum and maximum values of ρ_V are indicated below each plot. Bottom: activation times of the final beat in each monolayer.

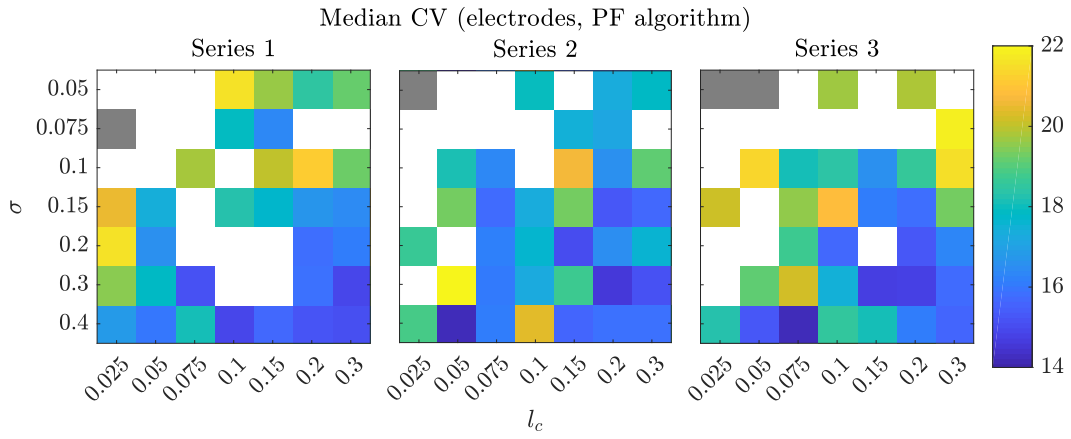

Figure 6.13: Conduction velocity in all simulated monolayers. Each of the three panels summarises the conduction velocities calculated from the monolayers with phenotype distributions shown in Figures 6.10 to 6.12. The same arrangement of l_c and σ is used across all plots. Values above the non-physiological limit of 22 cm/s are shaded white, and grey is used to show where the activation times were so similar that the CV calculation algorithms were unable to calculate a result.

in this figure, but there was very good agreement with those generated using the finite difference-based algorithm.

Figure 6.13 indicates that some combinations of Gaussian random field parameters regularly give phenotype distributions that result in unrealistically high values of CV that tend towards synchronisation. Given the lack of reports of synchronisation across hiPSC-CM monolayers in the literature, we cannot consider such monolayers to be representative of the physical case. The top left corner of each plot in Figure 6.13 is lacking in realistic CV values, suggesting that low values of both l_c and σ are unsuitable for simulations of the MEA. The small changes in ρ_{V} across these types of monolayer indicate that a sufficient amount of heterogeneity is required if rapid activation and synchronisation are to be avoided.

Unrealistic values of CV are regularly generated when $\sigma \leq 0.1$, regardless of the value of l_c. Although some monolayers generated with these parameters do show realistic CV values, this is not consistent throughout the different realisations of the field.

There is also a small region around $l_c = 0.2$, $\sigma = 0.3$, where a dual pacemaker system causes the CV algorithm to calculate a higher than expected velocity. In

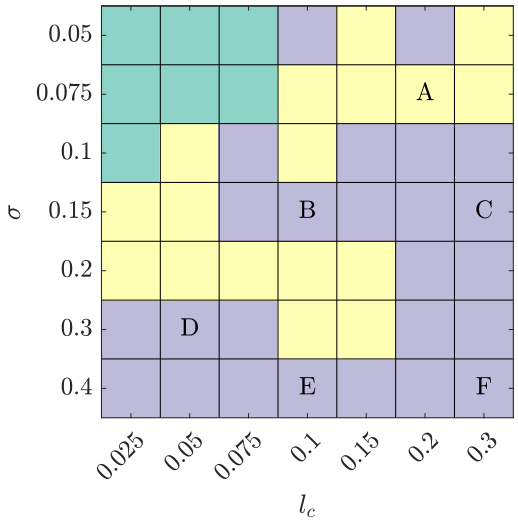

Figure 6.14: Gaussian random field parameters that produce realistic values of conduction velocity. Purple/Yellow/Green: all/one or two/none of the three tested field realisations gave realistic CV values. Pairs of l_c and σ carried forward for further simulations are marked with letters that denote the labels used in the next section.

these cases, two different pacemakers emerge, one on either side of the monolayer. The region where the electrodes are located therefore experiences two activation waves arriving from opposite directions. With very similar activation times across the electrode region, and only eight data points, the calculated CV values are consequently higher than would be expected from their activation time plots, where the contours are spaced at similar intervals to those in other simulated monolayers. Dual pacemaker systems have not been directly reported in the literature on hiPSC-CM monolayers, so at the present time it is unclear whether these random fields should be considered representative of the experimental case.

6.6.3 Choice of phenotype distribution for further investigation

From our analysis of CV in the different monolayers, we have determined that some values of l_c and σ regularly result in monolayers with very high values of CV that tend towards synchronisation. We summarise the values of l_c and σ that give monolayers with physiologically consistent values of CV in Figure 6.14.

Figure 6.14 indicates that a substantial fraction of the tested parameters do re-

sult in monolayers with physiologically reasonable CV values. We have therefore selected a subset of the fields that may be considered viable for further analysis. These are marked over the relevant parameter sets in Figure 6.14. These particular pairs of parameters were selected to provide good coverage of the range of l_c and σ where realistic CV values were observed. The number of parameter pairs was limited to six so that computational time could be invested in detailed investigation of these pairs.

6.7 Investigation of Biomarker Variability in Simulated and Experimental Monolayers

In the previous section, we demonstrated that a wide selection of phenotype distributions based on Gaussian random fields could produce field potentials with biomarkers that fell within physiological ranges. We now perform a more detailed investigation of the variability in biomarker values for monolayers with phenotype distributions based on different realisations of the same random field, and compare to experimental data in control (drug free) conditions.

6.7.1 Description of simulations

We simulated 10 s of activity in monolayers with phenotype distributions based on the values of l_c and σ determined in the previous section and marked in Figure 6.14. As we have narrowed down the range of parameters, there were fewer fields to investigate; we consequently simulated many more realisations of each. Having previously simulated the first three realisations of each field, we now simulated another 12 of each, giving 15 realisations in total for each field.

6.7.2 Variability of biomarkers

In Figure 6.15, we plot a sample field and action potential from each simulation, taken from Electrode 1 at the upper left corner of the electrode grid. Clearly, there are great amounts of variability in the signal morphology. While we focus

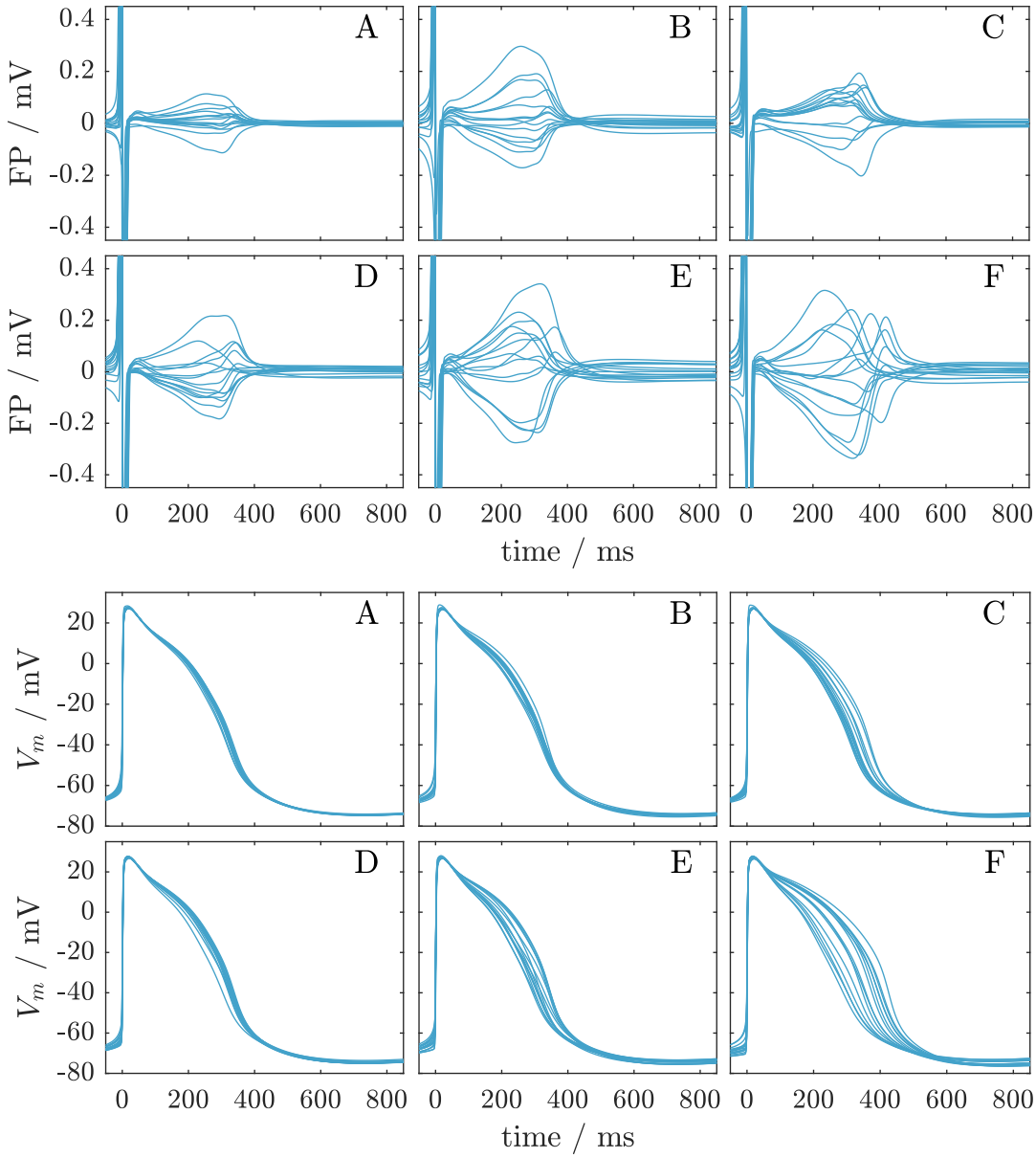

Figure 6.15: Field and action potentials from simulated monolayers with different phenotype distributions. Signals are shown from 15 realisations of each of the six fields selected in Section 6.6. The labels in the top right refer to the combinations of l_c and σ selected for further analysis in Section 6.6.3 and Figure 6.14.

on the field potential in our discussion here, it is also useful to note that the amount of variability in the action potential is linked to the parametrisation of the Gaussian random field used to determine the phenotype distribution. Fields with low σ exhibit little variability in the action potential, while at high σ, the action potential varies between more extreme atrial-like and ventricular-like morphologies.

In Figure 6.16, we plot the values of the conduction velocity, beat rate, spike amplitude, repolarising wave amplitude, field potential duration and corrected field potential duration in each of our simulated monolayers and from the control stages of the MEA studies carried out by our collaborators at Axion Biosystems.

Conduction velocity

The values of conduction velocity from simulations and experiments plotted in the top left panel of Figure 6.16 were calculated using the algorithm based on the polynomial surface fit-based method described in Section 6.2.3.

Values of CV are generally consistent between the experimental and simulated results, with the only notable exception being one data point from a monolayer generated with random field parametrisation A. On further investigation, this high CV value was found to arise due to two pacemaker regions being present in the simulated monolayer, leading to more rapid than usual activation in the central region where the recording electrodes are located. This may also be the case for monolayers with notably high values of CV in the experimental dataset, but without additional data on the activation sequence across the monolayers, it would be premature to conclude that a dual pacemaker system is responsible.

CV is primarily influenced by the intracellular conductivity, σ_i, which sets the ease with which the potential passes through the intracellular domain, and also by the upstroke velocity of the action potential model through the formulation of I_{Na}, the fast sodium current. The value of σ_i, was calibrated at the start of this chapter so that CV values consistent with experimental data were produced; our observation of a good match between the mean values of CV in the experimental and simulated datasets is therefore not particularly surprising.

Beat rate

The beat rate of simulated datasets was calculated using the Matlab code described in Section 6.2.3, while that of the experimental datasets was obtained from Axion Biosystems' own analysis pipeline. Beat rate is shown in the top

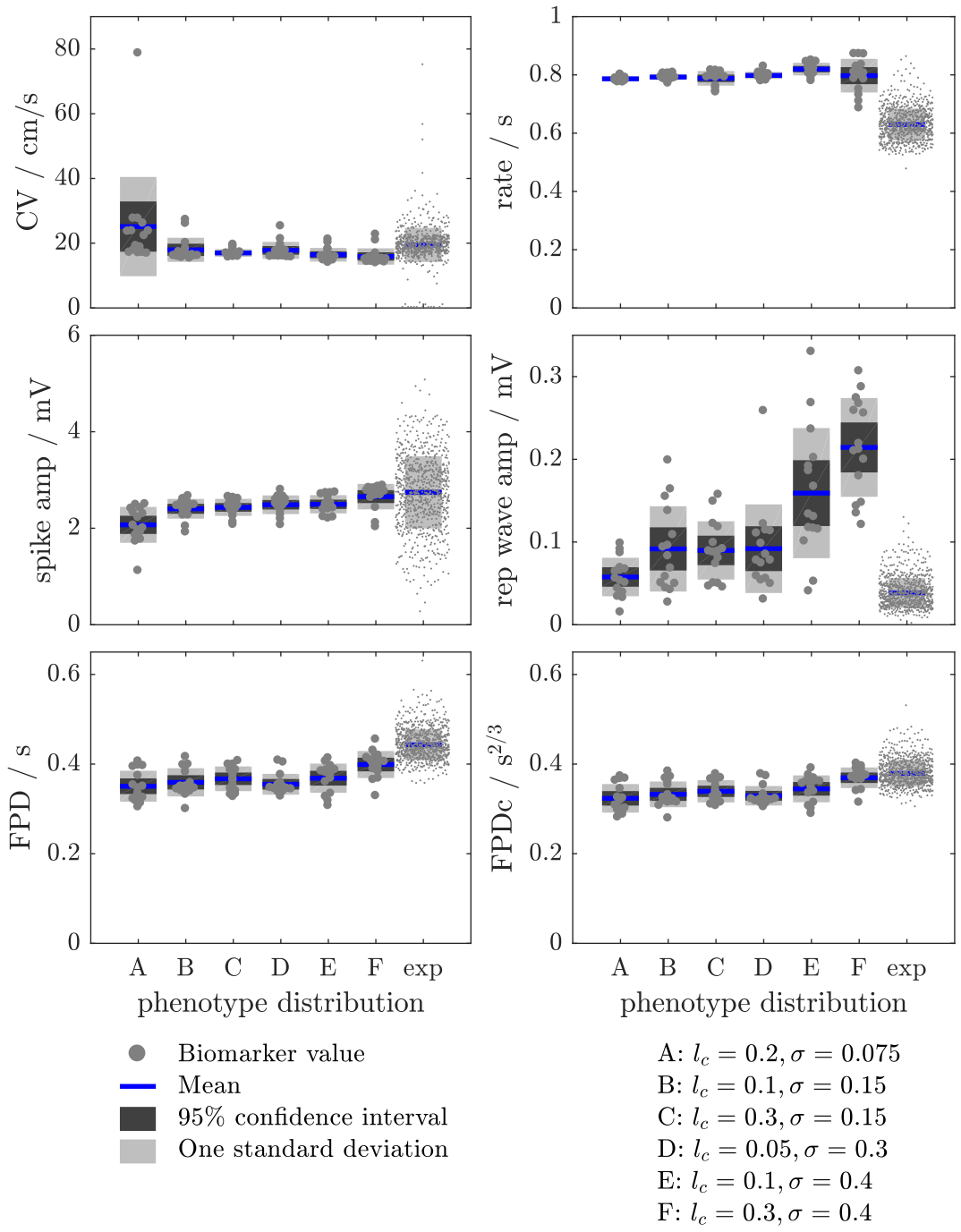

Figure 6.16: Variability in biomarkers from simulated and experimental data. Each panel shows the values of a different biomarker from the six simulated random fields (labelled A–F; see captions at top right for field parameters) and the experimental data under control conditions (labelled exp). The values of the biomarkers from each simulation/experiment are shown as grey points. Summary statistics of the mean, 95% confidence interval and one standard deviation are displayed using coloured lines or boxes.

right panel of Figure 6.16.

The beat rate of all simulated monolayers is noticeably faster than the experimental case, indicating that a useful branch of future work would be to undertake a closer analysis of pacemaker mechanisms within hiPSC-CM monolayers. In simulations with higher values of σ, the level of variability is closer to that observed experimentally.

The beat rate can be influenced by two factors: the properties of the cellular electrophysiology model and the phenotype arrangement. The combination of these two factors determines which regions of the monolayer act as pacemakers. We saw earlier in Figures 6.10 to 6.12 that large regions with a high proportion of the atrial-like cell model (and therefore the fastest intrinsic beat rate) often acted as the pacemaker in the simulated monolayers. The beat rate of the entire monolayer is therefore set by the pacemaker region.

There are several mechanisms by which the fast beat rate in the simulated monolayers could have occurred. We have so far assumed that the properties of the hiPSC-CM monolayer are well-represented by the Paci et al. (2013a) models of atrial-like and ventricular-like cellular electrophysiology, both of which spontaneously activate. However, beat rate has also been reported to slow as the cells mature (He et al., 2003). A parametrisation of the cellular electrophysiology model for more mature cells could therefore provide us with a means of slowing down the overall beat rate of the monolayer. Other options are considered following the discussion of FPD and FPDc.

Spike amplitude

The spike amplitude is plotted in the middle left panel of Figure 6.16. As for the beat rate, the spike amplitude of the simulated data was calculated using Matlab code, while that of the experimental data was calculated by Axion.

The mean simulated spike amplitude is a good match with the experimental case, but we do see a substantial difference in the amount of variability. This can perhaps be attributed to the quality of the cell-electrode contact and the filter-

ing methods used on the experimental data, and also the effects of the reference electrode, which we have not explicitly modelled in our simulated monolayers. Alternatively, the parametrisation of the sodium current in the cellular electrophysiology model may require further development, as discussed above for the FPD, FPDc and spike amplitude.

Repolarising wave amplitude

As the amplitude of the repolarising wave is not routinely calculated for pharmaceutical safety studies, values of the biomarker from both the simulated and experimental data were calculated following the description in Section 6.2.3. Values of the repolarising wave amplitude are plotted in the middle right panel of Figure 6.16.

In contrast to many of the other biomarkers, the values of and variability in repolarising wave amplitude are substantially influenced by the amount of variability in the underlying cellular phenotype. Fields E and F, both of which have the highest value of σ used in this study, exhibit significantly higher amplitudes than the experimental dataset. This effect can also be seen in Figure 6.15. The extent of this difference points to the other fields, parametrisations A–D, being a better representation of the spatial distribution of cellular phenotypes than field parametrisations E and F. We shall therefore focus a little more on fields A–D in some of our future simulations, but still retain E and F.

Field potential duration and corrected field potential duration

Field potential duration and the rate-corrected form of the same biomarker are shown in the lower two panels of Figure 6.16. The values of the biomarker in the simulated datasets were calculated using the previously described Matlab code, while in-house software from Axion Biosystems was used to derive the experimental values.

While there is a clear difference between the FPD of the simulated and experimental datasets, it is not so pronounced as that of the beat rate. Levels of

variability, however, are similar between the experimental and simulated datasets, and the difference is not so pronounced once the correction for beat rate is applied to yield the FPDc.

There are several mechanisms by which a small change in FPD could be achieved in order to bring the simulated case better into line with the experimental data, which could form interesting options for future work. Higher values of the mean value of ρ_{V} in the monolayer, μ, would be one option, as would be alterations to the repolarising currents in the Paci et al. (2013a) model. Both of these approaches would assist in parametrising the model for a given batch of cells — the proportions of the cellular phenotypes (and therefore μ) are likely to differ to a certain extent, and the action potential is known to be affected by the maturity and culture conditions of the cells.

6.7.3 Discussion

In several of the biomarkers, CV, spike amplitude and FPDc, a good match is achieved between the mean value of the biomarker in the simulated and experimental cases. While the simulated beat rate and FPD biomarkers were generally outside the range of the experimental case, the difference is not particularly great and future improvements to the model, both on the cellular and tissue scale, should be able to improve the agreement. The amplitude of the repolarising wave is particularly interesting in that it is the only biomarker which showed substantial differences in mean value and amount of variability between the different random field parametrisations. Field A is particularly promising in this regard, as the small amplitude provides the best match to the experimental data. Many of the biomarker values generated by fields B, C and D also fall into the experimental range, although they exhibit greater variability in their value.

At this stage, we have performed no additional tailoring of the Paci et al. (2013a) model to our experimental data, and so the differences between simulated and experimental FPD and beat rate values are not entirely unexpected. Nevertheless, we do see good qualitative agreement. All simulated biomarker

values are close to the experimentally observed range and the activation patterns match those often reported in experiments: we observed steady activation waves from a single, stable, origin in all but one of the monolayers we studied in Section 6.7. Interestingly, we see a few high CV values in our experimental dataset, which could feasibly also be due to the presence of multiple pacemaking sites.

The properties of hiPSC-CM action potential morphology have been reported to vary depending on culture density (Du et al., 2015) and maturation (Lundy et al., 2013); properties which are not included in the cellular electrophysiology model at this time. Work on tailoring cellular electrophysiology models to a particular batch of cells is underway as part of a collaboration between the University of Oxford's Computational Biology group and Roche (Basel, Switzerland); this type of approach is likely to provide improvements to the cellular electrophysiology models and therefore simulated biomarker values in the coming years (Lei et al., 2017).

6.8 Conclusions

In this chapter, we have examined the electrophysiological properties of hiPSC-CM monolayers with different distributions of atrial-like and ventricular-like phenotype.

We have shown that the morphology of the field potential is affected by the location of the pacemaker region in relation to the recording electrodes. In particular, the depolarising spike lacks an initial depolarisation phase when the field potential is examined close to the pacemaker. The polarity of the repolarising wave is affected by the proximity to the pacemaker and the repolarisation state of the rest of the monolayer at that time. We also observed how the size and the mix of phenotypes present in the pacemaker affect the magnitude of the repolarising wave.

We then used Gaussian random fields, generated with different input parameters, as the basis for the phenotype distributions of the simulated monolayers. Having tested a range of values of the correlation length, l_c, and the variance,

σ^2, we selected a range of parameters for further investigation. Use of Gaussian random fields for the phenotype distribution can produce monolayers with variability in biomarker values similar to that observed experimentally, although it is not yet possible to clearly identify one of the random field parametrisations as giving a consistently better match to the experimental biomarkers. Based on the repolarising wave amplitude, we can suggest that greater consideration be given to fields A–D, and particularly A, over E and F.

While we see differences in the mean values of beat rate and FPD between the experimental and simulated cases, we do achieve a good qualitative fit to the experimental data. We note that investigations of the effects of drugs consider the percentage change in biomarker values rather than the absolute values; our qualitative model is therefore a good starting point for such simulations.

We now move on to simulations of the cardiac safety assessment procedure using the MEA. Throughout this chapter we have seen how the arrangement of phenotypes has affected the field potential; we now turn our attention to the impact of the phenotype arrangement on the biomarkers of the MEA as the action of ion channel-blocking drugs is simulated, and an assessment of how well our model performs under such conditions. In Section 6.7.3, we noted that improvements to the cellular electrophysiology model and tissue-scale aspects of our micro-electrode array simulations are required if the properties of our simulated field potentials are to be quantitatively representative of the experimental case. By extending our study beyond control conditions, we are able to identify specific aspects of the model that are in need of further calibration against experimental data and comment on the impact of phenotypic variability on the field potential biomarkers.

Chapter 7

Investigation of Drug Action on Monolayers Containing Multiple Cellular Phenotypes

In Chapter 6, we examined how variability in cellular phenotype across stem cell-derived cardiomyocyte monolayers affected the values of biomarkers derived from simulated micro-electrode array recordings. We used the homogenised phenotypes model from Chapter 5 to represent the presence of variable cellular phenotypes. The ionic currents in the homogenised regions were represented by a weighted average of the contributions from atrial-like and ventricular-like models of human induced pluripotent stem cell-derived cardiomyocyte (hiPSC-CM) electrophysiology (Paci et al., 2013a).

We now utilise the model developed in Chapter 6 in a more applied context. The micro-electrode array (MEA) assay is a promising tool for the safety assessment of new drugs, and is set to become more widely used following the current proposals of the Comprehensive *in vitro* Proarrhythmia Assay initiative. In this chapter, we build upon our previous simulations of the electrical activity in hiPSC-CM monolayers to include the effects of drugs. We study the qualitative behaviour of the system, by investigating how well our model performs in terms

of predicting the trend and magnitude of changes to biomarkers derived from the field potential as the influence of ion channel-blocking drugs are simulated. We also examine how variability in the underlying distribution of cellular phenotypes contributes to the values of, and variability within, the biomarker values derived from the simulations.

We use the results of these simulations to guide our recommendations for future work on the individual components that make up our model of the micro-electrode array, and comment on how the introduction of phenotypic variability within our simulated monolayer relates to that observed experimentally.

7.1 Chapter Outline

Before starting the more complex tissue simulations, we first investigate the effects of two well-studied drugs on a single-cell model of hiPSC-CM electrophysiology in Section 7.2. This series of simulations demonstrates how the action potential adapts over time to the action of a drug. The results of this preliminary study influence the manner in which we implement the effects of ion channel blocking drugs on the monolayer.

We then return to simulations of the MEA, this time including the effects of ion channel block. In Section 7.3, we describe the implementation of the action of ion channel-blocking drugs on our bidomain simulations. We first consider the action of six hypothetical specific channel blockers in Section 7.4. By blocking one specific ion channel in each simulation, we are able to see how each ionic current influences the action and field potentials. We then develop the simulations further in Section 7.5, where we consider the action of three real drugs which block a range of single or multiple ion channels. We compare our simulations to experimental data provided by our collaborators at Axion Biosystems.

In Section 7.6, we summarise our findings on the ability of our simulations to capture the changes to and levels of variability in the biomarkers that have been reported from experimental MEA studies. Having evaluated the performance of our model, we then propose improvements that could be made in the future.

7.2 Drug Action on Stem Cell-Derived Cardiomyocytes

We open this chapter with a preliminary study of the effects of two well-studied drugs on the Paci et al. (2013a) model of ventricular-like hiPSC-CM electrophysiology. Upon simulating a drug's mechanism of action, the action potential does not immediately settle to a steady state. A study of this timecourse is therefore necessary before we can proceed with the tissue simulations later in this section, where the computational complexity of the simulation is such that it is important that reaching steady state takes as short a time as possible.

7.2.1 Implementation of ion channel block

We implement the action of a drug on a given ion channel using a simple pore-block model (Yifrach, 2004; Brennan et al., 2009). This model does not consider the effects of the drug on ion channel kinetics, but is nevertheless widely used throughout cardiac modelling studies (Mirams et al., 2011; Zemzemi et al., 2013).

The pore-block model scales the conductance, g, of an ion channel by a function dependent on two parameters: the IC_{50} value and the Hill coefficient. The IC_{50} value is the concentration at which the conductance of that channel is reduced to half of its original value, and the Hill coefficient is a measure of how many ion channels are, on average, blocked by each drug molecule. For ion channel i, the conductance following the addition of a drug can be expressed as

$$g_i = g_{i,\text{control}} \left(1 + \left(\frac{[D]}{[\text{IC}_{50}]_i} \right)^h \right)^{-1}, \tag{7.1}$$

where $[D]$ is the concentration of the drug and h is the Hill coefficient.

7.2.2 Description of simulations

In this preliminary study, we simulated the electrophysiological properties of a unit patch of hiPSC-CM cell membrane, which was represented by the ventricular-like cellular electrophysiology model of Paci et al. (2013a). The model is comprised of a system of ordinary differential equations which may be solved to

Drug	g_{CaL}		g_{Kr}		Concentration / nM			
	IC_{50}/nM	Hill	IC_{50}/nM	Hill	1	2	3	4
Cisapride	–	–	12	1.3	3.2	10	32	100
Terfenadine	700	0.7	19	0.6	1	10	100	1000
Diltiazem	112	0.7	6569	0.8	10	100	1000	10000

Table 7.1: Ion channel-blocking properties of Cisapride, Terfenadine and Diltiazem. The concentrations listed in the table are those used by Axion Biosystems for their CiPA validation study. IC_{50} and Hill coefficients are taken from Crumb Jr. et al. (2016). Cisapride and Terfenadine were used for the investigation into the initial conditions described in Section 7.2, and all three listed drugs were used for the monolayer simulations in Section 7.5.

yield the membrane voltage; this type of system was described previously in Section 3.2. The simulations were carried out using Chaste, which utilises CVODE, an adaptive ODE solver from the SUNDIALS software suite, to solve the cellular electrophysiology model.

Initial conditions of the model were set as listed in the supplement of Paci et al. (2013a). 600 s of activity were simulated under control conditions to allow the model to reach steady state.

The effects of two well-studied drugs, Cisapride and Terfenadine, were then introduced. Four further simulations were performed for each drug, with each simulation demonstrating the effect of the drug at one of the four concentrations tested in the experiments performed by Axion Biosystems, as listed in Table 7.1. At the start of the simulation for each of the four concentrations, the model was initialised with the final state of the control simulation described above. The ion channel conductances were then modified using the pore block model in equation (7.1) and the IC_{50} values and Hill coefficients from Table 7.1 to implement the effect of the drug. A further 600 s of activity were then simulated.

7.2.3 Results

To determine how the morphology of the action potential changed as the model settled to a steady state, we examined the action potential duration over the simulated timecourse. We considered the APD_{90}, the time taken for the mem-

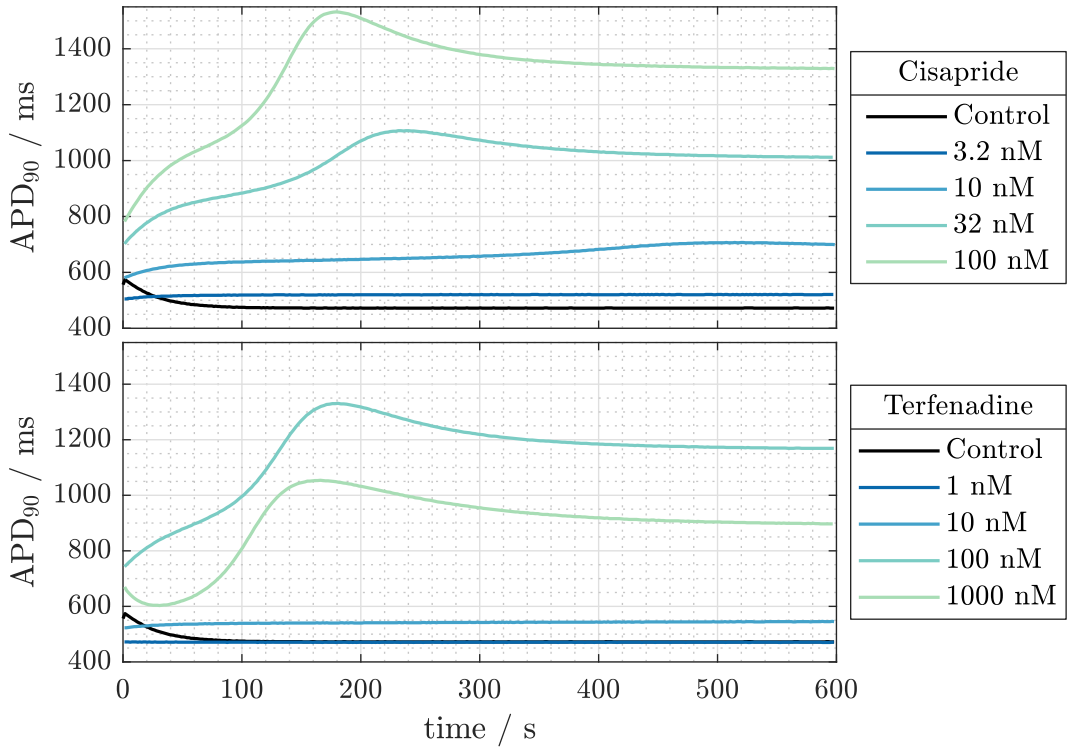

Figure 7.1: Simulated addition of Cisapride and Terfenadine to a single cell. The APD_{90} at each beat during the 600 s simulation is plotted. Simulated drug concentrations match those used in the experimental study of Axion Biosystems.

brane voltage to return to 90% of its minimum value following the upstroke of the action potential (see Figure 2.4 on page 15 for an example).

Cisapride

The APD_{90} of each beat of the ventricular-like Paci et al. (2013a) model is plotted in the top panel of Figure 7.1. While the APD_{90} of the control and lower two concentrations move close to their steady state value after around a minute, this is not the case at the higher two concentrations. At 32 and 100 nM of Cisapride, the APD_{90} overshoots its steady state value, taking over three minutes to settle to steady state following the overshoot.

Terfenadine

The dynamics of the APD_{90} following the addition of Terfenadine are similar to those observed with Cisapride. Again, Figure 7.1 demonstrates that steady state

is quickly reached at the lower concentrations, while the APD_{90} at the higher two concentrations takes around 8 minutes to approach steady state. Interestingly, the APD_{90} at 100 nM undergoes an initial decrease prior to overshooting above the steady state value.

7.2.4 Implications for tissue-scale simulations

It is clear that the extent of the changes to ion channel conductances at higher simulated concentrations lead to the single cell model requiring a long simulated time to reach steady state. The tissue simulations that we consider in the remainder of this chapter are far more computationally expensive to run, and it is therefore important that we ensure that the tissue-based system reaches steady state in a short amount of time. We therefore set the initial conditions of the cellular electrophysiology ODE systems to the steady state under drug block before using them in tissue-scale simulations, as described in the following section.

7.3 Model of Drug Action on Monolayers with Spatially Varying Phenotypes

In this section, we describe aspects of the monolayer simulation that have been changed or added since Chapter 6. The geometry of the 96-well MEA plate, the finite element meshes and cellular electrophysiology model were described in Section 6.4.

7.3.1 Variability in phenotype across the monolayer

Spatial heterogeneity in the cellular phenotype was modelled by setting ρ_V, the proportion of the ventricular-like cellular electrophysiology model, to the value of a Gaussian random field. We utilised the six random field-based phenotype arrangements (referred to as A–F) that we studied under control conditions in Section 6.7. The parameters of the six random fields are listed in Table 7.2.

In Section 6.7, we noted that fields A–D exhibited repolarising wave ampli-

Parameter	Values					
	A	B	C	D	E	F
l_c	0.2	0.1	0.3	0.05	0.1	0.3
σ	0.075	0.15	0.15	0.3	0.4	0.4

Table 7.2: Parameter values of the six Gaussian random fields A–F. These six parametrisations of the random field were selected for further investigation in Chapter 6. For further details, see Section 6.6. l_c is the correlation length, in cm (for comparison, the diameter of the monolayer is approximately 0.6 cm), and σ is a measure of the amount of variation in the field value.

.

tudes that were far closer to the experimental values than fields E and F. Some of the discussion of our simulations therefore focuses on an isolated example from one of these four fields when a closer look at a single field potential is useful.

7.3.2 Simulation of different drug concentrations

The MEA safety assessment assay at Axion Biosystems is performed by comparing the field potentials under control and dosed conditions. Initial recordings are gathered from all wells under control conditions. One of the four concentrations of the drug to be tested is then added to a number of the wells, and recordings of the field potential under these dosed conditions are gathered.

We have two methods by which we can implement the experimental procedure in our simulations, which are shown in Figure 7.2. In the previous section, we noted that it could take several minutes for a single simulated cell to reach steady state following the application of a drug. If we use default control initial conditions for the action potential model, we would have to simulate the electrical activity in the monolayer for several minutes before it would reach steady state. This would substantially increase the computation time. So instead we implement the steady-state action of the drug as part of the initial conditions for the action potential model.

Once initialised, 15 s of activity was simulated. This is longer than the 10 s simulated in the previous chapter to ensure that several beats were simulated even if the drug had a substantial slowing effect on the beat rate.

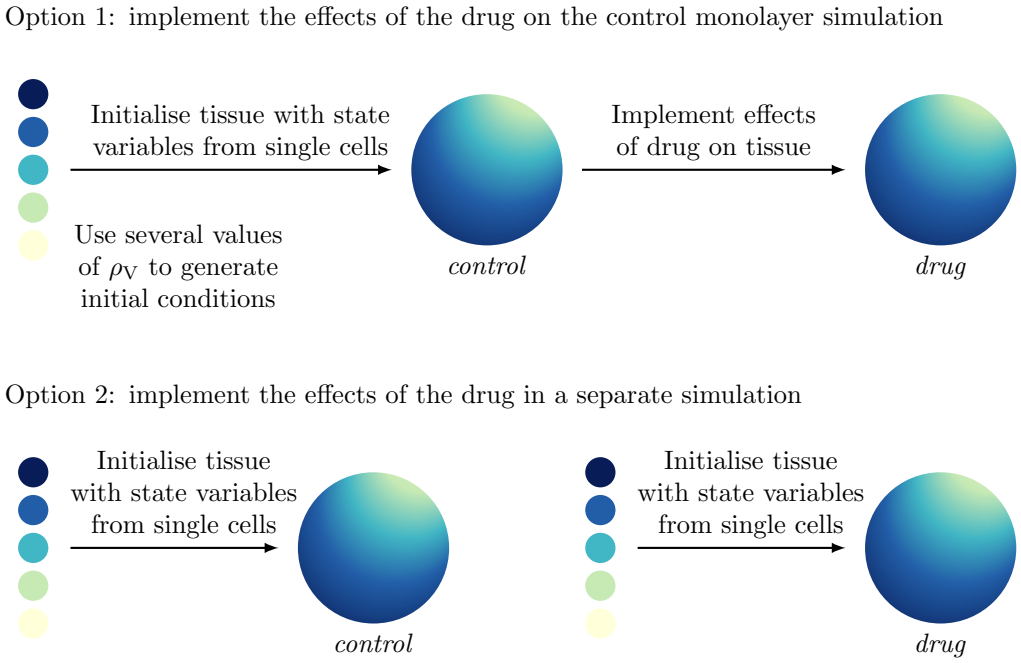

Figure 7.2: Methods for setting up a monolayer simulation with the effects of a drug. Option 1: the changes in conductance values due to the action of a drug can be applied directly to the monolayer. Option 2: alternatively, the initial conditions of the simulation can be prepared under the effects of a drug. The control and drug simulations are performed separately.

Initial conditions

The initial conditions of the cellular electrophysiology model vary from those described before in that the simulated effect of each drug is now taken into account.

As described previously, initial conditions were generated for a range of values of ρ_V, the proportion of the ventricular-like model. The membrane voltage was simulated for 600 s under control conditions, after which the effect of the selected drug at a particular concentration was applied by altering the relevant ion channel conductances according to equation (7.1), the IC_{50} values and Hill coefficients.

A further 600 s of activity was then simulated to allow the action potential to reach steady state. The initial conditions for the tissue simulation were then obtained by selecting the state variables at the time at which the membrane voltage increased past −70 mV during the depolarising phase of a spontaneous action potential. If the effects of the simulated drug were such that the membrane voltage did not fall below −70 mV, the initial conditions were instead taken at

the lowest value of the membrane voltage (typically still below $-65\,\mathrm{mV}$ in such cases).

Having obtained initial conditions for a range of ρ_V values, the instances of the cell model at the nodes of the finite element mesh were then set to have state variables based upon these initial conditions. If the value of ρ_V at the node did not exactly match the ρ_V of one of the pre-generated sets of state variables, linear interpolation was used to generate a suitable set of state variables for the initial conditions.

7.4 Hypothetical Specific Blockers

In this section, we examine the impact of the blocking of six ion channels individually on the activity of a simulated monolayer in the MEA.

7.4.1 Description of simulations

The six ion channels that we consider are those selected by the CiPA initiative for early-stage screening in the safety assessment process. We therefore reduced the values of the following conductances by 50% and 100%:

- g_CaL, L-type calcium,
- g_K1, inward rectifier (potassium),
- g_Kr, rapid delayed rectifier[1] (potassium),
- g_Ks, slow delayed rectifier (potassium),
- g_Na, fast sodium, and
- g_to, transient outward (potassium).

The simulation itself was performed as described in Section 7.3. Biomarkers were then calculated from the field potential at the locations of each of the eight electrodes. Methods for calculating the biomarkers used in this section (conduction velocity, beat rate, spike amplitude, field potential duration and corrected field potential duration) were described previously in Section 6.2.3.

[1]The rapid delayed rectifier current is also commonly referred to as the hERG current, after the human ether-à-go-go gene which encodes the structure of the ion channel.

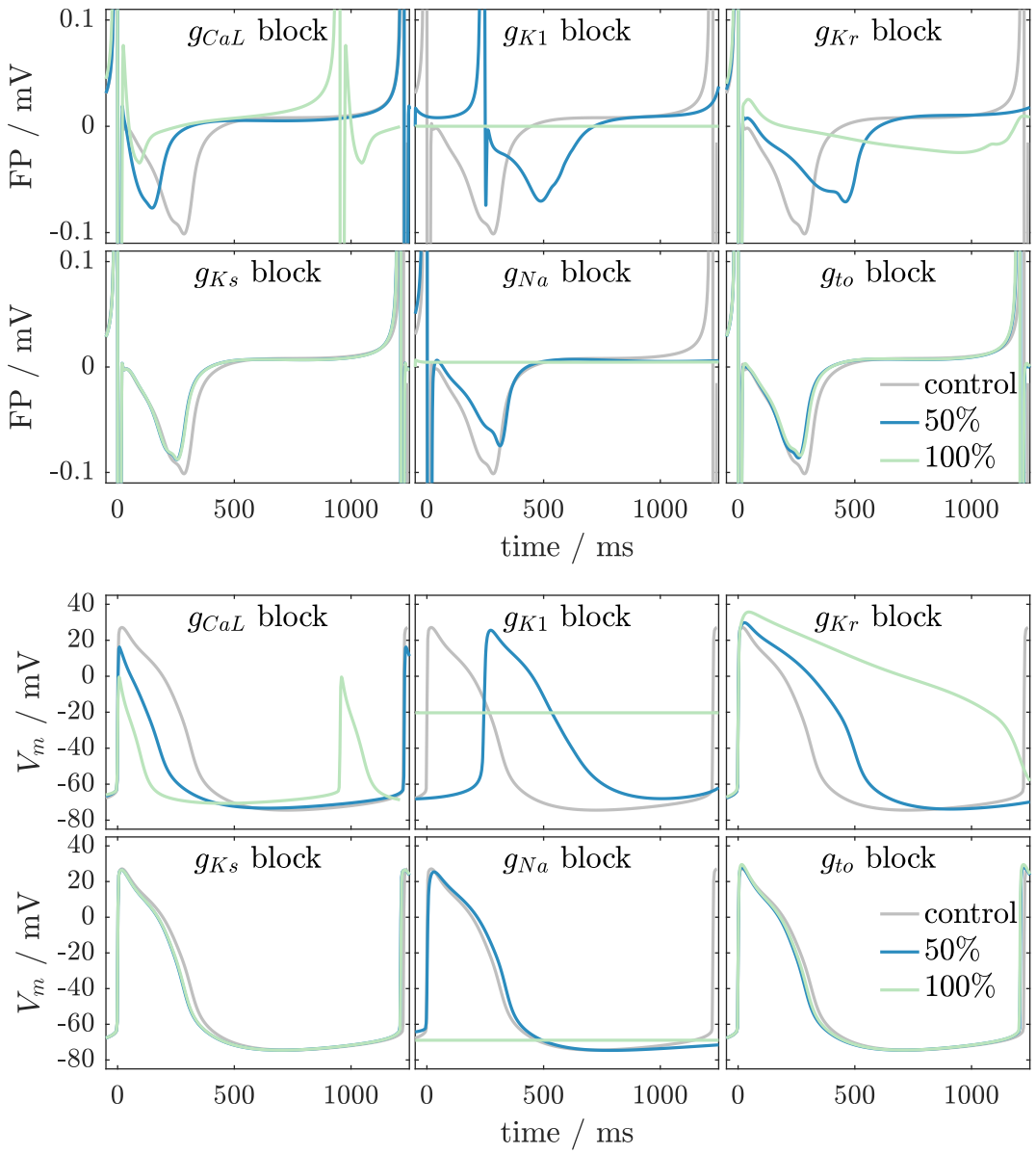

Figure 7.3: Field and action potentials from a simulated monolayer as different ion channels were blocked. These signals were generated from a monolayer where the phenotype distribution was set using field parametrisation C ($l_c = 0.3, \sigma = 0.15$). Ionic conductances g were reduced by 50 and 100% of their value under control conditions.

7.4.2 Examples of signals from a single monolayer

We begin our analysis of the effects of ion channel blockade by comparing the action and field potentials under the different interventions. As an example, we consider the potentials from the first realisation of random field parametrisation C. The action and field potentials from Electrode 1 are plotted in Figure 7.3.

We can immediately see that blockade of some ionic currents such as I_{CaL} and I_{Kr} have far more dramatic effects on signal morphology than others, such as I_{Ks} and I_{to}. The other currents, I_{Na} and I_{K1}, cause rather little change at 50% block but prevent activation entirely at 100% block.

We observe triangulation of the action potential as g_{CaL} is reduced, and prolongation of the action potential with the reduction in g_{Kr}, as expected from previous studies using adult cardiomyocyte models (Mirams et al., 2014). These changes are reflected in the field potential, with the repolarising wave occurring close to and further from the depolarising spike after the two respective changes to the ionic currents.

In Figure 7.4, we plot the activation sequence in this monolayer after blockade of each ion channel. In the control case, we can see that the bottom right region of the monolayer acts a a pacemaker, following the lower ρ_{V} in this area of the monolayer. This region consistently triggers activation following all changes to the ionic currents, apart from when the monolayer becomes quiescent at 100% block of I_{Na} and I_{K1} (at 50% I_{K1} block, the depolarising spike could not be consistently detected across the entire monolayer).

We can also identify some changes in the conduction velocity from the activation time gradients. As expected, we see that CV is considerably slower after 50% reduction in I_{Na} than in control. We also note lesser reductions following reduction in I_{CaL} and I_{Kr}, which we will return to following a more complete study of all the simulated monolayers.

7.4.3 Biomarker values from all simulated monolayers

In Figure 7.5, we plot the values of five biomarkers from the five realisations of the phenotype distribution generated by random fields A–F. The biomarkers, conduction velocity (CV), beat rate, spike amplitude (SA), field potential duration (FPD) and corrected field potential duration (FPDc) were described previously in Section 6.2.3.

A 50% blockade of the L-type calcium current causes small changes in CV, beat

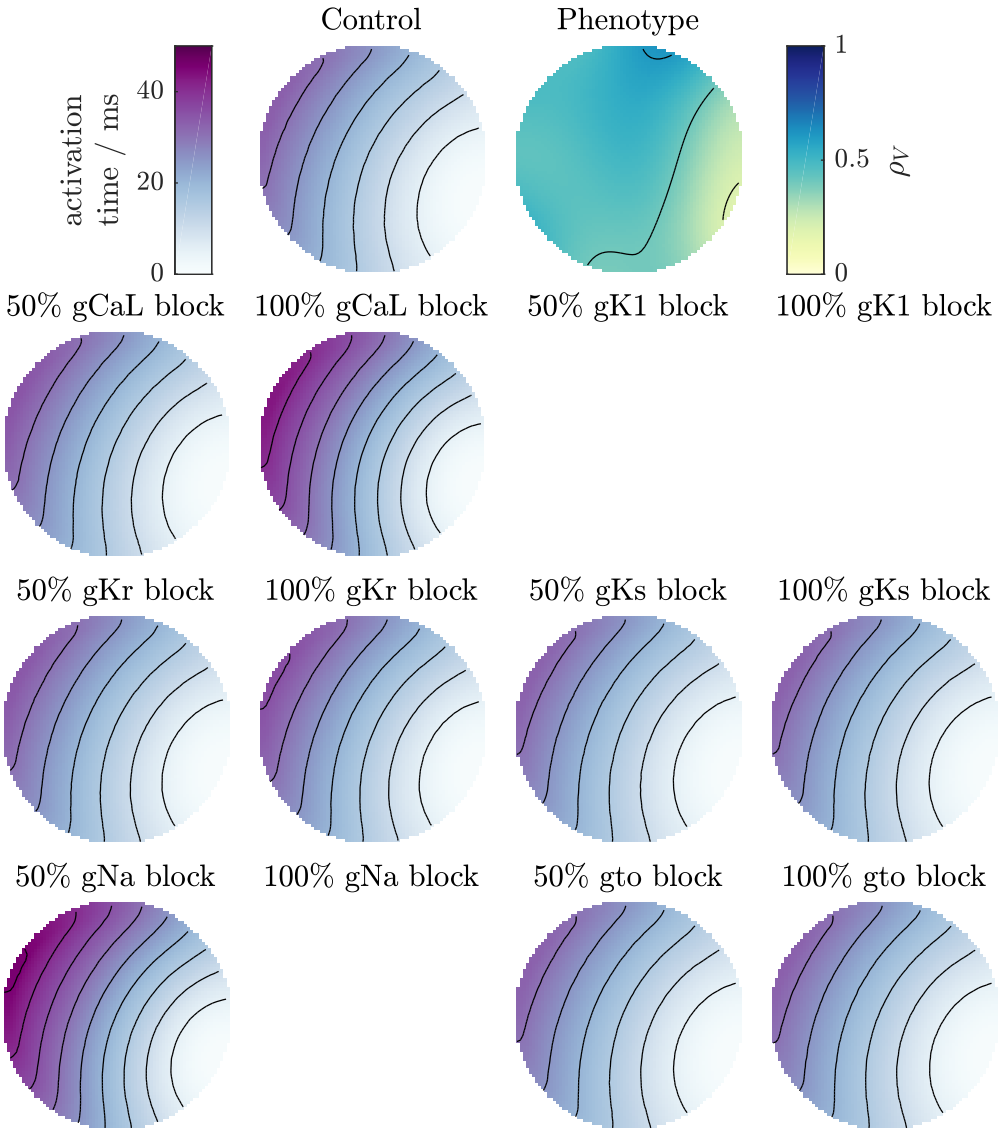

Figure 7.4: Activation patterns from simulated monolayers as a single ion channel was blocked. The activation patterns were derived from the final simulated beat of a monolayer generated with field parametrisation C (first field realisation). The underlying phenotype distribution is shown alongside the activation pattern during control conditions in the top row. The monolayers were quiescent following both levels of block of g_{K1} and 100% block of g_{Na}.

rate and SA, before causing more noticeable changes at 100% block. There is little variability in the values of, or the trend in, these three biomarkers across different parametrisations and realisations of the random field. At the highest level of block, the peak of the repolarising wave becomes harder to detect, resulting in the FPD and FPDc appearing to take different trends in different realisations of the same random field.

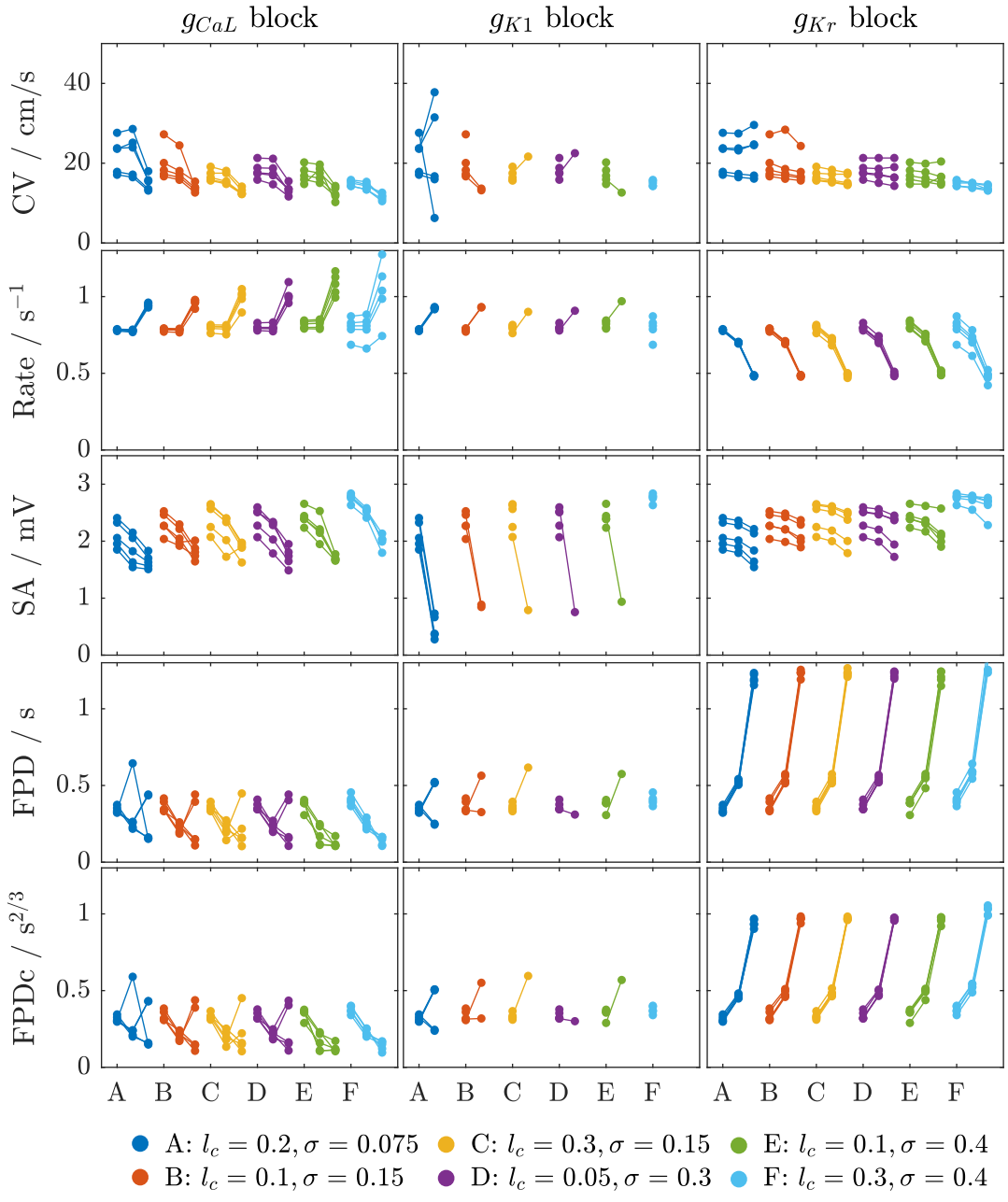

Figure 7.5: Biomarker values from simulated monolayers under blockade of a single type of ion channel. (1 of 2) The three columns show values of the biomarkers following reduction in the values of g_{CaL}, g_{K1} and g_{Kr}. Each set of three connected data points shows the biomarker value at 0, 50 and 100% block in a single monolayer. The parameters of the random field, l_c and σ, are indicated by the colour of the groups of data points. The five data series in each colour were generated with five realisations of the random field. Missing data points indicate cases where it was not possible to calculate the value of a biomarker, for instance due to the monolayer becoming quiescent.

As we noted previously, reduction of I_{K1} has an appreciable effect on the excitability of the monolayer; our example monolayer became quiescent at 100% block of the current. In many of the monolayers, it was impossible to calculate values of the biomarkers at even 50% block, implying that they too became quiescent. Beating was detected in none of the monolayers at 100% block.

Reduction in g_{Kr} is well-known for causing prolongation of the action potential, and as expected we can clearly see its effect on the FPD and FPDc of the simulated monolayers. The changes on CV and SA are rather small, but there is a reduction in beat rate across all monolayers which is notable when I_{Kr} is entirely removed.

Reduction in g_{Ks} and g_{to} produce rather similar effects on the biomarkers derived from the simulated monolayers. Even when changes occur, they are small — a slight decrease in FPD and FPDc at 50 and 100% block of the two currents, and increases in CV in some of the monolayers. The small magnitude of changes suggests that detecting I_{Ks} or I_{to} reduction using field potentials from MEA recordings will be difficult, if not impossible, in practise.

In contrast, reduction in g_{Na} has a far greater impact on the biomarkers. We noted previously that complete removal of I_{Na} caused the example monolayer to become quiescent; this is also the case in almost all the other simulated monolayers. In the monolayers where the depolarising spikes were detected, the SA was almost undetectably low and so the values of FPD from those monolayers should be treated with caution. At 50% block, a slight increase in FPD can be detected, along with more noticeable reductions in CV (which is typically the case in experimental preparations), beat rate and SA.

While most of the effects we see on the biomarkers are those that we anticipated and are well-understood, some do merit further mention. Slowing of the CV is typically associated with reduction in I_{Na}, but we also see a small yet consistent decrease following reduction in I_{Kr} and I_{CaL}. The association with hERG channel block has been previously reported (Caspi et al., 2008; Satin et al., 2004), but to our knowledge this is not the case for I_{CaL}.

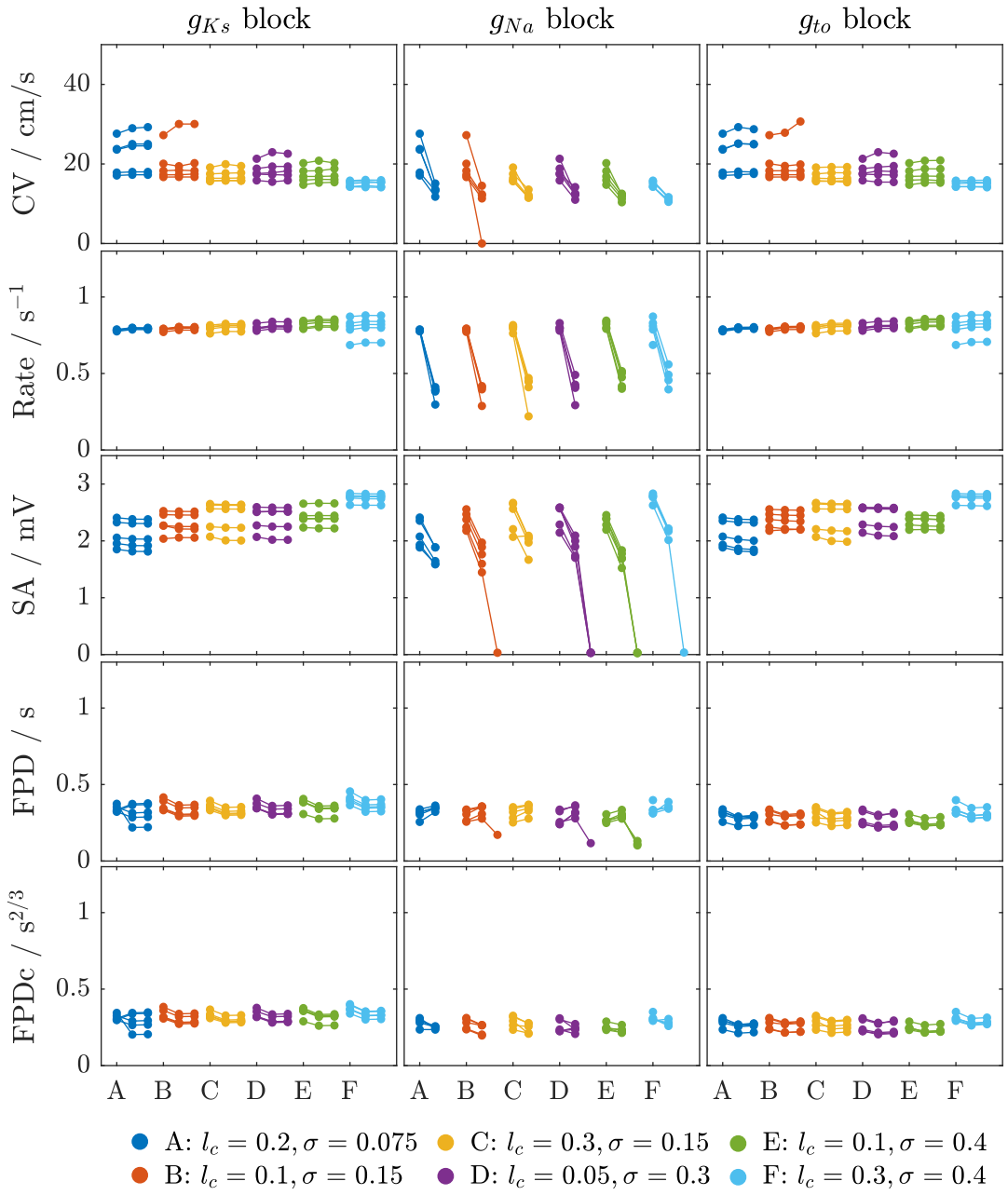

Figure 7.5: (2 of 2) Continued from page 171. The effects of applying 50 and 100% block to three further ion channels, g_{Ks}, g_{Na} and g_{to}.

7.5 CiPA Compounds

We now perform simulations of the action of real drugs on hiPSC-CM monolayers. The drugs that we use are selected from the CiPA validation study carried out by Axion Biosystems. Values of the IC_{50} and Hill coefficients have been published for the majority of the drugs in the CiPA validation study (Crumb Jr. et al., 2016);

we have selected three that exhibit a range of ion channel-blocking properties for this study. The selected drugs are Cisapride (a specific blocker of the hERG channel), Terfenadine (which also primarily reduces I_{Kr}, but also I_{CaL} at higher concentrations), and Diltiazem (which mainly reduces I_{CaL}, but also I_{Kr} at the highest tested concentration). The properties of the three drugs were summarised in Table 7.1, on page 162.

As in Chapter 6, we calculate biomarkers from the simulated field potentials and compare these to the experimental data provided by Axion Biosystems. Our analysis of this data takes us towards two aims. Our first aim is to assess how well our model is able to reproduce the experimentally-observed effects of each drug. This will help us to identify aspects of the model, on both the tissue and cellular scale, which can be improved upon in future. The second aim is to investigate how variability in cellular phenotype may affect the biomarker values and overall activity of the monolayer in ways not originally anticipated.

Extended versions of the figures in the following section, showing more examples of the action and field potentials and additional biomarkers, may be found in Appendix A4.

7.5.1 Cisapride

The drug Cisapride was used to treat heartburn up until the year 2000, when it was withdrawn from the market following reports of heart rhythm abnormalities (Henney, 2000). Cisapride binds to the hERG channel at rather low concentrations, and has been widely reported to increase the QT interval in the electrocardiogram (Wysowski and Bacsanyi, 1996) and the field potential duration in micro-electrode array studies (Harris et al., 2013).

We simulated the effects of Cisapride on 60 randomly generated hiPSC-CM monolayers following the procedure set out in Section 7.3. Ten realisations of the six previously described random fields A–F were used to generate the phenotype distributions used in this study. The concentrations of Cisapride were selected to match those used by Axion Biosystems in experimental studies, to which we

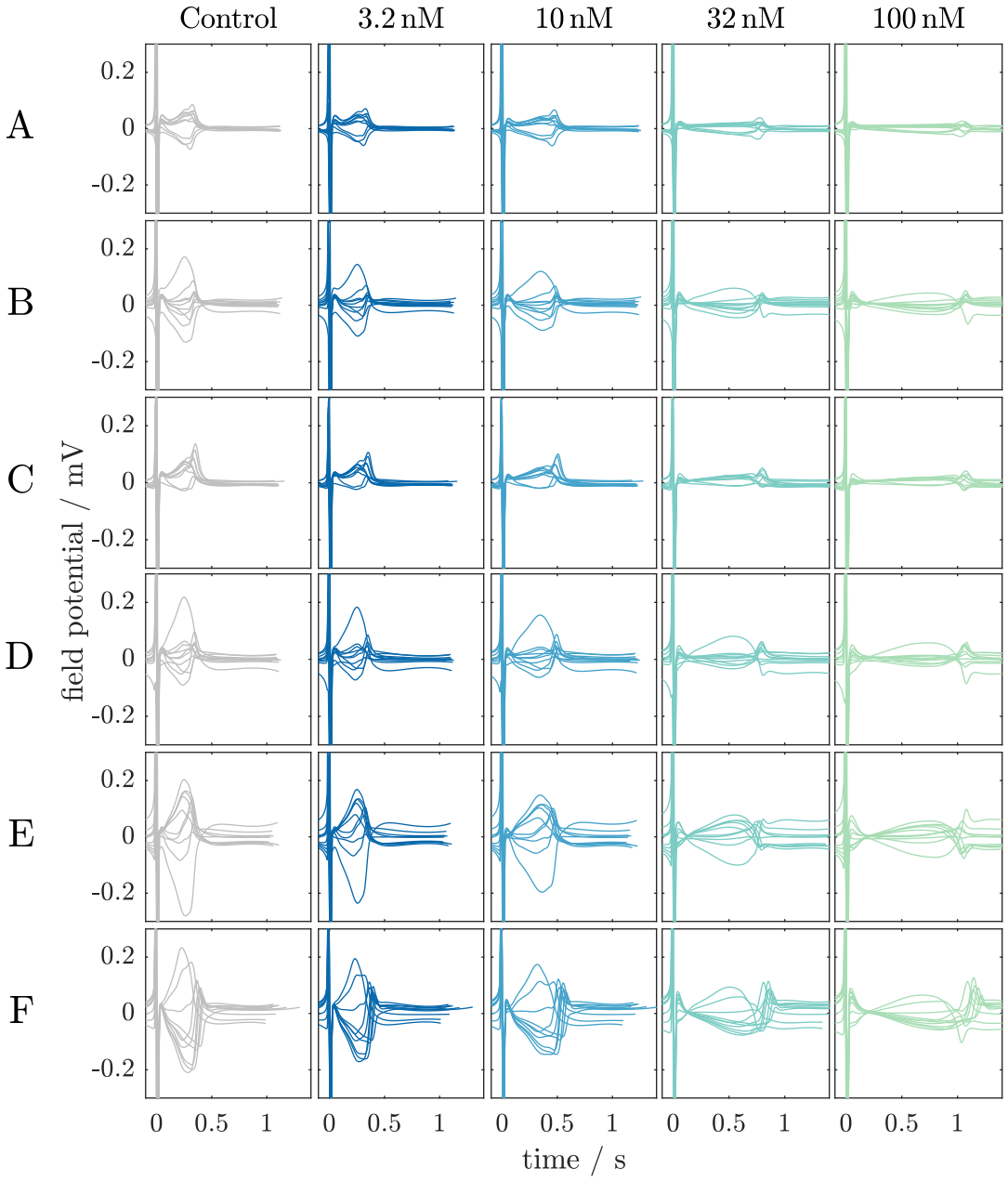

Figure 7.6: Simulated field potentials following the addition of Cisapride. The field potential during the last full beat of each simulation. Each panel contains one field potential from each of ten realisations of the random field parametrisation used to represent the phenotype distribution.

compare the results of our simulations.

To gain an initial assessment of the form of the field potential and how it can vary, we plot an example of a field potential from one electrode in each simulation in Figure 7.6. Each individual panel contains field potentials from ten realisations of each parametrisation of the random field A–F. Each row of

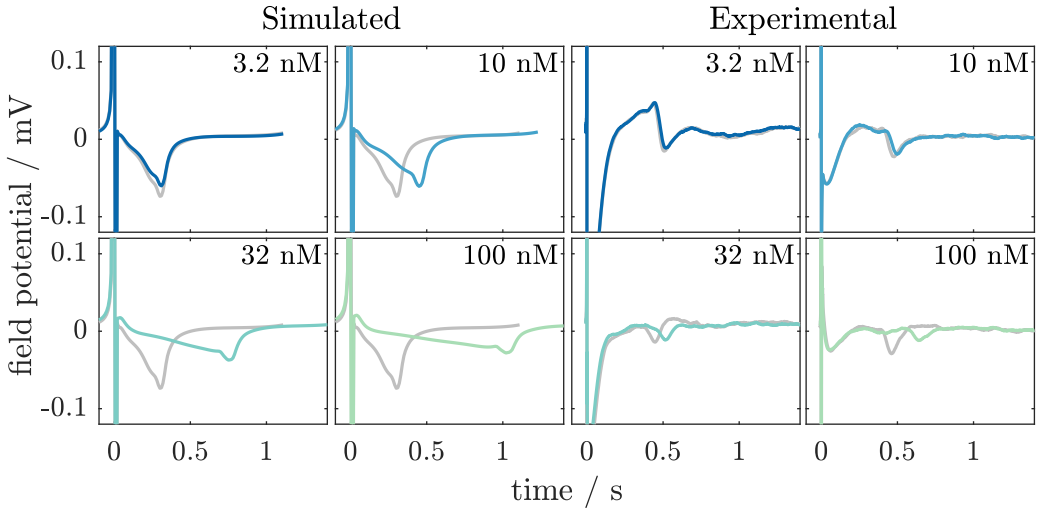

Figure 7.7: Comparison of simulated and experimental field potentials following the addition of Cisapride. Left: simulated field potentials generated using one realisation of phenotype field A. Right: experimental field potentials. Grey is used to indicate the field potential under control conditions, with shades of blue/green used for the dosed cases. Note that a different monolayer was used for each of the experimental control-dosed pairs, while the same phenotype layout was used for all the simulated signals shown in this figure.

the figure corresponds to one of the six random field parametrisations. The columns of the figure show field potentials from simulations with increasing drug concentrations. The field potentials were obtained from the final complete beat in each simulation. For clarity, we do not show the depolarising spike of the following beat.

As we noted in the previous chapter, there is substantial variability in the field potential morphology as a result of variability in phenotype. However, we do see the same general trend in the morphological changes as the drug concentration increases. The repolarising wave occurs at a later stage as a result of simulating the addition of Cisapride, as a consequence of the reduction in I_{Kr} causing prolongation of the action potential, and therefore also the field potential.

In Figure 7.7, we provide a more detailed view of the field potential. On the left, we compare the simulated field potential at each of the applied drug concentrations with the control simulation. The panels on the right have a similar layout, but experimental field potentials are shown. The simulated field potential

was selected from one realisation of those generated using field A. At the lowest concentration, we see a very slight reduction in the amplitude of the repolarising wave in both the experimental and simulated cases. As the concentration is increased, the peak of the repolarising wave occurs later in the dosed case than control, as we expect. However, the differences between the control and dosed cases are far more marked in the simulations rather than the experiments.

We now examine the biomarkers that are influenced by the action of Cisapride. Here, we focus on the FPD, and the closely-related beat rate and FPDc. Figure 7.8 shows the values of these biomarkers during each simulation. Biomarkers from experimental data are shown in grey on the right-hand side. An expanded version of this figure, showing additional biomarkers, may be found in Appendix A4. Figure 7.9 is plotted similarly, but shows the percentage change in the biomarker value at each of the four drug concentrations compared to control.

As expected, considering the percentage change in biomarkers rather than their absolute value removes a lot of the variability within the results from a given random field parametrisation. This is particularly notable in the beat rate.

If we now focus on Figure 7.9, we observe the correct qualitative trend in the biomarkers: FPD and FPDc increase as the concentration of Cisapride increases, and beat rate decreases at the highest tested concentration. As we noted in our preliminary observations of Figure 7.7, the magnitude of the change in these biomarker values is far larger in the simulated studies, regardless of phenotype arrangement, than in the experimental case.

The change in beat rate is of particular interest. At the lowest concentration of Cisapride, experimental monolayers undergo an increase in beat rate compared to control, an aspect which is not observed in any of the simulated monolayers. With little change in the FPD at this stage, we cannot attribute the difference in beat rate to the cell taking longer to return to a depolarised state. Instead, this is perhaps an effect which is unaccounted for in the present formulation of our model. We will return to this point in Section 7.5.4, following descriptions of the remaining drugs.

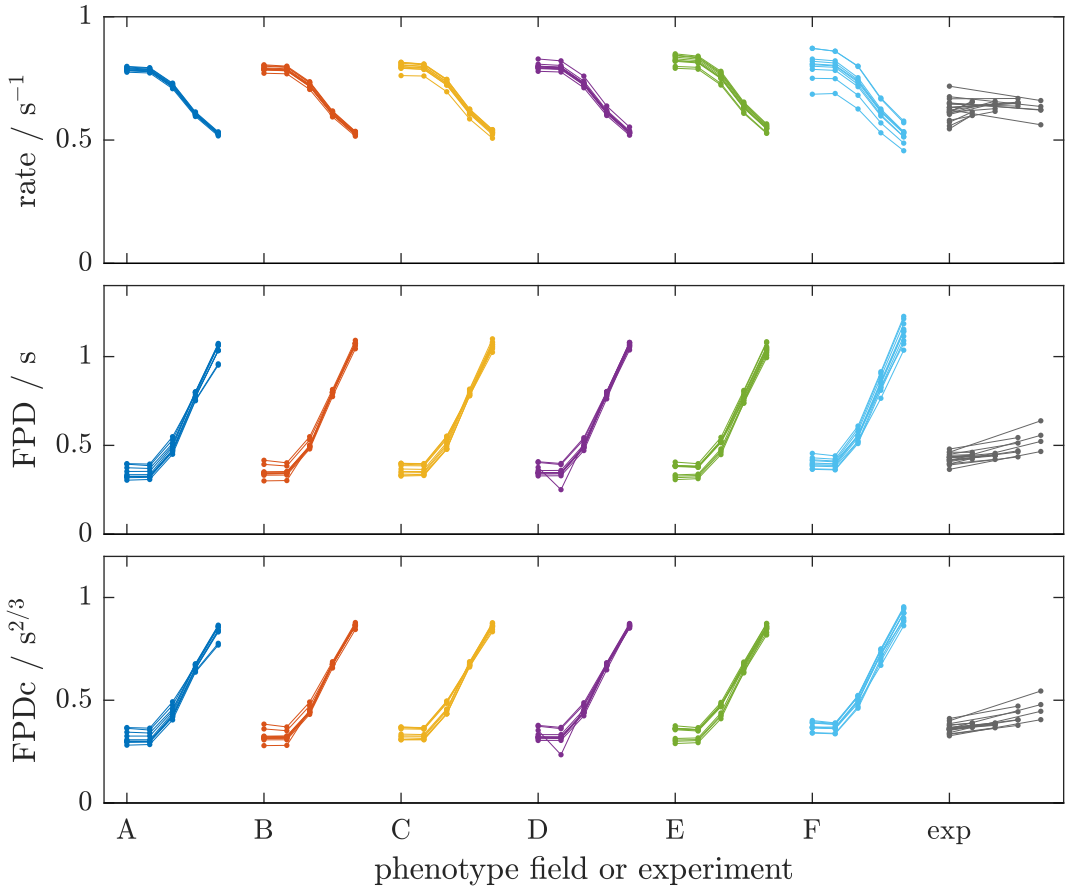

Figure 7.8: Selected biomarkers from simulated and experimental field potentials following the addition of Cisapride. Each five points linked by a line denotes the biomarker values under control conditions and the four increasing concentrations of Cisapride. Connected points indicate that the biomarker values were obtained from the same monolayer. Only one concentration of Cisapride was tested on each experimental monolayer, all lines in that section of the plot therefore link the control value to only one value obtained under dosed conditions.

7.5.2 Terfenadine

Terfenadine is a non-sedating antihistamine implicated in several occurrences of drug-induced Torsades de Pointes (Monahan et al., 1990). It was withdrawn from the market in 1997 once it became clear that the risks associated with the drug far outweighed the benefit of a reduced sedative effect in comparison to other antihistamines (Josefson, 1997). Like Cisapride, Terfenadine binds to the hERG channel and prolongs the QT interval, which can act as the trigger for TdP in susceptible patients. However, it also binds to the L-type calcium channel at higher concentrations, giving the profile of Terfenadine some interesting properties.

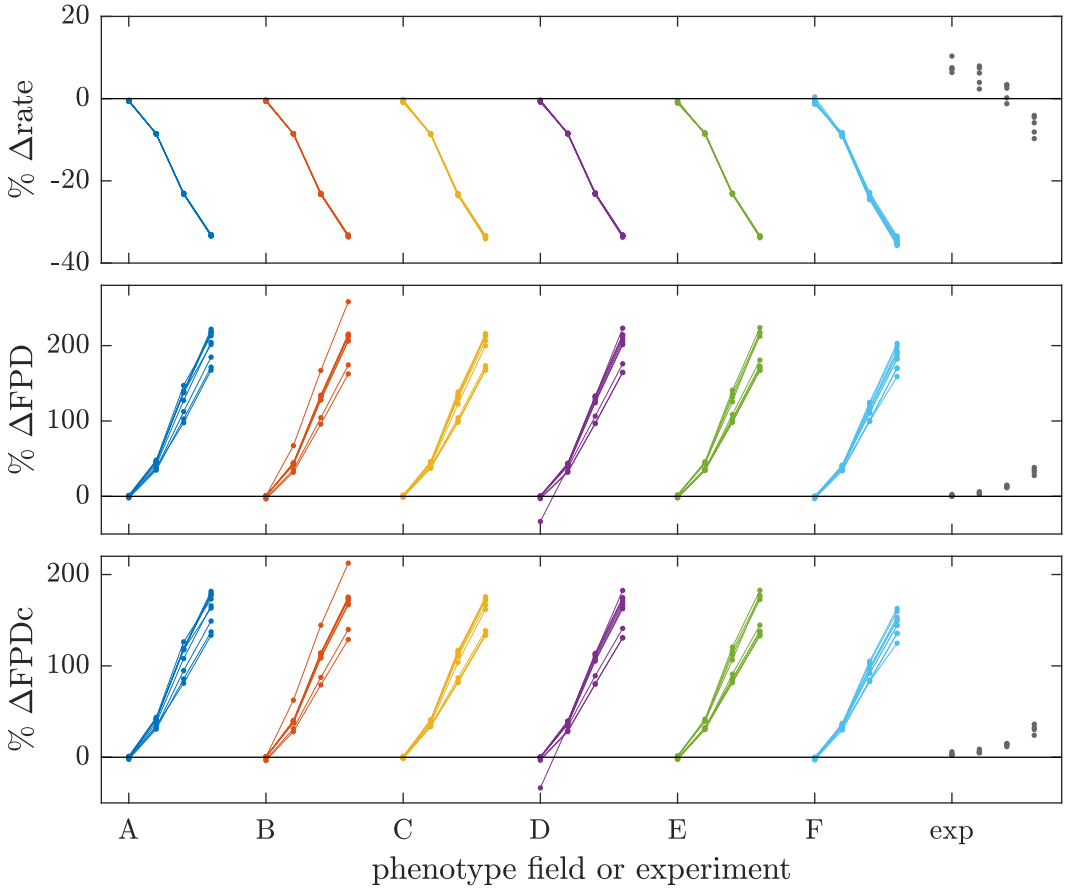

Figure 7.9: Percentage change in selected biomarkers from simulated and experimental field potentials following the addition of Cisapride. As in Figure 7.8, linked points show the values obtained from the same monolayer. The experimental data points were all gathered from different monolayers, so links are not shown.

In Figure 7.10, we show an example of the impact of Terfenadine on simulated and experimental field potentials. The simulated traces were obtained from a monolayer with phenotype layout generated using the B random field parametrisation. As we noted earlier for Cisapride, we see that our simulated field potentials show far more extensive differences between the control and dosed cases than the experimental field potentials do. At low concentrations, Terfenadine primarily blocks the I_{Kr} current; the prolongation of the field potential at the first three concentrations is observed as expected. The I_{CaL} blocking properties of the drug come into play at the highest tested concentration. In the experimental case, all monolayers became quiescent at 1000 nM. However, the simulated monolayers

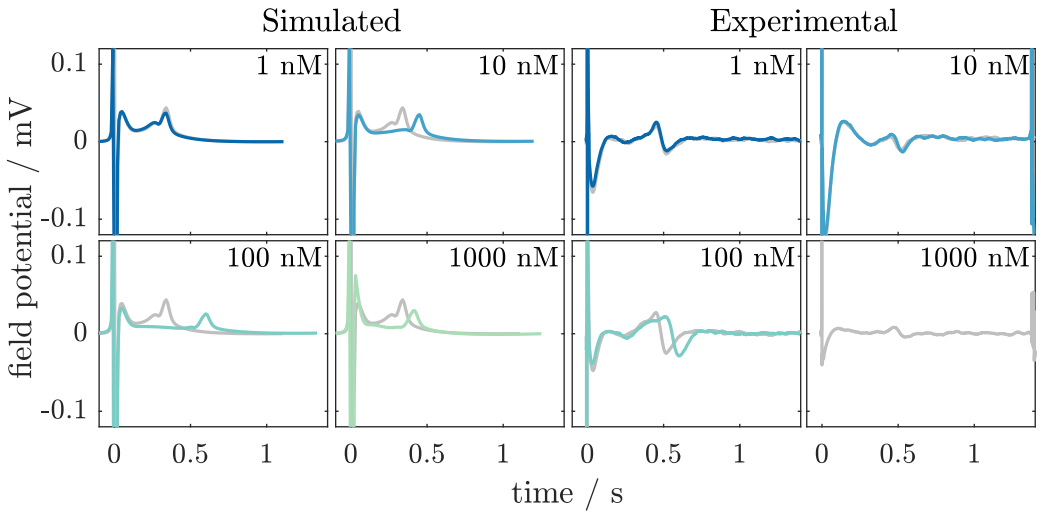

Figure 7.10: Comparison of simulated and experimental field potentials following the addition of Terfenadine. Left: simulated field potentials generated using one realisation of phenotype field A. Right: experimental field potentials. At the highest concentration of Terfenadine, all experimental monolayers were quiescent.

instead showed a reversal in the changes to the field potential duration. These differences at the highest concentration are not altogether unexpected; previous studies have reported both quiescence (Blinova et al., 2017) and reduction in FPD (Harris et al., 2013; Abi-Gerges et al., 2017) at concentrations of 800 nM or above.

To obtain a more precise view of the changes in field potential duration, we plot the percentage change relative to control of the beat rate, FPD and FPDc in Figure 7.11. The change in beat rate in our simulations follows an inverse pattern to the FPD, first decreasing and then increasing at the final concentration. Along with the differences between the simulated and experimental beat rates and the inability of the rate-correction in the FPDc to compensate, this suggests that the prolongation of the field potential is masking any changes to the beat rate.

Supplementary plots showing the full range of simulated action and field potentials from this series of simulations may be found in Section A4.1.2.

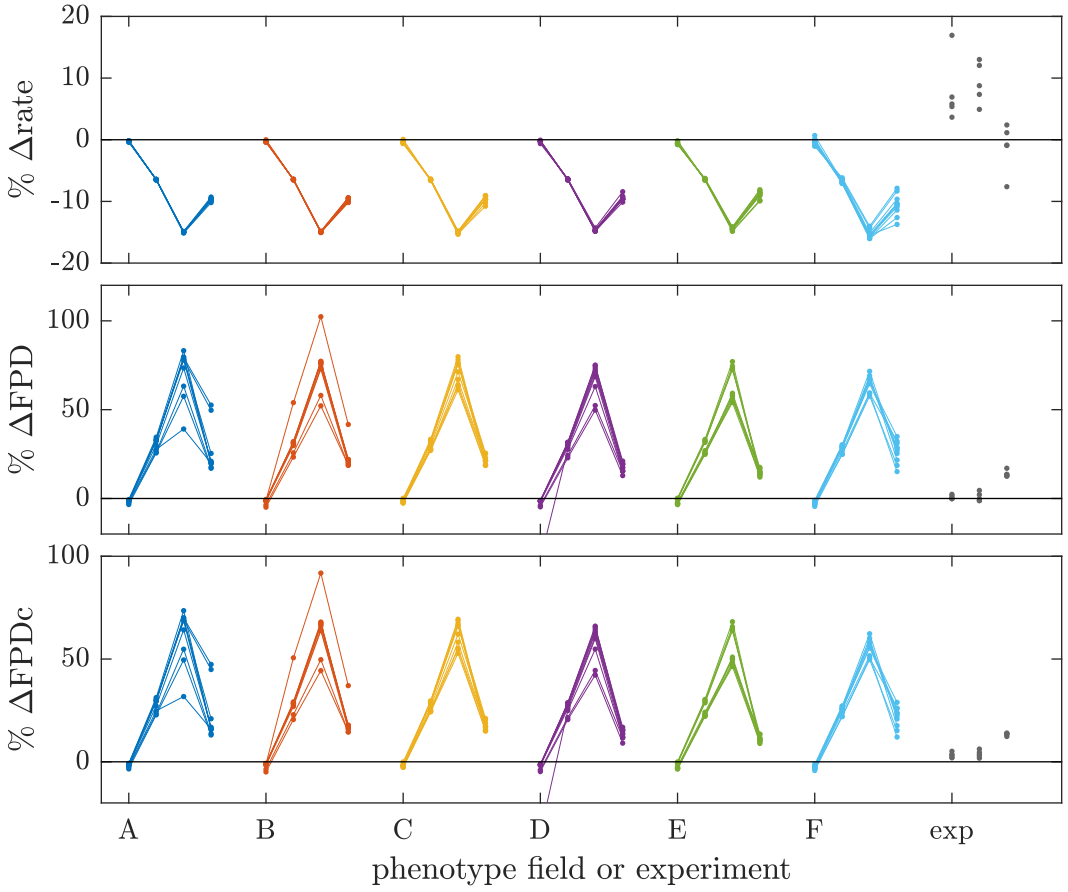

Figure 7.11: Percentage change in selected biomarkers from simulated and experimental field potentials following the addition of Terfenadine. Linked points show the percentage change in each biomarker compared to control for a given monolayer.

7.5.3 Diltiazem

Diltiazem is an anti-anginal and anti-arrhythmic drug considered to have a low-risk safety profile (Colatsky et al., 2016). Like Terfenadine, it blocks the hERG and L-type calcium currents, but does so at the opposite ends of the concentration scale: it primarily reduces I_{CaL} until, at very high concentrations, appreciable levels of I_{Kr} block also occur.

As for previous drugs, we begin with a comparison of one example field potential from simulated and experimental datasets. Figure 7.12 compares a simulated field potential from a monolayer generated using phenotype field B to experimental data. It again appears that the simulations overestimate the impact of the drug on the field potential at the lower concentrations, and we can see that the

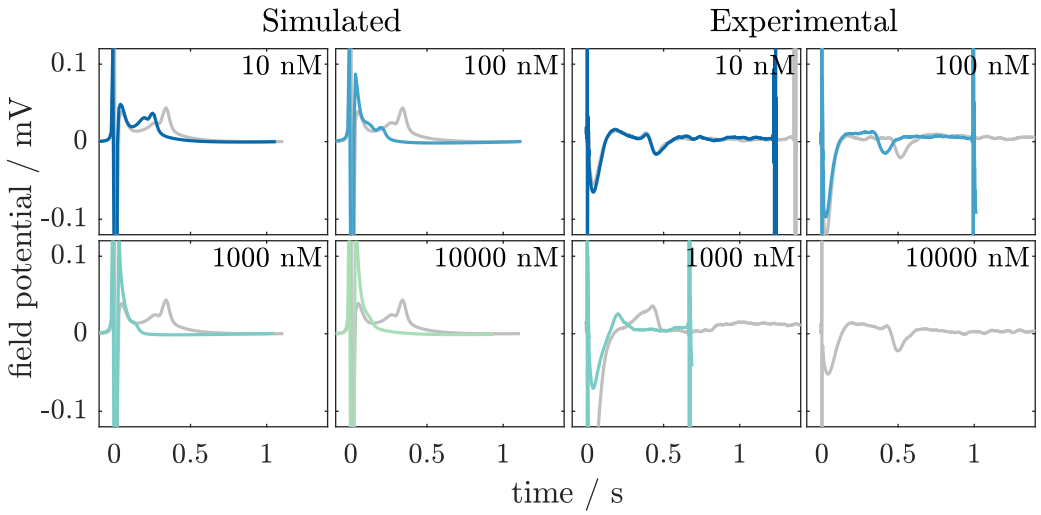

Figure 7.12: Comparison of simulated and experimental field potentials following the addition of Diltiazem. Left: simulated field potentials generated using one realisation of phenotype field A. Right: experimental field potentials. At the highest concentration of Diltiazem, all experimental monolayers were quiescent or it was not possible to detect the repolarising wave.

simulated field potentials remain robust at the highest concentration despite the experimental monolayer becoming quiescent.

The repolarising wave proved difficult for the automated algorithm to detect at the highest two concentrations (note, for example, how the repolarising wave is almost indistinguishable from the depolarising spike in the 1000 and 10 000 nM panels of Figure 7.12), so manual detection of the repolarising wave was applied in some cases. In Figure 7.13, we plot the percentage change in three biomarkers: the beat rate, conduction velocity and field potential duration. Plots showing the full set of biomarkers and their absolute values can be found in Section A4.1.3. Our simulations capture the experimentally observed increase in beat rate, but underestimate the degree of change. The change in CV is rather variable, but does reproduce the trend seen in the experiments. CV is greater than control at the simulated lowest concentration of Diltiazem, before returning close to the control value at the following concentration and then falling at higher concentrations. In contrast, the experimental data is less consistent, with some monolayers showing an increase in CV, and others a decrease, at all tested concentrations.

This implies that there are further levels of variability in the monolayers that

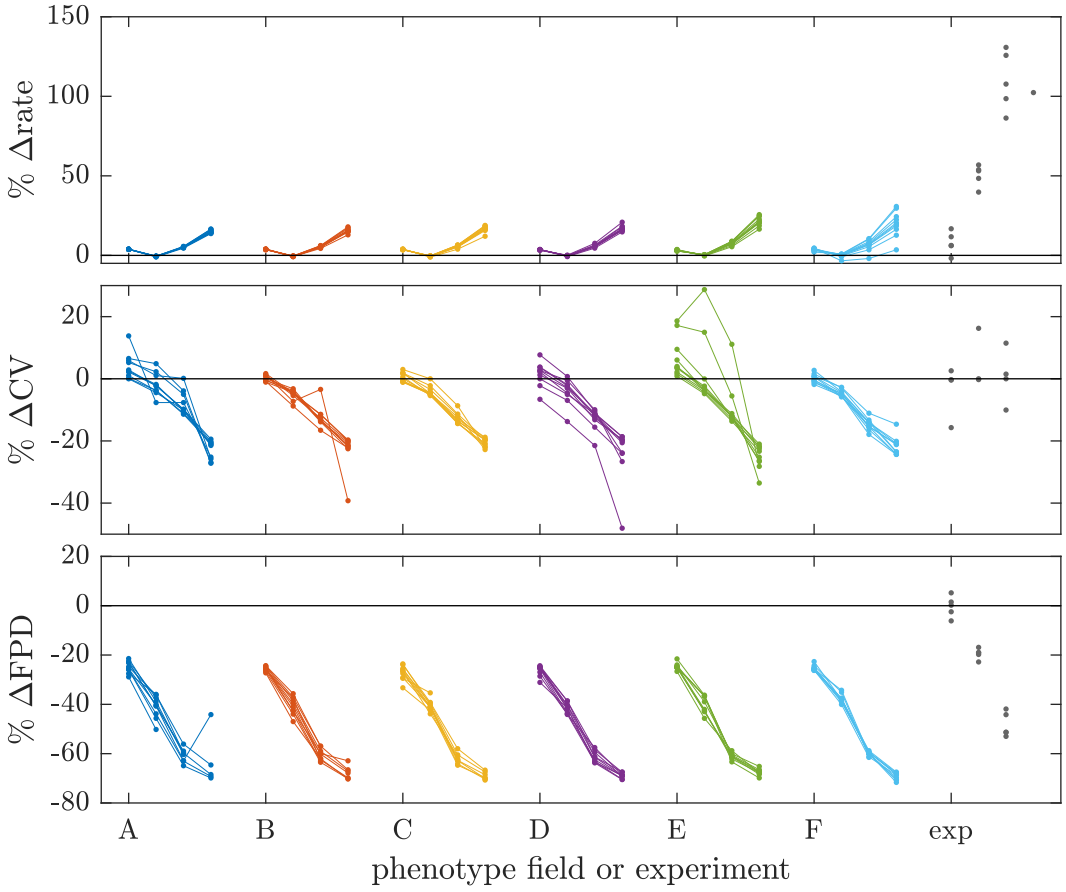

Figure 7.13: Percentage change in selected biomarkers from simulated and experimental field potentials following the addition of Diltiazem. Linked points show the percentage change in each biomarker compared to control for a given monolayer.

our simulations are, at this point, unable to capture. The implication is backed up further by the beat rate data. Our simulations do show an increase in variability in beat rate as the concentration increases, but not to the extent observed in the experimental data.

The previous two simulation studies, on Cisapride and Terfenadine, both exhibited far greater changes in FPD that were observed in the experiments. However, there is a far better quantitative fit for Diltiazem, the action of which shortens rather than prolongs the FPD. At 10 nM, the shortening is slightly greater in the simulation, while there is very little change in the experimental data compared to control. At the higher concentrations, the differences between experiments and simulation are far less than were seen for the other drugs.

7.5.4 Discussion

A common theme throughout all three studies of drug action is the observation that our model can qualitatively predict the changes observed in many experimentally-recorded field potential biomarkers but, in its present state, overestimates many of these changes.

For the I_{Kr} current, this observation is in agreement with the findings of Abbate et al. (2018). In their simulations of Dofetilide (like Cisapride, a drug that specifically reduces I_{Kr}), the increase in repolarisation time far exceeded that of the experimental data against which they compared. The two drugs that we tested, Cisapride and Terfenadine, both cause very high levels of hERG channel block at their highest tested concentrations (over 90%). Any errors in the IC_{50} values or Hill coefficients should therefore only have been responsible for small errors in the level of hERG channel block; we can therefore consider errors in the IC_{50} values or Hill coefficients to be an unlikely cause for the discrepancies in biomarker values.

We therefore propose that improvements to the I_{Kr} formulation in the Paci et al. (2013a) model may be able to improve the ability of our model to recapitulate the experimental state. The Paci et al. (2013a) model is based upon the ten Tusscher et al. (2004) model, a model not previously reported to overstate the effects of I_{Kr} reduction on the action potential duration (and, in consequence, the FPD) — other models, such as the O'Hara et al. (2011) model, show a much greater response (Mirams et al., 2011). If we return to Figure 7.1, we note that the APD_{90} at the highest tested concentrations of Cisapride and Terfenadine is very high, at over 1.1 s. Such a response with no sign of unusual effects such as early after-depolarisations is not found in adult models of cardiac electrophysiology (see Figure 7.14) and raises concerns as to the validity of the Paci et al. (2013a) model in this regime.

This feature of the Paci et al. (2013a) model explains our observations of larger than expected increases in FPD following blockade of I_{Kr}. We therefore propose that improvements to the kinetics and/or expression levels of I_{Kr} for both

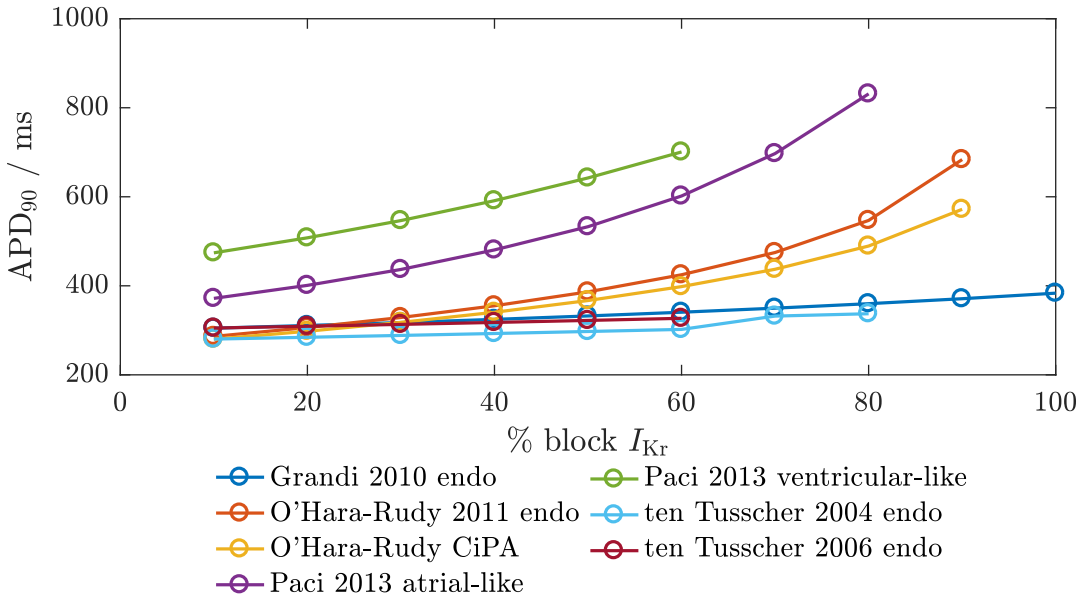

Figure 7.14: APD_{90} prolongation following I_{Kr} block in a range of cellular electrophysiology models. The Paci et al. (2013a) models exhibit far greater APD_{90} prolongation than the adult models following reduction in I_{Kr}. Data for the figure were generated using the Cardiac Electrophysiology Web Lab (Cooper et al., 2016). All models were stimulated at 1 Hz.

the atrial-like and ventricular-like variants should be a priority in future work. A recent development on this front was the tailoring of currents from the Paci et al. (2013a) ventricular-like model to individual hiPSC-CMs from two commercial suppliers (Lei et al., 2017). While changing the values of ion channel conductances improved the ability of the model to reproduce the effects of different drugs on the APD_{90}, Dofetilide (the specific I_{Kr} blocker) proved a particular challenge. This implies that merely tuning the values of the ion channel conductances is likely to be insufficient; instead, a thorough investigation of the ion channel kinetics may be merited, with particular emphasis on I_{Kr} (Beattie et al., 2018).

Discussion of the phenotypic variability within and between monolayers is best restricted to the Diltiazem study, where the impact of I_{Kr} is less overpowering. Throughout the studied biomarkers, we observed greater variability in the percentage change relative to control in the experimental data than in the simulated data. To achieve experimentally-observed levels of biomarker variability, we may have to include yet more variability-inducing factors into our model.

The inclusion of a model of nodal-like cellular electrophysiology (i.e. the third cellular phenotype) and greater consideration of the maturation state of the cells within the monolayer are two such factors. Each of these ideas would influence the beating characteristics of the monolayer, with the nodal-like model providing pacemaker regions with a potentially faster beat rate than the atrial-like model, and knowledge of the maturation state providing a mechanism by which some of the cell types could be less prone to spontaneous beating.

7.6 Conclusions

We began this chapter by demonstrating how signals recorded by the MEA are affected by reduction in individual major currents. We observed the expected qualitative effects, with reduction of I_{Kr} and I_{CaL} causing prolongation and shortening of the field potential duration respectively. The impact of I_{Na} block was clearly discerned by the reduction in spike amplitude and conduction velocity, while the effects of complete I_{K1} block manifested through cessation of spontaneous beating. Block of the remaining currents, I_{to} and I_{Ks}, produced comparatively negligible effects on all biomarkers. Such changes are therefore likely to prove difficult to detect in an experimental context.

Our comparison of simulated and experimental drug effects proved useful in narrowing down aspects of the Paci et al. (2013a) model that can be improved upon in future. The consistent overestimation of the increase in field potential duration caused by hERG-blocking drugs indicate that improvements to the formulation of the I_{Kr} current should be a priority for future work. Such a focus on the hERG channel has already proved useful in adult cardiac cell models, with revisions to the O'Hara et al. (2011) model improving the accuracy of its response to drugs that reduce I_{Kr} (Li et al., 2017; Dutta et al., 2017).

We demonstrated that variability in the phenotype distribution, represented through the use of different realisations of a random field to determine the phenotype layout, could produce levels of variability in the biomarkers similar to those observed experimentally. While this finding will need to be revisited once the

absolute changes in biomarkers are better represented by the underlying cellular electrophysiology model, we have shown that our method of simulating phenotypic variability using the homogenised phenotypes model and Gaussian random fields is a promising approach for future simulation studies.

Chapter 8

Conclusions

We now review the main findings of this thesis, and identify a number of promising avenues for further research along the same theme.

8.1 Implementation of Multiple Phenotypes in Cardiac Tissue Simulations

Tissue cultures of human stem cell-derived cardiomyocytes exhibit steady beating, with an activation wave that propagates outwards from a pacemaking region. This behaviour is inconsistent with the synchronous activation that we might expect from a system of homogeneous coupled oscillators, indicating that the electrophysiological properties of the tissue vary throughout space.

There are several potential mechanisms by which such variability can arise, for example, variations in the structure of the tissue through more crowded regions or holes in the monolayers, or small-scale variation in the action potential due to differences in the density of ion channels in different cell membranes. However, one mechanism stood out as being particularly fruitful for further investigation: single-cell studies of hSC-CM electrophysiology have widely reported that the action potentials can be classified into three subtypes, or phenotypes, that differ

considerably in their morphology.

Simulations of hSC-CMs on the tissue scale therefore need to incorporate such spatial variability. Our work in Chapter 5 compared two different models for the simulation of electrophysiological activity in tissue that possessed spatially varying types of cell. Existing methods for simulating tissue with spatially varying properties each have their disadvantages, as we discussed in Section 5.2, so we therefore investigated a novel method, the *homogenised phenotypes* model, which included the presence of different types of cell on a small spatial scale in its derivation. We compared the homogenised phenotypes model to the *partitioned phenotypes* model, an implementation of the bidomain equations where small regions of distinct cell type are partitioned in the finite element mesh.

In the limit of small partitioned regions, simulations that utilised the partitioned phenotypes and homogenised phenotypes gave similar results in terms of the propagation of the action potential and in biomarkers of the action potential across the spatial domain. We concluded that the homogenised phenotypes approach is valid for simulation of situations where there is small-scale spatial variation in phenotype.

We now have two options for the simulation of tissue containing multiple cell types, each better-suited to a specific situation. The homogenised phenotypes model is flexible in terms of the spatial distribution of different types of cell, and rapid spatial change in the relative mix of the two cell types can be simulated, as long as the mesh is sufficiently fine that the change in proportions across the mesh elements is well-captured. In contrast, the partitioned phenotypes model is useful for situations where the domain can be sub-divided into regions where exclusively one type of cell is present. Unlike the homogenised phenotypes model, the partitioned phenotypes model requires the structure of the mesh to reflect the regions of the domain where a single phenotype is present. While the necessity for accurate partitioning of the mesh could cause performance issues if regions of one phenotype are small, this case can now be better-handled by the homogenised phenotypes model, and those cases where the partitioned regions are large can

still be simulated using the partitioned phenotypes model.

Our one-dimensional simulations exhibited several behaviours characteristic of tissue cultures of hSC-CMs. When even small amounts of variation in phenotype were introduced, a stable pacemaker region triggered activation in the rest of the domain, as seen experimentally. We were also able to observe spatial changes in biomarker values as the underlying cell type changed. In addition, we made some predictions of behaviour that would be interesting to investigate further, if the opportunity for experimental work becomes available. We noted that the effects of oscillator coupling were apparent in cases where there was little spatial variation in cell type across the domain, and predict that these effects may still be noticeable in situations where there is sufficient variability for steady activation waves to occur. If external pacing is applied to the system, we might therefore expect to see a slower conduction velocity than we would from spontaneous activity as the tendency towards synchronisation is now entirely removed.

8.2 Simulation Study of Monolayers of Human Stem Cell-Derived Cardiomyocytes

In Chapters 6 and 7, we presented a qualitative study of simulated hSC-CM monolayers and their response to the blockade of certain ion channels by well-studied drugs. We compared field potential signals generated by the simulated monolayers to experimental data kindly provided by Axion Biosystems. This study aimed to investigate the impact of phenotypic variability on the monolayers and to understand how this variability propagates through into the biomarkers that are used for the safety assessment process.

We were able to identify how certain morphological features of the field potential were linked to the proximity of the location at which the measurement was obtained to the pacemaking region. We then investigated the properties of monolayers with gradual spatial changes in phenotype, generated using Gaussian random fields. This approach let us compare sets of monolayers with the same

statistical properties, and we were able to exclude some of these as too little variability in phenotype resulted in very high conduction velocities.

Monolayers with phenotype distributions generated using certain Gaussian random field parametrisations demonstrated better matches to the experimental field potentials than others, with the amplitude of the repolarising wave in particular showing that rapid changes between one phenotype and the other are less likely. Qualitatively, our homogenised phenotypes representation of the model produced field potential signals that were a good match to the experimental data, suggesting that modelling the hSC-CM monolayers in such a manner is indeed a good approach.

When we simulated the action of drugs, we found that the variability between biomarkers generated with different realisations of the random field increased, as was seen in the experimental dataset. While our simulated monolayers qualitatively exhibited the same responses to the tested drugs as the experimental data, discrepancies in the quantitative response indicated that further work on the cellular electrophysiology model is required. In Section 8.3, we outline some suggestions for further work that can improve the cell model, and better inform our design of the phenotype distributions in our monolayer simulations. Following these improvements, we will be able to return to further study of the simulated micro-electrode array in the future.

8.2.1 Limitations

As in any modelling study, there were some limitations in our approach that would be interesting to look into more in the future. We made several simplifying assumptions in our model of the micro-electrode array, namely that signals from the recording electrodes could be obtained by point measurements of the extracellular potential, and that explicit modelling of the reference electrode was not required. These assumptions made no difference to the qualitative behaviour of the signals we studied, but would nevertheless be an interesting topic for future research should a more quantitative approach be needed.

The mean potential over the recording electrodes could be used as an input to a model of the electrodes' electrical circuit (as in Moulin et al., 2008), yielding values of the field potential that include the effects of the resistance and capacitance of the electrodes. There are several options available for implementing the reference electrodes in Chaste; a study on the computational efficiency of the different approaches would provide guidance on the best option for future simulation studies.

We have also made some assumptions as to the type of cells present in the monolayer. At the time of writing, the only models of cardiac cellular electrophysiology specifically parametrised for hSC-CMs are those of Paci et al. (2013a). There are two variants of the model; one for atrial-like and the other for ventricular-like cells. We have therefore been unable to investigate the impact of nodal-like hSC-CMs in the work presented in this thesis. There have also been relatively few experimental studies regarding the distribution of cellular phenotypes through stem cell-derived cardiomyocyte tissue cultures; as more information becomes available in the coming years, we will be able to refine our modelling approach.

8.3 Future Work

There are several directions in which work building upon that presented in this thesis may be taken in the future, many of which call for a collaborative approach between experimentalists and simulation scientists.

8.3.1 Single-cell study of action potential variability and phenotype classification

Many studies of the action potential of isolated hSC-CMs have reported the presence of three different action potential morphologies, usually termed atrial-like, nodal-like and ventricular-like (He et al., 2003; Ma et al., 2011). Despite the prevalence of this mode of classification, there has been little research into the variability of the action potential, both within and amongst the different

classes and in whether or how the classification and variability change as the cells mature.

This has implications for both the viability of hSC-CMs for drug safety testing, and for the optimal approach for modelling the action potentials of these cells. We therefore propose that more detailed examination of the electrophysiology of hSC-CMs is merited. The classification criteria could be, as at present, based on action potential duration and maximum diastolic potential (Ma et al., 2011), or machine learning approaches could be investigated (Gorospe et al., 2014).

With well-defined classification criteria and a better understanding of the variability within each of the classes, we will be able to refine our modelling approach further. If there is so much variability in action potential morphology that the boundaries between phenotypes are difficult to define, we would have to question whether producing electrophysiology models for the three separate types is a good approach, or whether a model with continuous variation in phenotype would be more suitable. Given that cells in the various regions of the adult heart are more homogeneous in phenotype, we would expect the former case to be more likely, but a thorough investigation is still merited.

It would also be interesting to compare phenotype classification based upon properties of the action potential against methods based on genetic markers. The latter are already used for selection of one particular phenotype in enriched cultures (Bizy et al., 2013; Josowitz et al., 2014), and identification of phenotype based on such an approach may prove useful for determining the phenotype of hSC-CMs in tissue culture where definitive identification of cellular phenotype has so far proved challenging (Du et al., 2015; Giles and Noble, 2016; Kane et al., 2016; Bett et al., 2016; Zhu et al., 2016; Vestergaard et al., 2017).

8.3.2 Improvements to the stem cell-derived cardiomyocyte cellular electrophysiology model

In Chapter 7, we found that many of our simulations overestimated the changes to the action and field potential as the effects of drugs were added. While the

qualitative responses to our tested drugs were correct, the quantitative response differed more from the experiment at the highest concentrations of the drug. This indicates that further work on parametrising certain ionic currents in the electrophysiology model will be required before simulations of hSC-CMs can be considered for inclusion in the cardiac safety assessment process. The ionic currents in hSC-CMs have been reported to vary between batches of cells and over time as the cells mature, which poses additional challenges for the parametrisation of models of hSC-CM over those of adult cardiomyocytes and provides a likely reason for the discrepancies between model and experiment that we have so far observed.

Adjustments to the Paci et al. (2013a) model for specific experimental datasets are therefore a logical avenue of research, with investigation into cell line-specific parametrisations of the model already underway in our research group (Lei et al., 2017).

8.3.3 Application of tissue-scale simulations to safety pharmacology

Following work on the proposals described above, it would be natural to extend the work presented in Chapter 7 of this thesis.

Once the computational model is better-validated, it will then be possible to utilise it to the benefit of the safety pharmacology community. For instance, performing simulations of the micro-electrode array prior to the experiments could guide selection of which novel compounds are good candidates for further testing, and which concentrations of the compound should be applied. This approach is already taken with rabbit ventricular wedge experiments at GlaxoSmithKline using a computational assay developed by our research group (Beattie et al., 2013; Beattie, 2015). In addition, discrepancies between model and experiment could guide identification of aspects of the action of a novel compound that are not yet fully understood.

It would also be interesting to move from the "forward problem" outlined above to the "inverse problem", and use simulation of hSC-CM monolayers to

deduce how a drug affects each of the ion channels to produce the experimentally recorded effects on the field potential. However, this would require a large number of simulations to be performed for each drug, making the problem intractable until we have a better understanding of the levels and causes of variability in the assay and a more computationally efficient implementation of the bidomain solver. An alternative approach would be to construct an emulator of the field potential signals, which is already proving a promising method for investigating the action potential of single cardiomyocytes (Chang et al., 2015). The advantage of this approach would be the ability to refine the IC_{50} values from single ion channel screens into a more complete picture of the effects of the compound.

8.4 Concluding Remarks

The landscape of safety pharmacology is evolving rapidly at present, with a great amount of work being undertaken by the Comprehensive *in vitro* Assay initiative which will eventually lead to the next generation of guidelines for the cardiac safety assessment process. Recent years have seen *in silico* investigations of cardiac safety become a viable alternative to some of the animal-based safety studies that are routinely carried out, with the work of Beattie et al. (2013) leading to a substantial reduction in the number of rabbit-based assays performed at GlaxoSmithKline, and work by Passini et al. (2017) offering the chance to consider human-specific electrophysiology at an early stage of the cardiac safety assessment process via single-cell simulations. The proposals to use hSC-CMs as part of the CiPA paradigm offer a method by which human-based cells may be used for safety assessment studies; we hope that the *in silico* work presented in this thesis will offer a timely and valuable complement to these plans.

We have presented two major contributions to the simulation of human stem cell-derived cardiomyocyte electrophysiology in this thesis. First, we investigated and verified the homogenised phenotypes model, a novel method for simulation of cardiac tissue that contains a mixture of cellular phenotypes. This work has set a firm mathematical foundation for further tissue-scale simulation studies of hSC-

CMs. Second, we performed a pilot simulation study of monolayers of hSC-CMs, as used in the micro-electrode array assay. We showed that introducing variability in cell type leads to steady activation waves as reported experimentally, and comparison between biomarkers derived from the field potentials of our simulated and experimental datasets showed good agreement in terms of both mean value and the level of variability. Introducing the effects of drugs to this model highlighted some limitations in the models of specific ionic currents which we can use to guide the direction of our future work, and we were able to show good qualitative agreement with the changes in the field potentials that were reported experimentally. Improvements to the parametrisation of the tissue-scale model will be possible over the coming years, and we have outlined several potential directions for future research in this final chapter.

We hope that the issues and solutions that we came across during the development of our tissue-scale model will provide useful guidance for future researchers, and that *in silico* studies of human stem cell-derived cardiomyocyte electrophysiology through these means will assist in the interpretation of the micro-electrode array assay as it becomes more widely adopted in the cardiac safety assessment process.

Appendix 1

Computational Approaches

This Appendix contains details of the computational approaches used for the simulations and analysis presented in this thesis.

A1.1 Monodomain Simulations

In Section 5.3, we briefly described the approaches for implementing the partitioned phenotypes and homogenised phenotypes models. We now give specific details of how the implementation of the monodomain solver was modified for each of these cases.

A1.1.1 Implementation of the homogenised phenotypes model

If we refer back to Section 5.2.4 (page 76), the homogenised phenotypes model may be expressed as

$$\nabla \cdot (\sigma_i \nabla V_m + (\sigma_i + \sigma_e) \nabla \phi_e) = I_{total}^{\text{stim}} \tag{5.1}$$

$$\chi \left(C_m \frac{\partial V_m}{\partial t} + I_{\text{ion}} \right) - \nabla \cdot (\sigma_i \nabla (V_m + \phi_e)) = -I_i^{\text{stim}}, \tag{5.2}$$

for the bidomain case, with

$$C_m = \rho_1 C_{m1} + \rho_2 C_{m2}, \tag{5.3}$$

$$I_{\text{ion}} = \rho_1 I_{\text{ion},1}(V_m, \mathbf{u}_1) + \rho_2 I_{\text{ion},2}(V_m, \mathbf{u}_2). \tag{5.4}$$

The differences in implementation arise as a result of equations (5.3) and (5.4), where we must now calculate weighted averaged values of the membrane capacitance per unit area, and the ionic current. This is a simple process for scalar values of C_m, but the calculation of I_{ion} can become more complicated.

Depending on the underlying structure of the electrophysiology models, optimisations may be available. The ionic current is typically calculated as the sum of N currents that pass through different ion channels i, usually taking the form

$$I_{\text{ion}} = \sum_{i=1}^{N} g_i O_i (V_m - E_{\text{ion}}), \tag{A1.1}$$

where g_i is the maximum conductance of all channels of type i and O_n is the probability of those channels being open. The driving voltage is calculated by taking the difference between the membrane voltage V_m and the reversal potential, E_{ion}, of the ion that passes through channel i.

If the two electrophysiology models used in a given simulation share a common structure and several parameters (as many electrophysiology model variants for different cellular phenotypes do), the efficiency of the calculation of I_{ion} can be improved by creating a customised cell model based on equation (5.4) that reduces the size of the combined ODE system. For a given current i, the homogenised version can be constructed using

$$I_{\text{ionH},i} = \begin{cases} \rho_1 g_{i,1} \hat{O}_{i,1} + \rho_2 g_{i,2} \hat{O}_{i,2} & \text{if} \quad g_{i,1} \neq g_{i,2}, \hat{O}_{i,1} \neq \hat{O}_{i,2} \\ (\rho_1 g_{i,1} + \rho_2 g_{i,2}) \hat{O}_i & \text{if} \quad g_{i,1} \neq g_{i,2}, \hat{O}_{i,1} = \hat{O}_{i,2} \\ g_i \hat{O}_i & \text{if} \quad g_{i,1} = g_{i,2}, \hat{O}_{i,1} = \hat{O}_{i,2} \end{cases}, \tag{A1.2}$$

where we have defined $\hat{O} = O(V_m - E_{\text{ion}})$. The topmost option corresponds to calculating the particular current in full for both models, due to differences in the channel kinetics or dependence on state variables that differ between the two

models. In the middle option, the maximal ion channel conductances are different but the rest of the channel model has a common structure. An effective average conductance can therefore be used. In the final case, the two ionic currents are identical and depend on state variables that are the same in both cell models; in this case, there is no need to calculate the current for both cell models separately.

The simulations that we perform in Chapter 5 utilise the monodomain form of the homogenised phenotypes model, but the changes to the implementation are the same as they only concern changes to the values of the ionic currents.

A1.1.2 Implementation of the partitioned phenotypes model

It is common practise to calculate the integral of the ionic current that arises in the finite element formulation of the monodomain and bidomain equations by matrix-based assembly. However, special consideration must be applied when multiple cellular phenotypes are present. We now describe the two options that are available for implementing the partitioned phenotypes model in the context of the monodomain problem; the extension to the bidomain equations follows naturally.

Node-wise phenotype definition

We recall from Section 4.3.2 that we may assume that the ionic current can be considered as a linear interpolation of the values of the ionic current at the nodes of the finite element mesh. Integration of the term can therefore be performed by multiplying the vector of nodal ionic current values by the mass matrix, as in

$$\int_\Omega \phi_j I_{\text{ion}} \, \mathrm{d}\mathbf{x} = \sum_{j=0}^{M} \left(\int_\Omega \phi_i \, \phi_j \, \mathrm{d}\mathbf{x} \right) I_{\text{ion},j} \tag{A1.3}$$

$$= \mathbf{M}\mathbf{i}_{\text{ion}} \tag{A1.4}$$

which shows the integration of the ionic current term from equation (4.22). The functions ϕ_i and ϕ_j are a basis function and a test function (the basis functions are a suitable choice for the test functions) at mesh node j, and we have dropped

the notation indicating the time-step for clarity, and $\mathbf{i}_{\text{ion}}$ is the vector of nodal values of the ionic current.

The node-wise implementation for a two (or more) phenotype system may be simply performed by including the ionic current from different cellular electrophysiology models in the ionic current vector. The values in $\mathbf{i}_{\text{ion}}$ are affected, but no further changes are made to the implementation.

However, there are issues associated with this approach. Figure A1.1 shows how the ionic current (indicated by the black dots) is interpolated across the elements of the mesh. While the assumption that linearly interpreting the values of I_{ion} appears valid in the top panel, where the same cell type (and thus electrophysiology model) is present across the entire domain, this is not the case in the middle panel. Should we attempt to perform the integration across the fourth mesh element, there is no guarantee that the resulting value is correct.

Element-wise phenotype definition

We should therefore revise the assumption that the ionic current is a linear interpolation of the nodal values now that we are considering a multi-phenotype system. Figure A1.1 demonstrates that an element-wise definition of phenotype gives a more realistic indication of the ionic current. While we now have a discontinuity in the ionic current at the node bordered by elements of different phenotype, there no region where the current is ill-defined.

We therefore introduce a modified version of the mass matrix to carry out the integration step for the two phenotypes. In Section 4.2.4, we showed how the entries of along the main diagonal of the mass matrix are $2h/3$ (apart from the first and last, which are $h/3$) and the entries along the first diagonals are $h/6$ for the one-dimensional, linear basis function, case. Schematically, the structure of the mass matrix may be represented by

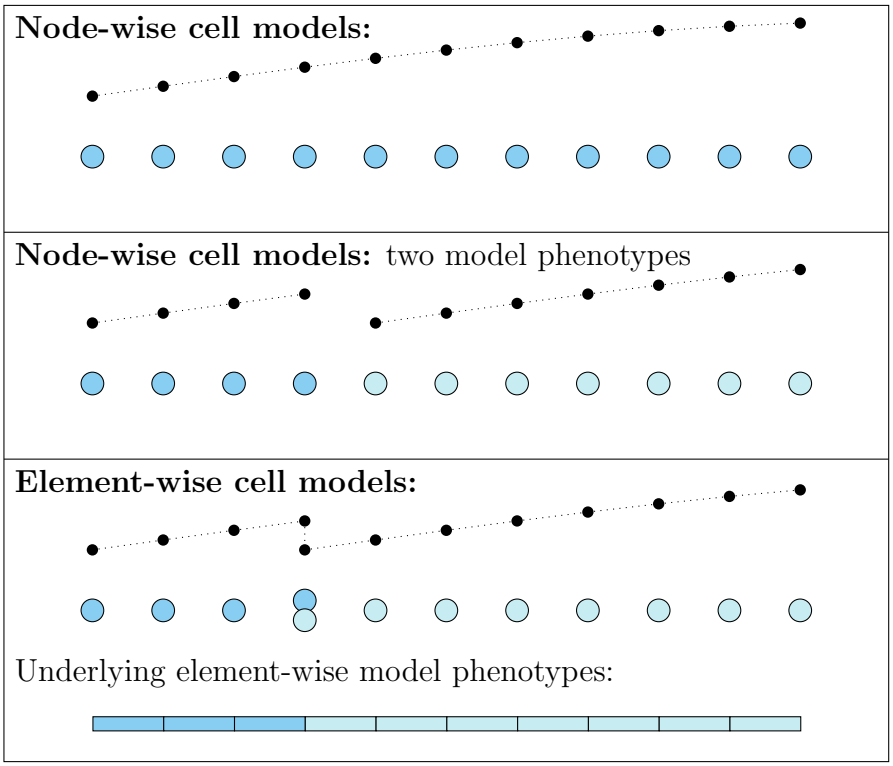

Figure A1.1: Comparison of the node-wise and element-wise implementations of the partitioned phenotypes model. Cell models of different phenotypes are denoted by dark and light blue circles, and the nodal ionic current is shown as black dots. Top: Assuming the ionic current over the domain to be the linear interpolant of the nodal values is reasonable in a single-phenotype tissue. Middle: Between nodes 3 and 4, there is a discontinuity in the ionic current as the boundary between the phenotypes is not clearly defined. Bottom: The element-wise implementation overcomes this problem by storing the ionic current of both phenotypes at nodes that lie on the region boundary. The appropriate value of ionic current can then be used in the interpolation step on either side of the boundary.

$$\mathbf{M} = \begin{pmatrix} \circ * & & & & & & & & & \\ * \bullet * & & & & & & & & & \\ & * \bullet * & & & & & & & & \\ & & * \bullet * & & & & & & & \\ & & & * \bullet * & & & & & & \\ & & & & * \bullet * & & & & & \\ & & & & & * \bullet * & & & & \\ & & & & & & * \bullet * & & & \\ & & & & & & & * \bullet * & & \\ & & & & & & & & * \bullet * & \\ & & & & & & & & * \circ \end{pmatrix} \tag{A1.5}$$

where we have used the one-dimensional, ten element example problem from Chapter 4. We have used the notation $\bullet = 2h/3$, $\circ = h/3$ (half of $\bullet$), $* = h/6$ and blank spaces represent empty entries.

In our modified mass matrices, the presence of these entries is dependent on the phenotype of the elements that neighbour the node linked to each matrix entry. The modified mass matrix for phenotype p therefore has entries of

$$\mathbf{M}_{\mathbf{p},i,i-1} = \int_{\Omega,p} \phi_i \phi_{i-1}\,\mathrm{d}x = \begin{cases} \frac{h}{6} & \text{if phenotype} = p \\ 0 & \text{otherwise} \end{cases} \tag{A1.6}$$

$$\mathbf{M}_{\mathbf{p},i,i} = \int_{\Omega,p} \phi_i \phi_i\,\mathrm{d}x \quad = \begin{cases} \frac{h}{3} & \text{if } i = 1 \text{ or } N+1 \text{ and phenotype} = p \\ \frac{h}{3} & \text{if phenotype} = p \text{ in one element} \\ \frac{2h}{3} & \text{if phenotype} = p \text{ in both elements} \\ 0 & \text{otherwise} \end{cases} \tag{A1.7}$$

$$\mathbf{M}_{\mathbf{p},i,i+1} = \int_{\Omega,p} \phi_i \phi_{i+1}\,\mathrm{d}x = \begin{cases} \frac{h}{6} & \text{if phenotype} = p \\ 0 & \text{otherwise.} \end{cases} \tag{A1.8}$$

The linear system used to solve a general partitioned phenotypes model with p types of cell is therefore

$$(\chi C_m \mathbf{M} + \sigma \mathbf{K})\mathbf{v}^n = \chi C_m \mathbf{M}\mathbf{v}^{n-1} - \Delta t \mathbf{M}\mathbf{i}_{\text{vol}}^{n-1} + \Delta t \chi \sum_p \mathbf{M}_{\mathbf{p}}\mathbf{i}_{\text{ion},p}^{n-1}, \tag{A1.9}$$

where $\mathbf{M}$ is the original mass matrix, $\mathbf{i}_{\text{vol}}$ is the vector of stimulus current values at the nodes, $\mathbf{M}_{\mathbf{p}}$ is the modified mass matrix for phenotype p and $\mathbf{i}_{\text{ion},p}$ is the vector of ionic current for phenotype p at the nodes. The stimulus current is now separated from the ionic current, in contrast to equation (5.7), as the stimulus is independent of the phenotype. If required, the stimulus current can also be defined in an element-wise manner through an analogous procedure.

The modified mass matrices for the ten-element example problem therefore have the structure

$$\mathbf{M}_1 = \begin{pmatrix} \circ & * & & & & & & & & \\ * & \bullet & * & & & & & & & \\ & * & \bullet & * & & & & & & \\ & & * & \circ & & & & & & \\ & & & & \circ & & & & & \\ & & & & & \circ & & & & \\ & & & & & & \circ & & & \\ & & & & & & & \circ & & \\ & & & & & & & & \circ & \\ & & & & & & & & & \circ \end{pmatrix} \quad \text{and} \quad \mathbf{M}_2 = \begin{pmatrix} \circ & & & & & & & & & \\ & \circ & & & & & & & & \\ & & \circ & & & & & & & \\ & & & \circ & * & & & & & \\ & & & * & \bullet & * & & & & \\ & & & & * & \bullet & * & & & \\ & & & & & * & \bullet & * & & \\ & & & & & & * & \bullet & * & \\ & & & & & & & * & \bullet & * \\ & & & & & & & & * & \circ \end{pmatrix}, \tag{A1.10}$$

where we have used $\circ$ to denote matrix entries which are now zero, but would have been non-zero in the original mass matrix.

In the Chaste library, the default behaviour is to use the node-wise definition of the cellular electrophysiology model. As part of this project, work was carried out to change to an element-wise definition of cellular electrophysiology models in tissue simulations. A description of this work may be found in Section A1.2.1.

A1.1.3 Typical simulation timings

The simulations in Chapter 5 were carried out on the University of Oxford's Advanced Research Computing[1] resources, specifically, the `arcus-b` cluster. The duration of the simulations that utilised the FitzHugh-Nagumo model (i.e. Sets 1–5, as described in Section 5.4.1), were not long, but the number of simulations performed meant that use of high performance computing resources was necessary.

The Matlab code used in these simulations was designed for ease of usability and clarity rather than efficiency, so the duration of these simulations is rather long compared to those performed in the later chapters of this thesis where the Chaste library was used. As an example, simulations from Set 5 (FitzHugh-Nagumo model with spatially varying phenotype) took approximately one hour, while those from Set 6 (Paci et al. (2013a) model with spatially varying phenotype) took approximately 15 hours. Each simulation utilised only one core in a given node, so it was possible to perform several at once (usually eight, depending on the amount of memory required to store the results). The simulations using the Paci et al. (2013a) model took substantially longer due to the greater complexity of the cellular electrophysiology model.

A1.2 Bidomain Simulations in Chaste

The additional computational effort involved in solving the bidomain equations, and our move to two-dimensional simulations over one-dimensional ones, meant that a more efficient approach to the Matlab solver was called for. The *Cancer, Heart and Soft Tissue Environment*, Chaste, was used for all the simulations in Chapters 6 and 7 of this thesis. We reviewed the main features of Chaste in Section 4.5.1; here, we describe our contributions to and our use of the library.

[1] `http://dx.doi.org/10.5281/zenodo.22558`

A1.2.1 Implementation of the partitioned phenotypes model

As part of this project, Chaste has been modified to solve monodomain and bidomain problems with element-wise cell models in the manner described in Section A1.1.2. This code is not included in the public release as it is not yet fully tested and would also cause changes to the results of existing simulations. It can be found in the `ElementWiseCellModels` branch of the SVN repository for the Chaste project.

In the new branch, attributes assigned to each element dictate the cellular electrophysiology models stored at each of the nodes associated with the element. Neighbouring elements with different attributes thus have more than one cell model stored at the node between them. In addition to the usual mass matrix, modified mass matrices are also created as described in Section A1.1.2.

The ionic current vectors are populated based on the model phenotype, and integrated by matrix-based assembly using the modified mass matrices. The solution for the membrane voltage is then calculated by solving the linear system stated in equation (A1.9).

We have also implemented the same procedure for the stimulus current, which until now was also defined node-wise. Previously, the total magnitude of the stimulus may have changed if the inter-node spacing was altered (for instance, if a stimulus was applied to only one node). With the recent changes, the addition of extra nodes between existing ones does not alter the extent of the mesh to which the stimulus is applied, thus giving more consistent results when different meshes are used.

A1.2.2 Contribution of the reference electrodes

In Section 6.4.3, we discussed the presence of a reference electrode in the micro-electrode array, and how it could be implemented in our bidomain simulations.

The Axion Biosystems 96-well MEA plates include four large reference electrodes, equally spaced close to the outer rim of the wells (see Figure 6.2 for a schematic). In Figure A1.2, we provide an example of the contribution of the

reference electrodes in our model to the overall field potential. Taking the mean potential of the reference electrodes to define $\int_{\Omega_{\text{ref}}} \phi_{e,\text{ref}} \, \mathrm{d}\mathbf{x} = 0$, rather than the using the average of the entire domain as a reference potential (as output by the solver), causes little change to the field potential at the recording electrodes.

In all examples of waves from different origins that we tested on this geometry, the field potential and ϕ_e at recording electrodes were very similar. The case where we might expect to see the most extreme discrepancy, that where we have a wave propagating outwards from the centre of the domain that crosses all four reference electrodes at the same time, was studied as part of the investigations in Section 6.5. In Figure A1.3, we show an example of the difference between ϕ_e and the field potential for this case: while there is a moderate difference in the spike amplitude, the repolarising wave is changed little, and the overall morphology of the wave is unaffected.

As the repolarising wave is the most relevant output for the safety assessment applications of our work, we should expect our approximation of FP $\approx \phi_e$ to have little effect on the conclusions drawn from our qualitative simulation study so we have simply used ϕ_e (relative to mean potential across the whole well) to represent the field potential in the main text.

This simplification will, of course, be heavily dependent upon the geometry of the reference electrode(s). For instance, the MEAs used at GlaxoSmithKline (produced by MultiChannel Systems), contain a single, large, reference electrode to the side of the recording electrodes. In that case, we expect the reference electrode potential may differ far more from the mean extracellular potential, and so the field potential should be calculated for each simulation.

The reference and field potentials in Figure A1.2 and Figure A1.3 were generated using custom-written Matlab code after the simulations had been performed. It would be preferable to calculate the field potential as part of the simulation itself (to minimise data storage requirements), which could be achieved via several methods in Chaste. The first would be to define an `OutputModifier` to calculate the mean potential across the reference electrodes, subtract this from

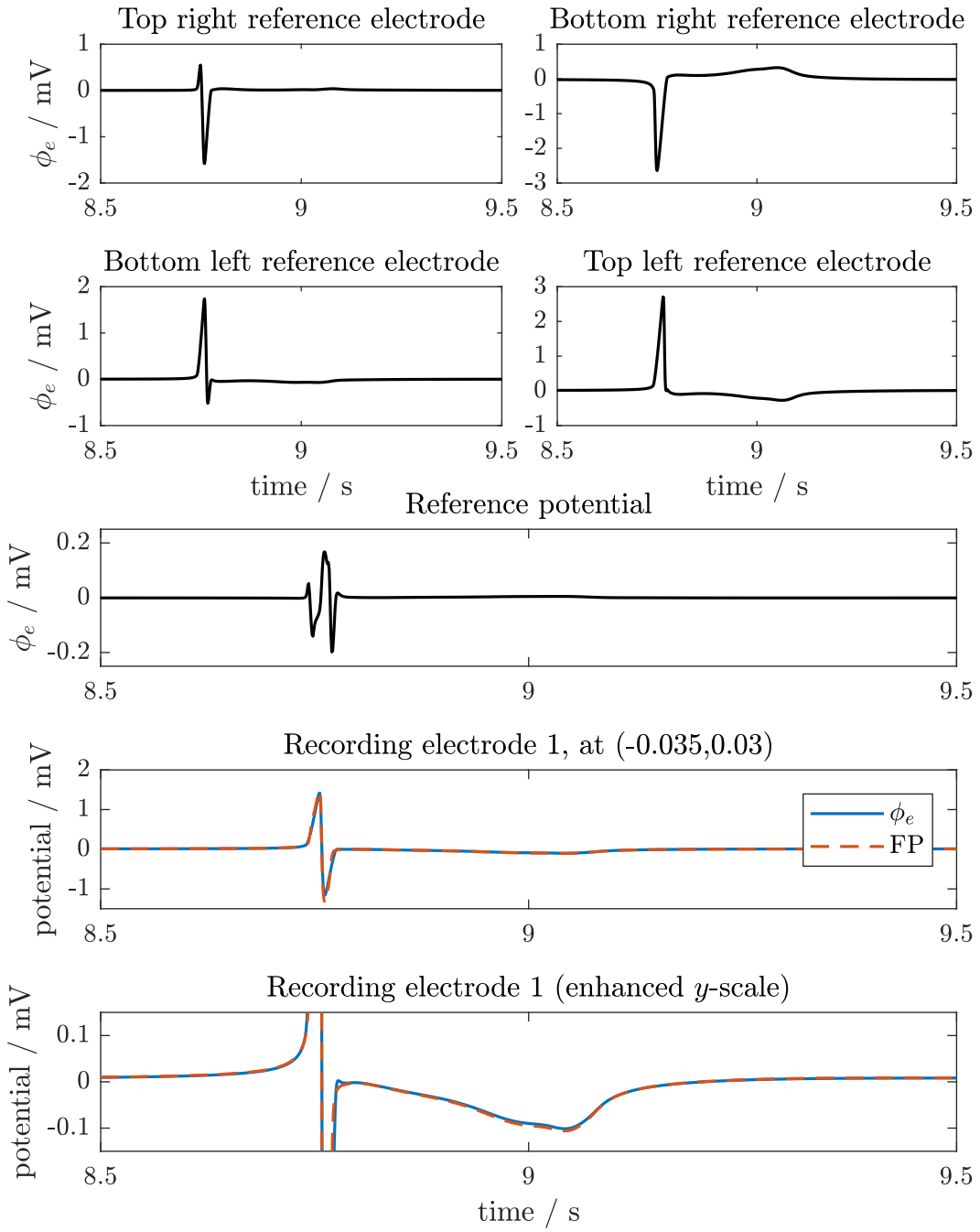

Figure A1.2: Contributions to the field potential in a monolayer with a randomly generated phenotype arrangement. The top four panels show the average extracellular potential across each of the four reference electrodes. The overall average reference potential is shown in the middle panel. The lower two panels demonstrate the differences between the extracellular potential at the recording electrode and the full field potential. This example was taken from a monolayer simulated under control conditions, with the phenotype distribution set using the first realisation of random field C. The simulation was performed as part of the investigation described in Section 6.7.

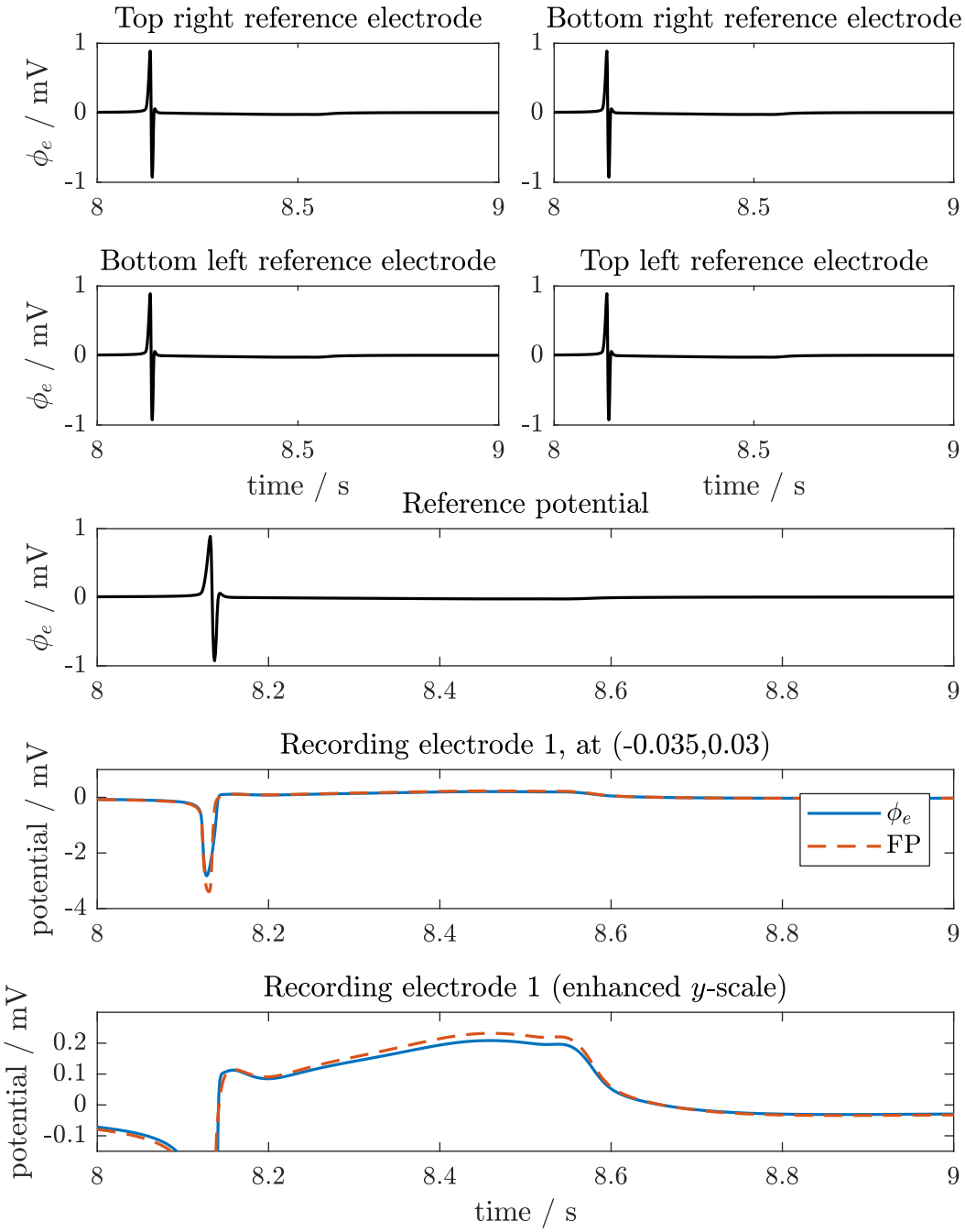

Figure A1.3: Contributions to the field potential in a monolayer with a central pacemaking region. As for Figure A1.2, the top four panels show the average extracellular potential at the four reference electrodes; this time all four exhibit the same shape of depolarising spike at the same time. The overall average potential in the middle panel is now closer to the extracellular potential at the recording electrodes than in the previous case, and so we see a difference in the spike amplitudes of the field and extracellular potentials in the panel below. However, the repolarising wave, shown in the lowest panel, is little affected. This simulation was performed as part of the investigation described in Section 6.5, with parameters $x = 0, y = 0, r = 0.1$ and $a = 1$ (see Table 6.2 for details of these parameters).

the values of extracellular potential, and output the field potential. The second method would be to alter the approach used when solving the linear system. Rather than using a null-space solver, an additional row could be added on to the linear system and used to select at which nodes the values of the extracellular potential should sum to zero (i.e. the nodes that are located within the reference electrode). As the system would now be non-symmetric, an alternative solver to conjugate gradients would have to be used; likely GMRES. This approach is compared to the null-space approach in Pathmanathan et al. (Section 5, 2010), where it was found that the GMRES solver would require far more iterations to solve the modified linear system. If the reference electrode is studied in more detail as part of future work, the efficiency of the approach used to model it should therefore also be taken into account.

A1.2.3 Typical simulation timings

In Chapter 6, we performed simulations of 10 s of activity across the monolayer. The simulations were extended to 15 s duration in Chapter 7. Due to the number of simulations that were performed (over 1000 in total), and the computational cost associated with each, all simulations were performed on the University of Oxford's Advanced Research Computing resources.

Each simulation utilised 16 cores on one node of the cluster, which was usually `arcus.ox.ac.uk`. The 10 s simulations typically required around one hour of walltime in this configuration, with the 15 s simulations needing approximately 90 minutes. The vast majority of the simulations took within ten minutes of the above time estimates; however, far longer durations (upwards of two hours) were required for some simulations, notably those approaching synchrony where the activation times were very similar across the monolayer.

The largest fraction of compute time was used for solving the system of ordinary differential equations, with this usually taking upwards of 80% of the total time. The next largest contributions were from the linear solver (around 10%) and output (around 5%).

A1.2.4 Analysis

Analysis of the action and field potentials generated by the simulations throughout Chapters 6 and 7 was carried out using custom Matlab routines. Chaste itself does contain the functionality to perform some of this analysis (for instance, generation of activation time maps and calculation of APD_{90}), but the routines in Chaste depend upon knowledge of the starting time of each beat — something which is not available to us when the simulated systems spontaneously activate.

The algorithms for calculating each of the biomarkers were described briefly in Section 6.2.3. At present, the code for analysis and generation of the figures found in Chapters 6 and 7 is stored in a private Github repository, to which access can be granted upon request.

Appendix 2

Supplementary Information for Chapter 5

This Appendix contains additional material relevant to the work covered in Chapter 5, Models of Multiple Cellular Phenotypes in Cardiac Tissue.

A2.1 Modification of the Bidomain Equations for Multiple Cellular Phenotypes

This derivation was prepared by Jonathan Whiteley for our paper "Representation of Multiple Cellular Phenotypes Within Tissue-Level Simulations of Cardiac Electrophysiology" (Bowler et al., 2019).

The derivation of the HP model is very similar to the derivation of the bidomain equations given by other authors (Neu and Krassowska, 1993; Keener and Panfilov, 1996; Keener and Sneyd, 2008; Hand and Griffith, 2010; Hand and Griffith, 2011; Richardson and Chapman, 2011; Bruce et al., 2014). By including different cell types in the spatial unit that we homogenise over we must take account of cell parameters that depend on the micro-scale coordinate. We therefore follow the approach of Bruce et al. (2014) who allowed some cell parameters to vary when modelling gap junctions. The derivation of the PP model is simpler

than that of the HP model, and follows naturally from the derivation of the latter. We therefore describe the derivation of the HP model first, and then explain how this may be modified to obtain the PP model.

In Section A2.1.1, we begin by writing down a discrete model that partitions cardiac tissue into an intracellular region and an extracellular region, and nondimensionalise the governing equations in Section A2.1.2. We then set the scene for the homogenisation by defining the macroscale and microscale coordinates, and the periodic unit that we homogenise over, in Section A2.1.3. We proceed with the derivation of the homogenised equations in intra and extracellular space in Sections A2.1.3 and A2.1.3 allowing us to write down the HP model for well-mixed cellular phenotypes in Section A2.1.4. The collapse of the HP model to the PP model is described in Section A2.1.5.

A2.1.1 The discrete domains model

We assume that cardiac tissue occupying a region can be partitioned into an intracellular region denoted by Ω_i, and an extracellular region denoted by Ω_e. These two regions are separated by the cell membrane, assumed to be of negligible thickness, denoted by Γ_m. The intracellular space and extracellular space have scalar conductivities σ_i and σ_e respectively. We will allow σ_i to vary spatially to take account of different cell types, but will assume that σ_e is constant. By Ohm's law, the intracellular and extracellular currents are given by

$$\mathbf{i}_i = -\sigma_i \nabla \phi_i, \qquad \mathbf{x} \in \Omega_i,$$
$$\mathbf{i}_e = -\sigma_e \nabla \phi_e, \qquad \mathbf{x} \in \Omega_e,$$

where ϕ_i, ϕ_e are the intracellular and extracellular potentials. Conservation of current in the intracellular and extracellular space then gives

$$\nabla \cdot (\sigma_i \nabla \phi_i) = 0, \qquad \mathbf{x} \in \Omega_i, \tag{A2.1}$$
$$\nabla \cdot (\sigma_e \nabla \phi_e) = 0, \qquad \mathbf{x} \in \Omega_e. \tag{A2.2}$$

The boundary conditions that model the flux of current across the cell membrane may be written

$$-\sigma_i \nabla\phi_i \cdot \mathbf{n} = I_m, \qquad -\sigma_e \nabla\phi_e \cdot \mathbf{n} = -I_m, \qquad \mathbf{x} \in \Gamma_m, \tag{A2.3}$$

where $\mathbf{n}$ is the unit vector, normal to Γ_m, that points from the intracellular space into the extracellular space, and I_m is the transmembrane current per unit area flowing into the intracellular space from the extracellular space. Modelling the cell membrane as a capacitor, I_m is given by

$$I_m = C_m \frac{\partial v}{\partial t} + I_{\text{ion}}, \tag{A2.4}$$

where C_m is the capacitance of the membrane per unit area, $v = \phi_i - \phi_e$ is the transmembrane potential, t is time, $I_{\text{ion}}(v; \mathbf{u})$ is the net current per unit area due to the flux of ions across the membrane, and $\mathbf{u}$ contains quantities that are specified by a model of the flow of ions across the cell membrane. As we are modelling more than one cell type we allow both C_m and I_{ion} to vary spatially.

A2.1.2 Nondimensionalisation

We nondimensionalise the equations given in Section A2.1.1 using the following scalings:

$$t = T\hat{t}, \qquad \mathbf{x} = L\hat{\mathbf{x}}, \qquad \sigma_i = \bar{\Sigma}\hat{\sigma}_i, \qquad \sigma_e = \bar{\Sigma}\hat{\sigma}_e,$$
$$\phi_i = \Phi\hat{\phi}_i, \qquad \phi_e = \Phi\hat{\phi}_e, \qquad v = \Phi\hat{v}, \qquad C_m = \bar{C}\hat{C}_m \qquad I_{\text{ion}} = \bar{I}\hat{I}_{\text{ion}},$$

where T is a typical timescale, L is a typical lengthscale for the solution (rather than the length of a myocyte), $\bar{\Sigma}$ is representative of the scalar conductivities, Φ is representative of the potential difference across the cell membrane, $\bar{C}$ is representative of the capacitance, and $\bar{I}$ is representative of the ionic current per unit area. Equations (A2.1) and (A2.2) may then be written in nondimensional form as

$$\nabla \cdot \left(\hat{\sigma}_i \nabla\hat{\phi}_i\right) = 0, \qquad \hat{\mathbf{x}} \in \Omega_i, \tag{A2.5}$$

$$\nabla \cdot \left(\hat{\sigma}_e \nabla\hat{\phi}_e\right) = 0, \qquad \hat{\mathbf{x}} \in \Omega_e, \tag{A2.6}$$

and we can reformulate the boundary conditions of equation (A2.3) using the definition of I_m from equation (A2.4) to give

$$-\hat{\sigma}_i \nabla \hat{\phi}_i \cdot \hat{\mathbf{n}} = \mathcal{A}\hat{C}_m \frac{\partial \hat{v}}{\partial \hat{t}} + \mathcal{B}\hat{I}_{\text{ion}}, \qquad \hat{\mathbf{x}} \in \Gamma_m, \tag{A2.7}$$

$$-\hat{\sigma}_e \nabla \hat{\phi}_e \cdot \hat{\mathbf{n}} = -\mathcal{A}\hat{C}_m \frac{\partial \hat{v}}{\partial \hat{t}} - \mathcal{B}\hat{I}_{\text{ion}}, \qquad \hat{\mathbf{x}} \in \Gamma_m, \tag{A2.8}$$

where the nondimensional constants $\mathcal{A}$ and $\mathcal{B}$ are given by

$$\mathcal{A} = \frac{\bar{C}L}{T\bar{\Sigma}}, \qquad \mathcal{B} = \frac{\bar{I}L}{\Phi\bar{\Sigma}}. \tag{A2.9}$$

For the remainder of this derivation we use the nondimensional equations (A2.5) to (A2.8) presented above, dropping hats for clarity.

A2.1.3 Derivation of the homogenised equations

To allow us to homogenise the equations presented in Section A2.1.2 we make the assumption that cardiac tissue is a periodic lattice of repeating cuboid units, where each unit contains a small number of cardiac cells. We showed a representation of this lattice in two dimensions previously in Figure 5.2, on page 77. No assumptions are made regarding the type of cells within each unit of the lattice: we allow the cells to have different shapes, sizes, capacitances and conductivities, and also allow the ionic current passing through the cell membrane to take different functional forms depending on which cell type the membrane belongs to. We assume that the dimensions of the cuboid unit is much smaller than the lengthscale for the solution, L.

The domains and coordinate systems

We assume that the lengthscale for the solution, L, is much greater than the lengthscale of each unit in the lattice, l. We then define the nondimensional parameter δ by

$$\delta = \frac{\text{lengthscale of unit we homogenise over } (= l)}{\text{lengthscale for solution } (= L)}, \tag{A2.10}$$

and note that our assumptions on the lengthscales allow us to deduce that $\delta \ll 1$.

In Section 2.5.1 we explained that hSC-CMs are small and rounded, with diameters of approximately 10–50 µm unless the maturation process is promoted by further means. Setting $l = 200\,\mu\text{m}$ allows us to homogenise over a unit containing several cells. Further, $L = 2000\,\mu\text{m}$ is a representative lengthscale of the solution, yielding $\delta = 0.1$, and $T = 10^{-2}\,\text{s}$ is a representative timescale of the solution. Other parameters that appear in the nondimensional constants $\mathcal{A}$ and $\mathcal{B}$ defined by equation (A2.9) are: $\bar{C} = 1\,\mu\text{F cm}^{-2}$ (from Table 5.2); $\bar{\Sigma} = 0.3\,\text{mS cm}^{-1}$ (from Table 5.2); $\bar{I} = 2 \times 10^{-5}\,\text{A cm}^{-2}$ (from Paci et al. (2013a)); and $\Phi = 7 \times 10^{-2}\,\text{V}$ (from (Paci et al., 2013a)). We may then deduce that the nondimensional constants $\mathcal{A}$ and $\mathcal{B}$ defined by equation (A2.9) satisfy $\mathcal{A} = \mathcal{O}(\delta)$ and $\mathcal{B} = \mathcal{O}(\delta)$, and write

$$\mathcal{A} = \mathcal{A}_1\delta, \qquad \mathcal{B} = \mathcal{B}_1\delta, \tag{A2.11}$$

where $\mathcal{A}_1 = \mathcal{O}(1)$, and $\mathcal{B}_1 = \mathcal{O}(1)$. This is identical to the distinguished limit investigated by Richardson and Chapman (2011) when deriving the tissue scale bidomain equations, and is consistent with the parameters used in typical bidomain simulations; see, for example, Morgan et al. (2009) and Bishop and Plank (2012).

We will utilise the separation of scales described above by introducing a microscale coordinate $\mathbf{z}$, defined by

$$\mathbf{z} = \frac{1}{\delta}\mathbf{x}, \tag{A2.12}$$

where $\mathbf{x}$ is the macroscale coordinate used in Section A2.1.1.

Derivation of the homogenised equation in intracellular space

We write $\phi_i = \phi_i(\mathbf{x}, \mathbf{z}, t)$, where ϕ_i is periodic in $\mathbf{z}$. Using the definition of the microscale and macroscale coordinates given by equation (A2.12) we see that

$$\nabla\phi_i = \nabla_{\mathbf{x}}\phi_i + \frac{1}{\delta}\nabla_{\mathbf{z}}\phi_i, \tag{A2.13}$$

where $\nabla_{\mathbf{x}}$ and $\nabla_{\mathbf{z}}$ are the gradient operators with respect to the $\mathbf{x}$ and $\mathbf{z}$ coordinates, respectively. We then write ϕ_i as a regular asymptotic expansion in the

parameter δ:

$$\phi_i(\mathbf{x},\mathbf{z},t) = \phi_0^{(\text{in})}(\mathbf{x},\mathbf{z},t) + \delta\phi_1^{(\text{in})}(\mathbf{x},\mathbf{z},t) + \delta^2\phi_2^{(\text{in})}(\mathbf{x},\mathbf{z},t) + \ldots, \tag{A2.14}$$

where all functions in the expansion are periodic in $\mathbf{z}$. We assume that $\sigma_i = \sigma_i(\mathbf{z})$ to allow for different conductivities should cell types with different conductivities be present in the unit that we homogenise over. Substituting equations (A2.13) and (A2.14) into equation (A2.5) and collecting equal powers of δ gives, for $\mathbf{z} \in \Omega_i$.

$$\delta^{-2}: \qquad \nabla_{\mathbf{z}} \cdot \left[\sigma_i(\mathbf{z})\nabla_{\mathbf{z}}\phi_0^{(\text{in})}\right] = 0, \tag{A2.15}$$

$$\delta^{-1}: \qquad \nabla_{\mathbf{x}} \cdot \left[\sigma_i(\mathbf{z})\nabla_{\mathbf{z}}\phi_0^{(\text{in})}\right] + \nabla_{\mathbf{z}} \cdot \left[\sigma_i(\mathbf{z})\left(\nabla_{\mathbf{x}}\phi_0^{(\text{in})} + \nabla_{\mathbf{z}}\phi_1^{(\text{in})}\right)\right] = 0, \tag{A2.16}$$

$$\delta^{0}: \quad \nabla_{\mathbf{x}} \cdot \left[\sigma_i(\mathbf{z})\left(\nabla_{\mathbf{x}}\phi_0^{(\text{in})} + \nabla_{\mathbf{z}}\phi_1^{(\text{in})}\right)\right] + \nabla_{\mathbf{z}} \cdot \left[\sigma_i(\mathbf{z})\left(\nabla_{\mathbf{x}}\phi_1^{(\text{in})} + \nabla_{\mathbf{z}}\phi_2^{(\text{in})}\right)\right] = 0. \tag{A2.17}$$

Similarly using equation (A2.7) and using equation (A2.11), we may equate powers of δ to generate the following boundary conditions:

$$\delta^{-1}: \qquad -\sigma_i(\mathbf{z})\nabla_{\mathbf{z}}\phi_0^{(\text{in})} \cdot \mathbf{n} = 0, \tag{A2.18}$$

$$\delta^{0}: \quad -\sigma_i(\mathbf{z})\left(\nabla_{\mathbf{x}}\phi_0^{(\text{in})} + \nabla_{\mathbf{z}}\phi_1^{(\text{in})}\right) \cdot \mathbf{n} = 0, \tag{A2.19}$$

$$\delta^{1}: \quad -\sigma_i(\mathbf{z})\left(\nabla_{\mathbf{x}}\phi_1^{(\text{in})} + \nabla_{\mathbf{z}}\phi_2^{(\text{in})}\right) \cdot \mathbf{n} = \mathcal{A}_1 C_m \frac{\partial v}{\partial t} + \mathcal{B}_1 I_{\text{ion}}. \tag{A2.20}$$

The differential equation (A2.15), and boundary condition (A2.18), are satisfied by

$$\phi_0^{(\text{in})} = \phi_0^{(\text{in})}(\mathbf{x},t), \tag{A2.21}$$

and so there is no $\mathbf{z}$ dependence in the solution for ϕ_i at leading order, as expected. We now turn our attention to the differential equation (A2.16), and boundary condition (A2.19). Equation (A2.21) allows us to deduce that the first term on the left hand side of equation (A2.16) is zero. The structure of this equation and boundary condition suggests seeking a solution

$$\phi_1^{(\text{in})}(\mathbf{x},\mathbf{z},t) = W_1^{(\text{in})}(\mathbf{z})\frac{\partial\phi_0^{(\text{in})}}{\partial x_1} + W_2^{(\text{in})}(\mathbf{z})\frac{\partial\phi_0^{(\text{in})}}{\partial x_2} + W_3^{(\text{in})}(\mathbf{z})\frac{\partial\phi_0^{(\text{in})}}{\partial x_3}, \tag{A2.22}$$

for functions $W_1^{(\text{in})}, W_2^{(\text{in})}, W_3^{(\text{in})}$ to be determined. The differential equation and boundary condition given by equations (A2.16) and (A2.19) are then satisfied providing, for $j = 1, 2, 3$,

$$\nabla_{\mathbf{z}} \cdot \left(\sigma_i(\mathbf{z}) \nabla_{\mathbf{z}} W_j^{(\text{in})} \right) = -\frac{\partial \sigma_i}{\partial z_j}, \qquad \mathbf{z} \in \Omega_i, \tag{A2.23}$$

$$\left(\sigma_i(\mathbf{z}) \nabla_{\mathbf{z}} W_j^{(\text{in})} \right) \cdot \mathbf{n} = -\sigma_i n_j, \qquad \mathbf{z} \in \Gamma_m, \tag{A2.24}$$

where $W_1^{(\text{in})}, W_2^{(\text{in})}, W_3^{(\text{in})}$ are periodic in $\mathbf{z}$, and n_j is component j of $\mathbf{n}$, $j = 1, 2, 3$.

Integrating equation (A2.17), the differential equation at order δ^0, over the intracellular space component of the unit we are homogenising over (denoted by $\hat{\Omega}_i$) yields

$$\int_{\hat{\Omega}_i} \nabla_{\mathbf{x}} \cdot \left[\sigma_i(\mathbf{z}) \left(\nabla_{\mathbf{x}} \phi_0^{(\text{in})} + \nabla_{\mathbf{z}} \phi_1^{(\text{in})} \right) \right] \mathrm{d}V_{\mathbf{z}} + \int_{\hat{\Omega}_i} \nabla_{\mathbf{z}} \cdot \left[\sigma_i(\mathbf{z}) \left(\nabla_{\mathbf{x}} \phi_1^{(\text{in})} + \nabla_{\mathbf{z}} \phi_2^{(\text{in})} \right) \right] \mathrm{d}V_{\mathbf{z}} = 0.$$

Applying the divergence theorem to the second integral in the equation above gives

$$\int_{\hat{\Omega}_i} \nabla_{\mathbf{x}} \cdot \left[\sigma_i(\mathbf{z}) \left(\nabla_{\mathbf{x}} \phi_0^{(\text{in})} + \nabla_{\mathbf{z}} \phi_1^{(\text{in})} \right) \right] \mathrm{d}V_{\mathbf{z}} + \int_{\partial \hat{\Omega}_i} \left[\sigma_i(\mathbf{z}) \left(\nabla_{\mathbf{x}} \phi_1^{(\text{in})} + \nabla_{\mathbf{z}} \phi_2^{(\text{in})} \right) \right] \cdot \mathbf{n} \, \mathrm{d}V_{\mathbf{z}} = 0.$$

Using the boundary condition given by equation (A2.20) and periodicity in $\mathbf{z}$ then gives

$$\int_{\hat{\Omega}_i} \nabla_{\mathbf{x}} \cdot \left[\sigma_i(\mathbf{z}) \left(\nabla_{\mathbf{x}} \phi_0^{(\text{in})} + \nabla_{\mathbf{z}} \phi_1^{(\text{in})} \right) \right] \mathrm{d}V_{\mathbf{z}} = \int_{\Gamma_m} \mathcal{A}_1 C_m \frac{\partial v}{\partial t} + \mathcal{B}_1 I_{\text{ion}} \, \mathrm{d}S_{\mathbf{z}}.$$

Denoting the volume of the repeating unit by $|\Omega|$, equations (A2.21) and (A2.22) then allow us to write

$$\nabla_{\mathbf{x}} \cdot \left(\Sigma_i \nabla_{\mathbf{x}} \phi_0^{(\text{in})} \right) = \frac{1}{|\Omega|} \int_{\Gamma_m} \left(\mathcal{A}_1 C_m \frac{\partial v}{\partial t} + \mathcal{B}_1 I_{\text{ion}} \right) \mathrm{d}S_{\mathbf{z}}, \tag{A2.25}$$

$$\text{with } \Sigma_i = \frac{1}{|\Omega|} \int_{\hat{\Omega}_i} \sigma_i(\mathbf{z}) \left(\mathcal{I} + \frac{\partial \mathbf{W}^{(\text{in})}}{\partial \mathbf{z}} \right) \mathrm{d}V_{\mathbf{z}}, \tag{A2.26}$$

where $\mathcal{I}$ is the identity matrix, and the matrix $\partial \mathbf{W}^{(\text{in})} / \partial \mathbf{z}$ has entries given by

$$\left(\frac{\partial \mathbf{W}^{(\text{in})}}{\partial \mathbf{z}} \right)_{jk} = \frac{\partial W_j^{(\text{in})}}{\partial z_k}, \quad j, k = 1, 2, 3.$$

We note that the homogenised conductivity tensor would not be calculated in practice using equation (A2.26) as this would require extremely high resolution imaging in three-dimensional space to determine the domain occupied by a cell. Rather, equation (A2.25) serves to demonstrate the structure of the differential equation satisfied by the leading order intracellular potential. The entries of the homogenised conductivity tensor are determined by fitting to experimental values of conduction velocity.

The homogenised equation in extracellular space

Using a similar argument we may also write ϕ_e as a regular asymptotic expansion in the variable δ:

$$\phi_e(\mathbf{x},\mathbf{z},t) = \phi_0^{(\mathrm{ex})}(\mathbf{x},\mathbf{z},t) + \delta\phi_1^{(\mathrm{ex})}(\mathbf{x},\mathbf{z},t) + \delta^2\phi_2^{(\mathrm{ex})}(\mathbf{x},\mathbf{z},t) + \ldots,$$

where all functions in the expansion are periodic in $\mathbf{z}$, and deduce that

$$\nabla_{\mathbf{x}} \cdot \left(\Sigma_e \nabla_{\mathbf{x}} \phi_0^{(\mathrm{ex})}\right) = -\frac{1}{|\Omega|}\int_{\Gamma_m} \left(\mathcal{A}_1 C_m \frac{\partial v}{\partial t} + \mathcal{B}_1 I_{\mathrm{ion}}\right) \mathrm{d}S_{\mathbf{z}}, \tag{A2.27}$$

$$\text{where } \Sigma_e = \frac{1}{|\Omega|}\int_{\hat{\Omega}_e} \sigma_e \left(\mathcal{I} + \frac{\partial \mathbf{W}^{(\mathrm{ex})}}{\partial \mathbf{z}}\right) \mathrm{d}V_{\mathbf{z}}, \tag{A2.28}$$

where $\hat{\Omega}_e$ is the extracellular space component of the unit we are homogenising over. Remembering that σ_e is assumed to be constant, the equations for the functions $W_1^{(\mathrm{ex})}, W_2^{(\mathrm{ex})}, W_3^{(\mathrm{ex})}$ satisfy simpler differential equations than the corresponding functions $W_1^{(\mathrm{in})}, W_2^{(\mathrm{in})}, W_3^{(\mathrm{in})}$ for the intracellular space, defined by equations (A2.23) and (A2.24). In this case the functions $W_1^{(\mathrm{ex})}, W_2^{(\mathrm{ex})}, W_3^{(\mathrm{ex})}$, periodic in $\mathbf{z}$, satisfy

$$\begin{aligned} \nabla_{\mathbf{z}}^2 W_j^{(\mathrm{ex})} &= 0, & \mathbf{z} &\in \Omega_e, \\ \nabla_{\mathbf{z}} W_j^{(\mathrm{ex})} \cdot \mathbf{n} &= -n_j, & \mathbf{z} &\in \Gamma_m. \end{aligned}$$

A2.1.4 The homogenised phenotypes model

Before we can write down the bidomain equations we need to evaluate the integral that appears on the right hand side of equations (A2.25) and (A2.27) when the

repeating unit that we homogenise over comprises two distinct varieties of cardiac cell. We write v as the asymptotic expansion given by

$$v(\mathbf{x}, \mathbf{z}, t) = V(\mathbf{x}, t) + \delta v_1(\mathbf{x}, \mathbf{z}, t) + \delta^2 v_2(\mathbf{x}, \mathbf{z}, t) + \ldots, \tag{A2.29}$$

We first partition the cell membrane into two regions, Γ_{m1} and Γ_{m2}, where Γ_{m1} represents the membrane between the first cell type and the extracellular space, and Γ_{m2} represents the membrane between the second cell type and the extracellular space. These two cell types have capacitances C_{m_1}, C_{m_2}, and ionic currents $I_{\text{ion},1}, I_{\text{ion},2}$. We may then write the integral on the right hand side of equations (A2.25) and (A2.27) as

$$\int_{\Gamma_m} \mathcal{A}_1 C_m \frac{\partial v}{\partial t} + \mathcal{B}_1 I_{\text{ion}} \, \mathrm{d}S_{\mathbf{z}} = \int_{\Gamma_{m1}} \mathcal{A}_1 C_{m_1} \frac{\partial v}{\partial t} + \mathcal{B}_1 I_{\text{ion},1}(v; \mathbf{u}_1) \, \mathrm{d}S_{\mathbf{z}} + \int_{\Gamma_{m2}} \mathcal{A}_1 C_{m_2} \frac{\partial v}{\partial t} + \mathcal{B}_1 I_{\text{ion},2}(v; \mathbf{u}_2) \, \mathrm{d}S_{\mathbf{z}}.$$

The surface area, S, of the membrane within the unit that we homogenise over is partitioned in the proportions ρ_1, ρ_2 of the cell membrane of cell types 1 and 2 within the unit volume. Using the asymptotic expansion of v given by equation (A2.29), we obtain, to leading order,

$$\int_{\Gamma_m} \mathcal{A}_1 C_m \frac{\partial v}{\partial t} + \mathcal{B}_1 I_{\text{ion}} \, \mathrm{d}S_{\mathbf{z}} = S\mathcal{A}_1 \big(\rho_1 C_{m_1} + \rho_2 C_{m_2}\big) \frac{\partial V}{\partial t} + S\mathcal{B}_1 \big(\rho_1 I_{\text{ion},1}(V; \mathbf{u}_1) + \rho_2 I_{\text{ion},2}(V; \mathbf{u}_2)\big). \tag{A2.30}$$

Using equations (A2.25), (A2.27) and (A2.30) we may write down the bidomain equations for our homogenised system,

$$\nabla \cdot (\Sigma_i \nabla \Phi_i) = \chi \bigg(\mathcal{A}_1 C_m \frac{\partial V}{\partial t} + \mathcal{B}_1 I_{\text{ion}} \bigg), \tag{A2.31}$$

$$\nabla \cdot (\Sigma_e \nabla \Phi_e) = -\chi \bigg(\mathcal{A}_1 C_m \frac{\partial V}{\partial t} + \mathcal{B}_1 I_{\text{ion}} \bigg), \tag{A2.32}$$

where the homogenised forms of C_m and I_{ion} are defined by

$$C_m = \rho_1 \, C_{m1} + \rho_2 \, C_{m2}, \tag{A2.33}$$

$$I_{\text{ion}} = \rho_1 \, I_{\text{ion},1}(V; \mathbf{u}_1) + \rho_2 \, I_{\text{ion},2}(V; \mathbf{u}_2), \tag{A2.34}$$

so that both the homogenised capacitance and ionic current are the proportional contributions from the two cell types, and we have $\chi = S/|\Omega|$. Note that extending this approach to further cell types would be a simple extension of equations (A2.33) and (A2.34) to add further terms and proportions of each phenotype.

When using the bidomain equations in practice it is common to eliminate Φ_i from equations (A2.31) and (A2.32), giving

$$\chi\left(\mathcal{A}_1 C_m \frac{\partial V}{\partial t} + \mathcal{B}_1 I_{\text{ion}}\right) = \nabla \cdot (\Sigma_i \nabla (V + \Phi_e)) \,, \tag{A2.35}$$

$$0 = \nabla \cdot (\Sigma_i \nabla V + (\Sigma_i + \Sigma_e) \nabla \Phi_e) \,. \tag{A2.36}$$

A2.1.5 The partitioned phenotypes model

When using the partitioned phenotypes model, we are able to partition the tissue into one set of regions containing only the first phenotype, and another set of regions where only the second phenotype exists. In the first of these regions we have $\rho_1 = 1, \rho_2 = 0$ allowing us to deduce that $C_m = C_{m1}$ from equation (A2.33) and that $I_{\text{ion}} = I_{\text{ion},1}$ from equation (A2.34). Similarly, in the second region we have $\rho_1 = 0, \rho_2 = 1$ and so $C_m = C_{m2}$ and $I_{\text{ion}} = I_{\text{ion},2}$. The solutions to the bidomain equations in these regions are then coupled by demanding that Φ_i, Φ_e and the homogenised intracellular and extracellular currents are continuous across the partition between these regions, i.e.:

$$(\Sigma_i \nabla \Phi_i) \cdot \mathbf{n}, \qquad \text{and} \qquad (\Sigma_e \nabla \Phi_e) \cdot \mathbf{n},$$

are continuous across the partition boundary, where $\mathbf{n}$ is a normal vector to the partition.

Appendix 3

Supplementary Information for Chapter 6

This Appendix contains additional material relevant to the work covered in Chapter 6, Simulations of Stem Cell-Derived Cardiomyocyte Monolayers in the Micro-Electrode Array.

A3.1 Convergence Analysis

Figure A3.1 shows the rates of convergence achieved in the simulations first described in Section 6.4.4. The expected rates of convergence, $\mathcal{O}(h^2)$ and $\mathcal{O}(t)$, are indicated by the gradients of the shaded triangles in each plot.

The convergence study was carried out on a structured mesh, with the same diameter as the unstructured meshes used for the simulations of the micro-electrode array in Chapter 6. This approach was taken to avoid differences in the positioning of the mesh nodes having an effect on the solution. Similarly to the simulations described in Section 6.5, we used the homogenised phenotypes model with a small pacemaker region in an otherwise ventricular-like domain, using the Paci et al. (2013a) models of stem cell-derived cardiomyocyte electrophysiology.

As an analytic solution to the bidomain equations is not available when a

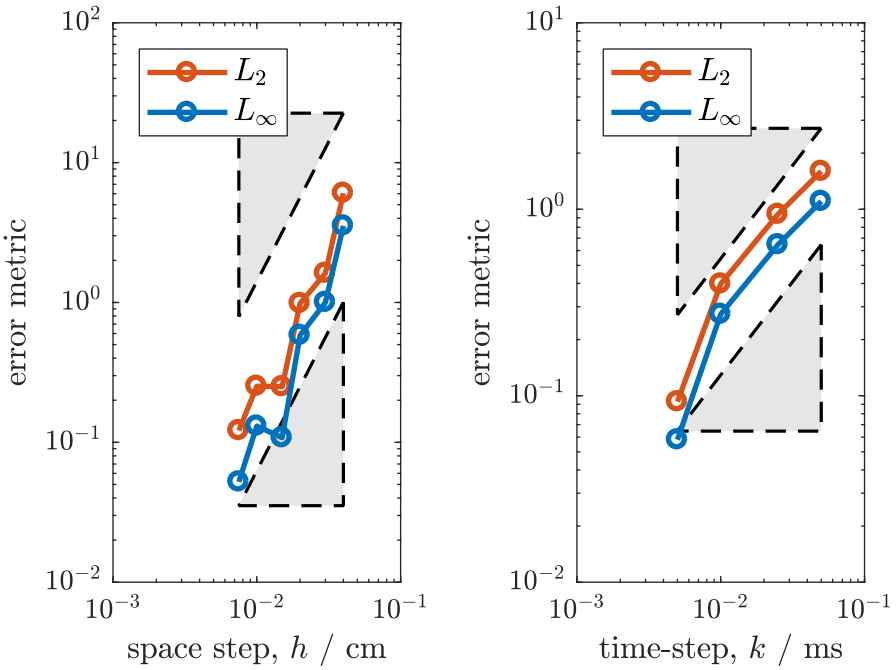

Figure A3.1: Rates of convergence in bidomain simulations. Left: Spatial convergence. Right: temporal convergence. Expected rates of convergence are indicated by the shaded triangles.

physiologically-based cellular electrophysiology model is used, each of the convergence simulations was compared to a reference solution. We therefore do not expect to see a perfect match between the actual and expected rates of convergence in these simulations, but note that the rates of convergence are close to the expected values in the cases plotted here.

We concluded that a mesh with an inter-node spacing of 150 µm would be suitable, but as described in Section 6.4.4, eventually opted for a slightly finer, 100 µm mesh. A PDE time-step of 0.01 ms was selected as this had a similar value of the error metrics to our selected mesh spacing.

A3.2 Algorithms for Calculation of the Conduction Velocity

Throughout Chapters 6 and 7, two algorithms were used for calculating the condition velocity, CV, of the activation wave. These algorithms, together with several others, are discussed in Cantwell et al. (2015).

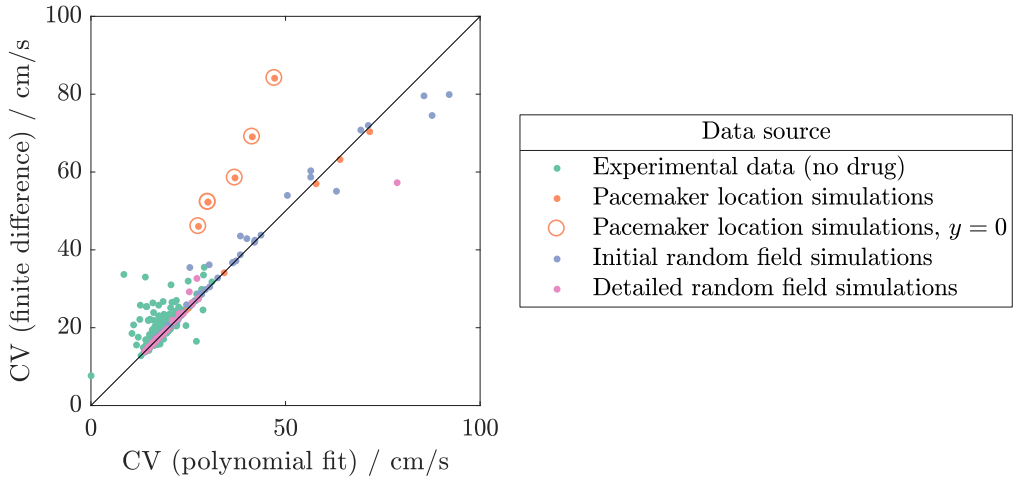

Figure A3.2: Comparison of CV values calculated using two different algorithms. Values of CV from several different simulations/experiments (listed in the legend) are shown. The black line indicates an exact correspondence between the polynomial surface fit and the finite difference-based algorithms. The two algorithms give very similar results, with exceptions more notable at the higher end of the CV range.

The activation time at each node was calculated as described in Section 6.2.3. Conduction velocity was then calculated at every node using one or both of the algorithms below. The two methods generally gave consistent results at physiological values of CV (i.e. below 50 cm/s), as can be seen in Figure A3.2. Deviations from consistency occurred when the pacemaker region was very close to the region where the CV was calculated, as indicated by the circled points in Figure A3.2 (in these simulations, the phenotype distribution was set to result in a pacemaker region at the centre of the monolayer). Variation in the estimated CV value can also be seen in the experimental data (where noise in the data may play a role) and at very high values of CV as the synchronised regime is approached (where the similarity between activation times across the electrodes increases the amount of error). However, the good agreement between the two methods in the physiological range indicates that either approach is suitable for the analysis in Chapters 6 and 7.

Once the CV at each node had been calculated, a summary value for the entire monolayer was generated. The median value of CV was generally preferred over the mean as it lessened the impact of any outlying values.

A3.2.1 Finite difference-based algorithm

A regular grid is required to use the finite difference-based method, so we begin by defining a regular grid of points that covers the region of interest. We then linearly interpolate the activation times at the nodes onto the new grid. The gradient of the activation time can then be found using

$$\mathrm{AT}_x = \frac{\mathrm{d}\,\mathrm{AT}}{\mathrm{d}x} \approx \frac{\mathrm{AT}_{i+1,j} - \mathrm{AT}_{i-1,j}}{2d} \quad \text{and} \tag{A3.1}$$

$$\mathrm{AT}_y = \frac{\mathrm{d}\,\mathrm{AT}}{\mathrm{d}y} \approx \frac{\mathrm{AT}_{i,j+1} - \mathrm{AT}_{i,j-1}}{2d}, \tag{A3.2}$$

where d is the inter-point spacing (normally set to a value slightly smaller than the original inter-node spacing).

We can determine the conduction velocity in vector form,

$$\mathbf{CV} = \frac{\mathrm{AT}_x}{\mathrm{AT}_x^2 + \mathrm{AT}_y^2}\mathbf{i} + \frac{\mathrm{AT}_y}{\mathrm{AT}_x^2 + \mathrm{AT}_y^2}\mathbf{j}, \tag{A3.3}$$

and obtain the conduction velocity at each node with

$$\mathrm{CV} = \sqrt{\left(\frac{\mathrm{AT}_x}{\mathrm{AT}_x^2 + \mathrm{AT}_y^2}\right)^2 + \left(\frac{\mathrm{AT}_y}{\mathrm{AT}_x^2 + \mathrm{AT}_y^2}\right)^2}. \tag{A3.4}$$

A3.2.2 Polynomial surface fit-based algorithm

In this algorithm, we generate an analytical expression for the activation time by taking the least-squares fit of a quadratic polynomial surface to the data. In the majority of our analysis, we work with the same data points available to experimentalists, i.e. activation times from the electrodes of the MEA. Due to the low number of data points and the general smoothness of the data, we use a quadratic surface even though, in theory, it is possible to use higher-order polynomial surfaces.

The quadratic surface can be expressed as

$$\mathrm{AT}(x, y) = ax^2 + by^2 + cxy + dx + ey + f. \tag{A3.5}$$

If we differentiate this expression with respect to x and y, we obtain

$$\mathrm{AT}_x = \frac{\mathrm{d}\,\mathrm{AT}}{\mathrm{d}x} = 2ax + cy + d \quad \text{and} \tag{A3.6}$$

$$\mathrm{AT}_y = \frac{\mathrm{d}\,\mathrm{AT}}{\mathrm{d}y} = 2by + cx + e. \tag{A3.7}$$

The conduction velocity at each node can then be obtained using equations (A3.3) and (A3.4).

A3.3 Gaussian Random Fields

We consider here the implementation of the random field generation algorithm, and refer the reader to Lord et al. (2014, Chapter 7) for the full mathematical detail of the derivations that underpin random fields.

A3.3.1 Karhunen-Loève expansion

The Karhunen-Loève theorem states that any second-order random field $Z(\mathbf{x}, \omega)$ (such as the Gaussian random fields we consider throughout Chapters 6 and 7), may be represented by

$$Z(\mathbf{x}, \omega) = \mu(\mathbf{x}) + \sum_{j=1}^{\infty} \sqrt{\lambda_j}\, \phi_j(\mathbf{x})\, \xi_j(\omega), \tag{A3.8}$$

where $\mu(\mathbf{x})$ is the mean value of the field, $\xi_j(\omega) \sim N(0,1)$[1] and λ_j and $\phi_j(\mathbf{x})$ are respectively the eigenvalues and eigenfunctions of a kernel function. Realisations of field $Z(\mathbf{x}, \omega)$ are obtained by sampling $\xi_j(\omega)$.

Any valid covariance function C may act as a kernel function (Betz et al., 2014). We have chosen to utilise a Gaussian covariance function,

$$C = \sigma^2 \exp\left(\frac{(\mathbf{x} - \mathbf{y})^2}{l_c^2}\right), \tag{A3.9}$$

where σ^2 is the variance and l_c is the correlation length. In practise, σ affects the amount of variation in the field value and l_c affects how rapidly the field varies through space. While there are many other options for the form of the covariance function, such as the exponential and Whittle-Matérn, we have opted for the Gaussian as the resulting fields are particularly smooth.

[1] $\xi_j(\omega)$ is normally distributed only for the particular case of a Gaussian random field; otherwise, the form of $\xi_j(\omega)$ is less simple.

A3.3.2 Truncated Karhunen-Loève expansion

Rather than generating a continuous field as outlined above, we require a Gaussian random field to be generated on our finite element mesh. We therefore use the discretised form of the above procedure to generate the Gaussian random fields.

The entries on our covariance matrix, C, are generated with

$$c_{i,j} = \sigma^2 \exp\left(\frac{(x_i - x_j)^2 + (y_i - y_j)^2}{l_c^2}\right), \qquad \text{for } i = 1, 2, ..., M, \tag{A3.10}$$

where M is the number of nodes in the mesh.

The random field is then constructed using

$$Z(\mathbf{x}, \omega) = \mu(\mathbf{x}) + \sum_{j=1}^{\tilde{M}} \sqrt{\lambda_j}\, \phi_j(\mathbf{x})\, \xi_j(\omega), \tag{A3.11}$$

where we utilise the first $\tilde{M}$ of M eigenvalues λ and eigenvectors $\phi(\mathbf{x})$ of covariance matrix C. λ and $\phi(\mathbf{x})$ are sorted in descending order of λ.

The ability to use the truncation above also permits us to avoid the negative eigenvalues that can result from numerical error when calculating the eigenvalues and eigenvectors of C.

A3.3.3 Gaussian random field generation algorithm

Algorithm 1 shows how the Gaussian random fields were generated using a Gaussian covariance function.

Due to limits on the accuracy of calculating the eigenvalues and eigenvectors of C, we did not utilise the full range of k in Algorithm 1. Instead, we truncated the series once the sum of the eigenvalues up to the final k reached 99.9% of the total sum of the eigenvalues. This prevented any spurious negative eigenvalues from affecting the field $Z(\mathbf{x}, \omega)$, without substantial loss of accuracy.

Algorithm 1 Generation of a Gaussian random field

$x \leftarrow x$-coordinates of the M nodes in the finite element mesh
$y \leftarrow y$-coordinates of the M nodes in the finite element mesh
$M \leftarrow$ number of nodes
$lc \leftarrow$ correlation length of the random field
$sigma \leftarrow$ standard deviation of the random field
$mu \leftarrow$ mean value of the random field
for $i = 1$ to M **do**
    for $j = 1$ to M **do**
        $C(i,j) \leftarrow sigma^2 \times \exp\left(\frac{(x(i)-x(j))^2+(y(i)-y(j))^2}{lc^2}\right)$
    end for
end for
$eig\_val \leftarrow$ eigenvalues of C, sorted in descending order
$eig\_vec \leftarrow$ eigenvectors of C, sorted in descending order of eigenvalues
$Z \leftarrow 1 \times M$ array of mu
$xi \leftarrow 1 \times M$ array of realisations of normally distributed random variables, $N(0,1)$
for $k = 1$ to M **do**
    $Z \leftarrow Z + xi(k) * \sqrt{eig\_val(k)} * eig\_vec(k)$
end for
return Z

A3.3.4 Use of Gaussian random fields to represent phenotype distribution

The random fields $Z(\mathbf{x}, \omega)$ defined above have properties well-suited for defining the phenotype present across the monolayer, which we write in terms of the proportion of the ventricular-like model, ρ_{V} (see equations (6.8) and (6.9)). As ρ_{V} is physically restricted to take values between 0 and 1, we define it in terms of the random field $Z(\mathbf{x}, \omega)$ as

$$\rho_{\mathrm{V}}(\mathbf{x}) = \begin{cases} 1, & \text{for } Z(\mathbf{x},\omega) > 1, \\ 0, & \text{for } Z(\mathbf{x},\omega) < 0, \\ Z(\mathbf{x},\omega) \sim N(\mu, C), & \text{otherwise.} \end{cases} \tag{A3.12}$$

Appendix 4

Supplementary Information for Chapter 7

This Appendix contains additional material relevant to the work covered in Chapter 7, Investigation of Drug Action on Monolayers Containing Multiple Cellular Phenotypes.

A4.1 Extended Biomarker Plots

In Section 7.5, we discussed the impact of three drugs on biomarkers from simulated and experimental monolayers. Fully demonstrating the range of variability in the simulated field and action potentials by necessity called for large figures; it was therefore not possible to show the full detail from every simulation in Section 7.5. In the following section, we present some additional plots that may be of interest to the reader.

A4.1.1 Cisapride

Cisapride is a specific blocker of the hERG channel which is well-known for prolonging the action potential. Its effect in our simulations was discussed in Section 7.5.1. In Figure A4.1, we present a plot of sample action potentials; one

from each of our simulations. This plot is complementary to the examples of field potentials shown in Figure 7.6, on page 175. We then extend Figures 7.8 and 7.9, the plots of the biomarkers and percentage change in their values, with some further biomarkers that were not discussed in the chapter itself. The full plots may be found in Figures A4.2 and A4.3.

A4.1.2 Terfenadine

We now show some additional plots that demonstrate the effects of Terfenadine, a drug with the primary effect of reducing I_{Kr}, and a secondary effect on I_{CaL} at higher concentrations. In Figures A4.4 and A4.5, we show the simulated field and action potentials from the full range of simulations. The values of the full range of biomarkers are shown in Figure A4.6. The percentage change in each of the biomarker values as the concentration of Terfenadine increased may be seen in Figure A4.7, which provides a more complete version of Figure 7.11.

A4.1.3 Diltiazem

Finally, we present some further plots showing the effects of Diltiazem. Identification of the repolarising wave proved particularly difficult at the highest two concentrations of Diltiazem, both using the peak detection algorithm and by manual analysis. The calculation of the FPD (by identifying the peak of the repolarising wave) was manually checked following use of the normal FPD calculation algorithm; any peaks which were inaccurately detected by the algorithm were manually tagged if they could be identified by eye. However, it still proved difficult to identify the peak of the repolarising wave at all in some cases at the highest two concentrations, so some data points are not shown in the later figures.

In Figures A4.8 and A4.9, we show the field and action potentials from each simulation (note that the repolarising wave almost merges with the depolarising spike at the highest two concentrations). Figures A4.10 and A4.11 show the values of all biomarkers and their percentage change as the drug concentration increases.

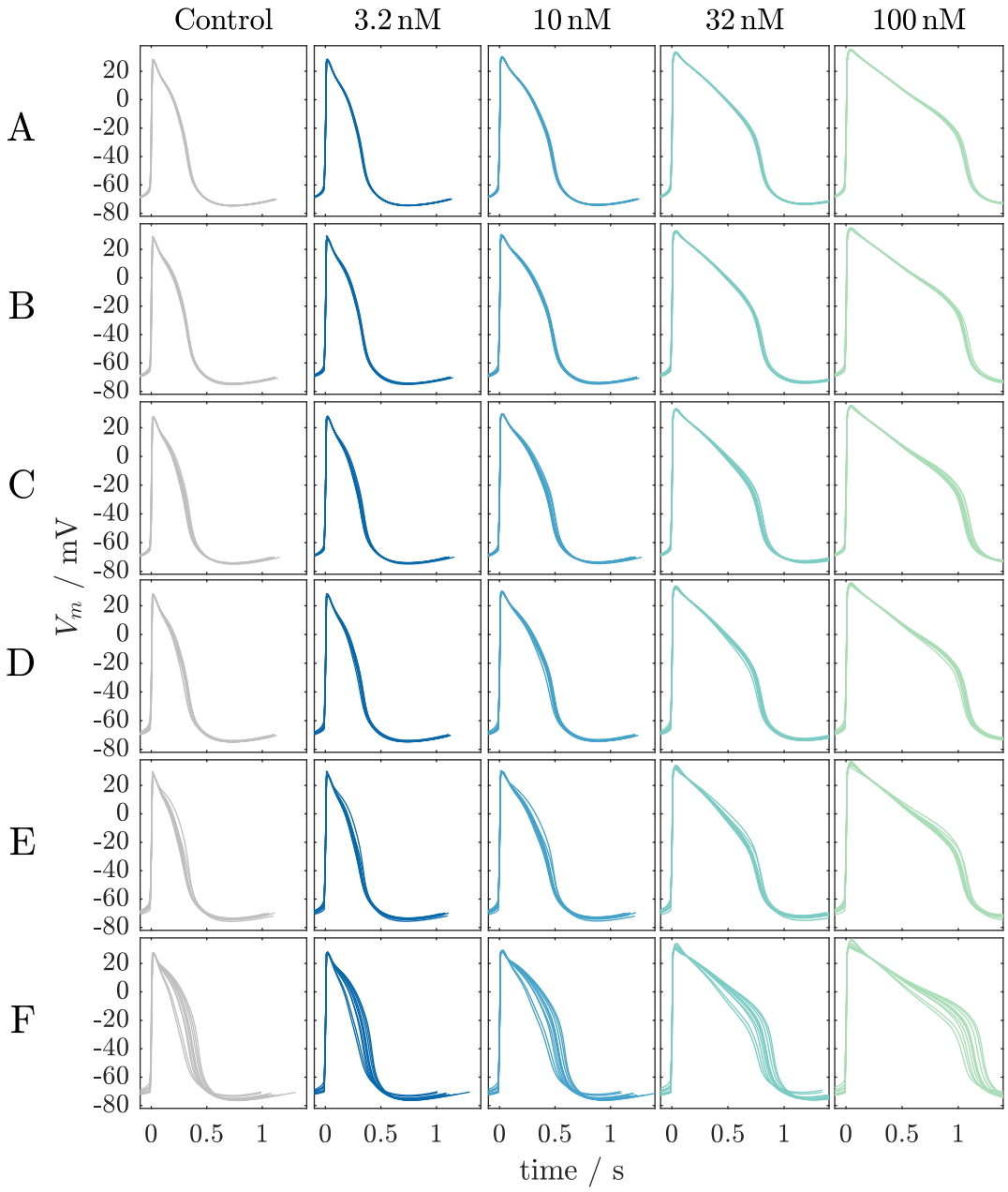

Figure A4.1: Simulated action potentials following the addition of Cisapride. The action potential during the last full beat of each simulation. Each panel contains one field potential from each of ten realisations of the random field parametrisation used to represent the phenotype distribution.

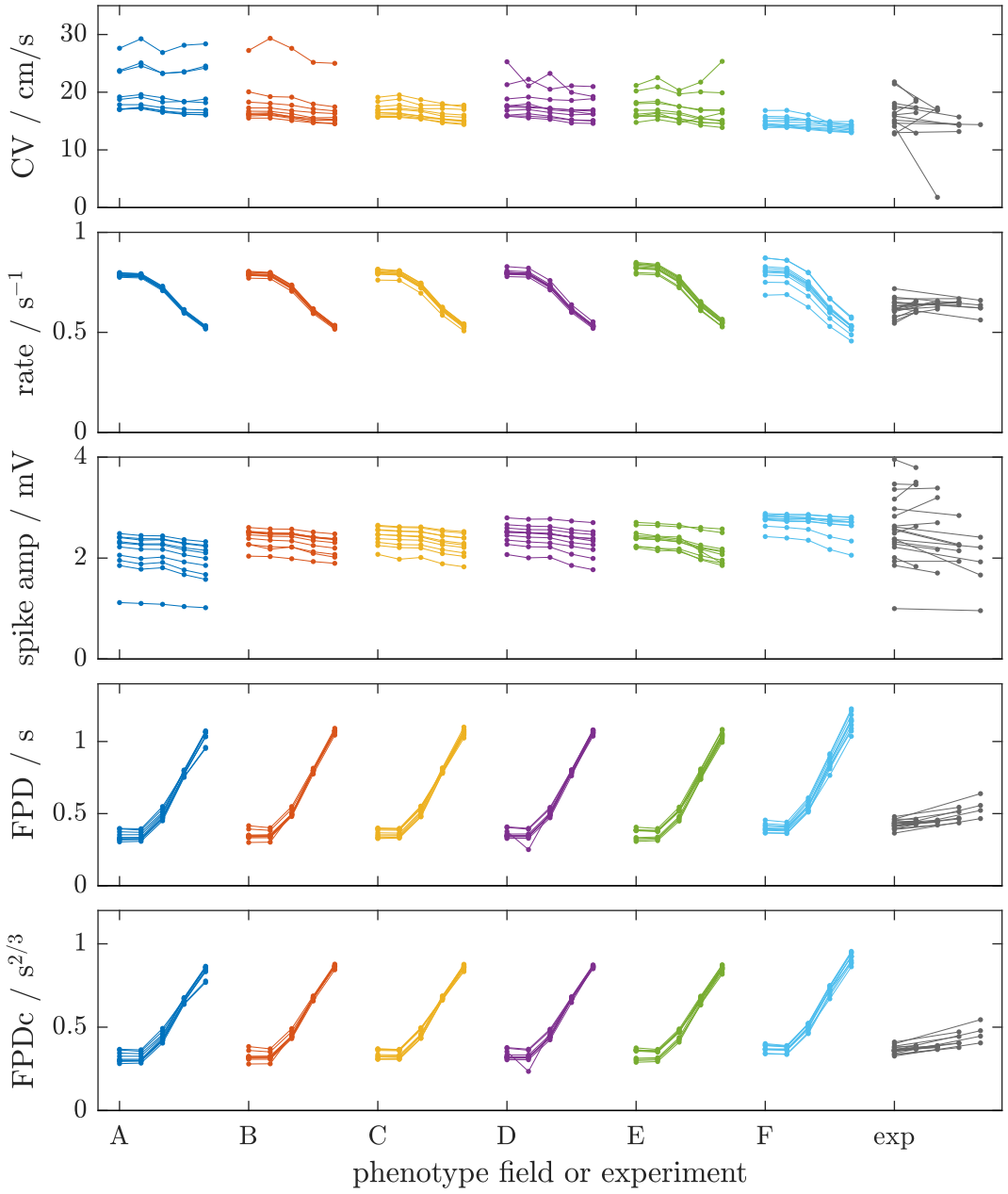

Figure A4.2: Biomarkers from simulated and experimental field potentials following the addition of Cisapride. The five points in each data series denote the biomarker values under control conditions and the four increasing concentrations of Cisapride. Connected points indicate that the biomarker values were obtained from the same monolayer. Only one concentration of Cisapride was tested on each experimental monolayer, all lines in that section of the plot therefore link the control value to only one value obtained under dosed conditions.

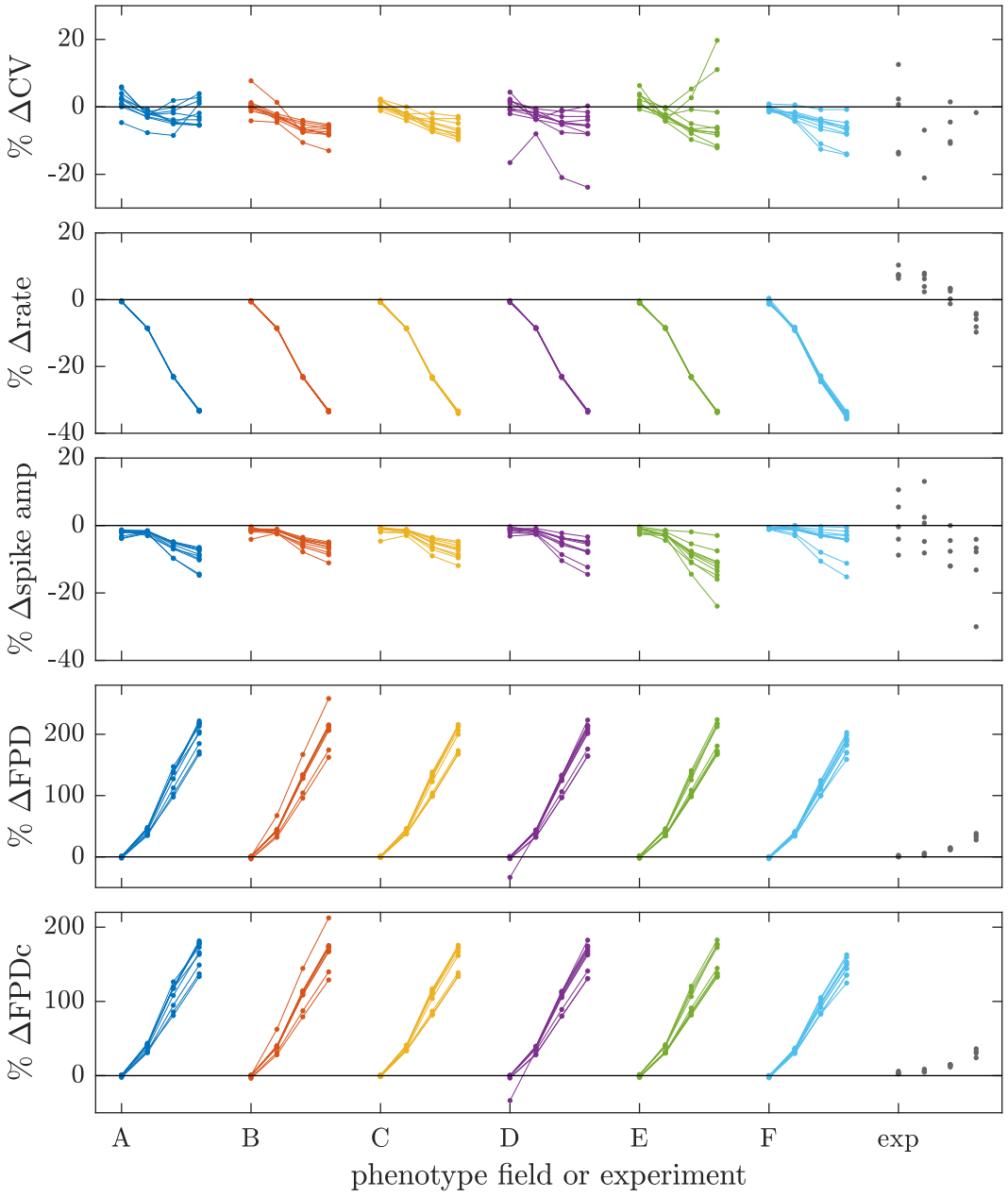

Figure A4.3: Percentage change in biomarkers from simulated and experimental field potentials following the addition of Cisapride. As in Figure A4.2, linked points show the values obtained from the same monolayer. The experimental data points were all gathered from different monolayers, so links are not shown.

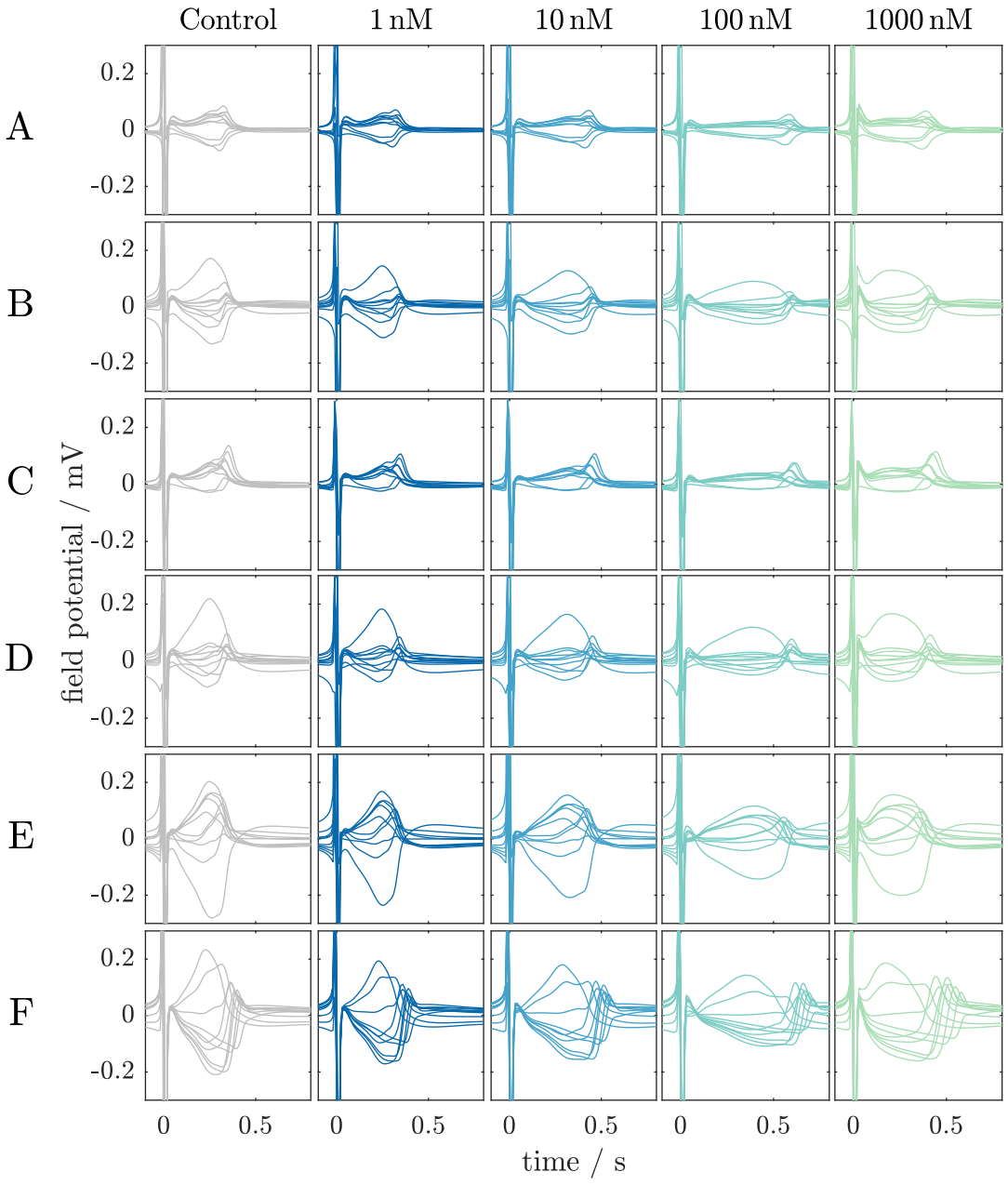

Figure A4.4: Simulated action potentials following the addition of Terfenadine. The field potential during the last full beat of each simulation. Each panel contains one field potential from each of ten realisations of the random field parametrisation used to represent the phenotype distribution.

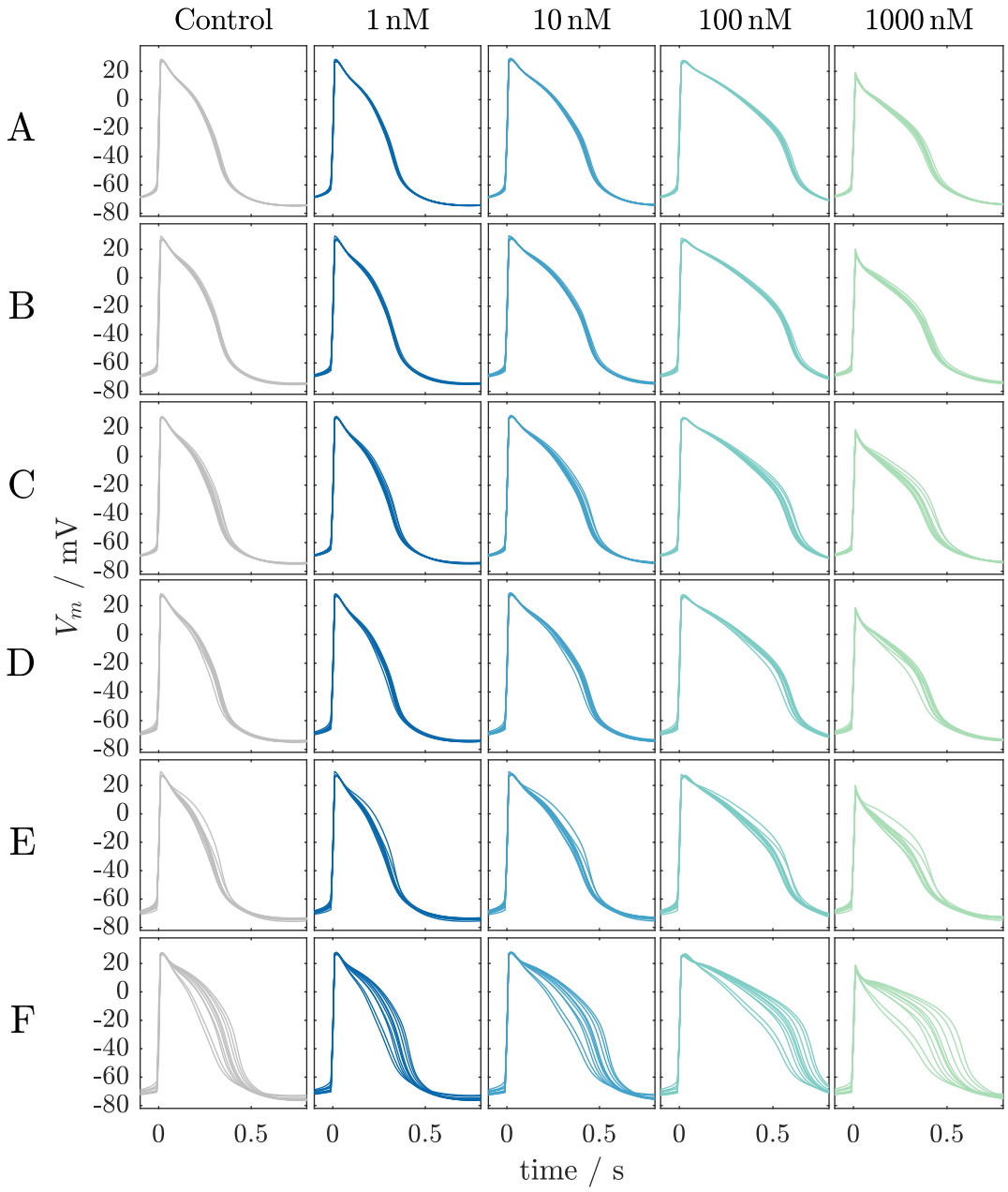

Figure A4.5: Simulated action potentials following the addition of Terfenadine. The action potential during the last full beat of each simulation. Each panel contains one field potential from each of ten realisations of the random field parametrisation used to represent the phenotype distribution.

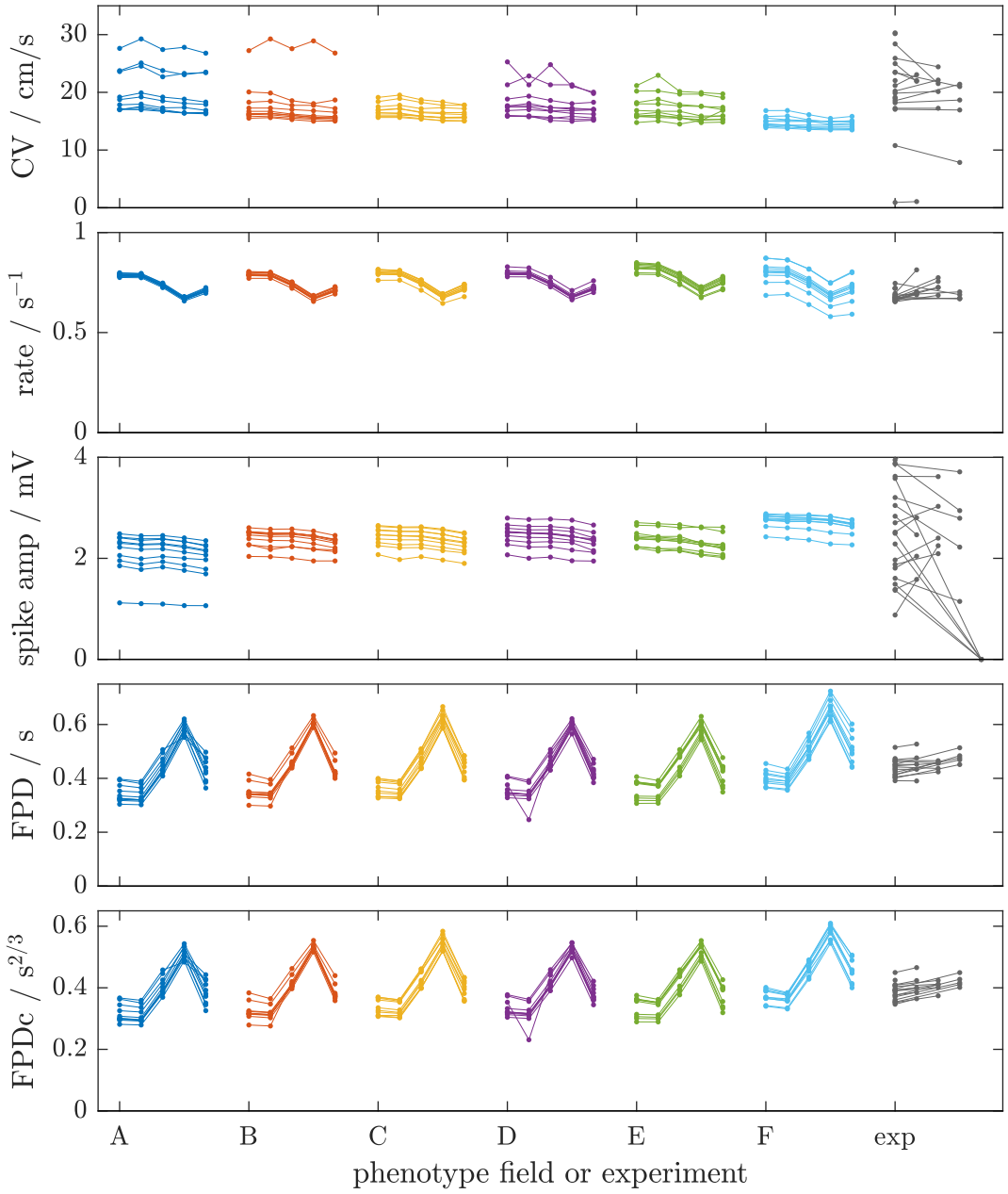

Figure A4.6: Biomarkers from simulated and experimental field potentials following the addition of Terfenadine. Figure content as for Figure A4.2, but for the drug Terfenadine.

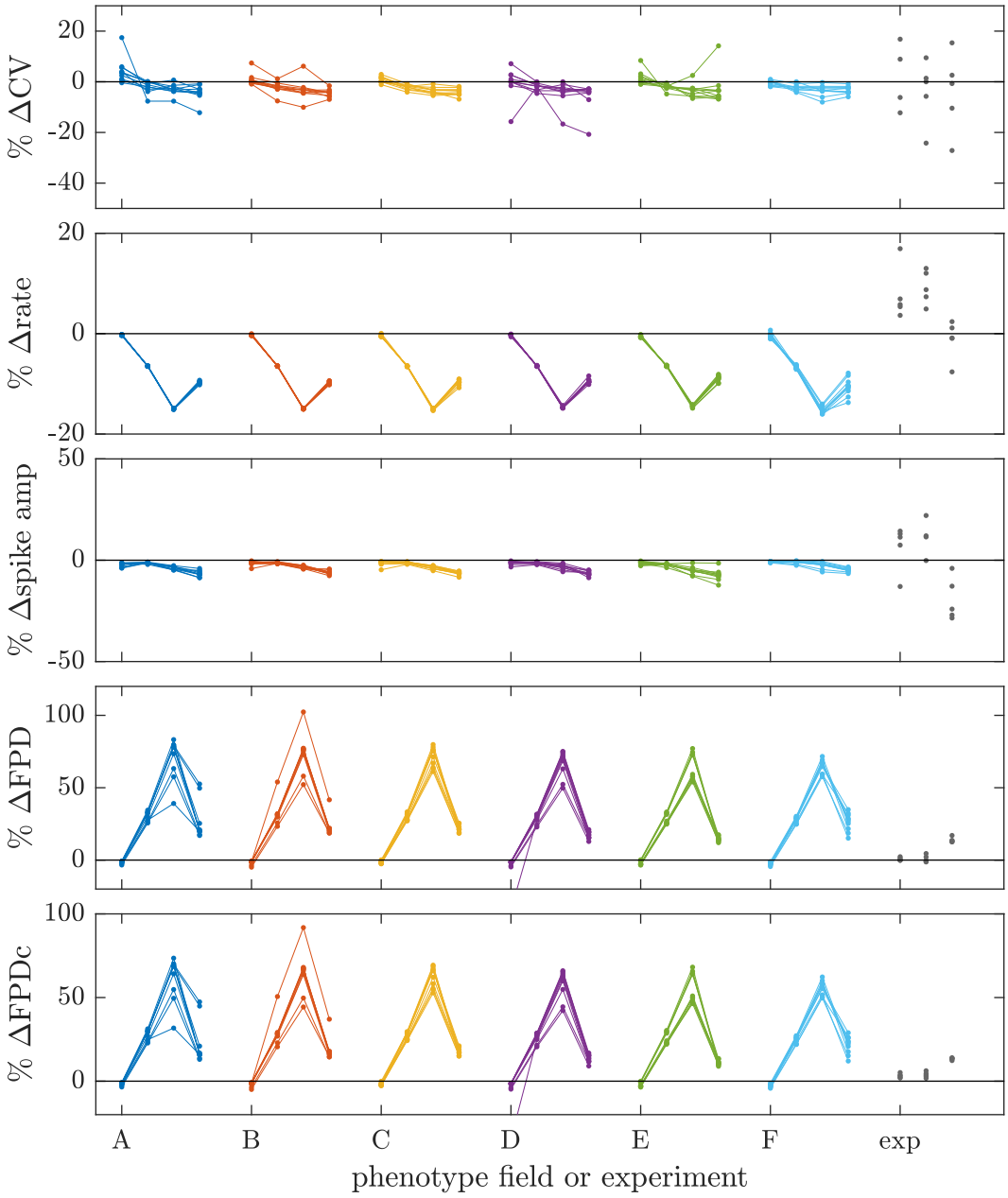

Figure A4.7: Percentage change in biomarkers from simulated and experimental field potentials following the addition of Terfenadine. Figure content as for Figure A4.3, but for the drug Terfenadine.

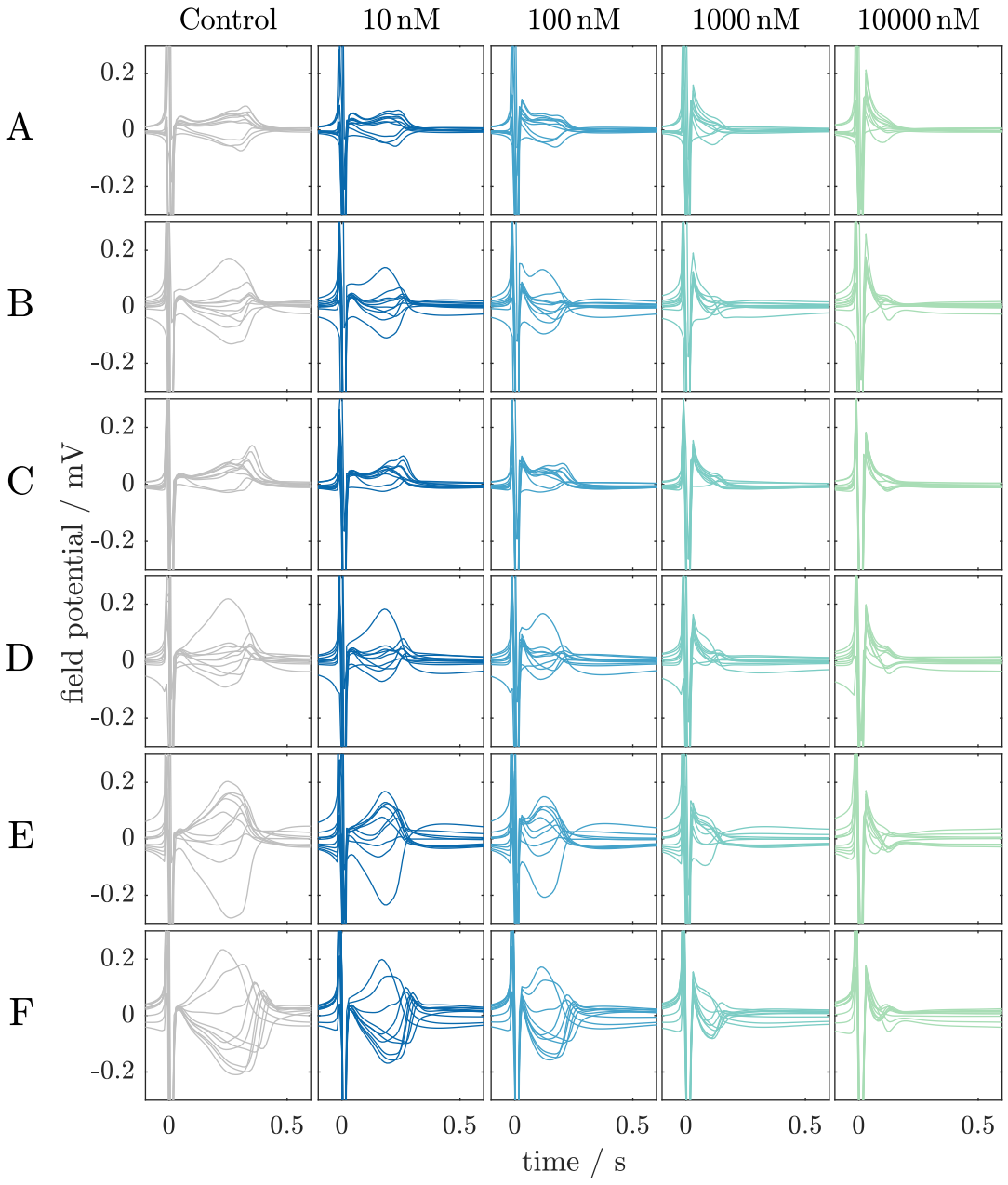

Figure A4.8: Simulated action potentials following the addition of Diltiazem. The field potential during the last full beat of each simulation. Each panel contains one field potential from each of ten realisations of the random field parametrisation used to represent the phenotype distribution.

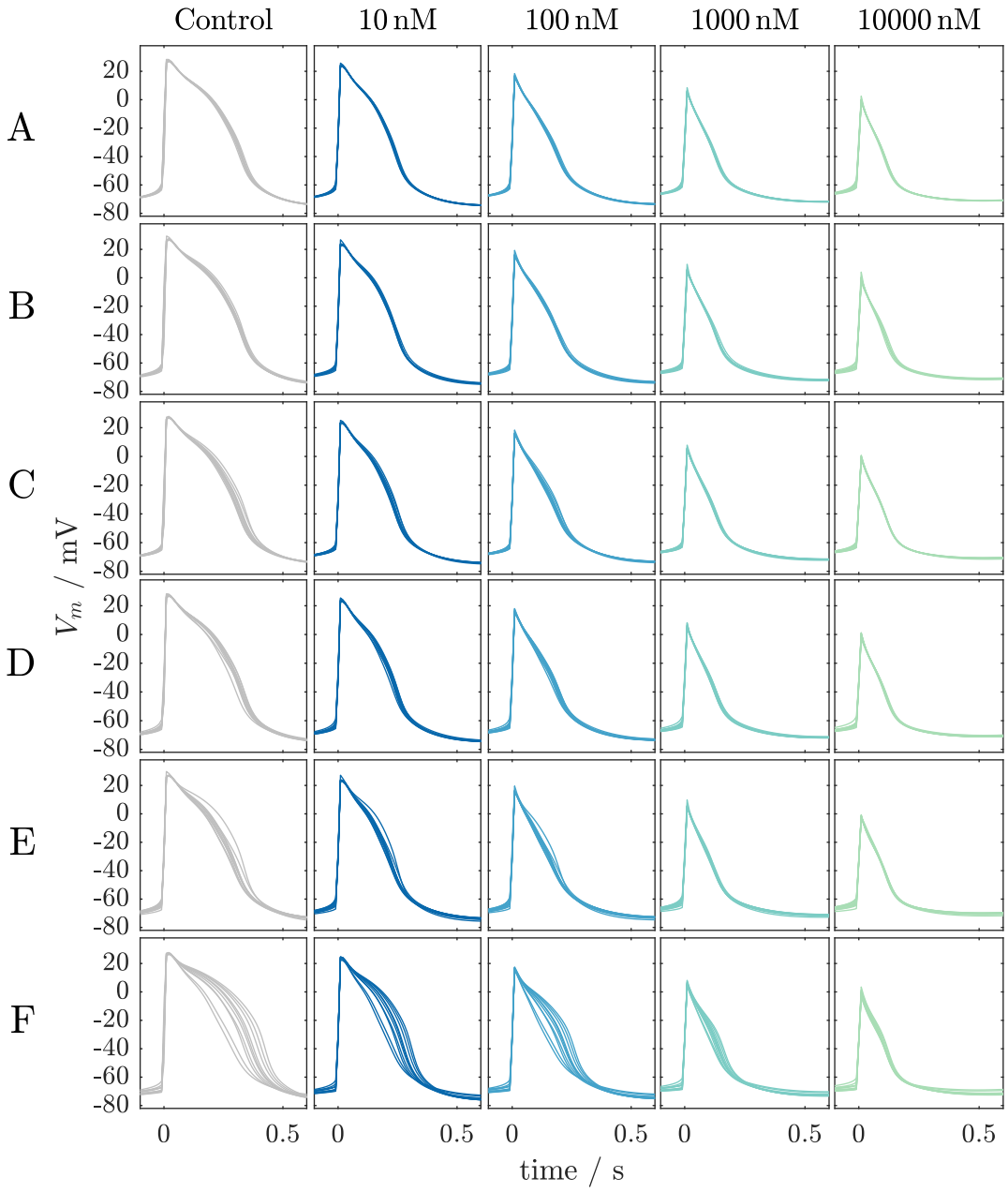

Figure A4.9: Simulated action potentials following the addition of Diltiazem. The action potential during the last full beat of each simulation. Each panel contains one field potential from each of ten realisations of the random field parametrisation used to represent the phenotype distribution.

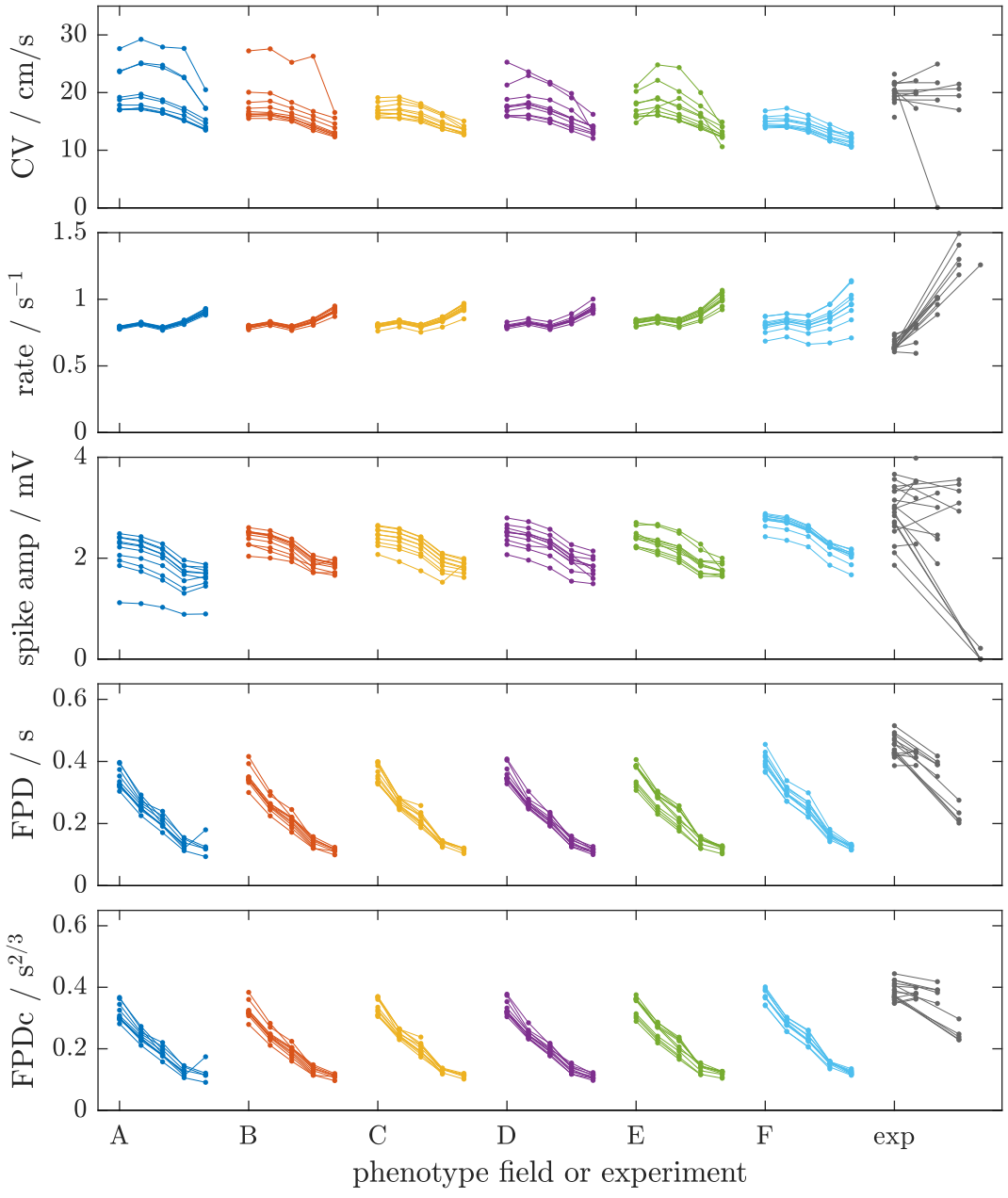

Figure A4.10: Biomarkers from simulated and experimental field potentials following the addition of Diltiazem. Figure content as for Figure A4.2, but for the drug Diltiazem.

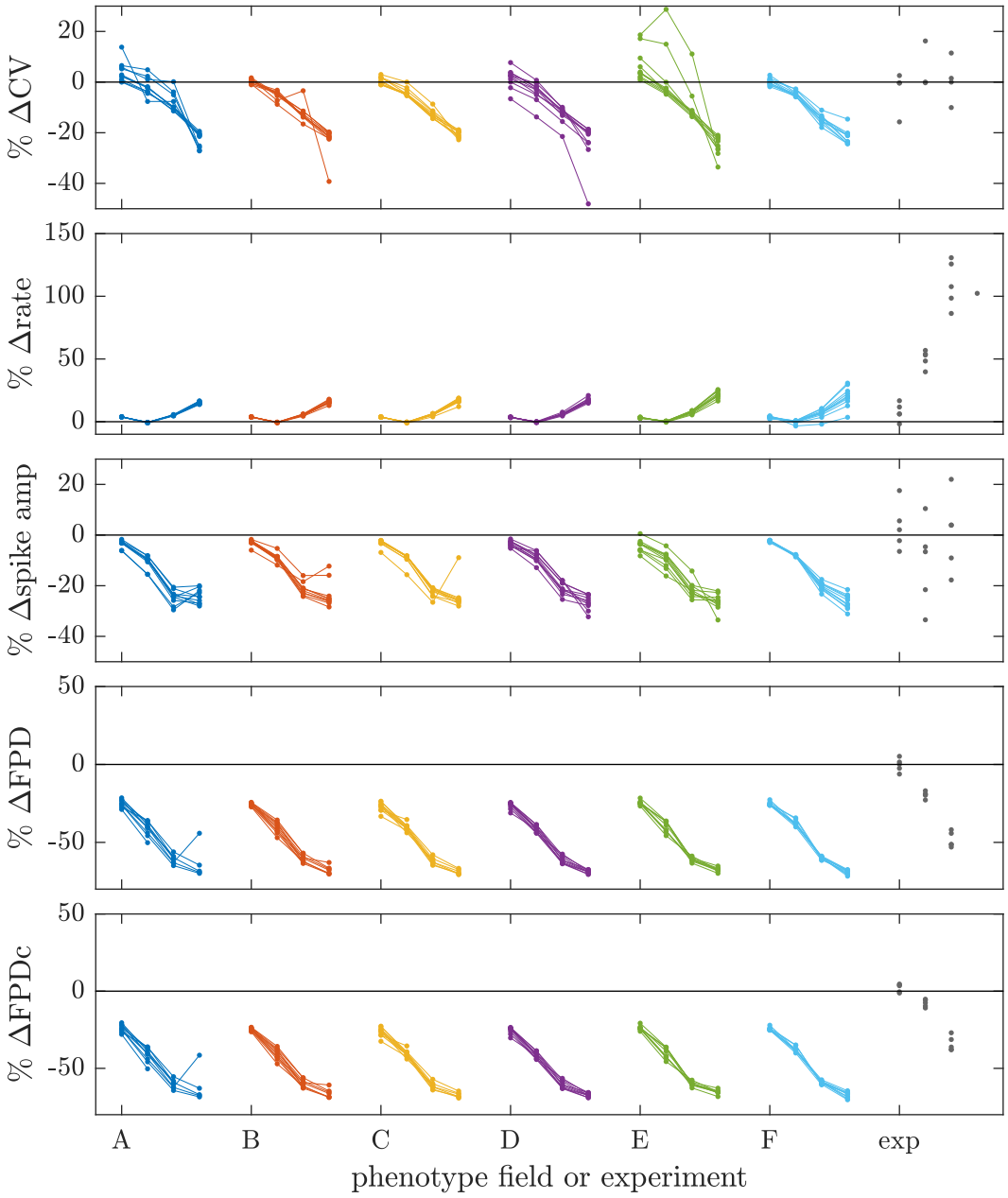

Figure A4.11: Percentage change in biomarkers from simulated and experimental field potentials following the addition of Diltiazem. Figure content as for Figure A4.3, but for the drug Diltiazem.

Bibliography

Abbate, E., M. Boulakia, Y. Coudière, J.-F. Gerbeau, P. Zitoun, and N. Zemzemi (2018). In silico assessment of the effects of various compounds in MEA/hiPSC-CM assays: Modeling and numerical simulations. *Journal of Pharmacological and Toxicological Methods* **89**(Supplement C) 59–72. DOI: 10.1016/j.vascn.2017.10.005.

Abi-Gerges, N., A. Pointon, K. L. Oldman, M. R. Brown, M. A. Pilling, C. E. Sefton, H. Garside, and C. E. Pollard (2017). Assessment of extracellular field potential and Ca2 + transient signals for early QT/pro-arrhythmia detection using human induced pluripotent stem cell-derived cardiomyocytes. *Journal of Pharmacological and Toxicological Methods* **83** 1–15. DOI: 10.1016/j.vascn.2016.09.001.

Amos, G. J., E. Wettwer, F. Metzger, Q. Li, H. M. Himmel, and U. Ravens (1996). Differences between outward currents of human atrial and subepicardial ventricular myocytes. *The Journal of Physiology* **491**(1) 31–50.

Arthurs, C. J., M. J. Bishop, and D. Kay (2012). Efficient simulation of cardiac electrical propagation using high order finite elements. *Journal of Computational Physics* **231**(10) 3946–3962. DOI: 10.1016/j.jcp.2012.01.037.

Asakura, K., C. Y. Cha, H. Yamaoka, Y. Horikawa, H. Memida, T. Powell, A. Amano, and A. Noma (2014). EAD and DAD mechanisms analyzed by developing a new human ventricular cell model. *Progress in Biophysics and Molecular Biology* **116**(1) 11–24. DOI: 10.1016/j.pbiomolbio.2014.08.008.

Attin, M. and W. T. Clusin (2009). Basic Concepts of Optical Mapping Techniques in Cardiac Electrophysiology. *Biological research for nursing* **11**(2) 195–207. DOI: 10.1177/1099800409338516.

Beattie, K. A. (2015). Mathematical modelling of drug-ion channel interactions for cardiac safety assessment. DPhil Thesis. University of Oxford.

Beattie, K. A., A. P. Hill, R. Bardenet, Y. Cui, J. I. Vandenberg, D. J. Gavaghan, T. P. de Boer, and G. R. Mirams (2018). Sinusoidal voltage protocols for rapid characterisation of ion channel kinetics. *The Journal of Physiology* (Early view) 1–16. DOI: 10.1113/JP275733.

Beattie, K. A., C. Luscombe, G. Williams, J. Munoz-Muriedas, D. J. Gavaghan, Y. Cui, and G. R. Mirams (2013). Evaluation of an in silico cardiac safety assay: Using ion channel screening data to predict QT interval changes in the rabbit ventricular wedge. *Journal of Pharmacological and Toxicological Methods* **68**(1) 88–96. DOI: 10.1016/j.vascn.2013.04.004.

Beeler, G. W. and H. Reuter (1977). Reconstruction of the action potential of ventricular myocardial fibres. *The Journal of Physiology* **268**(1) 177–210. DOI: 10.1113/jphysiol.1977.sp011853.

Belardinelli, L., J. C. Shryock, and H. Fraser (2006). Inhibition of the late sodium current as a potential cardioprotective principle: effects of the late sodium current inhibitor ranolazine. *Heart* **92**(Supplement 4) iv6–iv14. DOI: 10.1136/hrt.2005.078790.

Ben-Ari, M., R. Schick, L. Barad, A. Novak, E. Ben-Ari, A. Lorber, J. Itskovitz-Eldor, M. R. Rosen, A. Weissman, and O. Binah (2014). From beat rate variability in induced pluripotent stem cell–derived pacemaker cells to heart rate variability in human subjects. *Heart Rhythm* **11**(10) 1808–1818. DOI: 10.1016/j.hrthm.2014.05.037.

Bernabeu, M. O., P. Pathmanathan, J. Pitt-Francis, and D. Kay (2010). Stimulus Protocol Determines the Most Computationally Efficient Preconditioner for the Bidomain Equations. *IEEE Transactions on Biomedical Engineering* **57**(12) 2806–2815. DOI: 10.1109/TBME.2010.2078817.

Bers, D. M. (2002). Cardiac excitation–contraction coupling. *Nature* **415**(6868) 198–205. DOI: 10.1038/415198a.

Bers, D. M., W. H. Barry, and S. Despa (2003). Intracellular Na+ regulation in cardiac myocytes. *Cardiovascular Research* **57**(4) 897–912. DOI: 10.1016/S0008-6363(02)00656-9.

Bett, G. C. L., A. D. Kaplan, A. Lis, T. R. Cimato, E. S. Tzanakakis, Q. Zhou, M. J. Morales, and R. L. Rasmusson (2013). Electronic "expression" of the inward rectifier in cardiocytes derived from human-induced pluripotent stem cells. *Heart Rhythm* **10**(12) 1903–1910. DOI: 10.1016/j.hrthm.2013.09.061.

Bett, G. C. L., A. D. Kaplan, and R. L. Rasmusson (2016). Action Potential Shape Is a Crucial Measure of Cell Type of Stem Cell-Derived Cardiocytes. *Biophysical Journal* **110**(1) 284–286. DOI: 10.1016/j.bpj.2015.11.026.

Betz, W., I. Papaioannou, and D. Straub (2014). Numerical methods for the discretization of random fields by means of the Karhunen–Loève expansion. *Computer Methods in Applied Mechanics and Engineering* **271** 109–129. DOI: 10.1016/j.cma.2013.12.010.

Bishop, M. J. and G. Plank (2012). The role of fine-scale anatomical structure in the dynamics of reentry in computational models of the rabbit ventricles. *The Journal of Physiology* **590**(18) 4515–4535. DOI: 10.1113/jphysiol.2012.229062.

Bizy, A., G. Guerrero-Serna, B. Hu, D. Ponce-Balbuena, B. C. Willis, M. Zarzoso, R. J. Ramirez, M. F. Sener, L. V. Mundada, M. Klos, E. J. Devaney, K. L. Vikstrom, T. J. Herron, and J. Jalife (2013). Myosin light chain 2-based selection of human iPSC-derived early ventricular cardiac myocytes. *Stem Cell Research* **11**(3) 1335–1347. DOI: 10.1016/j.scr.2013.09.003.

Blinova, K., J. Stohlman, J. Vicente, D. Chan, L. Johannesen, M. P. Hortigon-Vinagre, V. Zamora, G. Smith, W. J. Crumb, L. Pang, B. Lyn-Cook, J. Ross, M. Brock, S. Chvatal, D. Millard, L. Galeotti, N. Stockbridge, and D. G. Strauss (2017). Comprehensive Translational Assessment of Human-Induced Pluripotent Stem Cell Derived Cardiomyocytes for Evaluating Drug-Induced

Arrhythmias. *Toxicological Sciences* **155**(1) 234–247. DOI: 10.1093/toxsci/kfw200.

Bosman, A., L. Sartiani, V. Spinelli, M. Del Lungo, F. Stillitano, D. Nosi, A. Mugelli, E. Cerbai, and M. Jaconi (2013). Molecular and Functional Evidence of HCN4 and Caveolin-3 Interaction During Cardiomyocyte Differentiation from Human Embryonic Stem Cells. *Stem Cells and Development* **22**(11) 1717–1727. DOI: 10.1089/scd.2012.0247.

Bowes, J., A. J. Brown, J. Hamon, W. Jarolimek, A. Sridhar, G. Waldron, and S. Whitebread (2012). Reducing safety-related drug attrition: the use of in vitro pharmacological profiling. *Nature Reviews Drug Discovery* **11**(12) 909–922. DOI: 10.1038/nrd3845.

Bowler, L. A., D. J. Gavaghan, G. R. Mirams, and J. P. Whiteley (2019). Representation of Multiple Cellular Phenotypes Within Tissue-Level Simulations of Cardiac Electrophysiology. *Bulletin of Mathematical Biology* **81**(1) 7–38. DOI: 10.1007/s11538-018-0516-1.

Braam, S. R., L. Tertoolen, S. Casini, E. Matsa, H. R. Lu, A. Teisman, R. Passier, C. Denning, D. J. Gallacher, R. Towart, and C. L. Mummery (2013). Repolarization reserve determines drug responses in human pluripotent stem cell derived cardiomyocytes. *Stem Cell Research* **10**(1) 48–56. DOI: 10.1016/j.scr.2012.08.007.

Braam, S. R., L. Tertoolen, A. van de Stolpe, T. Meyer, R. Passier, and C. L. Mummery (2010). Prediction of drug-induced cardiotoxicity using human embryonic stem cell-derived cardiomyocytes. *Stem Cell Research* **4**(2) 107–116. DOI: 10.1016/j.scr.2009.11.004.

Brennan, T., M. Fink, and B. Rodriguez (2009). Multiscale modelling of drug-induced effects on cardiac electrophysiological activity. *European Journal of Pharmaceutical Sciences* **36**(1) 62–77. DOI: 10.1016/j.ejps.2008.09.013.

Brenner, S. and L. R. Scott (2002). *The Mathematical Theory of Finite Element Methods*. Springer Science & Business Media. ISBN: 978-0-387-95451-6.

Bridgland-Taylor, M., A. Hargreaves, A. Easter, A. Orme, D. Henthorn, M. Ding, A. Davis, B. Small, C. Heapy, N. Abi-Gerges, F. Persson, I. Jacobson, M. Sullivan, N. Albertson, T. Hammond, E. Sullivan, J.-P. Valentin, and C. Pollard (2006). Optimisation and validation of a medium-throughput electrophysiology-based hERG assay using IonWorks HT. *Journal of Pharmacological and Toxicological Methods* **54**(2) 189–199. DOI: 10.1016/j.vascn.2006.02.003.

Bruce, D., P. Pathmanathan, and J. P. Whiteley (2014). Modelling the Effect of Gap Junctions on Tissue-Level Cardiac Electrophysiology. *Bulletin of Mathematical Biology* **76**(2) 431–454. DOI: 10.1007/s11538-013-9927-1.

Bueno-Orovio, A., E. M. Cherry, and F. H. Fenton (2008). Minimal model for human ventricular action potentials in tissue. *Journal of Theoretical Biology* **253**(3) 544–560. DOI: 10.1016/j.jtbi.2008.03.029.

Buist, M. L. and Y. C. Poh (2010). An Extended Bidomain Framework Incorporating Multiple Cell Types. *Biophysical Journal* **99**(1) 13–18. DOI: 10.1016/j.bpj.2010.03.054.

Burridge, P. W., S. Thompson, M. A. Millrod, S. Weinberg, X. Yuan, A. Peters, V. Mahairaki, V. E. Koliatsos, L. Tung, and E. T. Zambidis (2011). A Uni-

versal System for Highly Efficient Cardiac Differentiation of Human Induced Pluripotent Stem Cells That Eliminates Interline Variability. *PLoS ONE* **6**(4) e18293. DOI: 10.1371/journal.pone.0018293.

Cantwell, C. D., C. H. Roney, F. S. Ng, J. H. Siggers, S. J. Sherwin, and N. S. Peters (2015). Techniques for automated local activation time annotation and conduction velocity estimation in cardiac mapping. *Computers in Biology and Medicine* **65** 229–242. DOI: 10.1016/j.compbiomed.2015.04.027.

Cardone-Noott, L., A. Bueno-Orovio, A. Minchole, K. Burrage, M. Wallman, N. Zemzemi, E. Dall'Armellina, and B. Rodriguez (2014). A computational investigation into the effect of infarction on clinical human electrophysiology biomarkers. In *Computing in Cardiology 2014*, 673–676.

Carlsson, L., G. J. Amos, B. Andersson, L. Drews, G. Duker, and G. Wadstedt (1997). Electrophysiological Characterization of the Prokinetic Agents Cisapride and Mosapride in Vivo and in Vitro: Implications for Proarrhythmic Potential? *Journal of Pharmacology and Experimental Therapeutics* **282**(1) 220–227.

Carson, D., M. Hnilova, X. Yang, C. L. Nemeth, J. H. Tsui, A. S. Smith, A. Jiao, M. Regnier, C. E. Murry, C. Tamerler, and D.-H. Kim (2016). Nanotopography-Induced Structural Anisotropy and Sarcomere Development in Human Cardiomyocytes Derived from Induced Pluripotent Stem Cells. *ACS Applied Materials & Interfaces* **8**(34) 21923–21932. DOI: 10.1021/acsami.5b11671.

Caspi, O., I. Itzhaki, I. Kehat, A. Gepstein, G. Arbel, I. Huber, J. Satin, and L. Gepstein (2008). In Vitro Electrophysiological Drug Testing Using Human Embryonic Stem Cell Derived Cardiomyocytes. *Stem Cells and Development* **18**(1) 161–172. DOI: 10.1089/scd.2007.0280.

Cavero, I., J.-M. Guillon, V. Ballet, M. Clements, J.-F. Gerbeau, and H. Holzgrefe (2016). Comprehensive in vitro Proarrhythmia Assay (CiPA): Pending issues for successful validation and implementation. *Journal of Pharmacological and Toxicological Methods* **81** 21–36. DOI: 10.1016/j.vascn.2016.05.012.

Cavero, I. and H. Holzgrefe (2014). Comprehensive in vitro Proarrhythmia Assay, a novel in vitro/in silico paradigm to detect ventricular proarrhythmic liability: a visionary 21st century initiative. *Expert Opinion on Drug Safety* **13**(6) 745–758. DOI: 10.1517/14740338.2014.915311.

Chandler, N. J., I. D. Greener, J. O. Tellez, S. Inada, H. Musa, P. Molenaar, D. DiFrancesco, M. Baruscotti, R. Longhi, R. H. Anderson, R. Billeter, V. Sharma, D. C. Sigg, M. R. Boyett, and H. Dobrzynski (2009). Molecular Architecture of the Human Sinus Node. *Circulation* **119**(12) 1562–1575. DOI: 10.1161/CIRCULATIONAHA.108.804369.

Chang, E. T. Y., M. Strong, and R. H. Clayton (2015). Bayesian Sensitivity Analysis of a Cardiac Cell Model Using a Gaussian Process Emulator. *PLoS ONE* **10**(6) e0130252. DOI: 10.1371/journal.pone.0130252.

Chauveau, S., E. P. Anyukhovsky, M. Ben-Ari, S. Naor, Y.-P. Jiang, P. Danilo, T. Rahim, S. Burke, X. Qiu, I. A. Potapova, S. V. Doronin, P. R. Brink, O. Binah, I. S. Cohen, and M. R. Rosen (2017). Induced Pluripotent Stem Cell–Derived Cardiomyocytes Provide In Vivo Biological Pacemaker Function.

Circulation: Arrhythmia and Electrophysiology **10**(5) e004508. DOI: 10.1161/CIRCEP.116.004508.

Chen, Z., W. Xian, M. Bellin, T. Dorn, Q. Tian, A. Goedel, L. Dreizehnter, C. M. Schneider, D. Ward-van Oostwaard, J. K. M. Ng, R. Hinkel, L. S. Pane, C. L. Mummery, P. Lipp, A. Moretti, K.-L. Laugwitz, and D. Sinnecker (2016). Subtype-specific promoter-driven action potential imaging for precise disease modelling and drug testing in hiPSC-derived cardiomyocytes. *European Heart Journal* **38**(4) 292–301. DOI: 10.1093/eurheartj/ehw189.

Cherry, E. M. and F. H. Fenton (2011). Effects of boundaries and geometry on the spatial distribution of action potential duration in cardiac tissue. *Journal of Theoretical Biology* **285**(1) 164–176. DOI: 10.1016/j.jtbi.2011.06.039.

Chiu, P. J. S., K. F. Marcoe, S. E. Bounds, C.-H. Lin, J.-J. Feng, A. Lin, F.-C. Cheng, W. J. Crumb, and R. Mitchell (2004). Validation of a [3H]Astemizole Binding Assay in HEK293 Cells Expressing HERG K+ Channels. *Journal of Pharmacological Sciences* **95**(3) 311–319. DOI: 10.1254/jphs.FPE0040101.

Choi, S. W., H.-A. Lee, S.-H. Moon, S.-J. Park, H. J. Kim, K.-S. Kim, Y. H. Zhang, J. B. Youm, and S. J. Kim (2015). Spontaneous inward currents reflecting oscillatory activation of Na+/Ca2+ exchangers in human embryonic stem cell-derived cardiomyocytes. *Pflügers Archiv - European Journal of Physiology* **468**(4) 609–622. DOI: 10.1007/s00424-015-1769-2.

Christensen, K., K. A. Manani, and N. S. Peters (2015). Simple Model for Identifying Critical Regions in Atrial Fibrillation. *Physical Review Letters* **114**(2) 028104. DOI: 10.1103/PhysRevLett.114.028104.

Clayton, R. H., O. Bernus, E. M. Cherry, H. Dierckx, F. H. Fenton, L. Mirabella, A. V. Panfilov, F. B. Sachse, G. Seemann, and H. Zhang (2011). Models of cardiac tissue electrophysiology: Progress, challenges and open questions. *Progress in Biophysics and Molecular Biology* **104**(1–3) 22–48. DOI: 10.1016/j.pbiomolbio.2010.05.008.

Clements, M., V. Millar, A. S. Williams, and S. Kalinka (2015). Bridging Functional and Structural Cardiotoxicity Assays Using Human Embryonic Stem Cell-Derived Cardiomyocytes for a More Comprehensive Risk Assessment. *Toxicological Sciences* **148**(1) 241–260. DOI: 10.1093/toxsci/kfv180.

Clements, M. and N. Thomas (2014). High-Throughput Multi-Parameter Profiling of Electrophysiological Drug Effects in Human Embryonic Stem Cell Derived Cardiomyocytes Using Multi-Electrode Arrays. *Toxicological Sciences* **140**(2) 445–461. DOI: 10.1093/toxsci/kfu084.

Clerx, M., P. Collins, E. de Lange, and P. G. A. Volders (2016). Myokit: A simple interface to cardiac cellular electrophysiology. *Progress in Biophysics and Molecular Biology* **120**(1) 100–114. DOI: 10.1016/j.pbiomolbio.2015.12.008.

Cohen, J. D., J. E. Babiarz, R. M. Abrams, L. Guo, S. Kameoka, E. Chiao, J. Taunton, and K. L. Kolaja (2011). Use of human stem cell derived cardiomyocytes to examine sunitinib mediated cardiotoxicity and electrophysiological alterations. *Toxicology and Applied Pharmacology* **257**(1) 74–83. DOI: 10.1016/j.taap.2011.08.020.

Colatsky, T., B. Fermini, G. Gintant, J. B. Pierson, P. Sager, Y. Sekino, D. G. Strauss, and N. Stockbridge (2016). The Comprehensive in Vitro Proarrhyth-

mia Assay (CiPA) initiative — Update on progress. *Journal of Pharmacological and Toxicological Methods* **81**(Supplement C) 15–20. DOI: 10.1016/j.vascn.2016.06.002.

Cooper, J., M. Scharm, and G. R. Mirams (2016). The Cardiac Electrophysiology Web Lab. *Biophysical Journal* **110**(2) 292–300. DOI: 10.1016/j.bpj.2015.12.012.

Cooper, J., R. J. Spiteri, and G. R. Mirams (2015). Cellular cardiac electrophysiology modeling with Chaste and CellML. *Frontiers in Physiology* **5**(511) 1–16. DOI: 10.3389/fphys.2014.00511.

Corrias, A., P. Pathmanathan, D. J. Gavaghan, and M. L. Buist (2012). Modelling tissue electrophysiology with multiple cell types: applications of the extended bidomain framework. *Integrative Biology* **4**(2) 192. DOI: 10.1039/c2ib00100d.

Courtemanche, M., R. J. Ramirez, and S. Nattel (1998). Ionic mechanisms underlying human atrial action potential properties: insights from a mathematical model. *American Journal of Physiology - Heart and Circulatory Physiology* **275**(1) H301–H321.

Crumb Jr., W. J., J. Vicente, L. Johannesen, and D. G. Strauss (2016). An evaluation of 30 clinical drugs against the comprehensive in vitro proarrhythmia assay (CiPA) proposed ion channel panel. *Journal of Pharmacological and Toxicological Methods* **81** 251–262. DOI: 10.1016/j.vascn.2016.03.009.

Cummins Lancaster, M. and E. A. Sobie (2016). Improved prediction of drug-induced Torsades de Pointes through simulations of dynamics and machine learning algorithms. *Clinical Pharmacology & Therapeutics* **100**(4) 371–379. DOI: 10.1002/cpt.367.

Curran, M. E., I. Splawski, K. W. Timothy, G. M. Vincen, E. D. Green, and M. T. Keating (1995). A molecular basis for cardiac arrhythmia: HERG mutations cause long QT syndrome. *Cell* **80**(5) 795–803. DOI: 10.1016/0092-8674(95)90358-5.

Darpo, B. (2010). The thorough QT/QTc study 4 years after the implementation of the ICH E14 guidance. *British Journal of Pharmacology* **159**(1) 49–57. DOI: 10.1111/j.1476-5381.2009.00487.x.

Darpö, B. (2001). Spectrum of drugs prolonging QT interval and the incidence of torsades de pointes. *European Heart Journal Supplements* **3**(suppl_K) K70–K80. DOI: 10.1016/S1520-765X(01)90009-4.

Devalla, H. D., V. Schwach, J. W. Ford, J. T. Milnes, S. El-Haou, C. Jackson, K. Gkatzis, D. A. Elliott, S. M. C. d. S. Lopes, C. L. Mummery, A. O. Verkerk, and R. Passier (2015). Atrial-like cardiomyocytes from human pluripotent stem cells are a robust preclinical model for assessing atrial-selective pharmacology. *EMBO Molecular Medicine* **7**(4) 394–410. DOI: 10.15252/emmm.201404757.

Diaz, G. J., K. Daniell, S. T. Leitza, R. L. Martin, Z. Su, J. S. McDermott, B. F. Cox, and G. A. Gintant (2004). The [3H]dofetilide binding assay is a predictive screening tool for hERG blockade and proarrhythmia: Comparison of intact cell and membrane preparations and effects of altering [K+]o. *Journal of Pharmacological and Toxicological Methods* **50**(3) 187–199. DOI: 10.1016/j.vascn.2004.04.001.

DiFrancesco, D. (1993). Pacemaker Mechanisms in Cardiac Tissue. *Annual Review of Physiology* **55**(1) 455–472. DOI: 10.1146/annurev.ph.55.030193.002323.

DiFrancesco, D. and D. Noble (1985). A Model of Cardiac Electrical Activity Incorporating Ionic Pumps and Concentration Changes. *Philosophical Transactions of the Royal Society of London B: Biological Sciences* **307**(1133) 353–398. DOI: 10.1098/rstb.1985.0001.

DiMasi, J. A., R. W. Hansen, and H. G. Grabowski (2003). The price of innovation: new estimates of drug development costs. *Journal of Health Economics* **22**(2) 151–185. DOI: 10.1016/S0167-6296(02)00126-1.

Doherty, K. R., D. R. Talbert, P. B. Trusk, D. M. Moran, S. A. Shell, and S. Bacus (2015). Structural and functional screening in human induced-pluripotent stem cell-derived cardiomyocytes accurately identifies cardiotoxicity of multiple drug types. *Toxicology and Applied Pharmacology* **285**(1) 51–60. DOI: 10.1016/j.taap.2015.03.008.

Dolnikov, K., M. Shilkrut, N. Zeevi-Levin, A. Danon, S. Gerecht-Nir, J. Itskovitz-Eldor, and O. Binah (2005). Functional Properties of Human Embryonic Stem Cell-Derived Cardiomyocytes. *Annals of the New York Academy of Sciences* **1047**(1) 66–75. DOI: 10.1196/annals.1341.006.

Doss, M. X., J. M. Di Diego, R. J. Goodrow, Y. Wu, J. M. Cordeiro, V. V. Nesterenko, H. Barajas-Martínez, D. Hu, J. Urrutia, M. Desai, J. A. Treat, A. Sachinidis, and C. Antzelevitch (2012). Maximum Diastolic Potential of Human Induced Pluripotent Stem Cell-Derived Cardiomyocytes Depends Critically on IKr. *PLoS ONE* **7**(7) e40288. DOI: 10.1371/journal.pone.0040288.

Du, D. T. M., N. Hellen, C. Kane, and C. M. N. Terracciano (2015). Action Potential Morphology of Human Induced Pluripotent Stem Cell-Derived Cardiomyocytes Does Not Predict Cardiac Chamber Specificity and Is Dependent on Cell Density. *Biophysical Journal* **108**(1) 1–4. DOI: 10.1016/j.bpj.2014.11.008.

Dumaine, R., J. A. Towbin, P. Brugada, M. Vatta, D. V. Nesterenko, V. V. Nesterenko, J. Brugada, R. Brugada, and C. Antzelevitch (1999). Ionic Mechanisms Responsible for the Electrocardiographic Phenotype of the Brugada Syndrome Are Temperature Dependent. *Circulation Research* **85**(9) 803–809. DOI: 10.1161/01.RES.85.9.803.

Dunn, S.-J., I. S. Näthke, and J. M. Osborne (2013). Computational Models Reveal a Passive Mechanism for Cell Migration in the Crypt. *PLoS ONE* **8**(11) e80516. DOI: 10.1371/journal.pone.0080516.

Dutta, S., K. C. Chang, K. A. Beattie, J. Sheng, P. N. Tran, W. W. Wu, M. Wu, D. G. Strauss, T. Colatsky, and Z. Li (2017). Optimization of an In silico Cardiac Cell Model for Proarrhythmia Risk Assessment. *Frontiers in Physiology* **8** 616. DOI: 10.3389/fphys.2017.00616.

Elkins, R. C., M. R. Davies, S. J. Brough, D. J. Gavaghan, Y. Cui, N. Abi-Gerges, and G. R. Mirams (2013). Variability in high-throughput ion-channel screening data and consequences for cardiac safety assessment. *Journal of Pharmacological and Toxicological Methods* **68**(1) 112–122. DOI: 10.1016/j.vascn.2013.04.007.

Eng, G., B. W. Lee, L. Protas, M. Gagliardi, K. Brown, R. S. Kass, G. Keller, R. B. Robinson, and G. Vunjak-Novakovic (2016). Autonomous beating rate adaptation in human stem cell-derived cardiomyocytes. *Nature Communications* **7** 10312. DOI: 10.1038/ncomms10312.

Fejtl, M., A. Stett, W. Nisch, K.-H. Boven, and A. Möller (2006). On Micro-Electrode Array Revival: Its Development, Sophistication of Recording, and Stimulation. In *Advances in Network Electrophysiology*. Ed. M. Taketani and M. Baudry. Springer US, 24–37. ISBN: 978-0-387-25857-7 978-0-387-25858-4.

Fenichel, R. R., M. Malik, C. Antzelevitch, M. Sanguinetti, D. M. Roden, S. G. Priori, J. N. Ruskin, R. J. Lipicky, L. R. Cantilena, and Independent Academic Task Force (2004). Drug-Induced Torsades de Pointes and Implications for Drug Development. *Journal of Cardiovascular Electrophysiology* **15**(4) 475–495. DOI: 10.1046/j.1540-8167.2004.03534.x.

Fenton, F. and A. Karma (1998). Vortex dynamics in three-dimensional continuous myocardium with fiber rotation: Filament instability and fibrillation. *Chaos: An Interdisciplinary Journal of Nonlinear Science* **8**(1) 20–47. DOI: 10.1063/1.166311.

Fermini, B. and A. A. Fossa (2003). The impact of drug-induced QT interval prolongation on drug discovery and development. *Nature Reviews Drug Discovery* **2**(6) 439–447. DOI: 10.1038/nrd1108.

Fermini, B., J. C. Hancox, N. Abi-Gerges, M. Bridgland-Taylor, K. W. Chaudhary, T. Colatsky, K. Correll, W. Crumb, B. Damiano, G. Erdemli, G. Gintant, J. Imredy, J. Koerner, J. Kramer, P. Levesque, Z. Li, A. Lindqvist, C. A. Obejero-Paz, D. Rampe, K. Sawada, D. G. Strauss, and J. I. Vandenberg (2016). A New Perspective in the Field of Cardiac Safety Testing through the Comprehensive In Vitro Proarrhythmia Assay Paradigm. *Journal of Biomolecular Screening* **21**(1) 1–11. DOI: 10.1177/1087057115594589.

Fine, M., F.-M. Lu, M.-J. Lin, O. Moe, H.-R. Wang, and D. W. Hilgemann (2013). Human-induced pluripotent stem cell-derived cardiomyocytes for studies of cardiac ion transporters. *American Journal of Physiology - Cell Physiology* **305**(5) C481–C491. DOI: 10.1152/ajpcell.00143.2013.

Fink, M., S. A. Niederer, E. M. Cherry, F. H. Fenton, J. T. Koivumäki, G. Seemann, R. Thul, H. Zhang, F. B. Sachse, D. Beard, E. J. Crampin, and N. P. Smith (2011). Cardiac cell modelling: Observations from the heart of the cardiac physiome project. *Progress in Biophysics and Molecular Biology* **104**(1–3) 2–21. DOI: 10.1016/j.pbiomolbio.2010.03.002.

FitzHugh, R. (1961). Impulses and Physiological States in Theoretical Models of Nerve Membrane. *Biophysical Journal* **1**(6) 445–466.

Frotscher, R., J.-P. Koch, and M. Staat (2015). Computational investigation of drug action on human-induced stem cell-derived cardiomyocytes. *Journal of Biomechanical Engineering* **137**(7) 071002. DOI: 10.1115/1.4030173.

Frotscher, R., D. Muanghong, G. Dursun, M. Goßmann, A. Temiz-Artmann, and M. Staat (2016). Sample-specific adaption of an improved electro-mechanical model of in vitro cardiac tissue. *Journal of Biomechanics* **49**(12) 2428–2435. DOI: 10.1016/j.jbiomech.2016.01.039.

Garny, A. and P. J. Hunter (2015). OpenCOR: a modular and interoperable approach to computational biology. *Frontiers in Physiology* **6** 26. DOI: 10.3389/fphys.2015.00026.

Garny, A., D. P. Nickerson, J. Cooper, R. W. d. Santos, A. K. Miller, S. McKeever, P. M. F. Nielsen, and P. J. Hunter (2008). CellML and associated tools and techniques. *Philosophical Transactions of the Royal Society of London A: Mathematical, Physical and Engineering Sciences* **366**(1878) 3017–3043. DOI: 10.1098/rsta.2008.0094.

Geuzaine, C. and J.-F. Remacle (2009). Gmsh: A 3-D finite element mesh generator with built-in pre- and post-processing facilities. *International Journal for Numerical Methods in Engineering* **79**(11) 1309–1331. DOI: 10.1002/nme.2579.

Gherghiceanu, M., L. Barad, A. Novak, I. Reiter, J. Itskovitz-Eldor, O. Binah, and L. Popescu (2011). Cardiomyocytes derived from human embryonic and induced pluripotent stem cells: comparative ultrastructure. *Journal of Cellular and Molecular Medicine* **15**(11) 2539–2551. DOI: 10.1111/j.1582-4934.2011.01417.x.

Gibson, J. K., Y. Yue, J. Bronson, C. Palmer, and R. Numann (2014). Human stem cell-derived cardiomyocytes detect drug-mediated changes in action potentials and ion currents. *Journal of Pharmacological and Toxicological Methods* **70**(3) 255–267. DOI: 10.1016/j.vascn.2014.09.005.

Giles, W. R. and D. Noble (2016). Rigorous Phenotyping of Cardiac iPSC Preparations Requires Knowledge of Their Resting Potential(s). *Biophysical Journal* **110**(1) 278–280. DOI: 10.1016/j.bpj.2015.06.070.

Gima, K. and Y. Rudy (2002). Ionic Current Basis of Electrocardiographic Waveforms A Model Study. *Circulation Research* **90**(8) 889–896. DOI: 10.1161/01.RES.0000016960.61087.86.

Gintant, G., P. T. Sager, and N. Stockbridge (2016). Evolution of strategies to improve preclinical cardiac safety testing. *Nature Reviews Drug Discovery* **15**(7) 457–471. DOI: 10.1038/nrd.2015.34.

Goodrow, R. J., S. Desai, J. A. Treat, B. K. Panama, M. Desai, V. V. Nesterenko, and J. M. Cordeiro (2018). Biophysical comparison of sodium currents in native cardiac myocytes and human induced pluripotent stem cell-derived cardiomyocytes. *Journal of Pharmacological and Toxicological Methods* **90**(Supplement C) 19–30. DOI: 10.1016/j.vascn.2017.11.001.

Gorospe, G., R. Zhu, M. Millrod, E. Zambidis, L. Tung, and R. Vidal (2014). Automated Grouping of Action Potentials of Human Embryonic Stem Cell-Derived Cardiomyocytes. *IEEE Transactions on Biomedical Engineering* **61**(9) 2389–2395. DOI: 10.1109/TBME.2014.2311387.

Goversen, B., M. A. G. van der Heyden, T. A. B. van Veen, and T. P. de Boer (2017). The immature electrophysiological phenotype of iPSC-CMs still hampers in vitro drug screening: Special focus on IK1. *Pharmacology & Therapeutics* **183** 127–136. DOI: 10.1016/j.pharmthera.2017.10.001.

Grandi, E., S. V. Pandit, N. Voigt, A. J. Workman, D. Dobrev, J. Jalife, and D. M. Bers (2011). Human Atrial Action Potential and Ca2+ Model: Sinus Rhythm and Chronic Atrial Fibrillation. *Circulation Research*, 1055–1066. DOI: 10.1161/CIRCRESAHA.111.253955.

Grandi, E., F. S. Pasqualini, and D. M. Bers (2010). A novel computational model of the human ventricular action potential and Ca transient. *Journal of Molecular and Cellular Cardiology* **48**(1) 112–121. DOI: 10.1016/j.yjmcc.2009.09.019.

Grandi, E., F. S. Pasqualini, C. Pes, C. Corsi, A. Zaza, and S. Severi (2009). Theoretical investigation of action potential duration dependence on extracellular Ca2+ in human cardiomyocytes. *Journal of Molecular and Cellular Cardiology* **46**(3) 332–342. DOI: 10.1016/j.yjmcc.2008.12.002.

Grant, A. O. (2009). Cardiac Ion Channels. *Circulation: Arrhythmia and Electrophysiology* **2**(2) 185–194. DOI: 10.1161/CIRCEP.108.789081.

Greenstein, J. L., R. Wu, S. Po, G. F. Tomaselli, and R. L. Winslow (2000). Role of the Calcium-Independent Transient Outward Current Ito1 in Shaping Action Potential Morphology and Duration. *Circulation Research* **87**(11) 1026–1033. DOI: 10.1161/01.RES.87.11.1026.

Gu, M., P. K. Nguyen, A. S. Lee, D. Xu, S. Hu, J. R. Plews, L. Han, B. C. Huber, W. H. Lee, Y. Gong, P. E. d. Almeida, J. Lyons, F. Ikeno, C. Pacharinsak, A. J. Connolly, S. S. Gambhir, R. C. Robbins, M. T. Longaker, and J. C. Wu (2012). Microfluidic Single-Cell Analysis Shows That Porcine Induced Pluripotent Stem Cell–Derived Endothelial Cells Improve Myocardial Function by Paracrine Activation: Novelty and Significance. *Circulation Research* **111**(7) 882–893. DOI: 10.1161/CIRCRESAHA.112.269001.

Guo, L., R. M. C. Abrams, J. E. Babiarz, J. D. Cohen, S. Kameoka, M. J. Sanders, E. Chiao, and K. L. Kolaja (2011a). Estimating the Risk of Drug-Induced Proarrhythmia Using Human Induced Pluripotent Stem Cell–Derived Cardiomyocytes. *Toxicological Sciences* **123**(1) 281–289. DOI: 10.1093/toxsci/kfr158.

Guo, L., L. Coyle, R. M. C. Abrams, R. Kemper, E. T. Chiao, and K. L. Kolaja (2013). Refining the Human iPSC-Cardiomyocyte Arrhythmic Risk Assessment Model. *Toxicological Sciences* **136**(2) 581–594. DOI: 10.1093/toxsci/kft205.

Guo, L., J.-Y. Qian, R. Abrams, H.-M. Tang, T. Weiser, M. J. Sanders, and K. L. Kolaja (2011b). The Electrophysiological Effects of Cardiac Glycosides in Human iPSC-derived Cardiomyocytes and in Guinea Pig Isolated Hearts. *Cellular Physiology and Biochemistry* **27**(5) 453–462. DOI: 10.1159/000329966.

Halbach, M., U. Egert, J. Hescheler, and K. Banach (2003). Estimation of Action Potential Changes from Field Potential Recordings in Multicellular Mouse Cardiac Myocyte Cultures. *Cellular Physiology and Biochemistry* **13**(5) 271–284. DOI: 10.1159/000074542.

Hamlin, R. L., C. A. Cruze, S. W. Mittelstadt, A. Kijtawornrat, B. W. Keene, B. M. Roche, T. Nakayama, H. Nakayama, D. M. Hamlin, and T. Arnold (2004). Sensitivity and specificity of isolated perfused guinea pig heart to test for drug-induced lengthening of QTc. *Journal of Pharmacological and Toxicological Methods* **49**(1) 15–23. DOI: 10.1016/j.vascn.2003.08.003.

Hamlin, R. L. (2007). Animal models of ventricular arrhythmias. *Pharmacology & Therapeutics* **113**(2) 276–295. DOI: 10.1016/j.pharmthera.2006.08.006.

Hammond, T. G., L. Carlsson, A. S. Davis, W. G. Lynch, I. MacKenzie, W. S. Redfern, A. T. Sullivan, and A. J. Camm (2001). Methods of collecting and

evaluating non-clinical cardiac electrophysiology data in the pharmaceutical industry: results of an international survey. *Cardiovascular Research* **49**(4) 741–750. DOI: 10.1016/S0008-6363(00)00310-2.

Hand, P. E. and B. E. Griffith (2010). Adaptive multiscale model for simulating cardiac conduction. *Proceedings of the National Academy of Sciences* **107**(33) 14603–14608. DOI: 10.1073/pnas.1008443107.

Hand, P. E. and B. E. Griffith (2011). Empirical Study of an Adaptive Multiscale Model for Simulating Cardiac Conduction. *Bulletin of Mathematical Biology* **73**(12) 3071–3089. DOI: 10.1007/s11538-011-9661-5.

Harris, K., M. Aylott, Y. Cui, J. B. Louttit, N. C. McMahon, and A. Sridhar (2013). Comparison of Electrophysiological Data From Human-Induced Pluripotent Stem Cell-Derived Cardiomyocytes to Functional Preclinical Safety Assays. *Toxicological Sciences* **134**(2) 412–426. DOI: 10.1093/toxsci/kft113.

He, J.-Q., Y. Ma, Y. Lee, J. A. Thomson, and T. J. Kamp (2003). Human Embryonic Stem Cells Develop Into Multiple Types of Cardiac Myocytes: Action Potential Characterization. *Circulation Research* **93**(1) 32–39. DOI: 10.1161/01.RES.0000080317.92718.99.

Heidenreich, E. A., J. M. Ferrero, M. Doblaré, and J. F. Rodríguez (2010). Adaptive Macro Finite Elements for the Numerical Solution of Monodomain Equations in Cardiac Electrophysiology. *Annals of Biomedical Engineering* **38**(7) 2331–2345. DOI: 10.1007/s10439-010-9997-2.

Heijman, J., N. Voigt, L. G. Carlsson, and D. Dobrev (2014). Cardiac safety assays. *Current Opinion in Pharmacology* **15**(1) 16–21. DOI: 10.1016/j.coph.2013.11.004.

Henney, J. E. (2000). Withdrawal of troglitazone and cisapride. *Journal of the American Medical Association* **283**(17) 2228–2228. DOI: 10.1001/jama.283.17.2228.

Herron, T. J. (2016). Calcium and voltage mapping in hiPSC-CM monolayers. *Cell Calcium* **59**(2–3) 84–90. DOI: 10.1016/j.ceca.2016.02.004.

Herron, T. J., A. M. D. Rocha, K. F. Campbell, D. Ponce-Balbuena, B. C. Willis, G. Guerrero-Serna, Q. Liu, M. Klos, H. Musa, M. Zarzoso, A. Bizy, J. Furness, J. Anumonwo, S. Mironov, and J. Jalife (2016). Extracellular Matrix-Mediated Maturation of Human Pluripotent Stem Cell-Derived Cardiac Monolayer Structure and Electrophysiological Function. *Circulation: Arrhythmia and Electrophysiology* **9**(4) e003638. DOI: 10.1161/CIRCEP.113.003638.

Hindmarsh, A. C., P. N. Brown, K. E. Grant, S. L. Lee, R. Serban, D. E. Shumaker, and C. S. Woodward (2005). SUNDIALS: Suite of Nonlinear and Differential/Algebraic Equation Solvers. *ACM Transactions on Mathematical Software (TOMS)* **31**(3) 363–396. DOI: 10.1145/1089014.1089020.

Hodgkin, A. L. and A. F. Huxley (1952a). A quantitative description of membrane current and its application to conduction and excitation in nerve. *The Journal of Physiology* **117**(4) 500–544.

Hodgkin, A. L. and A. F. Huxley (1952b). Currents carried by sodium and potassium ions through the membrane of the giant axon of Loligo. *The Journal of Physiology* **116**(4) 449–472.

Hodgkin, A. L. and A. F. Huxley (1952c). The components of membrane conductance in the giant axon of Loligo. *The Journal of Physiology* **116**(4) 473–496. DOI: 10.1113/jphysiol.1952.sp004718.

Hodgkin, A. L. and A. F. Huxley (1952d). The dual effect of membrane potential on sodium conductance in the giant axon of Loligo. *The Journal of Physiology* **116**(4) 497–506.

Honda, M., J. Kiyokawa, M. Tabo, and T. Inoue (2011). Electrophysiological Characterization of Cardiomyocytes Derived From Human Induced Pluripotent Stem Cells. *Journal of Pharmacological Sciences* **117**(3) 149–159. DOI: 10.1254/jphs.11038FP.

Hondeghem, L. M. (2006). Thorough QT/QTc Not So Thorough: Removes Torsadogenic Predictors from the T-Wave, Incriminates Safe Drugs, and Misses Profibrillatory Drugs. *Journal of Cardiovascular Electrophysiology* **17**(3) 337–340. DOI: 10.1111/j.1540-8167.2006.00347.x.

Hwang, H. S., D. O. Kryshtal, T. K. Feaster, V. Sánchez-Freire, J. Zhang, T. J. Kamp, C. C. Hong, J. C. Wu, and B. C. Knollmann (2015). Comparable calcium handling of human iPSC-derived cardiomyocytes generated by multiple laboratories. *Journal of Molecular and Cellular Cardiology* **85** 79–88. DOI: 10.1016/j.yjmcc.2015.05.003.

ICH (2001). *ICH Topic S7A: Safety Pharmacology Studies for Human Pharmaceuticals*. Report: CPMP/ICH/539/00.

ICH (2005a). *ICH E14: Clinical evaluation of QT/QTc interval prolongation and proarrhythmic potential for non-antiarrhythmic drugs*. Report: CHMP/ICH/2/04.

ICH (2005b). *ICH Topic S7B: The Nonclinical Evaluation of the Potential for Delayed Ventricular Repolarization (QT Interval Prolongation) by Human Pharmaceuticals*. Report: CPMP/ICH/423/02.

Itzhaki, I., L. Maizels, I. Huber, L. Zwi-Dantsis, O. Caspi, A. Winterstern, O. Feldman, A. Gepstein, G. Arbel, H. Hammerman, M. Boulos, and L. Gepstein (2011). Modelling the long QT syndrome with induced pluripotent stem cells. *Nature* **471**(7337) 225–229. DOI: 10.1038/nature09747.

Ivashchenko, C. Y., G. C. Pipes, I. M. Lozinskaya, Z. Lin, X. Xiaoping, S. Needle, E. T. Grygielko, E. Hu, J. R. Toomey, J. J. Lepore, and R. N. Willette (2013). Human-induced pluripotent stem cell-derived cardiomyocytes exhibit temporal changes in phenotype. *American Journal of Physiology - Heart and Circulatory Physiology* **305**(6) H913–H922. DOI: 10.1152/ajpheart.00819.2012.

Iyer, V., R. Mazhari, and R. L. Winslow (2004). A Computational Model of the Human Left-Ventricular Epicardial Myocyte. *Biophysical Journal* **87**(3) 1507–1525. DOI: 10.1529/biophysj.104.043299.

Izumi-Nakaseko, H., Y. Kanda, Y. Nakamura, M. Hagiwara-Nagasawa, T. Wada, K. Ando, A. T. Naito, Y. Sekino, and A. Sugiyama (2017). Development of correction formula for field potential duration of human induced pluripotent stem cell-derived cardiomyocytes sheets. *Journal of Pharmacological Sciences* **135**(1) 44–50. DOI: 10.1016/j.jphs.2017.08.008.

Ji, J., J. Kang, and D. Rampe (2014). L-Type Ca2+ Channel Responses to Bay K 8644 in Stem Cell-Derived Cardiomyocytes Are Unusually Dependent on

Holding Potential and Charge Carrier. *ASSAY and Drug Development Technologies* **12**(6) 352–360. DOI: 10.1089/adt.2014.596.

Jiang, P., S. N. Rushing, C.-w. Kong, J. Fu, D. K.-T. Lieu, C. W. Chan, W. Deng, and R. A. Li (2010). Electrophysiological properties of human induced pluripotent stem cells. *American Journal of Physiology - Cell Physiology* **298**(3) C486–C495. DOI: 10.1152/ajpcell.00251.2009.

Jones, A. R., D. H. Edwards, M. J. Cummins, A. J. Williams, and C. H. George (2016). A Systemized Approach to Investigate Ca2+ Synchronization in Clusters of Human Induced Pluripotent Stem-Cell Derived Cardiomyocytes. *Frontiers in Cell and Developmental Biology* **3** 89. DOI: 10.3389/fcell.2015.00089.

Jonsson, M. K., G. Duker, C. Tropp, B. Andersson, P. Sartipy, M. A. Vos, and T. A. van Veen (2010). Quantified proarrhythmic potential of selected human embryonic stem cell-derived cardiomyocytes. *Stem Cell Research* **4**(3) 189–200. DOI: 10.1016/j.scr.2010.02.001.

Jonsson, M. K., M. A. Vos, G. R. Mirams, G. Duker, P. Sartipy, T. P. de Boer, and T. A. van Veen (2012). Application of human stem cell-derived cardiomyocytes in safety pharmacology requires caution beyond hERG. *Journal of Molecular and Cellular Cardiology* **52**(5) 998–1008. DOI: 10.1016/j.yjmcc.2012.02.002.

Josefson, D. (1997). Hay fever drug to be banned by the FDA. *British Medical Journal* **314**(7076) 248.

Josowitz, R., J. Lu, C. Falce, S. L. D'Souza, M. Wu, N. Cohen, N. C. Dubois, Y. Zhao, E. A. Sobie, G. I. Fishman, and B. D. Gelb (2014). Identification and Purification of Human Induced Pluripotent Stem Cell-Derived Atrial-Like Cardiomyocytes Based on Sarcolipin Expression. *PLoS ONE* **9**(7) e101316. DOI: 10.1371/journal.pone.0101316.

Kadota, S., I. Minami, N. Morone, J. E. Heuser, K. Agladze, and N. Nakatsuji (2013). Development of a reentrant arrhythmia model in human pluripotent stem cell-derived cardiac cell sheets. *European Heart Journal* **34**(15) 1147–1156. DOI: 10.1093/eurheartj/ehs418.

Kamakura, T., T. Makiyama, K. Sasaki, Y. Yoshida, Y. Wuriyanghai, J. Chen, T. Hattori, S. Ohno, T. Kita, M. Horie, S. Yamanaka, and T. Kimura (2013). Ultrastructural Maturation of Human-Induced Pluripotent Stem Cell-Derived Cardiomyocytes in a Long-Term Culture. *Circulation Journal* **77**(5) 1307–1314. DOI: 10.1253/circj.CJ-12-0987.

Kane, C., D. T. M. Du, N. Hellen, and C. M. Terracciano (2016). The Fallacy of Assigning Chamber Specificity to iPSC Cardiac Myocytes from Action Potential Morphology. *Biophysical Journal* **110**(1) 281–283. DOI: 10.1016/j.bpj.2015.08.052.

Kane, C. and C. M. N. Terracciano (2017). Concise Review: Criteria for Chamber-Specific Categorization of Human Cardiac Myocytes Derived from Pluripotent Stem Cells. *Stem Cells* **35**(8) 1881–1897. DOI: 10.1002/stem.2649.

Keener, J. P. and A. V. Panfilov (1996). A biophysical model for defibrillation of cardiac tissue. *Biophysical Journal* **71**(3) 1335–1345. DOI: 10.1016/S0006-3495(96)79333-5.

Keener, J. and J. Sneyd (2008). *Mathematical Physiology: I: Cellular Physiology*. Springer Science & Business Media. ISBN: 978-0-387-75846-6.

Keener, J. and J. Sneyd (2009). *Mathematical Physiology: II: Systems Physiology*. Springer Science & Business Media. ISBN: 978-0-387-79388-7.

Kehat, I., D. Kenyagin-Karsenti, M. Snir, H. Segev, M. Amit, A. Gepstein, E. Livne, O. Binah, J. Itskovitz-Eldor, and L. Gepstein (2001). Human embryonic stem cells can differentiate into myocytes with structural and functional properties of cardiomyocytes. *Journal of Clinical Investigation* **108**(3) 407–414. DOI: 10.1172/JCI12131.

Kienast, R., M. Stöger, M. Handler, F. Hanser, and C. Baumgartner (2014). Alterations of field potentials in isotropic cardiomyocyte cell layers induced by multiple endogenous pacemakers under normal and hypothermal conditions. *American Journal of Physiology - Heart and Circulatory Physiology* **307**(7) H1013–H1023. DOI: 10.1152/ajpheart.00097.2014.

Kim, C., M. Majdi, P. Xia, K. A. Wei, M. Talantova, S. Spiering, B. Nelson, M. Mercola, and H.-s. V. Chen (2009). Non-Cardiomyocytes Influence the Electrophysiological Maturation of Human Embryonic Stem Cell-Derived Cardiomyocytes During Differentiation. *Stem Cells and Development* **19**(6) 783–795. DOI: 10.1089/scd.2009.0349.

Kucera, J. P., Y. Prudat, I. C. Marcu, M. Azzarito, and N. D. Ullrich (2015). Slow Conduction in Mixed Cultured Strands of Primary Ventricular Cells and Stem Cell-Derived Cardiomyocytes. *Frontiers in Cell and Developmental Biology* **3** 58. DOI: 10.3389/fcell.2015.00058.

Kuramoto, Y. (1981). Rhythms and turbulence in populations of chemical oscillators. *Physica A: Statistical Mechanics and its Applications* **106**(1–2) 128–143. DOI: 10.1016/0378-4371(81)90214-4.

Laksman, Z., M. Wauchop, E. Lin, S. Protze, J. Lee, W. Yang, F. Izaddoustdar, S. Shafaattalab, L. Gepstein, G. F. Tibbits, G. Keller, and P. H. Backx (2017). Modeling Atrial Fibrillation using Human Embryonic Stem Cell-Derived Atrial Tissue. *Scientific Reports* **7**(1) 5268. DOI: 10.1038/s41598-017-05652-y.

Laverty, H., C. Benson, E. Cartwright, M. Cross, C. Garland, T. Hammond, C. Holloway, N. McMahon, J. Milligan, B. Park, M. Pirmohamed, C. Pollard, J. Radford, N. Roome, P. Sager, S. Singh, T. Suter, W. Suter, A. Trafford, P. Volders, R. Wallis, R. Weaver, M. York, and J. Valentin (2011). How can we improve our understanding of cardiovascular safety liabilities to develop safer medicines? *British Journal of Pharmacology* **163**(4) 675–693. DOI: 10.1111/j.1476-5381.2011.01255.x.

Lawrence, C. L., C. E. Pollard, T. G. Hammond, and J.-P. Valentin (2005). Nonclinical proarrhythmia models: Predicting Torsades de Pointes. *Journal of Pharmacological and Toxicological Methods* **52**(1) 46–59. DOI: 10.1016/j.vascn.2005.04.011.

Lee, J., A. Cookson, I. Roy, E. Kerfoot, L. Asner, G. Vigueras, T. Sochi, S. Deparis, C. Michler, N. Smith, and D. Nordsletten (2016a). Multiphysics Computational Modeling in CHeart. *SIAM Journal on Scientific Computing* **38**(3) C150–C178. DOI: 10.1137/15M1014097.

Lee, P., M. Klos, C. Bollensdorff, L. Hou, P. Ewart, T. J. Kamp, J. Zhang, A. Bizy, G. Guerrero-Serna, P. Kohl, J. Jalife, and T. J. Herron (2012). Simultaneous Voltage and Calcium Mapping of Genetically Purified Human Induced Pluripotent Stem Cell-Derived Cardiac Myocyte Monolayers. *Circulation Research* **110**(12) 1556–1563. DOI: 10.1161/CIRCRESAHA.111.262535.

Lee, S., H.-A. Lee, S. W. Choi, S. J. Kim, and K.-S. Kim (2016b). Evaluation of nefazodone-induced cardiotoxicity in human induced pluripotent stem cell-derived cardiomyocytes. *Toxicology and Applied Pharmacology* **296** 42–53. DOI: 10.1016/j.taap.2016.01.015.

Lee, W., S. A. Mann, M. J. Windley, M. S. Imtiaz, J. I. Vandenberg, and A. P. Hill (2016c). In silico assessment of kinetics and state dependent binding properties of drugs causing acquired LQTS. *Progress in Biophysics and Molecular Biology* **120**(1–3) 89–99. DOI: 10.1016/j.pbiomolbio.2015.12.005.

Lei, C. L., K. Wang, M. Clerx, R. H. Johnstone, M. P. Hortigon-Vinagre, V. Zamora, A. Allan, G. L. Smith, D. J. Gavaghan, G. R. Mirams, and L. Polonchuk (2017). Tailoring Mathematical Models to Stem-Cell Derived Cardiomyocyte Lines Can Improve Predictions of Drug-Induced Changes to Their Electrophysiology. *Frontiers in Physiology* **8** 986. DOI: 10.3389/fphys.2017.00986.

Levick, J. R. (2012). *An Introduction to Cardiovascular Physiology*. 5th ed. Hodder Education. ISBN: 978-1-4441-6647-7.

Li, Z., S. Dutta, J. Sheng, P. N. Tran, W. Wu, K. Chang, T. Mdluli, D. G. Strauss, and T. Colatsky (2017). Improving the In Silico Assessment of Proarrhythmia Risk by Combining hERG (Human Ether-à-go-go-Related Gene) Channel–Drug Binding Kinetics and Multichannel Pharmacology. *Circulation: Arrhythmia and Electrophysiology* **10**(2) e004628. DOI: 10.1161/CIRCEP.116.004628.

Lieu, D. K., J.-D. Fu, N. Chiamvimonvat, K. C. Tung, G. P. McNerney, T. Huser, G. Keller, C.-W. Kong, and R. A. Li (2013). Mechanism-Based Facilitated Maturation of Human Pluripotent Stem Cell–Derived Cardiomyocytes. *Circulation: Arrhythmia and Electrophysiology* **6**(1) 191–201. DOI: 10.1161/CIRCEP.111.973420.

Lopez-Izquierdo, A., M. Warren, M. Riedel, S. Cho, S. Lai, R. L. Lux, K. W. Spitzer, I. J. Benjamin, M. Tristani-Firouzi, and C. J. Jou (2014). A near-infrared fluorescent voltage-sensitive dye allows for moderate-throughput electrophysiological analyses of human induced pluripotent stem cell-derived cardiomyocytes. *American Journal of Physiology - Heart and Circulatory Physiology* **307**(9) H1370–H1377. DOI: 10.1152/ajpheart.00344.2014.

Lord, G. J., C. E. Powell, and T. Shardlow (2014). *An Introduction to Computational Stochastic PDEs*. Cambridge University Press. ISBN: 978-0-521-89990-1.

Lundy, S. D., W.-Z. Zhu, M. Regnier, and M. A. Laflamme (2013). Structural and Functional Maturation of Cardiomyocytes Derived from Human Pluripotent Stem Cells. *Stem Cells and Development* **22**(14) 1991–2002. DOI: 10.1089/scd.2012.0490.

Luo, C. H. and Y. Rudy (1991). A model of the ventricular cardiac action potential. Depolarization, repolarization, and their interaction. *Circulation Research* **68**(6) 1501–1526. DOI: 10.1161/01.RES.68.6.1501.

Luo, C. H. and Y. Rudy (1994). A dynamic model of the cardiac ventricular action potential. I. Simulations of ionic currents and concentration changes. *Circulation Research* **74**(6) 1071–1096. DOI: 10.1161/01.RES.74.6.1071.

Ma, J., L. Guo, S. J. Fiene, B. D. Anson, J. A. Thomson, T. J. Kamp, K. L. Kolaja, B. J. Swanson, and C. T. January (2011). High purity human-induced pluripotent stem cell-derived cardiomyocytes: electrophysiological properties of action potentials and ionic currents. *American Journal of Physiology - Heart and Circulatory Physiology* **301**(5) H2006–H2017. DOI: 10.1152/ajpheart.00694.2011.

Maillet, A., K. Tan, X. Chai, S. N. Sadananda, A. Mehta, J. Ooi, M. R. Hayden, M. A. Pouladi, S. Ghosh, W. Shim, and L. R. Brunham (2016). Modeling Doxorubicin-Induced Cardiotoxicity in Human Pluripotent Stem Cell Derived-Cardiomyocytes. *Scientific Reports* **6** 25333. DOI: 10.1038/srep25333.

Malik, M., E. M. v. Gelderen, J. H. Lee, D. L. Kowalski, M. Yen, R. Goldwater, S. K. Mujais, M. P. Schaddelee, P. d. Koning, A. Kaibara, S. S. Moy, and J. J. Keirns (2012). Proarrhythmic Safety of Repeat Doses of Mirabegron in Healthy Subjects: A Randomized, Double-Blind, Placebo-, and Active-Controlled Thorough QT Study. *Clinical Pharmacology & Therapeutics* **92**(6) 696–706. DOI: 10.1038/clpt.2012.181.

Mandel, Y., A. Weissman, R. Schick, L. Barad, A. Novak, G. Meiry, S. Goldberg, A. Lorber, M. R. Rosen, J. Itskovitz-Eldor, and O. Binah (2012). Human Embryonic and Induced Pluripotent Stem Cell–Derived Cardiomyocytes Exhibit Beat Rate Variability and Power-Law Behavior. *Circulation* **125**(7) 883–893. DOI: 10.1161/CIRCULATIONAHA.111.045146.

Marsh, M. E., S. T. Ziaratgahi, and R. J. Spiteri (2012). The Secrets to the Success of the Rush-Larsen Method and its Generalizations. *IEEE Transactions on Biomedical Engineering* **59**(9) 2506–2515. DOI: 10.1109/TBME.2012.2205575.

Matsa, E., D. Rajamohan, E. Dick, L. Young, I. Mellor, A. Staniforth, and C. Denning (2011). Drug evaluation in cardiomyocytes derived from human induced pluripotent stem cells carrying a long QT syndrome type 2 mutation. *European Heart Journal* **32**(8) 952–962. DOI: 10.1093/eurheartj/ehr073.

McAllister, R. E., D. Noble, and R. W. Tsien (1975). Reconstruction of the electrical activity of cardiac Purkinje fibres. *The Journal of Physiology* **251**(1) 1–59.

McMillan, B., D. J. Gavaghan, and G. R. Mirams (2017). Early afterdepolarisation tendency as a simulated pro-arrhythmic risk indicator. *Toxicology Research* **6**(6) 912–921. DOI: 10.1039/C7TX00141J.

Mehta, A., Y. Y. Chung, A. Ng, F. Iskandar, S. Atan, H. Wei, G. Dusting, W. Sun, P. Wong, and W. Shim (2011). Pharmacological response of human cardiomyocytes derived from virus-free induced pluripotent stem cells. *Cardiovascular Research* **91**(4) 577–586. DOI: 10.1093/cvr/cvr132.

Millard, D., Q. Dang, H. Shi, X. Zhang, C. Strock, U. Kraushaar, H. Zeng, P. Levesque, H.-R. Lu, J.-M. Guillon, J. C. Wu, Y. Li, G. Luerman, B. Anson, L. Guo, M. Clements, Y. A. Abassi, J. Ross, J. Pierson, and G. Gintant (2018). Cross-Site Reliability of Human Induced Pluripotent stem cell-derived

Cardiomyocyte Based Safety Assays Using Microelectrode Arrays: Results from a Blinded CiPA Pilot Study. *Toxicological Sciences* **164**(2) 550–562. DOI: 10.1093/toxsci/kfy110.

Mirams, G. R., C. J. Arthurs, M. O. Bernabeu, R. Bordas, J. Cooper, A. Corrias, Y. Davit, S.-J. Dunn, A. G. Fletcher, D. G. Harvey, M. E. Marsh, J. M. Osborne, P. Pathmanathan, J. Pitt-Francis, J. Southern, N. Zemzemi, and D. J. Gavaghan (2013). Chaste: An Open Source C++ Library for Computational Physiology and Biology. *PLoS Computational Biology* **9**(3) e1002970. DOI: 10.1371/journal.pcbi.1002970.

Mirams, G. R., Y. Cui, A. Sher, M. Fink, J. Cooper, B. M. Heath, N. C. McMahon, D. J. Gavaghan, and D. Noble (2011). Simulation of multiple ion channel block provides improved early prediction of compounds' clinical torsadogenic risk. *Cardiovascular Research* **91**(1) 53–61. DOI: 10.1093/cvr/cvr044.

Mirams, G. R., M. R. Davies, S. J. Brough, M. H. Bridgland-Taylor, Y. Cui, D. J. Gavaghan, and N. Abi-Gerges (2014). Prediction of Thorough QT study results using action potential simulations based on ion channel screens. *Journal of Pharmacological and Toxicological Methods* **70**(3) 246–254. DOI: 10.1016/j.vascn.2014.07.002.

Mirollo, R. and S. Strogatz (1990). Synchronization of Pulse-Coupled Biological Oscillators. *SIAM Journal on Applied Mathematics* **50**(6) 1645–1662. DOI: 10.1137/0150098.

Mistry, H. B., M. R. Davies, and G. Y. Di Veroli (2015). A new classifier-based strategy for in-silico ion-channel cardiac drug safety assessment. *Predictive Toxicology* **6** 59. DOI: 10.3389/fphar.2015.00059.

Molokhia, M., A. Pathak, M. Lapeyre-Mestre, L. Caturla, J. L. Montastruc, and P. McKeigue (2008). Case ascertainment and estimated incidence of drug-induced long-QT syndrome: study in Southwest France. *British Journal of Clinical Pharmacology* **66**(3) 386–395. DOI: 10.1111/j.1365-2125.2008.03229.x.

Monahan, B. P., C. L. Ferguson, E. S. Killeavy, B. K. Lloyd, J. Troy, and L. R. Cantilena (1990). Torsades de Pointes Occurring in Association With Terfenadine Use. *Journal of the American Medical Association* **264**(21) 2788–2790. DOI: 10.1001/jama.1990.03450210088038.

Moreau, A., A. Mercier, O. Thériault, M. Boutjdir, B. Burger, D. I. Keller, and M. Chahine (2017). Biophysical, Molecular, and Pharmacological Characterization of Voltage-Dependent Sodium Channels From Induced Pluripotent Stem Cell-Derived Cardiomyocytes. *Canadian Journal of Cardiology* **33**(2) 269–278. DOI: 10.1016/j.cjca.2016.10.001.

Morgan, S. W., G. Plank, I. V. Biktasheva, and V. N. Biktashev (2009). Low Energy Defibrillation in Human Cardiac Tissue: A Simulation Study. *Biophysical Journal* **96**(4) 1364–1373. DOI: 10.1016/j.bpj.2008.11.031.

Moulin, C., A. Gliere, D. Barbier, S. Joucla, B. Yvert, P. Mailley, and R. Guillemaud (2008). A New 3-D Finite-Element Model Based on Thin-Film Approximation for Microelectrode Array Recording of Extracellular Action Potential. *IEEE Transactions on Biomedical Engineering* **55**(2) 683–692. DOI: 10.1109/TBME.2007.903522.

Mummery, C. L., J. Zhang, E. S. Ng, D. A. Elliott, A. G. Elefanty, and T. J. Kamp (2012). Differentiation of Human Embryonic Stem Cells and Induced Pluripotent Stem Cells to Cardiomyocytes A Methods Overview. *Circulation Research* **111**(3) 344–358. DOI: 10.1161/CIRCRESAHA.110.227512.

Nagumo, J., S. Arimoto, and S. Yoshizawa (1962). An Active Pulse Transmission Line Simulating Nerve Axon. *Proceedings of the IRE* **50**(10) 2061–2070. DOI: 10.1109/JRPROC.1962.288235.

Nalos, L., R. Varkevisser, M. Jonsson, M. Houtman, J. Beekman, R. van der Nagel, M. Thomsen, G. Duker, P. Sartipy, T. de Boer, M. Peschar, M. Rook, T. van Veen, M. van der Heyden, and M. Vos (2012). Comparison of the IKr blockers moxifloxacin, dofetilide and E-4031 in five screening models of pro-arrhythmia reveals lack of specificity of isolated cardiomyocytes. *British Journal of Pharmacology* **165**(2) 467–478. DOI: 10.1111/j.1476-5381.2011.01558.x.

Nattel, S. and L. Carlsson (2006). Innovative approaches to anti-arrhythmic drug therapy. *Nature Reviews Drug Discovery* **5**(12) 1034–1049. DOI: 10.1038/nrd2112.

Navarrete, E. G., P. Liang, F. Lan, V. Sanchez-Freire, C. Simmons, T. Gong, A. Sharma, P. W. Burridge, B. Patlolla, A. S. Lee, H. Wu, R. E. Beygui, S. M. Wu, R. C. Robbins, D. M. Bers, and J. C. Wu (2013). Screening Drug-Induced Arrhythmia Events Using Human Induced Pluripotent Stem Cell-Derived Cardiomyocytes and Low-Impedance Microelectrode Arrays. *Circulation* **128**(11, Supplement 1) S3–S13. DOI: 10.1161/CIRCULATIONAHA.112.000570.

Nerbonne, J. M. and R. S. Kass (2005). Molecular Physiology of Cardiac Repolarization. *Physiological Reviews* **85**(4) 1205–1253. DOI: 10.1152/physrev.00002.2005.

Neu, J. C. and W. Krassowska (1993). Homogenization of syncytial tissues. *Critical Reviews in Biomedical Engineering* **21**(2) 137–199.

Nickerson, D. P., D. Ladd, J. R. Hussan, S. Safaei, V. Suresh, P. J. Hunter, and C. P. Bradley (2015). Using CellML with OpenCMISS to Simulate Multi-Scale Physiology. *Frontiers in Bioengineering and Biotechnology* **2** 79. DOI: 10.3389/fbioe.2014.00079.

Niederer, S. A., M. Fink, D. Noble, and N. P. Smith (2009). A meta-analysis of cardiac electrophysiology computational models. *Experimental Physiology* **94**(5) 486–495. DOI: 10.1113/expphysiol.2008.044610.

Niederer, S. A., E. Kerfoot, A. P. Benson, M. O. Bernabeu, O. Bernus, C. Bradley, E. M. Cherry, R. Clayton, F. H. Fenton, A. Garny, E. Heidenreich, S. Land, M. Maleckar, P. Pathmanathan, G. Plank, J. F. Rodríguez, I. Roy, F. B. Sachse, G. Seemann, O. Skavhaug, and N. P. Smith (2011). Verification of cardiac tissue electrophysiology simulators using an N-version benchmark. *Philosophical Transactions of the Royal Society A: Mathematical, Physical and Engineering Sciences* **369**(1954) 4331–4351. DOI: 10.1098/rsta.2011.0139.

Noble, D. (1962). A modification of the Hodgkin-Huxley equations applicable to Purkinje fibre action and pacemaker potentials. *The Journal of Physiology* **160**(2) 317–352.

Noble, D. and P. J. Noble (2006). Late sodium current in the pathophysiology of cardiovascular disease: consequences of sodium–calcium overload. *Heart* **92**(Supplement 4) iv1–iv5. DOI: 10.1136/hrt.2005.078782.

Noble, D., A. Garny, and P. J. Noble (2012). How the Hodgkin–Huxley equations inspired the Cardiac Physiome Project. *The Journal of Physiology* **590**(11) 2613–2628. DOI: 10.1113/jphysiol.2011.224238.

Nozaki, Y., Y. Honda, S. Tsujimoto, H. Watanabe, T. Kunimatsu, and H. Funabashi (2014). Availability of human induced pluripotent stem cell-derived cardiomyocytes in assessment of drug potential for QT prolongation. *Toxicology and Applied Pharmacology* **278**(1) 72–77. DOI: 10.1016/j.taap.2014.04.007.

Obergrussberger, A., K. Juhasz, U. Thomas, S. Stölzle-Feix, N. Becker, L. Dörr, M. Beckler, C. Bot, M. George, and N. Fertig (2016). Safety pharmacology studies using EFP and impedance. *Journal of Pharmacological and Toxicological Methods* **81** 223–232. DOI: 10.1016/j.vascn.2016.04.006.

O'Hara, T., L. Virág, A. Varró, and Y. Rudy (2011). Simulation of the Undiseased Human Cardiac Ventricular Action Potential: Model Formulation and Experimental Validation. *PLoS Computational Biology* **7**(5) e1002061. DOI: 10.1371/journal.pcbi.1002061.

Oren, R. V. and C. E. Clancy (2010). Determinants of Heterogeneity, Excitation and Conduction in the Sinoatrial Node: A Model Study. *PLoS Computational Biology* **6**(12) e1001041. DOI: 10.1371/journal.pcbi.1001041.

Otsuji, T. G., I. Minami, Y. Kurose, K. Yamauchi, M. Tada, and N. Nakatsuji (2010). Progressive maturation in contracting cardiomyocytes derived from human embryonic stem cells: Qualitative effects on electrophysiological responses to drugs. *Stem Cell Research* **4**(3) 201–213. DOI: 10.1016/j.scr.2010.01.002.

Paci, M., J. Hyttinen, K. Aalto-Setälä, and S. Severi (2013a). Computational Models of Ventricular- and Atrial-Like Human Induced Pluripotent Stem Cell Derived Cardiomyocytes. *Annals of Biomedical Engineering* **41**(11) 2334–2348. DOI: 10.1007/s10439-013-0833-3.

Paci, M., J. Hyttinen, B. Rodriguez, and S. Severi (2015). Human induced pluripotent stem cell-derived versus adult cardiomyocytes: an in silico electrophysiological study on effects of ionic current block. *British Journal of Pharmacology* **172**(21) 5147–5160. DOI: 10.1111/bph.13282.

Paci, M., J. Hyttinen, and S. Severi (2013b). Computational modelling of LQT1 in human induced pluripotent stem cell derived cardiomyocytes. In *Computing in Cardiology 2013*, 1239–1242.

Paci, M., L. Sartiani, M. D. Lungo, M. Jaconi, A. Mugelli, E. Cerbai, and S. Severi (2012). Mathematical modelling of the action potential of human embryonic stem cell derived cardiomyocytes. *BioMedical Engineering OnLine* **11**(1) 61. DOI: 10.1186/1475-925X-11-61.

Paci, M., S. Severi, and J. Hyttinen (2014). Computational modeling supports induced pluripotent stem cell-derived cardiomyocytes reliability as a model for human LQT3. In *Computing in Cardiology 2014*, 69–72.

Pasqualini, F. S., S. P. Sheehy, A. Agarwal, Y. Aratyn-Schaus, and K. K. Parker (2015). Structural Phenotyping of Stem Cell-Derived Cardiomyocytes. *Stem Cell Reports* **4**(3) 340–347. DOI: 10.1016/j.stemcr.2015.01.020.

Passini, E., O. J. Britton, H. R. Lu, J. Rohrbacher, A. N. Hermans, D. J. Gallacher, R. J. H. Greig, A. Bueno-Orovio, and B. Rodriguez (2017). Human In Silico Drug Trials Demonstrate Higher Accuracy than Animal Models in Predicting Clinical Pro-Arrhythmic Cardiotoxicity. *Frontiers in Physiology* **8** DOI: 10.3389/fphys.2017.00668.

Pathmanathan, P. (2012). *Finite Element Implementations in Chaste*. Report: DOI: 10.6084/m9.figshare.3843825.v1.

Pathmanathan, P., M. O. Bernabeu, R. Bordas, J. Cooper, A. Garny, J. M. Pitt-Francis, J. P. Whiteley, and D. J. Gavaghan (2010). A numerical guide to the solution of the bidomain equations of cardiac electrophysiology. *Progress in Biophysics and Molecular Biology* **102**(2–3) 136–155. DOI: 10.1016/j.pbiomolbio.2010.05.006.

Pathmanathan, P. and R. A. Gray (2014). Verification of computational models of cardiac electro-physiology. *International Journal for Numerical Methods in Biomedical Engineering* **30**(5) 525–544. DOI: 10.1002/cnm.2615.

Pekkanen-Mattila, M., H. Chapman, E. Kerkelä, R. Suuronen, H. Skottman, A.-P. Koivisto, and K. Aalto-Setälä (2010). Human embryonic stem cell-derived cardiomyocytes: demonstration of a portion of cardiac cells with fairly mature electrical phenotype. *Experimental Biology and Medicine* **235**(4) 522–530. DOI: 10.1258/ebm.2010.009345.

Pitt-Francis, J., P. Pathmanathan, M. O. Bernabeu, R. Bordas, J. Cooper, A. G. Fletcher, G. R. Mirams, P. Murray, J. M. Osborne, A. Walter, S. J. Chapman, A. Garny, I. M. M. van Leeuwen, P. K. Maini, B. Rodríguez, S. L. Waters, J. P. Whiteley, H. M. Byrne, and D. J. Gavaghan (2009). Chaste: A test-driven approach to software development for biological modelling. *Computer Physics Communications* **180**(12) 2452–2471. DOI: 10.1016/j.cpc.2009.07.019.

Potse, M., B. Dube, J. Richer, A. Vinet, and R. Gulrajani (2006). A Comparison of Monodomain and Bidomain Reaction-Diffusion Models for Action Potential Propagation in the Human Heart. *IEEE Transactions on Biomedical Engineering* **53**(12) 2425–2435. DOI: 10.1109/TBME.2006.880875.

Priebe, L. and D. J. Beuckelmann (1998). Simulation Study of Cellular Electric Properties in Heart Failure. *Circulation Research* **82**(11) 1206–1223. DOI: 10.1161/01.RES.82.11.1206.

Pullan, A. J., L. K. Cheng, and M. L. Buist (2005). *Mathematically Modelling the Electrical Activity of the Heart: From Cell to Body Surface and Back Again*. World Scientific. ISBN: 978-981-256-373-6.

Rast, G., J. Weber, C. Disch, E. Schuck, C. Ittrich, and B. D. Guth (2015). An integrated platform for simultaneous multi-well field potential recording and Fura-2-based calcium transient ratiometry in human induced pluripotent stem cell (hiPSC)-derived cardiomyocytes. *Journal of Pharmacological and Toxicological Methods* **75** 91–100. DOI: 10.1016/j.vascn.2015.04.005.

Redfern, W. S., I. D. Wakefield, H. Prior, C. E. Pollard, T. G. Hammond, and J.-P. Valentin (2002). Safety pharmacology – a progressive approach. *Fundamental*

& Clinical Pharmacology **16**(3) 161–173. DOI: 10.1046/j.1472-8206.2002.00098.x.

Ribeiro, M. C., L. G. Tertoolen, J. A. Guadix, M. Bellin, G. Kosmidis, C. D'Aniello, J. Monshouwer-Kloots, M.-J. Goumans, Y.-l. Wang, A. W. Feinberg, C. L. Mummery, and R. Passier (2015). Functional maturation of human pluripotent stem cell derived cardiomyocytes in vitro – Correlation between contraction force and electrophysiology. *Biomaterials* **51** 138–150. DOI: 10.1016/j.biomaterials.2015.01.067.

Richardson, G. and S. Chapman (2011). Derivation of the Bidomain Equations for a Beating Heart with a General Microstructure. *SIAM Journal on Applied Mathematics* **71**(3) 657–675. DOI: 10.1137/090777165.

Riedel, M., C. J. Jou, S. Lai, R. L. Lux, A. P. Moreno, K. W. Spitzer, E. Christians, M. Tristani-Firouzi, and I. J. Benjamin (2014). Functional and Pharmacological Analysis of Cardiomyocytes Differentiated from Human Peripheral Blood Mononuclear-Derived Pluripotent Stem Cells. *Stem Cell Reports* **3**(1) 131–141. DOI: 10.1016/j.stemcr.2014.04.017.

Robertson, C., D. D. Tran, and S. C. George (2013). Concise Review: Maturation Phases of Human Pluripotent Stem Cell-Derived Cardiomyocytes. *Stem Cells* **31**(5) 829–837. DOI: 10.1002/stem.1331.

Rocha, A. M., K. Campbell, S. Mironov, J. Jiang, L. Mundada, G. Guerrero-Serna, J. Jalife, and T. J. Herron (2017). hiPSC-CM Monolayer Maturation State Determines Drug Responsiveness in High Throughput Pro-Arrhythmia Screen. *Scientific Reports* **7**(1) 13834. DOI: 10.1038/s41598-017-13590-y.

Roden, D. M., R. Lazzara, M. Rosen, P. J. Schwartz, J. Towbin, and G. M. Vincent (1996). Multiple Mechanisms in the Long-QT Syndrome. *Circulation* **94**(8) 1996–2012. DOI: 10.1161/01.CIR.94.8.1996.

Roy, M.-L., R. Dumaine, and A. M. Brown (1996). HERG, a Primary Human Ventricular Target of the Nonsedating Antihistamine Terfenadine. *Circulation* **94**(4) 817–823. DOI: 10.1161/01.CIR.94.4.817.

Rush, S. and H. Larsen (1978). A Practical Algorithm for Solving Dynamic Membrane Equations. *IEEE Transactions on Biomedical Engineering* **25**(4) 389–392. DOI: 10.1109/TBME.1978.326270.

Sachse, F. B., A. P. Moreno, G. Seemann, and J. A. Abildskov (2009). A Model of Electrical Conduction in Cardiac Tissue Including Fibroblasts. *Annals of Biomedical Engineering* **37**(5) 874–889. DOI: 10.1007/s10439-009-9667-4.

Sadrieh, A., L. Domanski, J. Pitt-Francis, S. A. Mann, E. C. Hodkinson, C.-A. Ng, M. D. Perry, J. A. Taylor, D. Gavaghan, R. N. Subbiah, J. I. Vandenberg, and A. P. Hill (2014). Multiscale cardiac modelling reveals the origins of notched T waves in long QT syndrome type 2. *Nature Communications* **5** 5069. DOI: 10.1038/ncomms6069.

Sager, P. T., G. Gintant, J. R. Turner, S. Pettit, and N. Stockbridge (2014). Rechanneling the cardiac proarrhythmia safety paradigm: A meeting report from the Cardiac Safety Research Consortium. *American Heart Journal* **167**(3) 292–300. DOI: 10.1016/j.ahj.2013.11.004.

Sarganas, G., E. Garbe, A. Klimpel, R. C. Hering, E. Bronder, and W. Haverkamp (2014). Epidemiology of symptomatic drug-induced long QT syndrome and

torsade de pointes in Germany. *EP Europace* **16**(1) 101–108. DOI: 10.1093/europace/eut214.

Sartiani, L., E. Bettiol, F. Stillitano, A. Mugelli, E. Cerbai, and M. E. Jaconi (2007). Developmental Changes in Cardiomyocytes Differentiated from Human Embryonic Stem Cells: A Molecular and Electrophysiological Approach. *Stem Cells* **25**(5) 1136–1144. DOI: 10.1634/stemcells.2006-0466.

Satin, J., I. Kehat, O. Caspi, I. Huber, G. Arbel, I. Itzhaki, J. Magyar, E. A. Schroder, I. Perlman, and L. Gepstein (2004). Mechanism of spontaneous excitability in human embryonic stem cell derived cardiomyocytes. *The Journal of Physiology* **559**(2) 479–496. DOI: 10.1113/jphysiol.2004.068213.

Schoenwolf, G. C., S. B. Bleyl, P. R. Brauer, and P. H. Francis-West (2014). *Larsen's Human Embryology E-Book*. Elsevier Health Sciences. ISBN: 978-1-4557-2791-9.

Schwartz, P. J. and R. L. Woosley (2016). Predicting the Unpredictable: Drug-Induced QT Prolongation and Torsades de Pointes. *Journal of the American College of Cardiology* **67**(13) 1639–1650. DOI: 10.1016/j.jacc.2015.12.063.

Schweizer, P. A., F. F. Darche, N. D. Ullrich, P. Geschwill, B. Greber, R. Rivinius, C. Seyler, K. Müller-Decker, A. Draguhn, J. Utikal, M. Koenen, H. A. Katus, and D. Thomas (2017). Subtype-specific differentiation of cardiac pacemaker cell clusters from human induced pluripotent stem cells. *Stem Cell Research & Therapy* **8** 229. DOI: 10.1186/s13287-017-0681-4.

Seemann, G., F. B. Sachse, M. Karl, D. L. Weiss, V. Heuveline, and O. Dössel (2010). Framework for Modular, Flexible and Efficient Solving the Cardiac Bidomain Equations Using PETSc. In *Progress in Industrial Mathematics at ECMI 2008*. Ed. A. D. Fitt, J. Norbury, H. Ockendon, and E. Wilson. Mathematics in Industry 15, Springer Berlin Heidelberg, 363–369. ISBN: 978-3-642-12109-8 978-3-642-12110-4. DOI: 10.1007/978-3-642-12110-4_55.

Seemann, G., C. Höper, F. B. Sachse, O. Dössel, A. V. Holden, and H. Zhang (2006). Heterogeneous three-dimensional anatomical and electrophysiological model of human atria. *Philosophical Transactions of the Royal Society of London A: Mathematical, Physical and Engineering Sciences* **364**(1843) 1465–1481. DOI: 10.1098/rsta.2006.1781.

Shah, R. R. (2005). Drugs, QT Interval Prolongation and ICH E14. *Drug Safety* **28**(2) 115–125. DOI: 10.2165/00002018-200528020-00003.

Shen, N., A. Knopf, C. Westendorf, U. Kraushaar, J. Riedl, H. Bauer, S. Pöschel, S. L. Layland, M. Holeiter, S. Knolle, E. Brauchle, A. Nsair, S. Hinderer, and K. Schenke-Layland (2017). Steps toward Maturation of Embryonic Stem Cell-Derived Cardiomyocytes by Defined Physical Signals. *Stem Cell Reports* **9**(1) 122–135. DOI: 10.1016/j.stemcr.2017.04.021.

Shimizu, W. and C. Antzelevitch (1998). Cellular Basis for the ECG Features of the LQT1 Form of the Long-QT Syndrome. *Circulation* **98**(21) 2314–2322. DOI: 10.1161/01.CIR.98.21.2314.

Snir, M., I. Kehat, A. Gepstein, R. Coleman, J. Itskovitz-Eldor, E. Livne, and L. Gepstein (2003). Assessment of the ultrastructural and proliferative properties of human embryonic stem cell-derived cardiomyocytes. *American Journal of Physiology - Heart and Circulatory Physiology* **285**(6) H2355–H2363. DOI: 10.1152/ajpheart.00020.2003.

Spira, M. E. and A. Hai (2013). Multi-electrode array technologies for neuroscience and cardiology. *Nature Nanotechnology* **8**(2) 83–94. DOI: 10.1038/nnano.2012.265.

Stancescu, M., P. Molnar, C. W. McAleer, W. McLamb, C. J. Long, C. Oleaga, J.-M. Prot, and J. J. Hickman (2015). A phenotypic in vitro model for the main determinants of human whole heart function. *Biomaterials* **60** 20–30. DOI: 10.1016/j.biomaterials.2015.04.035.

Strogatz, S. H. (2000). From Kuramoto to Crawford: exploring the onset of synchronization in populations of coupled oscillators. *Physica D: Nonlinear Phenomena* **143**(1–4) 1–20. DOI: 10.1016/S0167-2789(00)00094-4.

Süli, E. (2012). *Lecture Notes on Finite Element Methods for Partial Differential Equations*. Mathematical Institute, University of Oxford.

Süli, E. and D. F. Mayers (2003). *An Introduction to Numerical Analysis*. Cambridge University Press. ISBN: 978-1-139-43788-2.

Synnergren, J., C. Améen, A. Jansson, and P. Sartipy (2012). Global transcriptional profiling reveals similarities and differences between human stem cell-derived cardiomyocyte clusters and heart tissue. *Physiological Genomics* **44**(4) 245–258. DOI: 10.1152/physiolgenomics.00118.2011.

Takahashi, K., K. Tanabe, M. Ohnuki, M. Narita, T. Ichisaka, K. Tomoda, and S. Yamanaka (2007). Induction of Pluripotent Stem Cells from Adult Human Fibroblasts by Defined Factors. *Cell* **131**(5) 861–872. DOI: 10.1016/j.cell.2007.11.019.

Talbert, D. R., K. R. Doherty, P. B. Trusk, D. M. Moran, S. A. Shell, and S. Bacus (2015). A Multi-parameter In Vitro Screen in Human Stem Cell-Derived Cardiomyocytes Identifies Ponatinib-Induced Structural and Functional Cardiac Toxicity. *Toxicological Sciences* **143**(1) 147–155. DOI: 10.1093/toxsci/kfu215.

Tang, W., J. Kang, X. Wu, D. Rampe, L. Wang, H. Shen, Z. Li, D. Dunnington, and T. Garyantes (2001). Development and Evaluation of High Throughput Functional Assay Methods for hERG Potassium Channel. *Journal of Biomolecular Screening* **6**(5) 325–331. DOI: 10.1177/108705710100600506.

Ten Tusscher, K. H. W. J., D. Noble, P. J. Noble, and A. V. Panfilov (2004). A model for human ventricular tissue. *American Journal of Physiology - Heart and Circulatory Physiology* **286**(4) H1573–H1589. DOI: 10.1152/ajpheart.00794.2003.

Ten Tusscher, K. H. W. J. and A. V. Panfilov (2006). Alternans and spiral breakup in a human ventricular tissue model. *American Journal of Physiology - Heart and Circulatory Physiology* **291**(3) H1088–H1100. DOI: 10.1152/ajpheart.00109.2006.

Thomas Jr., C. A., P. A. Springer, G. E. Loeb, Y. Berwald-Netter, and L. M. Okun (1972). A miniature microelectrode array to monitor the bioelectric activity of cultured cells. *Experimental Cell Research* **74**(1) 61–66. DOI: 10.1016/0014-4827(72)90481-8.

Thomson, J. A., J. Itskovitz-Eldor, S. S. Shapiro, M. A. Waknitz, J. J. Swiergiel, V. S. Marshall, and J. M. Jones (1998). Embryonic Stem Cell Lines Derived from Human Blastocysts. *Science* **282**(5391) 1145–1147. DOI: 10.1126/science.282.5391.1145.

Tixier, E., F. Raphel, D. Lombardi, and J.-F. Gerbeau (2018). Composite Biomarkers Derived from Micro-Electrode Array Measurements and Computer Simulations Improve the Classification of Drug-Induced Channel Block. *Frontiers in Physiology* **8** 1096. DOI: 10.3389/fphys.2017.01096.

Toyoshima, S., A. Kanno, T. Kitayama, K. Sekiya, K. Nakai, M. Haruna, T. Mino, H. Miyazaki, K. Yano, and K. Yamamoto (2005). QT PRODACT: In Vivo QT Assay in the Conscious Dog for Assessing the Potential for QT Interval Prolongation by Human Pharmaceuticals. *Journal of Pharmacological Sciences* **99**(5) 459–471. DOI: 10.1254/jphs.QT-A2.

Trayanova, N. A., J. Constantino, and V. Gurev (2011). Electromechanical models of the ventricles. *American Journal of Physiology - Heart and Circulatory Physiology* **301**(2) H279–H286. DOI: 10.1152/ajpheart.00324.2011.

Tung, L. (1978). A bi-domain model for describing ischemic myocardial d-c potentials. PhD Thesis. Massachusetts Institute of Technology.

Vaidyanathan, R., Y. S. Markandeya, T. J. Kamp, J. C. Makielski, C. T. Janaury, and L. L. Eckhardt (2016). IK1-Enhanced Human Induced Pluripotent Stem Cell-Derived Cardiomyocytes: An Improved Cardiomyocyte Model to Investigate Inherited Arrhythmia Syndromes. *American Journal of Physiology - Heart and Circulatory Physiology* **310**(11) H1611–H1621. DOI: 10.1152/ajpheart.00481.2015.

Van den Heuvel, N. H. L., T. A. B. van Veen, B. Lim, and M. K. B. Jonsson (2014). Lessons from the heart: Mirroring electrophysiological characteristics during cardiac development to in vitro differentiation of stem cell derived cardiomyocytes. *Journal of Molecular and Cellular Cardiology* **67** 12–25. DOI: 10.1016/j.yjmcc.2013.12.011.

Veerman, C. C., I. Mengarelli, K. Guan, M. Stauske, J. Barc, H. L. Tan, A. A. M. Wilde, A. O. Verkerk, and C. R. Bezzina (2016). hiPSC-derived cardiomyocytes from Brugada Syndrome patients without identified mutations do not exhibit clear cellular electrophysiological abnormalities. *Scientific Reports* **6** 30967. DOI: 10.1038/srep30967.

Verkerk, A. O., C. C. Veerman, J. G. Zegers, I. Mengarelli, C. R. Bezzina, and R. Wilders (2017). Patch-Clamp Recording from Human Induced Pluripotent Stem Cell-Derived Cardiomyocytes: Improving Action Potential Characteristics through Dynamic Clamp. *International Journal of Molecular Sciences* **18**(9) 1873. DOI: 10.3390/ijms18091873.

Vestergaard, M. L., S. Grubb, K. Koefoed, Z. Anderson-Jenkins, K. Grunnet-Lauridsen, K. Calloe, C. Clausen, S. T. Christensen, K. Møllgård, and C. Y. Andersen (2017). Human Embryonic Stem Cell-Derived Cardiomyocytes Self-Arrange with Areas of Different Subtypes During Differentiation. *Stem Cells and Development* **26**(21) 1566–1577. DOI: 10.1089/scd.2017.0054.

Vigmond, E. J., M. Hughes, G. Plank, and L. J. Leon (2003). Computational tools for modeling electrical activity in cardiac tissue. *Journal of Electrocardiology* **36**(Supplement 1) 69–74. DOI: 10.1016/j.jelectrocard.2003.09.017.

Vigmond, E., R. Weber dos Santos, A. Prassl, M. Deo, and G. Plank (2008). Solvers for the cardiac bidomain equations. *Progress in Biophysics and Molecular Biology* **96**(1–3) 3–18. DOI: 10.1016/j.pbiomolbio.2007.07.012.

Wang, D., C. Patel, C. Cui, and G.-X. Yan (2008). Preclinical assessment of drug-induced proarrhythmias: Role of the arterially perfused rabbit left ventricular wedge preparation. *Pharmacology & Therapeutics* **119**(2) 141–151. DOI: 10.1016/j.pharmthera.2008.02.009.

Wang, J., R. H. Schwinger, K. Frank, J. Müller-Ehmsen, P. Martin-Vasallo, T. A. Pressley, A. Xiang, E. Erdmann, and A. A. McDonough (1996). Regional expression of sodium pump subunits isoforms and Na+-Ca++ exchanger in the human heart. *Journal of Clinical Investigation* **98**(7) 1650–1658. DOI: 10.1172/JCI118960.

Wang, Q., J. Shen, I. Splawski, D. Atkinson, Z. Li, J. L. Robinson, A. J. Moss, J. A. Towbin, and M. T. Keating (1995). SCN5A mutations associated with an inherited cardiac arrhythmia, long QT syndrome. *Cell* **80**(5) 805–811. DOI: 10.1016/0092-8674(95)90359-3.

Weng, Z., C.-W. Kong, L. Ren, I. Karakikes, L. Geng, J. He, M. Z. Y. Chow, C. F. Mok, W. Keung, H. Chow, A. Y. H. Leung, R. J. Hajjar, R. A. Li, and C. W. Chan (2014). A Simple, Cost-Effective but Highly Efficient System for Deriving Ventricular Cardiomyocytes from Human Pluripotent Stem Cells. *Stem Cells and Development* **23**(14) 1704–1716. DOI: 10.1089/scd.2013.0509.

Werley, C. A., M.-P. Chien, J. Gaublomme, K. Shekhar, V. Butty, B. A. Yi, J. M. Kralj, W. Bloxham, L. A. Boyer, A. Regev, and A. E. Cohen (2017). Geometry-dependent functional changes in iPSC-derived cardiomyocytes probed by functional imaging and RNA sequencing. *PLoS ONE* **12**(3) e0172671. DOI: 10.1371/journal.pone.0172671.

Whiteley, J. (2017). *Finite Element Methods: A Practical Guide*. Springer. ISBN: 978-3-319-49971-0.

Winfree, A. T. (1967). Biological rhythms and the behavior of populations of coupled oscillators. *Journal of Theoretical Biology* **16**(1) 15–42. DOI: 10.1016/0022-5193(67)90051-3.

Winslow, R. L., A. L. Kimball, A. Varghese, and D. Noble (1993). Simulating cardiac sinus and atrial network dynamics on the connection machine. *Physica D: Nonlinear Phenomena* **64**(1–3) 281–298. DOI: 10.1016/0167-2789(93)90260-8.

Wiśniowska, B., Z. Tylutki, and S. Polak (2017). Thorough QT (TQT) studies: concordance with torsadogenesis and an evolving cardiac safety testing paradigm. *Drug Discovery Today* **22**(10) 1460–1465. DOI: 10.1016/j.drudis.2017.04.017.

Wysowski, D. K. and J. Bacsanyi (1996). Cisapride and Fatal Arrhythmia. *New England Journal of Medicine* **335**(4) 290–291. DOI: 10.1056/NEJM199607253350416.

Xu, B., S. Binczak, S. Jacquir, O. Pont, and H. Yahia (2014). Parameters analysis of FitzHugh-Nagumo model for a reliable simulation. In *2014 36th Annual International Conference of the IEEE Engineering in Medicine and Biology Society*, 4334–4337. DOI: 10.1109/EMBC.2014.6944583.

Xu, C., S. Police, N. Rao, and M. K. Carpenter (2002). Characterization and Enrichment of Cardiomyocytes Derived From Human Embryonic Stem Cells.

Circulation Research **91**(6) 501–508. DOI: 10.1161/01.RES.0000035254.80718.91.

Yang, X., M. Rodriguez, L. Pabon, K. A. Fischer, H. Reinecke, M. Regnier, N. J. Sniadecki, H. Ruohola-Baker, and C. E. Murry (2014). Tri-iodo-l-thyronine promotes the maturation of human cardiomyocytes-derived from induced pluripotent stem cells. *Journal of Molecular and Cellular Cardiology* **72** 296–304. DOI: 10.1016/j.yjmcc.2014.04.005.

Yap, Y. G. and A. J. Camm (2003). Drug induced QT prolongation and torsades de pointes. *Heart* **89**(11) 1363–1372. DOI: 10.1136/heart.89.11.1363.

Yechikov, S., R. Copaciu, J. M. Gluck, W. Deng, N. Chiamvimonvat, J. W. Chan, and D. K. Lieu (2016). Same-Single-Cell Analysis of Pacemaker-Specific Markers in Human Induced Pluripotent Stem Cell-Derived Cardiomyocyte Subtypes Classified by Electrophysiology. *Stem Cells* **34**(11) 2670–2680. DOI: 10.1002/stem.2466.

Yifrach, O. (2004). Hill Coefficient for Estimating the Magnitude of Cooperativity in Gating Transitions of Voltage-Dependent Ion Channels. *Biophysical Journal* **87**(2) 822–830. DOI: 10.1529/biophysj.104.040410.

Yokoo, N., S. Baba, S. Kaichi, A. Niwa, T. Mima, H. Doi, S. Yamanaka, T. Nakahata, and T. Heike (2009). The effects of cardioactive drugs on cardiomyocytes derived from human induced pluripotent stem cells. *Biochemical and Biophysical Research Communications* **387**(3) 482–488. DOI: 10.1016/j.bbrc.2009.07.052.

Yuan, Y., X. Bai, C. Luo, K. Wang, and H. Zhang (2015). The virtual heart as a platform for screening drug cardiotoxicity. *British Journal of Pharmacology* **172**(23) 5531–5547. DOI: 10.1111/bph.12996.

Zemzemi, N., M. O. Bernabeu, J. Saiz, J. Cooper, P. Pathmanathan, G. R. Mirams, J. Pitt-Francis, and B. Rodriguez (2013). Computational assessment of drug-induced effects on the electrocardiogram: from ion channel to body surface potentials. *British Journal of Pharmacology* **168**(3) 718–733. DOI: 10.1111/j.1476-5381.2012.02200.x.

Zhang, D., I. Y. Shadrin, J. Lam, H.-Q. Xian, H. R. Snodgrass, and N. Bursac (2013). Tissue-engineered cardiac patch for advanced functional maturation of human ESC-derived cardiomyocytes. *Biomaterials* **34**(23) 5813–5820. DOI: 10.1016/j.biomaterials.2013.04.026.

Zhang, J., G. F. Wilson, A. G. Soerens, C. H. Koonce, J. Yu, S. P. Palecek, J. A. Thomson, and T. J. Kamp (2009). Functional Cardiomyocytes Derived From Human Induced Pluripotent Stem Cells. *Circulation Research* **104**(4) e30–e41. DOI: 10.1161/CIRCRESAHA.108.192237.

Zhang, Q., J. Jiang, P. Han, Q. Yuan, J. Zhang, X. Zhang, Y. Xu, H. Cao, Q. Meng, L. Chen, T. Tian, X. Wang, P. Li, J. Hescheler, G. Ji, and Y. Ma (2011). Direct differentiation of atrial and ventricular myocytes from human embryonic stem cells by alternating retinoid signals. *Cell Research* **21**(4) 579–587. DOI: 10.1038/cr.2010.163.

Zhu, H., K. S. Scharnhorst, A. Z. Stieg, J. K. Gimzewski, I. Minami, N. Nakatsuji, H. Nakano, and A. Nakano (2017). Two dimensional electrophysiological characterization of human pluripotent stem cell-derived cardiomyocyte system. *Scientific Reports* **7** 43210. DOI: 10.1038/srep43210.

Zhu, R., A. Blazeski, E. Poon, K. D. Costa, L. Tung, and K. R. Boheler (2014). Physical developmental cues for the maturation of human pluripotent stem cell-derived cardiomyocytes. *Stem Cell Research & Therapy* **5**(5) 1–18. DOI: 10.1186/scrt507.

Zhu, R., M. A. Millrod, E. T. Zambidis, and L. Tung (2016). Variability of Action Potentials Within and Among Cardiac Cell Clusters Derived from Human Embryonic Stem Cells. *Scientific Reports* **6** 18544.

Zipes, D. P. and J. Jalife (2009). *Cardiac Electrophysiology: From Cell to Bedside*. 5th ed. Saunders/Elsevier. ISBN: 978-1-4160-5973-8.